Cardiac Mechanical Model Personalisation and its Clinical Applications

By

Jiahe XI

A thesis submitted in partial fulfillment of the requirements for the degree

of

DOCTOR OF PHILOSOPHY

Supervised by Professor Nicolas Smith and Dr. Pablo Lamata

Computational Biology Group, Department of Computer Science

Christ Church College

University of Oxford

June 30, 2013

Abstract

An increasingly important research area within the field of cardiac modelling is the development and study of methods of model-based parameter estimation from clinical measurements of cardiac function. This provides a powerful approach for the quantification of cardiac function, with the potential to ultimately lead to the improved stratification and treatment of individuals with pathological myocardial mechanics. In particular, the diastolic function (i.e., blood filling) of left ventricle (LV) is affected by its capacity for relaxation, or the decay in residual active tension (AT) whose inhibition limits the relaxation of the LV chamber, which in turn affects its compliance (or its reciprocal, stiffness). The clinical determination of these two factors, corresponding to the diastolic residual AT and passive constitutive parameters (stiffness) in the cardiac mechanical model, is thus essential for assessing LV diastolic function. However these parameters are difficult to be assessed *in vivo*, and the traditional criterion to diagnose diastolic dysfunction is subject to many limitations and controversies. In this context, the objective of this study is to develop model-based applicable methodologies to estimate in vivo, from 4D imaging measurements and LV cavity pressure recordings, these clinically relevant parameters (passive stiffness and active diastolic residual tension) in computational cardiac mechanical models, which enable the quantification of key clinical indices characterising cardiac diastolic dysfunction.

Firstly, a sequential data assimilation framework has been developed, covering various types of existing Kalman filters, outlined in chapter 3. Based on these developments, chapter 4 demonstrates that the novel reduced-order unscented Kalman filter can accurately retrieve the homogeneous and regionally varying constitutive parameters from the synthetic noisy motion measurements. This work has been published in Xi et al. 2011a.

Secondly, this thesis has investigated the development of methods that can be applied to clinical practise, which has, in turn, introduced additional difficulties and opportunities. This thesis has presented the first study, to our best knowledge, in literature estimating human constitutive parameters using clinical data, and demonstrated, for the first time, that while an end-diastolic MR measurement does not constrain the mechanical parameters uniquely, it does provide a potentially robust indicator of myocardial stiffness. This work has been published in Xi et al. 2011b. However, an unresolved issue in patients with diastolic dysfunction is that the estimation of myocardial stiffness cannot be decoupled from diastolic residual AT because of the impaired ventricular relaxation during diastole. To further address this problem, chapter 6 presents the first study to estimate diastolic parameters of the left ventricle (LV) from cine and tagged MRI measurements and LV cavity pressure recordings, separating the passive myocardial constitutive properties and diastolic residual AT. We apply this framework to three clinical cases, and the results show that the estimated constitutive parameters and residual active tension appear to be a promising candidate to delineate healthy and pathological cases. This work has been published in Xi et al. 2012a. Nevertheless, the need to invasively acquire LV pressure measurement limits the wide application of this approach. Chapter 7 addresses this issue by analysing the feasibility of using two kinds of non-invasively available pressure measurements for the purpose of inverse parameter estimation. The work has been submitted for publication in Xi et al. 2012b.

Acknowledgements

It would not have been possible to complete this work without the generous help, guidance and support from so many people, to only some of whom it is possible to give particular mention here. I received great supervision and support from my supervisors, Professor Nic Smith and Dr. Pablo Lamata. I am sincerely thankful to Nic for his consistent high-quality mentoring over these three years. As a great supervisor, he patiently introduced me in my first year into the cardiac mechanical modelling field and steering me into the right direction for the subsequent research. He arranged a number of external collaborations with INRIA group in France and medical imaging processing group in Imperial College, without which many ideas and work would not happen. In addition, he patiently read each of paper drafts for tens of times, and always gave detailed and constructive feedbacks. During the FIMH conference, Nic gave me very detailed guidance for my oral presentation, not only in term of content, but also the overall presentation tips, without which I would not have been able to deliver a well received talk. I also owe my great gratitude to Dr. Pablo Lamata, who is not only a good supervisor, but also a close friend who is ready to help at all time. I spent a lot of time working side by side with Pablo, and he has discussed with and encouraged me so many times when unexpected research problems turned up. Pablo also read my document drafts at the preliminary stage, and provided very helpful suggestions as well as critics. I also want to thank Dr. Steve Niederer, who has given invaluable amount of his time and effort to discuss and provide feedbacks for my work. It has been a tremendous privilege to be working closely in an extremely supportive and caring team, and I owe my gratitude to every single member for your technical, social and moral support, especially Dr. Jack Lee and Sander Land. In addition, I want to thank my office mates in the computing lab and the computational biology group for the nice, caring and supportive social and working environment. I want to thank my College – Christ Church for providing wonderful accommodation, meals and a socialising venue. I want to thank my friends with whom I have been through these years of life of joy, happiness as well as sadness and frustration in Oxford. Finally, I owe my deepest gratitude to my parents far away in China, who have given my tremendous moral support. To invite them to Oxford to witness my degree ceremony is my biggest dream at the moment. Thank you all for making Oxford and UK an amazing place with memories to cherish for decades to come.

Table of Contents

List of Figures

List of Tables

Part I

Background and Introduction

Chapter 1

Introduction

I found the task so truly arduous... that I was almost tempted to think... that the movement of the heart was only to be comprehended by God. For I could neither rightly perceive at first when the systole and when the diastole took place by reason of the rapidity of the movement... (Power 1897) – William Harvey (1578-1657)

1.1 Background and Motivation

1.1.1 The Human Heart and Cardiac Disease

The heart, as the most important organ in the human circulatory system, is responsible for pumping blood throughout the body by repeated, rhythmic contractions. As recognised by researchers for many centuries, including Galen, da Vinci and Harvey (Brain 1986, Popham 1945, Harvey et al. 1889), an essential step in understanding the heart's function is defining its structure and anatomy. The heart has four chambers, two superior atria and two inferior ventricles (e.g. see figure 1.1 (a)). The atria are the receiving chambers and the ventricles are the discharging chambers. The right ventricle discharges into the lungs to oxygenate the blood. The left ventricle discharges its blood toward the rest of the body via the aorta. Blood flows through the heart in one direction, from the atria to

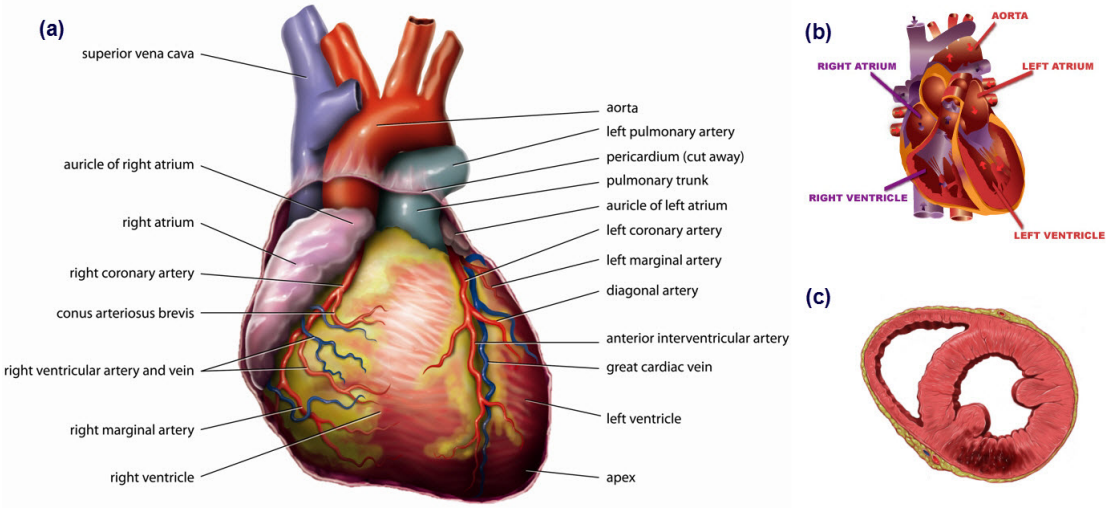

Figure 1.1: Anatomy (a), blood pathway (b), and wall infarction (c) of the human heart. (van Brussel 2010; Patrick J. Lynch 2010).

the ventricles, and out of the great arteries (figure 1.1 (b)).

A token of the importance of this fundamental physiological function is the widespread prevalence of cardiovascular disease (CVD), e.g. myocardial infarction (figure 1.1 (c)), which has a significant impact on the European society in terms of mortality, morbidity and allied healthcare costs. It causes over 2.0 million deaths in the European Union every year (42% of all deaths) with a total estimated cost of 192 billion Euros (Allender et al. 2008).

1.1.2 Clinical Measurements and Cardiac Computational Modelling

For the diagnosis and treatment planning of CVD, medical imaging measurements provide valuable assistance. Within these medical imaging technologies are the specific modalities of X-ray Computed Tomography (CT) and Magnetic Resonance Imaging (MRI) (figure 1.2 (a),(b)). The development of medical image processing methodologies and tools is one of the main focuses of imaging research communities (e.g. automatic whole-heart segmentation based on the surface model in figure 1.2(a)).

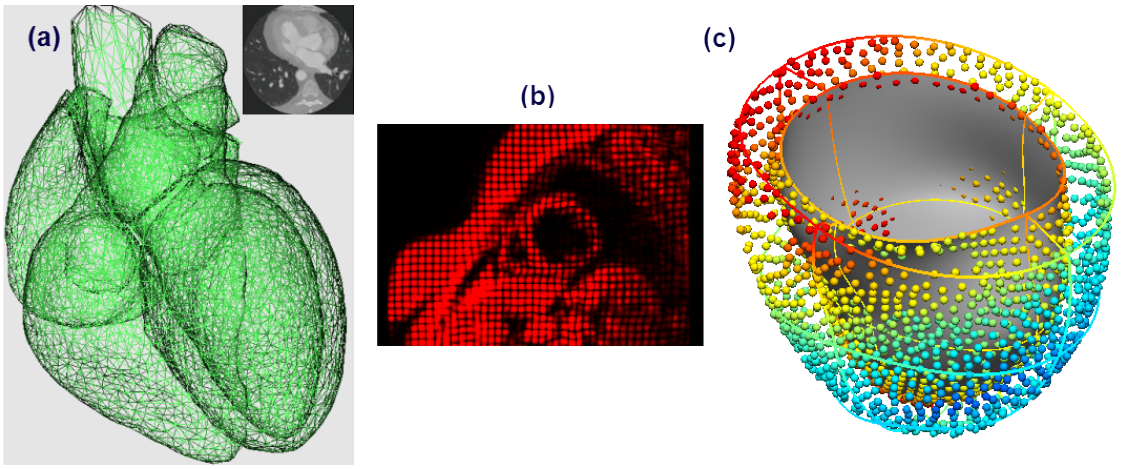

Figure 1.2: Examples of imaging data of the heart and the geometrical model of the heart. a: CT imaging data along with the surface mesh used for model-based segmentation (Ecabert et al. 2008). b: Short-axis tagged MR image. c: Patient-specific geometrical model colour coded with displacements of data points extracted from (a).

In parallel with these developments, the discipline of computational physiology provides a set of complementary tools to quantitatively describe and analyse physiological behaviour across a range of time scales and anatomical levels using mathematical and computational models (Hunter et al. 2008). Recent advances have enabled multi-level and multi-physics models, which link molecular, sub-cellular and cellular functions to whole organ performance (Lee et al. 2009). Within these developments, the heart is arguably the most advanced current exemplar of this approach (Bassingthwaighte et al. 2009).

1.1.3 The Image-driven Estimation of Cardiac Functions

The current developments of imaging measurements and computational modelling indicate that quantitative physiological models now have the potential to make a significant impact in the management of CVD in the clinic. The abnormality of myocardial mechanical and electrical properties, quantified by parameters in cardiac electro-mechanical models, could be a clinically relevant indication of cardiac diseases such as regional myocardial infarction (Abraham et al. 2006; Shishido et al. 1998). Specifically, impaired

ventricular relaxation (one of the lusitropic abnormalities commonly present in heart failure, Katz 2010) has the possibility to be directly characterised by estimating the time course of residual active tension during the diastolic phase of the heart cycle.

One of the central challenges to realising this potential is the personalisation of model parameters to individual patients. However these parameters are generally difficult to determine *ex vivo*, because obtaining viable human tissue presents a number of significant logistical and ethical challenges. Furthermore *in vivo* myocardium tissue is highly likely to display very different behaviour than that in *ex vivo* experiments. Therefore there is an obvious interest in being able to perform *in vivo* parameter estimation by coupling biophysically-based cardiac models with clinical *in vivo* imaging measurements of the cardiac motion and function.

Focus of the D.Phil.

As one of the fundamental aspects involved in the clinical personalisation of quantitative physiological models (figure 1.3), the theme of this study is focused on developing applicable methodologies to estimate, from 4D imaging measurements and LV cavity pressure recordings, the clinically relevant parameters in computational cardiac mechanical models. The specific contributions of this study are summarised below in section 1.4 after a brief overview of the existing cardiac modelling and inverse parameter estimation works in literature.

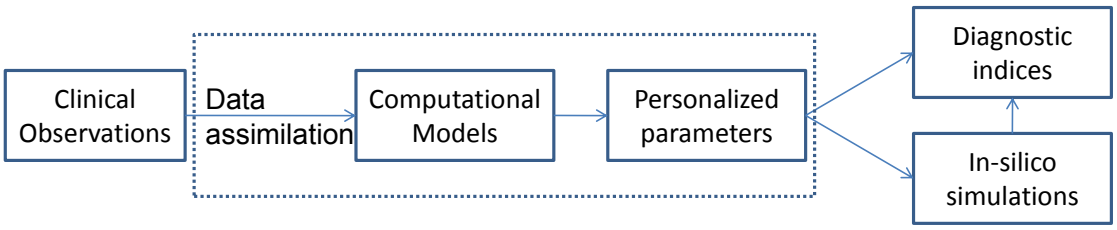

Figure 1.3: The process of clinical personalising of computational models, in which the dashed box indicates the scope of this study.

1.2 Introduction to Cardiac Mechanical Modelling

In this section, we briefly introduce the cardiac mechanical model considered in this study, i.e. an anatomically personalised mechanical model of the left ventricle, with a focus on the passive constitutive properties and active tension parameters of the myocardium. The interaction between this mechanical model with cell and activation models is illustrated in figure 1.4. This brief introduction serves as the prerequisite for reviewing the most relevant parameter estimation works in literature in the next section, and more detailed explanations are provided in chapter 2.

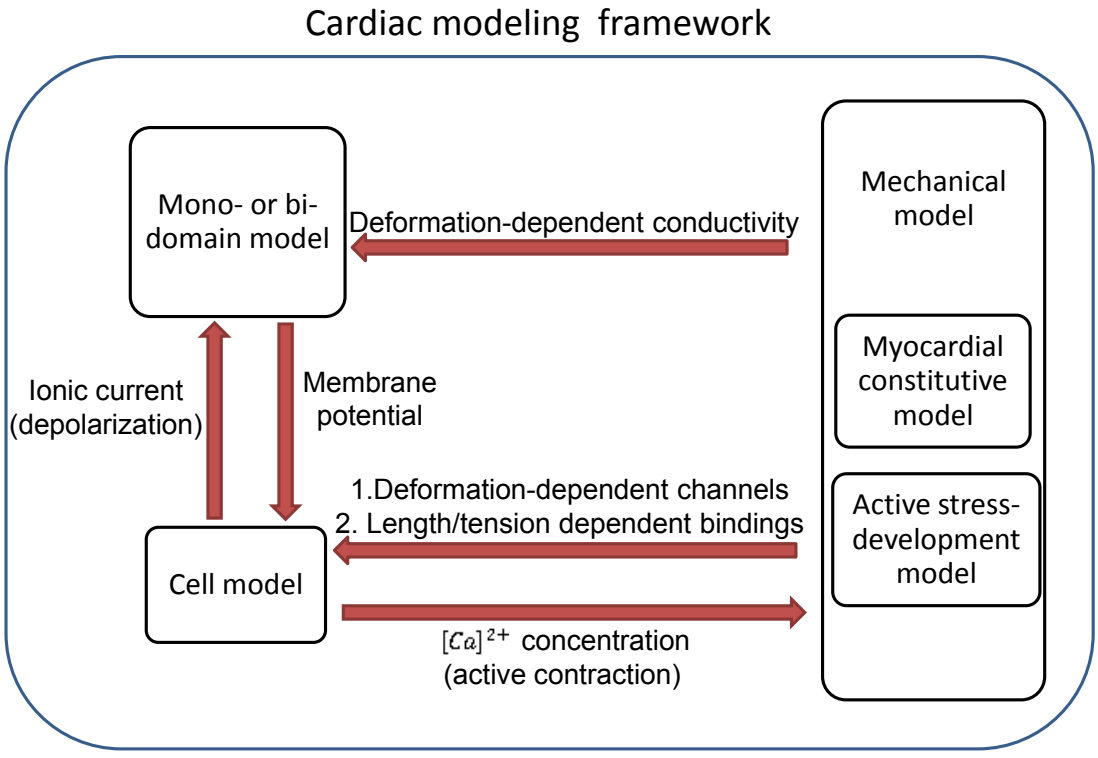

Figure 1.4: Overview of the components and interactions of cardiac models within finite element computational framework considered in this study. These components are further explained in section 1.2 .Cell and activation models are outside the scope of this work.

1.2.1 Geometric model

For functional simulation of the heart, an anatomically accurate and computationally efficient geometric and laminar tissue micro-structural model (LeGrice et al. 1995) provides the foundation for applying appropriate numerical solution techniques to solve the governing continuum equations. Cubic-Hermite finite element interpolation provides a convenient and efficient representation of geometry when compared to the more commonly used linearly interpolated tetrahedral meshes due to its C^1 continuity (Pathmanathan et al. 2009). For this reason, it has been employed by researchers in the cardiac modelling community for more than a decade (Bradley et al. 1997, Nash and Hunter 2000, Smith et al. 2004, Wang et al. 2009). Following this approach in this study, patient-specific cubic-Hermite finite element meshes of the human ventricular myocardium were created based on clinical MRI measurements (Lamata et al. 2011). The finite element ventricular meshes, together with finite element solution techniques, provide a geometric and computational framework within which to embed continuum mathematical models as those outlined in figure 1.4.

1.2.2 Mechanical Model of Finite Deformation

In order to predict the deformation of myocardium under applied stresses, a standard finite deformation mechanics model (Bonet and Wood 1997, Nash 1998) is utilised. Central to this mechanical model is the stress equilibrium governing equations, which are derived from the laws of conservation of mass, linear momentum, angular momentum and the principle of virtual work. Details of stress equilibrium governing equations are explained below in chapter 2.

1.2.3 Myocardial Constitutive Models

Models of stress development, embedded in a cardiac finite deformation mechanics model, relate the tissue-level stress to the tissue-level strain and cellular-level calcium transient. These two aspects of stress development, i.e. the passive constitutive strain-stress relation and the active stress generation model, are described in the following sections.

Passive Constitutive Properties of Myocardium

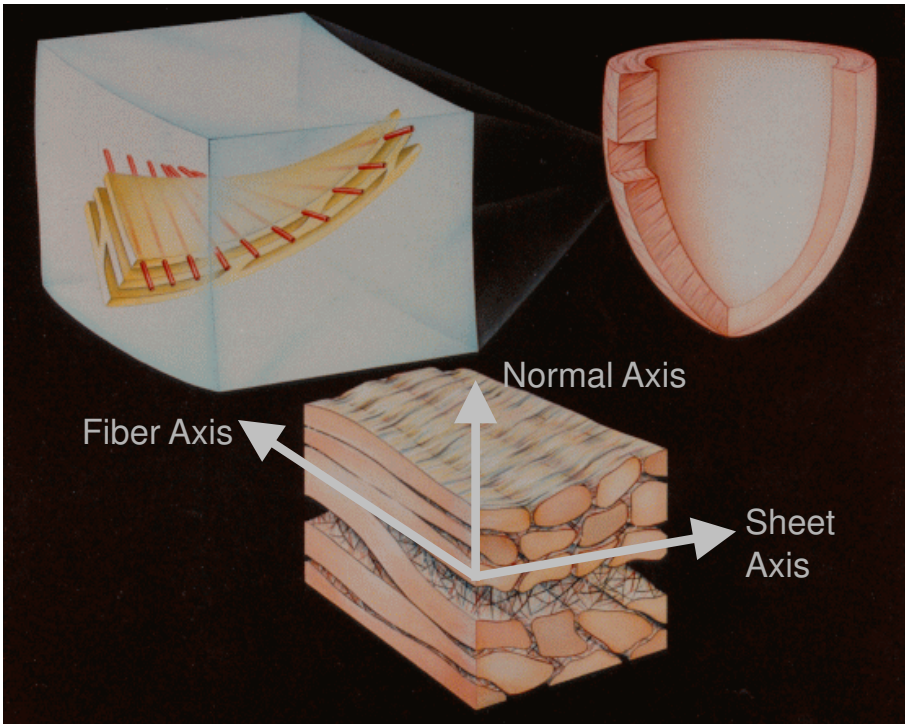

Figure 1.5: Microstructure of myocardium, showing three material directions (Nash 1998).

The deformation of the heart tissue, linked through the constitutive strain-stress relationship, give rises to the passive stress, and this mechanism plays a major role in diastolic function of the heart (Wang et al. 2009). This constitutive strain-stress relation is highly dependent on the microstructure of myocardium. The cardiac muscle, like skeletal muscle, is composed of tubular cells called myocytes, also known as *muscle fibres* (see figure

1.5). It has been shown that the myocardium is stiffer along the direction of the muscle fibres, characterised most often via a nonlinear stress-strain relationship. In order to capture these properties, Guccione et al. (1991) proposed a transversely isotropic exponential strain-energy function $\bar{W}$ with four parameters. The strain-energy function $\bar{W}$ is expressed as a functional of six independent components of Lagrange Green's strain tensor $\boldsymbol{E}$ defined in fibre (f), sheet (s) and sheet-normal (n) coordinates (detailed in chapter 2). This exponential constitutive relationship has been shown, by Schmid et al. 2008, to be most suitable for inverse parameter estimation through shear-stress tests, compared to several popular alternatives such as the pole-zero law (Nash and Hunter 2000). The *in-vivo* estimation of Guccione law parameters using MRI measurements has been studied by various researchers (Wang et al. 2009, Sun et al. 2009), which will be discussed further in section 1.3 below. In the first part of this study, we develop methodologies to estimated these constitutive properties from clinical measurements, and apply our methods, to our best knowledge for the first time in literature, to estimate constitutive properties of human subjects.

Myofibre Active Tension Development

In addition to the passive stresses developed because of the stress-strain relationship as the heart deforms, the active stress is also induced since the myocardial cells themselves are excitable. When stimulated by the electrical impulse generated repeatedly and rhythmically by the sinoatrial node, the myocardium will thus develop active stress causing the heart to contract. The mechanism of contraction is explained by the sliding filament theory (Huxley and Niedergerke 1954, Huxley et al. 1954). As shown in figure 1.6, the cardiac muscle fibre contains many chains of myofibrils, formed by alternating segments of thick and thin protein filaments, i.e. actin and myosin proteins. When the cell is depolarised, calcium ions are released into the muscle cell, and bound to troponin molecules. Calcium binding changes the shape of troponin, causing tropomyosin to move deeper into

the groove of the actin dimer, therefore causing the myosin binding sites on the actin protein to be exposed. Myosin binds to the now-exposed binding sites, and muscle contracts as the thick and thin filaments slide into each other.

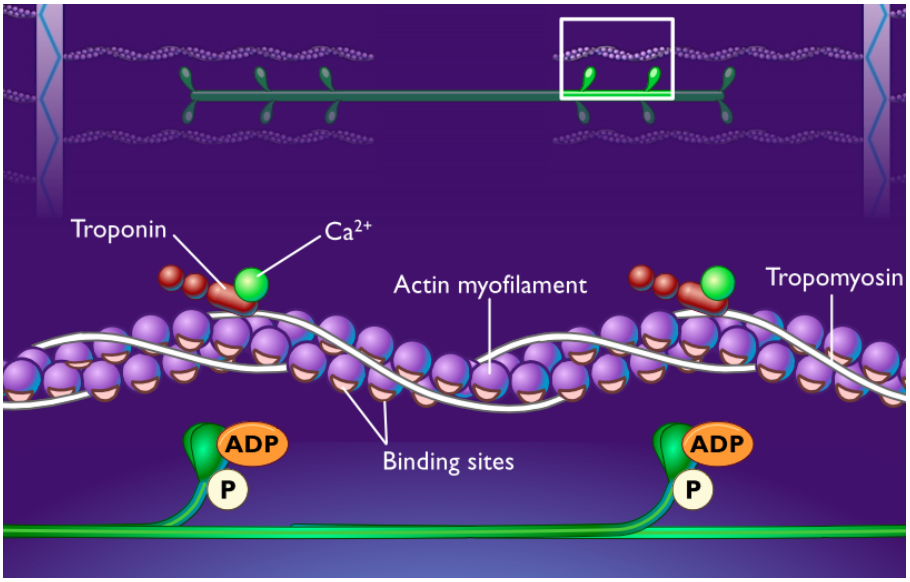

Figure 1.6: Sliding filament theory: cross-bridge movement during cardiac muscle fibre contraction generating active tension (McKinley and O'loughlin 2006, chapter 10).

For this process, there has been a set of hierarchical models for the active stress development, from the simple empirical model (Nash 1998, chapter 5, Guccione and McCulloch 1993, Guccione et al. 1993) to the detailed cellular electrophysiology models (ten Tusscher et al. 2004; ten Tusscher and Panfilov 2006; Grandi et al. 2010). Nash (1998) employed a simple empirical model to simulate the cardiac systole. This model links the active stress along fibre direction to the level of activation Ca_{actn} ($0 \leq Ca_{actn} \leq 1$) and the fibre stretch ratio λ ($\lambda > 0$).

$$T_0(\lambda, Ca_{actn}) = \frac{(Ca_{actn}[Ca^{2+}]_{max})^h}{(Ca_{actn}[Ca^{2+}]_{max})^h + (c_{50})^h} T_{ref}(1 + \beta(\lambda - 1)) \tag{1.1}$$

The parameters for this empirical model are summarised in table 1.1. In this study, the combined $\frac{(Ca_{actn}[Ca^{2+}]_{max})^h}{(Ca_{actn}[Ca^{2+}]_{max})^h + (c_{50})^h} T_{ref}$, renamed as T_z, will be estimated from clinical measurement of heart failure patients (chapter 6). This parameter characterises the

Table 1.1: Parameters in model of active stress development (Nash 1998, Chapter 5).

$[Ca^{2+}]_{max}$	Normalized (0-1) Ca^{2+} concentration at the maximal activation level	1.0
c_{50}	Normalized (0-1) Ca^{2+} concentration at 50% activation level	0.5
h	Hill coefficient, determining the slope of the curve	3.0
T_{ref}	Isometric stress	100 kPa
β	Linear slope for the depedence of stress on the sarcomere length	1.45

amount of active contractile tension developed in systole, and in case where there is significant residual tension in diastole as well. In the latter case, the estimated residual active tension has the potential to provide an important metric for understanding the cardiac relaxation profile of diastolic heart failure patients.

1.3 Overview of Related Works on *in-vivo* Estimation of Parameters in Cardiac Models

Parallel to the development of cardiac mechanics models, the research on estimating parameters in these models has also been carried out for a number of decades. From the one-dimensional and bi-axial data of tissue samples (Fung 1993) to the three dimensional simple shear experiments (Dokos et al. 2002), there have been numerous *ex vivo* experiments to quantify mechanical properties of the myocardium. Based on their research, it is now well established that myocardium exhibits three-dimensionally anisotropic and nonlinear (deformation-dependent) properties (Guccione et al. 1991; Hunter 1995; Costa et al. 2001). Furthermore, recent studies have been able to quantify the passive material parameters from these *ex vivo* experiments through nonlinear optimisation that matches a force-displacement curve (Schmid et al. 2006; Schmid et al. 2008; Schmid et al. 2009).

Beyond these *ex vivo* experiments, there has been an increasing interest in estimating passive constitutive material parameters and parameters characterising the contractile properties of the heart directly from *in vivo* imaging data. This work was motivated and enabled by the advances of medical imaging technologies, e.g. the specific modalities

of X-ray computed tomography (CT) and magnetic resonance imaging (MRI), and the development of medical image processing algorithms (Ecabert et al. 2008; Peters et al. 2009).

In the following section, we will review the relevant studies (Wang et al. 2009, Sun et al. 2009, Moireau et al. 2008, and Moireau and Chapelle 2011) on parameter estimation from *in vivo* or *in silico* [1] imaging measurements, with a focus on the scope of parameters that have been estimated within a range of models and methodology for solving those inverse estimation problems. Further reviews are provided at the beginning of each of the following result chapters (chapter 4-7).

1.3.1 Scope of Related Studies

Parameter estimation for the simulation of cardiac mechanics essentially falls into two categories: the stiffness related parameters for the passive constitutive material law and the contractility related parameters for the active tension development models, both of which are outlined as follows.

Both Wang et al. (2009) and Sun et al. (2009) applied a similar cardiac modelling approach based on quasi-static finite deformation mechanics, in which they employed a transversely isotropic material model of myocardium (the *Guccione law* introduced in previous section, Guccione et al. 1991). Sun et al. (2009) also considered the active stress development model of myocardium introduced in previous section (Guccione and McCulloch 1993, Guccione et al. 1993) for the simulation of the cardiac systolic phase. For parameter estimation, Wang et al. (2009) focused on the four homogeneous constitutive parameters in Guccione's passive material model, while Sun et al. (2009) estimated the maximum isometric stress parameter (T_{max}) of two myocardial regions.

[1] *In silico* data refers to the synthetic results numerically generated from model simulations.

In contrast to the quasi-static finite deformation model used by Wang et al. (2009) and Sun et al. (2009), the mechanical models of Moireau et al. (2008) and Moireau and Chapelle (2011) have incorporated inertial and viscous terms – these frameworks are dynamic models of cardiac mechanics. Moireau et al. (2008) adopted the assumption of liner elasticity, with viscoelastic isotropic material model characterised by Young's modulus, Poisson ratio and a viscoelastic coefficient. For active stress development, values were prescribed via an activation profile. Myocardial contractility, represented by the scale factors of the active stress (called *pre-stress term*), were estimated regionally. In addition, myocardial stiffness, defined by Young's modulus in 18 regions, was also estimated separately. Later, Moireau and Chapelle (2011) extended this mechanical model from linear to nonlinear elasticity, with a hyperelastic isotropic material model given by the Ciarlet-Geymonat potential (Le Tallec 1994).

Discussion and motivation for this study

Extensive works have been done on estimating constitutive parameters using mammalian hearts. However, there is currently still a lack of an automatic pipeline that can be applied clinically to assimilate available measurements to identify human myocardial mechanical parameters. In addition, an unsolved problem in patients with diastolic dysfunction is that the estimation of myocardial stiffness (constitutive properties) cannot be decoupled from impaired ventricular relaxation – one of the lusitropic abnormalities commonly present in heart failure (Katz 2010). For this reason, the development of methods which can robustly estimate both the stiffness (passive properties) and diastolic residual AT (active properties), would have significant potential for application within clinical cardiology.

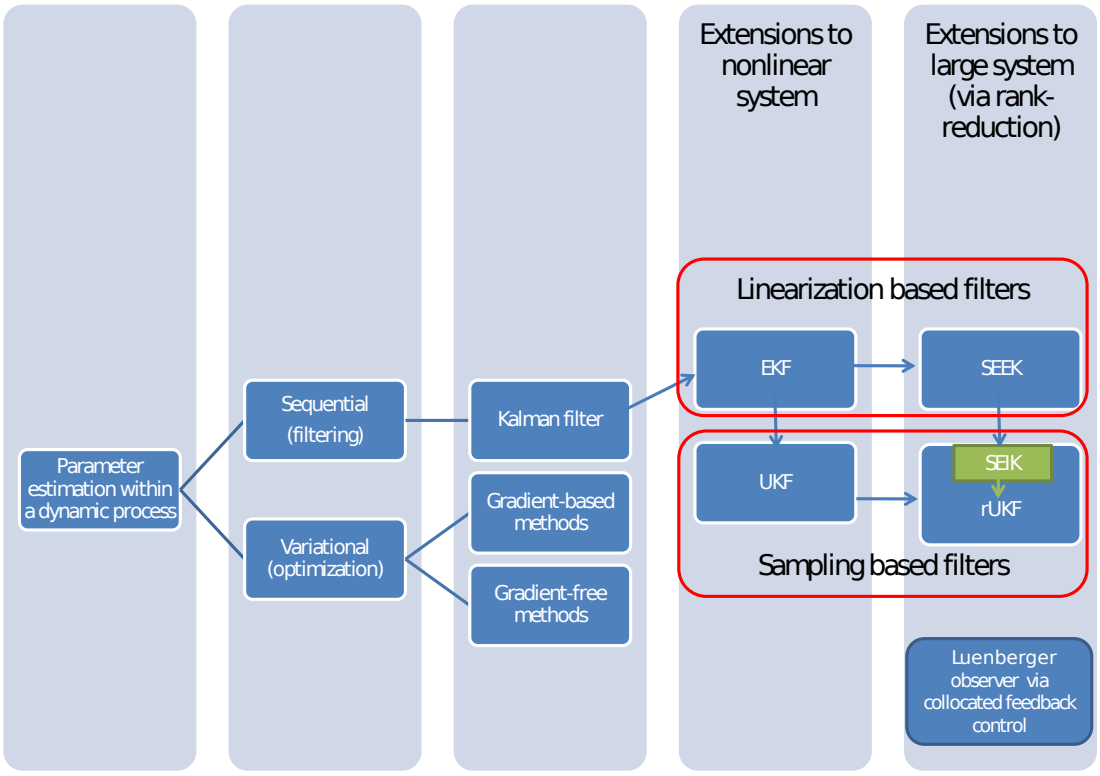

Figure 1.7: Overview of the approaches of parameter estimation within a dynamic process, and relationships between various Kalman filters. See text for explanations.

1.3.2 Methodology of Related Studies

Parameter estimation fundamentally involves solving an inverse problem, for which there are two main approaches in the field of data assimilation [2]: variational (optimisation) and sequential (filtering) procedures (see figure 1.7). Variational approaches consist of minimising, with respect to all unknown parameters, a functional criterion based on the discrepancy between model prediction and measurement, with the model equations taken as constraints; the sequential approaches refer to filtering methods typically, using Kalman filter (Kalman 1960) and its extensions to nonlinear systems.

[2]Data assimilation refers to the process which aims to estimate the state (and unknown parameters) of dynamical systems based on observations, and has origins in fields such as meteorology.

Nonlinear optimisation based approach

Both Wang et al. (2009) and Sun et al. (2009) employed traditional nonlinear optimisation formulations. Specifically, their objective function was defined as the root mean squared error (RMSE) between model predication and observation. The error was defined based on end-diastolic displacements (Wang et al. 2009) or strains (Sun et al. 2009) of a set of data points. To minimise this objective function, Wang et al. (2009) used a gradient-based method (Sequential Quadratic Programming, or SQP). They reported a 19% decrease in objective function, the value of which was reported to be insensitive to the fourth parameter of the Guccione constitutive law (shear stiffness in the fibre-sheet and fibre-normal plane). In contrast to the gradient-based method, Sun et al. (2009) chose the so-called *successive response surface* method (gradient-free). In their study, it was reported that convergence was reached under various parameter initialisation and the estimated parameter values agreed with the *ex vivo* experiments on dissected samples from the corresponding regions of the cardiac ventricles.

Among the gradient-based and gradient-free methods, the gradient-free method is, in general, believed to be more suitable for application to the *in vivo* estimation problem because of its global convergent properties and robustness. However, we are aware that in practice the passive constitutive parameters (with an exponential relationship between stress and strain) in Wang et al. 2009, are more challenging to estimate than the active-stress parameters (with linear relationship to stress) in Sun et al. (2009).

Filtering based approaches

Researchers, such as Moireau et al. (2008) and Moireau and Chapelle (2011), explored the possibilities of applying sequential approaches to address the parameter estimation problem in cardiac models, namely via Kalman filtering based methods (see figure 1.7).

The most widely used nonlinear Kalman filters are extended Kalman filter (EKF) and unscented Kalman filter (UKF) (Welch and Bishop 1995, Julier and Uhlmann 1997, Simon 2006). However, these filters are full-rank, and thus they require calculation and manipulation of covariance matrices of the same dimension as the state [3] space (typically 10^3 to 10^6). This makes the problem of parameter estimation from computationally expensive models intractable.

This intractability has motivated development of techniques to reduce the computational requirements of classic filters. The rank-reduction by singular value decomposition (SVD) of the covariance matrix is the main approach that has been explored, which has given rise to the singular evolutive extended Kalman filter (SEEK, Pham 1995, Pham et al. 1998b; also see Brasseur and Verron 2006 for review of its recent development), the singular evolutive interpolated Kalman filter (SEIK, Pham 1996, Pham et al. 1998a, Pham 2001, Pham and Hoteit 2002), and reduced-order UKF (rUKF, Moireau and Chapelle 2011, derived in chapter 3 independently). Apart from the SVD approach, other researchers (Moireau et al. 2008) achieved rank-reduction by introducing the so-called *dual Luenberger observer*, which is analogous to "friction force" feedback control strategy to change the dynamics of the mechanical model in order to reduce the discrepancy between the model prediction and measurements. For conceptional illustration of the relationships among the aforementioned filters, readers are referred to figure 1.7.

Among these filters, Moireau et al. (2008) based the parameter estimation on the extended Kalman filter (EKF), whose "reduced-order" version is obtained via the novel technique called *direct velocity feedback control* (DVF) – a simple collocated feedback control mechanism to act as a Luenberger observer (Luenberger 1971). Applying this "reduced-order" EKF estimator, local regions with abnormal material parameters were identified by the estimator from *in silico* data with velocity measurements. These measurements

[3] The state of a system refers to the variables that can fully present the current status of that system at a given time instance (Simon 2006). This is not a rigorous definition, but sufficient for this introductory purpose.

were subsequently down-sampled into 10 x 10 x 15 measurement cells, and corrupted by additive Gaussian-type white noise with a standard derivation corresponding to 10% of maximum velocity. Using these data, Moireau and Chapelle (2011) coupled their rank-reduction strategy with a reduced-order unscented Kalman filter, which was reported to give an estimation error of around 10%.

Discussion and motivation for this study

The non-invasive determination of passive constitutive parameters still remains a challenging inverse problem when we increase the model complexity by using anisotropic and nonlinear myocardial constitutive laws (e.g. Guccione et al. 1991; Hunter 1995; Costa et al. 2001). As outlined above, in previous studies (Omens et al. 1993; Augenstein et al. 2005; Wang et al. 2009; Sun et al. 2009) this inverse problem was typically formulated as a nonlinear optimisation problem to minimise, with respect to all unknown parameters, a functional criterion based on the observation error, with the model equations taken as constraints. However, the highly nonlinear dependency of the simulated mechanical behaviour on material parameters and the interdependence between material parameters, typically compromises the ability of an optimiser to retrieve the parameter values correctly. This situation is further exacerbated by the introduction of inevitable measurement noise.

An alternative to the traditional nonlinear optimisation formulation is the filtering approach (Simon 2006), which can naturally incorporate the knowledge of model error and measurement noise to improve the estimation result. Among the filtering approaches, the state-of-the-art approach based on the Reduced-order Unscented Kalman Filter (rUKF) provided a tractable filtering algorithm (Moireau and Chapelle 2011). Nevertheless, the feasibility of identifying material parameters using rUKF in the context of a detailed nonlinear mechanical models with microstructurally based transversely isotropic constitutive

law has not yet been investigated in literature.

1.4 Contributions of This Study

Building on the literature outlined above the central contributions in this thesis are summarised below and outlined in detail in the following chapters.

1. **In-silico constitutive parameter estimation using reduced-order unscented Kalman filter**

   We have developed a sequential data assimilation framework covering various types of Kalman filters, outlined in chapter 3. Based on this theoretical development, we applied the reduced-order unscented Kalman filter (rUKF, independently derived in chapter 3) to the nonlinear cardiac mechanical model (chapter 4). The rUKF is shown to be well adapted for solving the inverse problem of estimating the constitutive parameters (stiffness) in the widely employed Guccione's constitutive law. We demonstrate that the novel rUKF approach can accurately retrieve the homogeneous and regionally varying Guccione's constitutive parameters. We also show that these material parameters can be accurately estimated from the synthetic noisy measurements of material displacements of data points from the epi- and endocardium. This work has been published in Xi et al. 2011a, and detailed in chapter 3 & 4.

2. **Passive constitutive parameter estimation from clinical data**

   Following the estimation of constitutive parameters from synthetic data, we have investigated the development of methods, which can be applied to clinical data. Through this work, we have performed the first study in literature estimating human constitutive parameters using clinical data. Specifically, we present an au-

tomatic workflow for extracting myocardial constitutive parameters from clinical data. Our framework assimilates cine and tagged Magnetic Resonance Images (MRI) together with left ventricular (LV) cavity pressure recordings to characterise the mechanics of the LV. We apply our framework to two heart failure patient cases and one normal case. These results indicate that while the diastolic motion (the myocardium displacements between beginning of diastole and end of diastole) does not constrain the mechanical parameters uniquely, it does provide a potentially robust indicator of myocardial stiffness. In addition, we have explicitly revealed the identifiability of widely used Guccione parameters through a reformulation of the Guccione law. This work has been published in Xi et al. 2011b, and is detailed in chapter 5.

3. **Diastolic active tension estimation from clinical data**[4]

An unresolved issue in patients with diastolic dysfunction is that the estimation of myocardial stiffness cannot be decoupled from diastolic residual AT, because of the impaired ventricular relaxation during diastole. To further address this problem, chapter 6 presents the first study, to our best knowledge, to estimate diastolic mechanical parameters of the left ventricle (LV) from cine and tagged MRI measurements and LV cavity pressure recordings, separating the passive myocardial constitutive properties and diastolic residual AT. We apply this framework to three clinical cases, and the results show that the estimated constitutive parameters and residual active tension appear to be a promising candidate to delineate healthy and pathological cases. In particular, the difference in diastolic residual active tension profiles may have the potential to differentiate diastolic heart failure (DHF) patients from the systolic heart failure cases (SHF), which would make a significant clinical contribution to the understanding and diagnosis of DHF. This work has been

[4]The author believes this is one of the key contributions of this thesis.

published in Xi et al. 2012a, and detailed in chapter 6.

4. **The need of LV pressure recordings for estimating diastolic LV functions**
   The need to invasively acquire LV pressure measurement limits the wide application of this approach. Chapter 7 presents the first study, to our best knowledge, to address this issue by analysing the feasibility of using two kinds of non-invasively obtained pressure measurements for the purpose of inverse parameter estimation. It is concluded that the knowledge of LV pressure transient is required for the estimation of cardiac diastolic properties. Without this knowledge, the information implied by the estimation parameters are no more useful than that extracted from the imaging measurements – the stiffness is correlated with the ejection fraction calculated from the volume transients. The relative LV pressure can be used for estimating parameters, with errors quantified in this study as 11% for stiffness and 22% for residual active tension with averaged 0.17 kPa error in pressure measurement using the state-of-art non-invasive pressure estimation method. The accuracy of pressure offset is important for the estimation of parameters, and given a fixed accuracy of pressure measurement, increased resolution of diastolic MR measurements could improve the accuracy of estimated parameters. This work has been submitted for publication in Xi et al. 2012b, and detailed in chapter 7.

This thesis is structured as follows. Chapter 2 details the finite deformation theory for modelling ventricular mechanics, following the brief introduction of cardiac mechanical modelling in this chapter. Estimation methodologies are developed in chapter 3–7 which enables the personalisation of this mechanical model to synthetic (chapter 3 & 4) and clinical measurements (chapter 5, 6 & 7). As outlined above, the main body of chapters 4-7 consists respectively of the following four publications resulted from this study.

[1] Xi, J., Lamata, P., Lee, J., Moireau, P., Chapelle, D., and Smith, N. (2011a). Myocardial transversely isotropic material parameter estimation from in-silico mea-

surements based on a reduced-order unscented kalman filter. *Journal of the Mechanical Behaviour of Biomedical Materials*, 4(7):1090-1102.

[2] Xi, J., Lamata, P., Shi, W., Niederer, Land, S., S., Rueckert, D., Duckett, S., Shetty, A., Rinald, A., Razavi, R. and Smith, N. (2011b). An automatic data assimilation framework for patient-specific myocardial mechanical parameter estimation. *Lecture Notes on Computer Science*. 6666:392-400. (FIMH 2011, oral presentation).

[3] Xi, J., Lamata, P., Niederer, S., Land, S., Shi, W., Zhuang, X., Ourelin, S., Rueckert, D., Duckett, S., Shetty, A., Rinald, A., Razavi, R. and Smith, N. (2012a). The estimation of patient-specific cardiac diastolic functions from clinical measurements. *Medical Image Analysis*. (In publication).

[4] Xi, J., Lamata, P., and Smith, N. (2012b). Understanding the need of LV pressure for the estimation of LV diastolic function. *Biomechanics and Modelling in Mechanobiology*. (Submitted for publication).

Part II

Theories of Nonlinear Mechanics and Kalman Filter

Chapter 2

Theories of Nonlinear Mechanics and FEM for Modelling LV Deformation

It is only the impossible that is possible for God. He has given over the possible to the mechanics of matter and the autonomy of his creatures – Simone Weil (1909-1943)

The left ventricle (LV) is the largest and most important chamber in the human heart. It pumps the oxygenated blood into the aorta, through the rhythmic contraction and inflation. During the contraction, the LV myocardium can result in strains of up to 30%. To model this amount of large deformation, this chapter details the fundamental theory of finite deformation elasticity theory, followed by the explanation of the numerical solution process based on the finite element method (FEM).

2.1 Finite Deformation Elasticity

Deformation is the transformation of a body from a reference configuration to a current configuration. A *configuration* is a set containing the positions of all particles of the body. Deformation can be described in terms of rigid body movement (including translation and rotation), and relative movement of particles in the body. *Strain* is such a description of deformation in terms of relative displacement of particles in the body. Deformations of

elastic material (such as rubber) in which both rotations and strains are arbitrarily large is considered to be finite (as opposite to infinitesimal), and is described by the theory of *finite deformation elasticity*.

2.1.1 Kinematics

Kinematics is the subject concerning about describing the deformation without reference to the cause. Let $\boldsymbol{x} = (x_1, x_2, x_3)$ stands for the current position in rectangular Cartesian coordinates of a material particle that occupied the position $\mathbf{X} = (X_1, X_2, X_3)$ in the reference or undeformed state.

Deformation Gradient

The *deformation gradient tensor* **F** is defined as a linear transformation, which maps the undeformed line segment $d\boldsymbol{X}$ to the corresponding deformed line segment $d\boldsymbol{x}$ by

$$d\boldsymbol{x} = \boldsymbol{F}\, d\boldsymbol{X}, \text{ where } \boldsymbol{F} = \frac{\partial \boldsymbol{x}}{\partial \boldsymbol{X}}. \tag{2.1}$$

Polar decomposition,

$$\boldsymbol{F} = \boldsymbol{R}\boldsymbol{U} = \boldsymbol{V}\boldsymbol{R} \tag{2.2}$$

splits F into the product of an orthonormal rotation tensor, $\boldsymbol{R}$, and a symmetric positive definite stretch tensor, $\boldsymbol{U}$ or $\boldsymbol{V}$, which contains a complete description of the material strain, independent of any rigid body motion.

Using eigendecomposition, the real symmetric matrix $\boldsymbol{V}$ can be decomposed as

$$\boldsymbol{V} = \boldsymbol{Q}\boldsymbol{\Lambda}\boldsymbol{Q}^{-1} = \boldsymbol{Q}\begin{pmatrix} \lambda_1 & 0 & 0 \\ 0 & \lambda_2 & 0 \\ 0 & 0 & \lambda_3 \end{pmatrix}\boldsymbol{Q}^{-1}, \tag{2.3}$$

where $\boldsymbol{Q}$ is a square matrix whose columns are the eigenvectors of $\boldsymbol{V}$, and $\lambda_1, \lambda_2, \lambda_3 > 0$ are the eigenvalues of $\boldsymbol{V}$, denoting the *stretch ratios* along the three eigenvector directions. These stretch ratios are conceptually useful for the understanding of the strain tensors presented below. Similarly the stretch tensor $\boldsymbol{U}$ can also be written as

$$\boldsymbol{U} = \boldsymbol{R^T V R} = \boldsymbol{R^T Q \Lambda} (\boldsymbol{R^T Q})^{-1} = \boldsymbol{R^T Q} \begin{pmatrix} \lambda_1 & 0 & 0 \\ 0 & \lambda_2 & 0 \\ 0 & 0 & \lambda_3 \end{pmatrix} (\boldsymbol{R^T Q})^{-1}. \tag{2.4}$$

Strain Tensors

As mentioned earlier, *strain* is a measure of deformation in terms of relative displacement of particles in the body, independent of translation and rotation. Consider three representative particles $\boldsymbol{X}_0$, $\boldsymbol{X}_1$ and $\boldsymbol{X}_2$ which are infinitely close to each other in the reference configuration. To describe the strain at these points, consider the change in the scalar product of the two elemental vectors $d\boldsymbol{X}_1 = \boldsymbol{X}_1 - \boldsymbol{X}_0$ and $d\boldsymbol{X}_2 = \boldsymbol{X}_2 - \boldsymbol{X}_0$, which involve both the stretching (that is, change in length) and changes in the enclosed angle between the two vectors. Suppose $d\boldsymbol{X}_1$ and $d\boldsymbol{X}_2$ deform to $d\boldsymbol{x}_1$ and $d\boldsymbol{x}_2$, then we can find tensors $\boldsymbol{E}$ (named as *Lagrangian or Green strain tensor*) or $\boldsymbol{e}$ (named as *Eulerian or Almansi strain tensor*) such that the change in the scalar product of the two elemental vectors can be expressed as the scalar product of the elemental vectors transformed by these strain tensors in either reference or spatial configuration.

$$\frac{1}{2}(d\boldsymbol{x}_1 \cdot d\boldsymbol{x}_2 - d\boldsymbol{X}_1 \cdot d\boldsymbol{X}_2) = d\boldsymbol{X}_1 \cdot \boldsymbol{E} d\boldsymbol{X}_2, \tag{2.5}$$

$$\frac{1}{2}(d\boldsymbol{x}_1 \cdot d\boldsymbol{x}_2 - d\boldsymbol{X}_1 \cdot d\boldsymbol{X}_2) = d\boldsymbol{x}_1 \cdot \boldsymbol{e} d\boldsymbol{x}_2. \tag{2.6}$$

Using the definition of deformation gradient tensor $\boldsymbol{F}$ in equation 2.1, $\boldsymbol{E}$ can be expressed as

$$\boldsymbol{E} = \frac{1}{2}(\boldsymbol{F}^T \boldsymbol{F} - \boldsymbol{I}) = \frac{1}{2}(\boldsymbol{U}^2 - \boldsymbol{I}) = \boldsymbol{R^T Q} \begin{pmatrix} \frac{\lambda_1^2 - 1}{2} & 0 & 0 \\ 0 & \frac{\lambda_2^2 - 1}{2} & 0 \\ 0 & 0 & \frac{\lambda_3^2 - 1}{2} \end{pmatrix} (\boldsymbol{R^T Q})^{-1}, \tag{2.7}$$

and $\boldsymbol{e}$ can be expressed using the deformation gradient tensor $\boldsymbol{F}$ as

$$\boldsymbol{e} = \frac{1}{2}(\boldsymbol{I} - (\boldsymbol{F}\boldsymbol{F}^T)^{-1}) = \frac{1}{2}(\boldsymbol{I} - \boldsymbol{V}^{-2}) = \boldsymbol{Q}\begin{pmatrix} \frac{1-\lambda_1^{-2}}{2} & 0 & 0 \\ 0 & \frac{1-\lambda_2^{-2}}{2} & 0 \\ 0 & 0 & \frac{1-\lambda_3^{-2}}{2} \end{pmatrix}\boldsymbol{Q}^{-1}, \quad (2.8)$$

by noticing

$$d\boldsymbol{X}_1 \cdot \boldsymbol{E}\, d\boldsymbol{X}_2 = (\boldsymbol{F}\, d\boldsymbol{x}_1) \cdot \boldsymbol{E}(\boldsymbol{F}\, d\boldsymbol{x}_2) = d\boldsymbol{x}_1 \cdot (\boldsymbol{F}^T\boldsymbol{E}\boldsymbol{F})\, d\boldsymbol{x}_2 = d\boldsymbol{x}_1 \cdot \boldsymbol{e}\, d\boldsymbol{x}_2, \quad (2.9)$$

and thus the relationships between Lagrangian Green strain tensor $\boldsymbol{E}$ and Eulerian Almansi strain tensor $\boldsymbol{e}$ are that

$$\boldsymbol{F}^T\boldsymbol{E}\boldsymbol{F} = \boldsymbol{e}, \text{ or } \boldsymbol{F}^{-T}\boldsymbol{e}\boldsymbol{F}^{-1} = \boldsymbol{E}. \quad (2.10)$$

Strain Tensors in Local Material Coordinates

For inhomogeneous, anisotropic materials the orientation of the material axes may vary with location, for example fibre direction changes spatially throughout the myocardium. Thus it is no longer practical to identify the material axes in the undeformed body with the reference coordinates (X_1, X_2, X_3). Instead, a new material coordinate system (ν_1, ν_2, ν_3) is introduced which is aligned with the microstructural features of the material. For myocardium, a natural set of material axes are formed by identifying $\nu_i (i = 1, 2, 3)$ with muscle fibre direction ($\boldsymbol{f}$), sheet direction ($\boldsymbol{s}$) and sheet-normal direction ($\boldsymbol{n}$) (Smith et al. 2004). The transformation between strain in X-Y-Z coordinate system ($\boldsymbol{E}$) and strain in f-s-n coordinate system ($\boldsymbol{E}_{fsn}$) is given by

$$\boldsymbol{E} = \begin{pmatrix} \boldsymbol{f}^T \\ \boldsymbol{s}^T \\ \boldsymbol{n}^T \end{pmatrix} \boldsymbol{E}_{fsn} \begin{pmatrix} \boldsymbol{f} & \boldsymbol{s} & \boldsymbol{n} \end{pmatrix}, \text{ or} \quad (2.11)$$

$$\boldsymbol{E}_{fsn} = \begin{pmatrix} \boldsymbol{f} & \boldsymbol{s} & \boldsymbol{n} \end{pmatrix} \boldsymbol{E} \begin{pmatrix} \boldsymbol{f}^T \\ \boldsymbol{s}^T \\ \boldsymbol{n}^T \end{pmatrix}, \quad (2.12)$$

where $\boldsymbol{f}$, $\boldsymbol{s}$, and $\boldsymbol{n}$ are three mutually orthogonal unit vectors expressed in X-Y-Z coordinate system. This formula can be derived from the strain's definition (equation 2.5) by noticing that

$$d\boldsymbol{X}_1^{fsn} \cdot \boldsymbol{E}_{fsn} d\boldsymbol{X}_2^{fsn} = \left(\begin{pmatrix} \boldsymbol{f} & \boldsymbol{s} & \boldsymbol{n} \end{pmatrix} d\boldsymbol{X}_1\right) \cdot \boldsymbol{E}_{fsn} \left(\begin{pmatrix} \boldsymbol{f} & \boldsymbol{s} & \boldsymbol{n} \end{pmatrix} d\boldsymbol{X}_2\right) \tag{2.13}$$

$$= d\boldsymbol{X}_1 \cdot \left(\begin{pmatrix} \boldsymbol{f}^T \\ \boldsymbol{s}^T \\ \boldsymbol{n}^T \end{pmatrix} \boldsymbol{E}_{fsn} \begin{pmatrix} \boldsymbol{f} & \boldsymbol{s} & \boldsymbol{n} \end{pmatrix} \right) d\boldsymbol{X}_2 \tag{2.14}$$

$$= d\boldsymbol{X}_1 \cdot \boldsymbol{E} d\boldsymbol{X}_2 \tag{2.15}$$

2.1.2 Stress Analysis

Stress analysis is the determination of the internal distribution of stresses in a structure. The state of stress at any internal point of a structure is defined by all of the 3-dimensional forces (called the *stress vectors*) experienced at that point when the structure is sliced by all planes (infinite in number) that pass through that point (Chen et al. 2007). Therefore in the first instance it would seem that in order to being able to define the stress at a point, an infinite number of stress vectors are needed. However, the *Cauchy's stress theorem*, developed by Augustin-Louis Cauchy in the early 19th century, states that these infinite number of stress vectors on any plane passing through that point can be found through a linear combination of only three stress vectors on three mutually perpendicular planes. This theorem can be proved by analysing the stress of an infinitesimal tetrahedron using Newton's second law of motion (Atanackovic and Guran 2000).

Cauchy Stress Tensor

If $\boldsymbol{t}_n$ denotes the stress vector on plane $\boldsymbol{n}$, $\boldsymbol{t}_{e_1}$,$\boldsymbol{t}_{e_2}$ and $\boldsymbol{t}_{e_3}$ denote the stress vectors on three mutually perpendicular planes $\boldsymbol{e_1}$, $\boldsymbol{e_2}$ and $\boldsymbol{e_3}$, and

$$\boldsymbol{n} = n_1\boldsymbol{e_1} + n_2\boldsymbol{e_2} + n_3\boldsymbol{e_3} = \begin{pmatrix} \boldsymbol{e_1} & \boldsymbol{e_2} & \boldsymbol{e_3} \end{pmatrix} \begin{pmatrix} n_1 \\ n_2 \\ n_3 \end{pmatrix}, \tag{2.16}$$

then Cauchy's stress theorem states that

$$\boldsymbol{t}_n = n_1\boldsymbol{t}_{e_1} + n_2\boldsymbol{t}_{e_2} + n_3\boldsymbol{t}_{e_3} \tag{2.17}$$

$$= \begin{pmatrix} \boldsymbol{t}_{e_1} & \boldsymbol{t}_{e_2} & \boldsymbol{t}_{e_3} \end{pmatrix} \begin{pmatrix} n_1 \\ n_2 \\ n_3 \end{pmatrix}, \tag{2.18}$$

$$= \begin{pmatrix} t^1_{e_1} & t^1_{e_2} & t^1_{e_3} \\ t^2_{e_1} & t^2_{e_2} & t^2_{e_3} \\ t^3_{e_1} & t^3_{e_2} & t^3_{e_3} \end{pmatrix} \begin{pmatrix} n_1 \\ n_2 \\ n_3 \end{pmatrix}, \tag{2.19}$$

$$= \begin{pmatrix} \sigma_{11} & \sigma_{12} & \sigma_{13} \\ \sigma_{21} & \sigma_{22} & \sigma_{23} \\ \sigma_{31} & \sigma_{32} & \sigma_{33} \end{pmatrix} \begin{pmatrix} n_1 \\ n_2 \\ n_3 \end{pmatrix}, \tag{2.20}$$

$$= \boldsymbol{\sigma}\boldsymbol{n}. \tag{2.21}$$

$\boldsymbol{\sigma}$ defined in the above equations is the *Cauchy stress tensor*, which is a 3 by 3 matrix whose columns are the three stress vectors on three mutually perpendicular planes $\boldsymbol{e_1}$, $\boldsymbol{e_2}$ and $\boldsymbol{e_3}$.

The Cauchy stress tensor can be further decomposed into the sum of two parts – a mean *hydrostatic stress tensor* or *volumetric stress tensor* $p\boldsymbol{I}$, which tends to change the volume of the stressed body, and *deviatoric stress tensor* $\boldsymbol{\sigma}'$, which tends to distort the body.

$$\boldsymbol{\sigma} = \boldsymbol{\sigma}' + p\boldsymbol{I}, \tag{2.22}$$

$$\boldsymbol{\sigma}' = \begin{pmatrix} \sigma_{11} - p & \sigma_{12} & \sigma_{13} \\ \sigma_{21} & \sigma_{22} - p & \sigma_{23} \\ \sigma_{31} & \sigma_{32} & \sigma_{33} - p \end{pmatrix}, \tag{2.23}$$

$$p = \frac{1}{3}tr(\boldsymbol{\sigma}) = \frac{1}{3}\boldsymbol{\sigma} : \boldsymbol{I} = \frac{1}{3}(\sigma_{11} + \sigma_{22} + \sigma_{33}), \tag{2.24}$$

$$\mathrm{tr}(\boldsymbol{\sigma}') = 0. \tag{2.25}$$

Newton's Second Law of Motion

Consider a body of volume deformed by (external) surface traction $\boldsymbol{t}$ per unit deformed area and (external) body force $\boldsymbol{b}$ per unit deformed volume. $\boldsymbol{x}$ denotes the position of the body, Ω denotes the 3D space occupied by the body, $\partial\Omega_N$ denotes the surface on which the external traction is applied, and ρ denotes the mass density of the deformed body.

A body can be viewed as a system of infinite number of particles. According to Newton's second law, the rate of change of the momentum of a particle is proportional to the resultant force acting on the particle and is in the direction of that force. And therefore by applying Newton's second law, we have

$$\frac{\partial}{\partial t}(\int_{\Omega} \rho \dot{\boldsymbol{x}} dV) = \int_{\partial\Omega_N} \boldsymbol{t} dS + \int_{\Omega} \rho \boldsymbol{b} dV, \tag{2.26}$$

$$= \int_{\partial\Omega_N} \boldsymbol{\sigma} \boldsymbol{n} dS + \int_{\Omega} \rho \boldsymbol{b} dV, \tag{2.27}$$

$$= \int_{\Omega} (\boldsymbol{\sigma} \nabla_{\boldsymbol{x}} + \rho \boldsymbol{b}) dV, \tag{2.28}$$

$$= \int_{\Omega} (\mathsf{div}\boldsymbol{\sigma} + \rho \boldsymbol{b}) dV. \tag{2.29}$$

Equilibrium Equation

For static equilibrium of the material, important in solid mechanics, the left-hand-side acceleration term in the above equation vanishes. Furthermore, if the above equation is to be valid for arbitrary volume, equation 2.29 must hold at every point and thus the integrated mush vanish as well. Therefore, under these two assumptions, the above equation becomes

$$\mathsf{div}\boldsymbol{\sigma} + \rho \boldsymbol{b} = 0, \tag{2.30}$$

which holds for every point inside the deformed body Ω.

Principle of Virtual Work

Define the residual force vector $\boldsymbol{r}$ as

$$\boldsymbol{r} = \mathsf{div}\boldsymbol{\sigma} + \rho \boldsymbol{b}. \tag{2.31}$$

The virtual work, δw, per unit volume done by the residual force $\boldsymbol{r}$ during this virtual

displacement $\boldsymbol{\delta v}$ is $\boldsymbol{r} \cdot \boldsymbol{\delta v}$, and the equilibrium equation ($\boldsymbol{r}$ is zero) implies,

$$\delta w = \boldsymbol{r} \cdot \boldsymbol{\delta v} = 0, \qquad \text{for any } \boldsymbol{\delta v}. \tag{2.32}$$

Note that the above scalar equation 2.32 is essentially equivalent to the vector equation 2.30 due to the fact that $\boldsymbol{\delta v}$ is arbitrary.

Next we integrate the equation 2.32 over the small body volume v (of each finite element) to give a weak statement of the static equilibrium of the body:

$$\begin{aligned}
\delta W &= \int_\Omega (\mathsf{div}\boldsymbol{\sigma} + \boldsymbol{b}) \cdot \boldsymbol{\delta v} dV && (2.33)\\
&= \int_\Omega (\mathsf{div}\boldsymbol{\sigma}) \cdot \boldsymbol{\delta v} dV + \int_\Omega \boldsymbol{b} \cdot \boldsymbol{\delta v} dV && (2.34)\\
&= \int_\Omega \mathsf{div}(\boldsymbol{\sigma}\boldsymbol{\delta v}) dV - \int_\Omega \boldsymbol{\sigma} : \nabla \boldsymbol{\delta v} dV + \int_\Omega \boldsymbol{b} \cdot \boldsymbol{\delta v} dV, && (2.35)\\
&= \int_{\partial\Omega} \boldsymbol{n} \cdot \boldsymbol{\sigma}\boldsymbol{\delta v} dS - \int_\Omega \boldsymbol{\sigma} : \nabla \boldsymbol{\delta v} dV + \int_\Omega \boldsymbol{b} \cdot \boldsymbol{\delta v} dV, && (2.36)\\
&= \int_{\partial\Omega} \boldsymbol{\delta v} \cdot \boldsymbol{\sigma}^T \boldsymbol{n} dS - \int_\Omega \boldsymbol{\sigma} : \nabla \boldsymbol{\delta v} dV + \int_\Omega \boldsymbol{b} \cdot \boldsymbol{\delta v} dV, && (2.37)\\
&= \int_{\partial\Omega} \boldsymbol{\delta v} \cdot \boldsymbol{\sigma}\boldsymbol{n} dS - \int_\Omega \boldsymbol{\sigma} : \nabla \boldsymbol{\delta v} dV + \int_\Omega \boldsymbol{b} \cdot \boldsymbol{\delta v} dV, && (2.38)\\
&= \underbrace{\int_{\delta\Omega} \boldsymbol{t} \cdot \boldsymbol{\delta v} dS + \int_\Omega \boldsymbol{b} \cdot \boldsymbol{\delta v} dV}_{\text{external work}} - \underbrace{\int_\Omega \boldsymbol{\sigma} : \nabla \boldsymbol{\delta v} dV}_{\text{internal work}} = 0 && (2.39)
\end{aligned}$$

The equation 2.39 is the fundamental scalar equation and states the static equilibrium of a deformable body. In the above equations, $\nabla\boldsymbol{\delta v}$ is the gradient of virtual displacement $\boldsymbol{\delta v}$. The above derivation uses the following equations.

$$\boldsymbol{\sigma n} = \boldsymbol{t}^n \text{ (Cauchy stress theorem, eq. 2.21)} \tag{2.40}$$

$$\boldsymbol{\sigma} = \boldsymbol{\sigma}^T \text{ (Symmetry of Cauchy stress tensor)} \tag{2.41}$$

$$\mathsf{div}(\boldsymbol{\sigma}\boldsymbol{\delta v}) = (\mathsf{div}\boldsymbol{\sigma}) \cdot \boldsymbol{\delta v} + \boldsymbol{\sigma} : \nabla \boldsymbol{\delta v} \text{ (Divergence operator property)} \tag{2.42}$$

$$\int_\Omega \mathsf{div}(\boldsymbol{\sigma}\boldsymbol{\delta v}) dV = \int_{\delta\Omega} \boldsymbol{n} \cdot (\boldsymbol{\sigma}\boldsymbol{\delta v}) dS \text{ (Divergence theorem)} \tag{2.43}$$

$$\boldsymbol{n} \cdot \boldsymbol{\sigma}\boldsymbol{\delta v} = \boldsymbol{\delta v} \cdot \boldsymbol{\sigma}^T \boldsymbol{n} \text{ (Rule for commuting dot product)} \tag{2.44}$$

Remark 2.1.1. *The kinematics and equilibrium equations can be established in either the material (undeformed) configuration or the spatial (deformed) configuration. Either of these configurations can be used to derive the discretised equilibrium equations for finite element method (see below), although only the spatial version has been discussed here because of its relative simplicity for implementation. However, in case of inhomogeneous and anisotropic materials of myocardium, it's often convenient to express the stress in term of the strain in undeformed material configuration, using the second Piola-Kirchhoff tensor $\boldsymbol{T}$. Then the deformation gradient $\boldsymbol{F}$ is used to transform the second Piola-Kirchhoff tensor defined in the undeformed configuration into the Cauchy stress tensor defined in the deformed configuration by*

$$\boldsymbol{\sigma} = \frac{1}{\det \boldsymbol{F}} \boldsymbol{F}\boldsymbol{T}\boldsymbol{F}^{\boldsymbol{T}}, \tag{2.45}$$

which can be derived by using the relationship between force vector in the deformed configuration ($\boldsymbol{\sigma}\boldsymbol{n}\,da$) and force vector in undeformed configuration ($\boldsymbol{T}\boldsymbol{N}\,dA$) over the same small internal clipping plane of the body, i.e.

$$\boldsymbol{\sigma}\boldsymbol{n}\,da = \boldsymbol{F}(\boldsymbol{T}\boldsymbol{N}\,dA) = \boldsymbol{F}(\boldsymbol{T}(\boldsymbol{F}^T\boldsymbol{n}\frac{1}{\det(\boldsymbol{F})}\,da) = (\frac{1}{\det(\boldsymbol{F})}\boldsymbol{F}\boldsymbol{T}\boldsymbol{F}^T)\boldsymbol{n}\,da. \tag{2.46}$$

In the above equation, the relationship between undeformed area $\boldsymbol{N}\,dA$ and deformed area $\boldsymbol{T}\boldsymbol{N}\,dA$ is used (Bonet and Wood 1997).

The second Piola-Kirchhoff tensor $\boldsymbol{T}$ is related to the Lagrangian or Green strain tensor $\boldsymbol{E}$ via the constitutive equation, which depends on the material of the deformed body. The LV myocardial constitutive equation, introduced previously in chapter 1, will be detailed later in chapter 4 for modelling the nonlinear material behaviour of the myocardium.

2.2 Finite Element Discretisation

The static equilibrium equation 2.39 that govern the finite deformation must be solved in order to analyse the deformation under certain loading conditions. For bodies with regu-

lar geometrical shape and simple mechanical properties this can be achieved analytically. However, for practical applications the domain on which the problem is defined is often irregular and materials behave nonlinearly. Irregular domains can be discretised into a finite number of sub-domains (called *elements*), over which the quantities involved in the governing equations are continuously approximated by interpolation functions (called *basis functions*). For each element, the finite elastic deformation governing equations are expressed in terms of material properties and discretised displacements of element vertices (referred to as *nodes*) together with nodal basis functions. Element-wise contributions are assembled into a global system of equations, and this nonlinear system, with boundary conditions and constraints, are solved to yield a set of nodal displacement from which the deformation field of the body is approximated using interpolations.

2.2.1 Discretised Representation of Continuous Fields

Let us begin describing the finite element theory with the idea of representing a continuous field $u(\xi_1, \xi_2, \xi_3)$ over a small domain $\Omega^{\xi}_{(e)} = 0 \leq \xi_i \leq 1, i = 1, 2, 3$ by a finite number of variables $u^m \, (m = 1, 2, ..., N)$ at some discretised points.

$$u(\xi_1, \xi_2, \xi_3) = \sum_m \psi_m u_m, \tag{2.47}$$

where ψ_m is the interpolation/weighting function (called *basis function*) associated with each discretised point (called *nodes*). The entire problem domain $\Omega^x \subset R^3$ can be subdivided into such small domains (called *elements*) $\Omega_{(e)}$ in which a local coordinate system $\{g_{(\xi_i)}, i = 1, 2, 3\}$ is used.

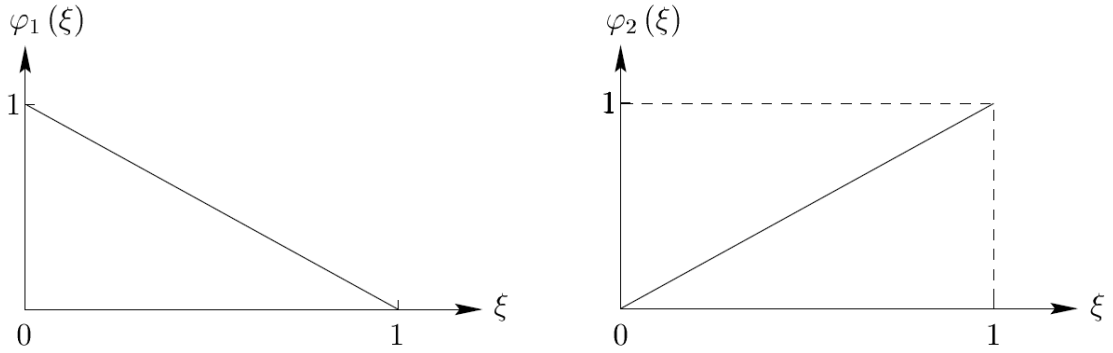

Figure 2.1: One-dimensional linear basis functions.

Linear Lagrangian Basis Function

The one-dimensional linear Lagrangian basis function (shown in figure 2.1) is defined as

$$\psi_1(\xi) = 1 - \xi, \tag{2.48}$$

$$\psi_2(\xi) = \xi, \tag{2.49}$$

where $0 \leq \xi \leq 1$ is the local element coordinate takes value of 0 at node 1 and 1 at node 2.

A continuous field variable u (scalar, vector or tensor) is interpolated using the basis function as

$$u(\xi) = \psi_1(\xi)u_1 + \psi_2(\xi)u_2, \tag{2.50}$$

where u_1 and u_2 are field values at element node 1 and node 2.

Quadratic Lagrangian Basis Function

It's useful to view basis functions in FEM as weighing functions on the nodal variables, and the weight function associated with a particular node takes the value of 1 when evaluated at that node and zeros at every other node in the same element (Hunter and Pullan

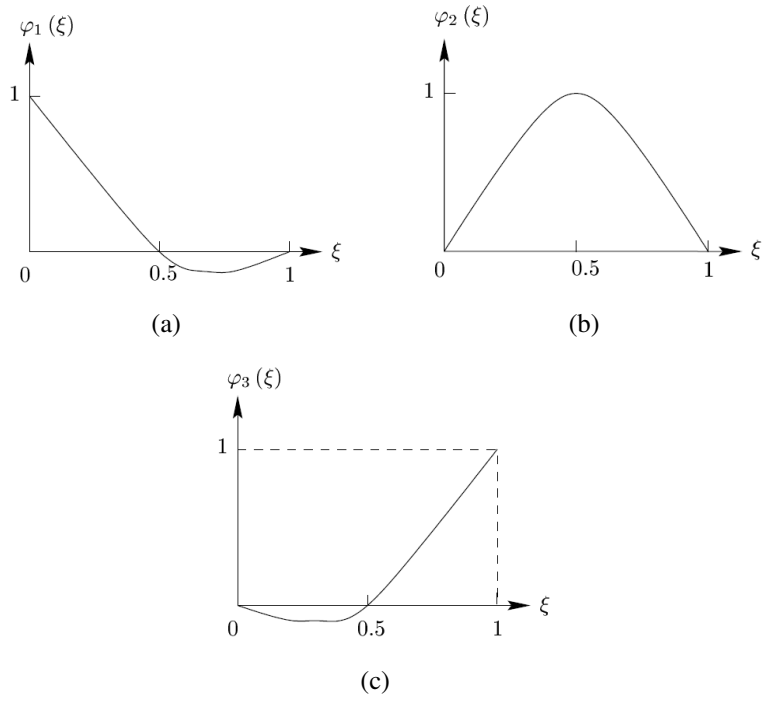

Figure 2.2: One-dimensional quadratic basis functions.

2001). That is, the nodal value has whole control on the field value at that particular node and no control at other nodes of the same element, unlike B-spline interpolation functions in which the control points typically don't lie in the spline. This property is the key to establishing other high-order interpolation functions. For example, the quadratic basis functions (figure 2.2) can be derived from this property as

$$\psi_1(\xi) = 2(\xi - 1)(\xi - 0.5), \tag{2.51}$$

$$\psi_2(\xi) = 4\xi(1 - \xi), \tag{2.52}$$

$$\psi_3(\xi) = 2\xi(\xi - 0.5), \tag{2.53}$$

$$u(\xi) = \psi_1(\xi)u_1 + \psi_2(\xi)u_2 + \psi_3(\xi)u_3, \tag{2.54}$$

where u_1, u_2 and u_3 are field values at element node 1 ,2 and 3, $0 \leq \xi \leq 1$ is the local element coordinate takes value of 0 at node 1, 0.5 at node 2 and 1 at node 3, and u is the continuous scalar, vector or tensor field variable.

Two- and Three-Dimensional Basis Functions

Let us assume that there are k_i $(i = 1, 2, 3)$ nodal variables in ξ_i direction, then three-dimensional basis functions, with a total number of $k1 \times k2 \times k3$, can be simply constructed from the products of the appropriate 1D basis functions as follows

$$\psi_{(l,m,n)}(\xi_1, \xi_2, \xi_3) = \psi_l(\xi_1)\psi_m(\xi_2)\psi_n(\xi_3), \tag{2.55}$$

$$u(\xi_1, \xi_2, \xi_3) = \psi_{(l,m,n)}(\xi_1, \xi_2, \xi_3)u_{(l,m,n)}, \tag{2.56}$$

where $l = 1, 2, ..., k_1$, $m = 1, 2, ..., k_2$, $n = 1, 2, ..., k_3$ are the basis function index in each spatial directions, and $u_{(l,m,n)}$ are the field values at the element grid points.

2.2.2 Discretisation of Finite Deformation Elasticity

The kinematics and equilibrium equations have been established in terms of a material or a spatial description. Either of these descriptions can be used to derive the discretised equilibrium equations for finite element method implementation.

Discretised Kinematics

Let us use $\{\psi_a(\xi_1, \xi_2, \xi_3)\}(a = 1, 2, ..., n)$ to denote the standard three-dimensional *basis function* or *shape functions* associated with node a, with n denoting the total number of nodes.

The continuous vector field variables, previously defined for the governing equations of finite deformation mechanics, can be presented by the corresponding nodal variables

together with the basis functions as follows.

$$\boldsymbol{\xi} = \sum_{a=1}^{n} \psi_a \boldsymbol{\xi}_a, \tag{2.57}$$

$$\boldsymbol{X} = \sum_{a=1}^{n} \psi_a \boldsymbol{X}_a, \tag{2.58}$$

$$\boldsymbol{x} = \sum_{a=1}^{n} \psi_a \boldsymbol{x}_a, \tag{2.59}$$

$$\boldsymbol{\delta v} = \sum_{a=1}^{n} \psi_a(\xi_1, \xi_2, \xi_3) \boldsymbol{\delta v}_a. \tag{2.60}$$

The continuous tensor field variables, describing the deformation tensors for the process of $d\boldsymbol{\xi} \rightarrow d\boldsymbol{X} \rightarrow d\boldsymbol{x}$, can be obtained using the above equations as follows.

$$\frac{\partial \boldsymbol{X}}{\partial \boldsymbol{\xi}} = \frac{\partial (\sum_{a=1}^{n} \psi_a \boldsymbol{X}_a)}{\partial \boldsymbol{\xi}} = \sum_{a=1}^{n} \boldsymbol{X_a} \otimes \frac{\partial \psi_a}{\partial \boldsymbol{\xi}}, \tag{2.61}$$

$$\frac{\partial \boldsymbol{x}}{\partial \boldsymbol{X}} = \frac{\partial (\sum_{a=1}^{n} \psi_a \boldsymbol{x}_a)}{\partial \boldsymbol{X}} = \sum_{a=1}^{n} \boldsymbol{x_a} \otimes \frac{\partial \psi_a}{\partial \boldsymbol{X}}, \tag{2.62}$$

$$\frac{\partial \boldsymbol{\delta v}}{\partial \boldsymbol{x}} = \sum_{a=1}^{n} \delta \boldsymbol{v_a} \otimes \frac{\partial \psi_a}{\partial \boldsymbol{x}}, \tag{2.63}$$

where $\otimes$ denotes the tensor product operator, and $\frac{\partial \psi_a}{\partial \boldsymbol{X}}$ and $\frac{\partial \psi_a}{\partial \boldsymbol{x}}$ in the above equations are obtained using differentiation rules as

$$\frac{\partial \psi_a}{\partial \boldsymbol{X}} = (\frac{\partial \boldsymbol{\xi}}{\partial \boldsymbol{X}})^T \frac{\partial \psi_a}{\partial \boldsymbol{\xi}} = (\frac{\partial \boldsymbol{X}}{\partial \boldsymbol{\xi}})^{-T} \frac{\partial \psi_a}{\partial \boldsymbol{\xi}}, \tag{2.64}$$

$$\frac{\partial \psi_a}{\partial \boldsymbol{x}} = (\frac{\partial \boldsymbol{\xi}}{\partial \boldsymbol{x}})^T \frac{\partial \psi_a}{\partial \boldsymbol{\xi}} = (\frac{\partial \boldsymbol{x}}{\partial \boldsymbol{\xi}})^{-T} \frac{\partial \psi_a}{\partial \boldsymbol{\xi}} = (\frac{\partial \boldsymbol{x}}{\partial \boldsymbol{X}} \frac{\partial \boldsymbol{X}}{\partial \boldsymbol{\xi}})^{-T} \frac{\partial \psi_a}{\partial \boldsymbol{\xi}}. \tag{2.65}$$

Discretised Stress Equilibrium Equation

In order to obtain the discretised version of spatial static equilibrium equations for FEM usage, recall the spatial virtual work Equation (2.39) given as the total virtual work done by the residual force $\boldsymbol{r}$ along an arbitrary virtual velocity vector $\boldsymbol{\delta v}$ as,

$$\delta W(\boldsymbol{\delta v}) = \underbrace{\int_{\delta\Omega} \boldsymbol{t} \cdot \boldsymbol{\delta v} dS + \int_{\Omega} \boldsymbol{b} \cdot \boldsymbol{\delta v} dV}_{\text{external work}} - \underbrace{\int_{\Omega} \boldsymbol{\sigma} : \nabla \boldsymbol{\delta v} dV}_{\text{internal work}} = 0 \tag{2.66}$$

Consider the contribution to $\delta W(\boldsymbol{\delta v})$ caused by a single virtual nodal velocity $\boldsymbol{\delta v_a}$ occurring at a typical node a of element e. Substituting $\boldsymbol{\delta v}$ and $\nabla \boldsymbol{\delta v}$ given by equation 2.60 and 2.63, using the symmetry property of Cauchy stress tensor $\boldsymbol{\sigma}$ and the property that

$$\boldsymbol{\sigma} : (\boldsymbol{u} \otimes \boldsymbol{v}) = \boldsymbol{u} \cdot (\boldsymbol{\sigma v}) \quad \text{for any vector } \boldsymbol{u} \text{ and } \boldsymbol{v}, \tag{2.67}$$

the virtual work done by moving a single node a of element e by a virtual displacement $\boldsymbol{\delta v_a}$ can be obtained as

$$\delta W^{(e,a)}(\psi_a \boldsymbol{\delta v_a}) \tag{2.68}$$

$$= \int_{\Omega^{(e)}} \boldsymbol{b} \cdot (\psi_a \boldsymbol{\delta v}_a) dV + \int_{\delta\Omega^{(e)}} \boldsymbol{t} \cdot (\psi_a \boldsymbol{\delta v}_a) dS - \int_{\Omega^{(e)}} \boldsymbol{\sigma} : (\boldsymbol{\delta v_a} \otimes \nabla \psi_a) dV \tag{2.69}$$

$$= \boldsymbol{\delta v_a} \cdot \Big(\underbrace{\int_{\Omega^{(e)}} \boldsymbol{b} \psi_a dV + \int_{\delta\Omega^{(e)}} \boldsymbol{t} \psi_a dS}_{\text{external equivalent nodal force}} - \underbrace{\int_{\Omega^{(e)}} \boldsymbol{\sigma} \nabla \psi_a dV}_{\text{internal equivalent nodal force}} \Big) \tag{2.70}$$

$$= \boldsymbol{\delta v_a} \cdot (\boldsymbol{F}_{EX}^{(e,a)} - \boldsymbol{F}_{IN}^{(e,a)}) \tag{2.71}$$

which is the element-wise *fundamental discretised version of the static equilibrium equation*. It's instructive to think of the above equation in terms of nodal forces based on the simple fact that the amount of the work done is the product of force and distance along the force direction. The internal and external equivalent nodal forces $\boldsymbol{F}_{IN}^{(e,a)}$ and $\boldsymbol{F}_{EX}^{(e,a)}$ are defined in the above equations.

By assembling the local equivalent nodal forces $\boldsymbol{F}_{EX}^{(e,a)}$ and $\boldsymbol{F}_{IN}^{(e,a)}$ (defined in equation 2.70) into the equivalent global nodal internal and external force vector $\boldsymbol{F}_{EX}$ and $\boldsymbol{F}_{IN}$ (e.g., detailed by Hunter and Pullan 2001), we have the equivalent global residual force vector

$$\boldsymbol{R}(\boldsymbol{x}) = \boldsymbol{F}_{EX} - \boldsymbol{F}_{IN} = 0, \tag{2.72}$$

where is the $\boldsymbol{x}$ is the global vector of nodal free variables. The numerical solution of this system is discussed in the next subsection.

Incompressibility Constraints

For incompressible materials, an additional constraint, which guarantees that the volume of each element does not change, is needed, i.e.,

$$\det(\boldsymbol{F}) - 1 = 0. \tag{2.73}$$

If this constraint is added via the Lagrange Multiplier Method, an additional degree of freedom p (named as *hydrostatic pressure*) is introduced. For a Galerkin or weak formulation, the virtual work done by changing hydrostatic pressure at node a of element e is given by

$$\delta W^{(e,a)}(\psi_a^p \delta p_a) = \delta p_a \int_{\Omega}^{(e)} (\det(\boldsymbol{F}) - 1)\psi^p dV = 0 \tag{2.74}$$

where $\Omega^{(e)}$ denotes the deformed domain of the element and ψ^p are the basis functions used to approximate the three-dimensional hydrostatic pressure field. This derivation is similar to the virtual work in equation 2.69, and the details can be founded in Bonet and Wood 1997.

Remark 2.2.1. *Oden 1972 and Golub et al. 2005 suggest that the interpolation scheme chosen to describe the deformed geometric coordinate should be of higher order than those chosen to approximate the hydrostatic pressure field. Smith et al. 2004 points out that the strain energy contribution to the stress component is related to the first derivatives of the geometric displacement fields, whereas the hydrostatic pressure directly contributes to the stress component. For consistency, and to avoid numerical ill-conditioning when calculating components of the stress tensor, the two contributions should vary in a similar manner.*

2.3 Numerical solution

2.3.1 Numerical integration using Gaussian Quadrature

The calculation of surface and volume integrals is essential and common when FEM is used. Often these integrals can not be determined analytically. For this reason numerical or *quadrature* based integration is therefore required and one of schemes for efficiently integrating the expressions that arise in FEM is *Gauss-Legendre quadrature* (hereafter referred as Gaussian quadrature), which approximates the integrals using a weighted sum of function values at specified points within the domain of integration.

Integration In One-Dimension

To illustrate the idea of Gaussian quadrature scheme, let's consider the problem of integrating $f(\xi)$ between 0 and 1. Approximating this by

$$\int_0^1 f(\xi)\,d\xi = \sum_{i=1}^{I} W_i f(\xi_i) + E \tag{2.75}$$

where W_i are the weights associated with sample points ξ_i (called *Gauss Points*), I is the number of Gauss points (called the *order of quadrature scheme*) and E is the error in the approximation. We now choose the Gauss points and weights to exactly integrate a polynomial of degree $2I-1$ with I-th order quadrature scheme (since a general polynomial of degree $2I-1$ has $2I$ arbitrary coefficients and there are $2I$ Gauss points and weights to fit).

For example, with $I=2$ we can exactly integrate a polynomial

$$f(\xi) = a + b\xi + c\xi^2 + d\xi^3 \tag{2.76}$$

of degree 3 by

$$\int_0^1 f(\xi)\,d\xi = W_1 f(\xi_1) + W_2 f(\xi_2) \tag{2.77}$$

$$= a\int_0^1 d\xi + b\int_0^1 \xi\,d\xi + c\int_0^1 \xi^2\,d\xi + d\int_0^1 \xi^3\,d\xi. \tag{2.78}$$

By choosing $f(\xi) = 1, \xi, \xi^2, \xi^3$ respectively in the above equation, we get four equations for four unknowns, and the Gauss points and weights are fully determined as follows.

$$\xi_1 = \frac{1}{2} - \frac{1}{2\sqrt{3}}, \tag{2.79}$$

$$\xi_2 = \frac{1}{2} + \frac{1}{2\sqrt{3}}, \tag{2.80}$$

$$W_1 = W_2 = \frac{1}{2}. \tag{2.81}$$

Integration in Two- and Three-Dimensions

To approximate surface and volume integrals using Gaussian quadrature, one-dimensional schemes are set up in each dimension, such as

$$\int_0^1\int_0^1 f(\xi^1,\xi^2)\,d\xi^1\,d\xi^2 = \int_0^1 (\sum_{i=1}^{I} W_i f(\xi_i,\xi^2) + E_I)\,d\xi^2 \tag{2.82}$$

$$= \sum_{i=1}^{I}\sum_{j=1}^{J} W_i W_j f(\xi_i,\xi_j) + E_I E_J \tag{2.83}$$

$$\approx \sum_{i=1}^{I}\sum_{j=1}^{I} W_i W_j f(\xi_i,\xi_j) \tag{2.84}$$

$$= \sum_{g=1}^{I^2} \bar{\bar{W}}_g f(\boldsymbol{\xi}_g), \tag{2.85}$$

where $\bar{\bar{W}}_g$, defined in the above equation, are the weights on the function values at $\boldsymbol{\xi}_g$ over a 2D domain.

Similarly for three-dimensional integrals, the three-dimensional integration is approxi-

mated as a weighted sum of functions values by

$$\int_0^1 \int_0^1 \int_0^1 f(\xi^1,\xi^2,\xi^3)\,d\xi^1\,d\xi^2\,d\xi^3 = \sum_{i=1}^{I}\sum_{j=1}^{I}\sum_{k=1}^{I} W_i W_j W_k f(\xi_i,\xi_j,\xi_k) + E_I E_J E_K \tag{2.86}$$

$$\approx \sum_{i=1}^{I}\sum_{j=1}^{I}\sum_{k=1}^{I} W_i W_j W_k f(\xi_i,\xi_j,\xi_k) \tag{2.87}$$

$$= \sum_{g=1}^{I^3} \bar{\bar{\bar{W}}}_g f(\boldsymbol{\xi}_g), \tag{2.88}$$

where $\bar{\bar{\bar{W}}}_g$,defined in the above equation, are the weights on the functions values at $\boldsymbol{\xi}_g$ over a 3D domain.

Remark 2.3.1. *The number of Gauss points I chosen for each ξ_i-direction is governed by the complexity of the integrand in that direction, including the degree of basis function in ξ_i-direction and any additional multiplication terms such as $\frac{\partial \xi_i}{x_j}$ coming from the inverse of the matrix $[\frac{\partial x_i}{\xi_j}]$ (Hunter and Pullan 2001). The quadrature error must be balanced against the discretisation error. For example, if the cubic-linear interpolation used for two-dimension interpolation, three and two (for cubic and for linear interpolation respectively) Gauss points in each respective direction is sufficient to exactly integrate these basis functions. In the practice of implementation, it's suggested to check error convergence against the number of Gauss points to give a reasonable feeling about the number of Gauss points needed in a particular application.*

Rewriting Residual Vector using Gaussian Quadrature

Using the Gaussian quadrature outlined above, the integrals in equation 2.70 for defining the external and internal nodal force vectors can be written as :

$$\boldsymbol{F}_{EX}^{(e,a)} = \int_{\Omega^{(e)}} \boldsymbol{b}\psi_a\,dV + \int_{\delta\Omega^{(e)}} \boldsymbol{t}\psi_a\,dS \tag{2.89}$$

$$= \sum_{\boldsymbol{\xi}_g\in\Omega^{(e)},g=1}^{I^3} \bar{\bar{\bar{W}}}_g \boldsymbol{b}\psi_a \det(\frac{\partial \boldsymbol{x}}{\partial \boldsymbol{\xi}}) + \sum_{k=1}^{6} \sum_{\boldsymbol{\xi}_g\in\delta\Omega_k^{(e)},g=1}^{I^2} \bar{\bar{\bar{W}}}_g \boldsymbol{t}\psi_a \det(\frac{\partial \boldsymbol{x}^k}{\partial \boldsymbol{\xi}^k}), \tag{2.90}$$

where the first summation is over all the Gauss points $\boldsymbol{\xi}_g$ within the 3D eight-node hexahedral element e volume $\Omega^{(e)}$, and the second summation is over all the Gaussian points $\boldsymbol{\xi}_g$ over six 2D quadrilateral elements $\{\delta\Omega_k^{(e)} \mid k = 1, ..., 6\}$ on the boundaries of element e.

Similarly the volume integral in internal nodal force vector can be written as

$$\boldsymbol{F}_{IN}^{(e,a)} = \int_{\Omega^{(e)}} \boldsymbol{\sigma}\nabla\psi_a dV \tag{2.91}$$

$$= \sum_{\boldsymbol{\xi}_g \in \Omega^{(e)}, g=1}^{I^3} \bar{\bar{\bar{W}}}_g \boldsymbol{\sigma}\nabla\psi_a \det(\frac{\partial \boldsymbol{x}}{\partial \boldsymbol{\xi}}). \tag{2.92}$$

2.3.2 Solving Nonlinear Systems using Newton-Raphson Method

The nonlinear equation 2.72 needs to be numerically solved, and Newton-Raphson algorithm is a commonly-used iterative method to solve such a nonlinear system. Specifically, given a solution estimate $\boldsymbol{x_k}$ at iteration k, a new value is obtained in terms of an increment $\boldsymbol{u}$, i.e.

$$\boldsymbol{x}_{k+1} = \boldsymbol{x}_k + \boldsymbol{u}, \tag{2.93}$$

such that

$$\boldsymbol{R}(\boldsymbol{x}_{k+1}) = \boldsymbol{R}(\boldsymbol{x_k}) + \mathcal{D}\boldsymbol{R}(\boldsymbol{x_k})[\boldsymbol{u}] = 0, \tag{2.94}$$

where $\mathcal{D}\boldsymbol{R}(\boldsymbol{x_k})[\boldsymbol{u}]$, called the *directional increment*, is the incremental of $\boldsymbol{R}(\boldsymbol{x_k})$ if $\boldsymbol{x_k}$ is increased by $\boldsymbol{u}$. The directional increment can be approximated linearly by forward difference scheme as

$$\mathcal{D}\boldsymbol{R}(\boldsymbol{x_k})[\boldsymbol{u}] \approx \boldsymbol{K}\boldsymbol{u}, \text{ where} \tag{2.95}$$

$$K_{ij}(\boldsymbol{x_k}) = \frac{\partial R_i}{\partial x_j} \mid_{\boldsymbol{x_k}} \text{, i,j = 1,..., NDOF.} \tag{2.96}$$

In the above equations, matrix $\boldsymbol{K}$ is usually called the *stiffness matrix*.

Thus a linear system is formulated at each iteration as

$$\boldsymbol{K}(\boldsymbol{x_k})\boldsymbol{u} = -\boldsymbol{R}(\boldsymbol{x_k}). \tag{2.97}$$

Line Search Algorithm

During the course of a complex deformation process, the search space for incremental $\boldsymbol{u}$ is often highly nonlinear and the straight application of Newton-Raphson method may be insufficient to achieve a fast convergence. "Post-processing" techniques, at the end of each Newton-Raphson iteration, are often needed to give better convergence result. Among them, the *line search* method is a simple yet effective candidate, which interprets the displacement vector **u** obtained from equation (2.97) as an optimal direction of advance toward the solution but allows the magnitude of step to be controlled by an additional parameter η as

$$\boldsymbol{x}_{k+1} = \boldsymbol{x_k} + \eta\boldsymbol{u}. \tag{2.98}$$

The value of η is normally chosen so that the residual at the state of $\boldsymbol{x_k}+\eta\boldsymbol{u}$ is orthogonal to the direction of $\boldsymbol{u}$ (Bonet and Wood 1997), that is,

$$R(\eta) = \boldsymbol{u}^T\boldsymbol{R}(\boldsymbol{x_k} + \eta\boldsymbol{u}) = 0. \tag{2.99}$$

In practice, we relax this stringent condition to find η values satisfying

$$|R(\eta)| = \rho\,|R(0)|\,, \tag{2.100}$$

where ρ=0.5 typically sufficient even for highly nonlinear function of $R(\eta)$.

If we approximate $R(\eta)$ as a quadratic function of η, only parameters are needed to fully determined $R(\eta)$ locally. By noticing

$$R'(0) = \left.\frac{dR}{d\eta}\right|_{\eta=0} = \boldsymbol{u^T}\left.\frac{\partial \boldsymbol{R}}{\partial \boldsymbol{x}}\right|_{\boldsymbol{x}=\boldsymbol{x_k}}\boldsymbol{u} = \boldsymbol{u^T}\boldsymbol{K}(\boldsymbol{x_k})\boldsymbol{u} = -\boldsymbol{u^T}\boldsymbol{R}(\boldsymbol{x_k}) = -R(0), \tag{2.101}$$

thus $R(0)$ and $R'(0)$ are ready to use without the extra computation cost to evaluate $\boldsymbol{R}(\boldsymbol{x}_k)$. Finally, a third value is typically the standard value of the residual force for which $\eta = 1$, that is,

$$R(1) = \boldsymbol{u}^{\boldsymbol{T}}\boldsymbol{R}(\boldsymbol{x_k} + \boldsymbol{u}). \tag{2.102}$$

Using $R(0)$, $R(1)$ and $R'(0)$, the local quadratic approximation of R is thus obtained as

$$R(\eta) \approx (1-\eta)R(0) + R(1)\eta^2 = 0. \tag{2.103}$$

Setting the first-order derivative of $R(\eta)$ with respect to $R\eta$ to the zero, the optimal value η is found to be

$$\eta = \begin{cases} \frac{\alpha}{2} + \sqrt{(\frac{\alpha}{2})^2 - \alpha}, & \alpha < 0 \\ \frac{\alpha}{2}, & \alpha > 0 \end{cases} \text{, where} \tag{2.104}$$

$$\alpha = R(0)/R(1). \tag{2.105}$$

2.4 Summary

In this chapter, we explained the fundamental theory of finite deformation mechanics and its relevant numerical techniques, whose implementation lies at the foundation of modelling and simulating the cardiac ventricular deformation. In the following chapters, we will explain the parameterization of the mechanical model using patient-specific clinic measurements.

Chapter 3

Kalman filters

"The most probable value of the unknown quantities will be that in which the sum of squares of the differences between the actually observed and the computed values multiplied by numbers that measure the degree of precision is a minimum". – Karl Friedrich Gauss

The Kalman filter is a mathematical method named after Rudolf E. Kalman (Kalman 1960). It uses a system's dynamics model (e.g., physical laws of motion), known control inputs to that system, and measurements (from sensors) to form an estimate of the system's varying quantities (its state) that is better than the estimate obtained by using measurement alone. To simultaneously estimate both state variables and parameters, the principle of joint state-parameter estimation is commonly employed, in which the system's state is augmented with its parameters to form a joint state-parameter vector, and this vector is recursively estimated (Chen et al. 2008).

In this chapter, as the theoretical foundation of the parameter estimation approach in chapter 4, we derive, from Kalman filters, its four extensions to the nonlinear systems and reduced-order versions. This foundation forms the basis of the reduced-order unscented Kalman filter (rUKF) which will later be employed as an inverse approach for the estimation of myocardial constitutive material parameters in chapter 4.

In section 3.1, the development of the classic Kalman filter is presented. Following this review, its extensions and generalisations are also developed. Its extension to nonlinear systems, namely the extended Kalman filter (EKF) and unscented Kalman filter (UKF), are derived in section 3.2 and 3.3 respectively, where the joint state-parameter estimation problem is formulated. Finally the *reduced-order* extensions of EKF and UKF to large systems are developed in sections 3.4 and 3.5. The derivations for KF, EKF, UKF and reduced-order EKF (or SEEK) in section 3.1 to 3.4 are based on existing literature and reduced-order UKF (or SEUK) in section 3.5 is self-derived in this thesis.

3.1 Derivation of discrete Kalman filter (KF)

As the foundation of the Kalman filter extensions (EKF and UKF in this chapter and reduced-order UKF in the next chapter), the derivation of the Kalman filter following Kalman (1960) is presented (Simon 2006).

3.1.1 Derivation of measurement update component of KF

Suppose we want to *recursively* estimate a *constant* vector $\boldsymbol{x} \in \mathbb{R}^{n^x}$ (i.e., no transient changes in time, or updates as stated below in equation 3.6) and we obtained a set of measurements $\{\boldsymbol{y}_k \in \mathbb{R}^m,\ k = 1, ..., K\}$ which is related to $\boldsymbol{x}$ by

$$\boldsymbol{y}_k = \boldsymbol{H}_k \boldsymbol{x} + \boldsymbol{v}_k, \tag{3.1}$$

where $\boldsymbol{H}_k \in \mathbb{M}^{m \times n^x}$ is the (linear) *observational operator*, and $\boldsymbol{v}_k$ is the additive *measurement noise* of Gaussian type with mean $\boldsymbol{0}$ and constant covariance matrix $\boldsymbol{R}$, that is,

$$\mathbb{E}\left[\boldsymbol{v}_k\right] = \boldsymbol{0}, k = 1, ..., K \tag{3.2}$$

$$\mathbb{E}\left[\boldsymbol{v}_i \boldsymbol{v}_i^T\right] = \boldsymbol{R}, i = 1, ..., K, \tag{3.3}$$

where $\mathbb{E}[\cdot]$ is the mean or expectation of a random variable, and $\boldsymbol{R} \in \mathbb{M}^{m\times m}$ is the *measurement error covariance*. From now on, the Gaussian-type noise $\boldsymbol{v}_k$ satisfying the above two equations will be denoted by

$$\boldsymbol{v}_k \sim \mathcal{N}(\boldsymbol{0}, \boldsymbol{R}), \tag{3.4}$$

and for justification of this Gaussian distribution assumption, see Remark 3.3.1. Further we assume the measurement noise $\boldsymbol{v}_k$ is white (no temporal auto-correlation), i.e.,

$$\mathbb{E}\left[\boldsymbol{v}_i \boldsymbol{v}_j^T\right] = \boldsymbol{O},\ i \neq j. \tag{3.5}$$

The constant vector $\boldsymbol{x}$ is recursively estimated, from the time point[1] $(k-1)^+$ ($k = 1, 2, ..., K$) to k^- (*time update*), and from k^- to k^+ (*measurement update*), that is,

$$\hat{\boldsymbol{x}}_k^- = \hat{\boldsymbol{x}}_{k-1}^+, \tag{3.6}$$

$$\hat{\boldsymbol{x}}_k^+ = \boldsymbol{K}_k(\boldsymbol{y}_k - \boldsymbol{H}_k\hat{\boldsymbol{x}}_k^-), \tag{3.7}$$

where $\hat{\cdot}$ denotes the variable estimated, and $\boldsymbol{K} \in \mathbb{M}^{n^x\times m}$ is the *(Kalman) gain matrix* which we will derive based on criterion 3.8 below. Note that since we want to estimate a constant vector $\boldsymbol{x}$, therefore there is no transient between the prior estimation at time point $k+1$ and the posterior estimation at time point k (equation 3.6).

The *optimality criterion* J_k at time k to be minimised by equation 3.7 is the total uncertainty of the estimation, which can be written as the sum of variances of the estimation error

$$J_k = \mathrm{tr}(\mathbb{E}\left[(\boldsymbol{x} - \hat{\boldsymbol{x}}_k^+)(\boldsymbol{x} - \hat{\boldsymbol{x}}_k^+)^T\right]), \tag{3.8}$$

$$= \mathrm{tr}(\mathbb{E}\left[\boldsymbol{\epsilon}_{x,k}^+(\boldsymbol{\epsilon}_{x,k}^+)^T\right]), \tag{3.9}$$

$$= \mathrm{tr}(\boldsymbol{P}_k^+), \tag{3.10}$$

[1] k^- and k^+ denote the time point just before and after assimilating the measurement at time point k (also called the *prior* and *posterior* time point k). 0^+ is the initialisation point.

where $\boldsymbol{\epsilon}_{x,k}$, the *estimation error*, and $\boldsymbol{P}_k$, the *estimation error covariance* are defined by the above equation. That is, the posterior estimation error $\boldsymbol{\epsilon}^+_{x,k}$ and estimation error covariance $\boldsymbol{P}^+_k$ are given by

$$\boldsymbol{\epsilon}^+_{x,k} = \boldsymbol{x} - \hat{\boldsymbol{x}}^+_k, \tag{3.11}$$

$$\boldsymbol{P}^+_k = \mathbb{E}\left[\boldsymbol{\epsilon}^+_{x,k}(\boldsymbol{\epsilon}^+_{x,k})^T\right]. \tag{3.12}$$

And similarly the prior estimation error $\boldsymbol{\epsilon}^-_{x,k}$ and estimation error covariance $\boldsymbol{P}^-_k$ are calculated by

$$\boldsymbol{\epsilon}^-_{x,k} = \boldsymbol{x} - \hat{\boldsymbol{x}}^-_k, \tag{3.13}$$

$$\boldsymbol{P}^-_k = \mathbb{E}\left[\boldsymbol{\epsilon}^-_{x,k}(\boldsymbol{\epsilon}^-_{x,k})^T\right]. \tag{3.14}$$

Substituting from equation 3.1 for $\boldsymbol{y}_k$ into equation 3.7, and then substituting from equation 3.7 for $\boldsymbol{x}^+_k$ in equation 3.11, we can rewrite equation 3.12, by simple algebra, as

$$\boldsymbol{P}^+_k = \mathbb{E}\left[\boldsymbol{\epsilon}^+_{x,k}(\boldsymbol{\epsilon}^+_{x,k})^T\right] \tag{3.15}$$

$$= \mathbb{E}\left[((\boldsymbol{I} - \boldsymbol{K}_k\boldsymbol{H}_k)\boldsymbol{\epsilon}^-_{x,k} - \boldsymbol{K}_k\boldsymbol{v}_k)((\boldsymbol{I} - \boldsymbol{K}_k\boldsymbol{H}_k)\boldsymbol{\epsilon}^-_{x,k} - \boldsymbol{K}_k\boldsymbol{v}_k)^T\right] \tag{3.16}$$

$$= (\boldsymbol{I} - \boldsymbol{K}_k\boldsymbol{H}_k)\mathbb{E}\left[(\boldsymbol{\epsilon}^-_{x,k})(\boldsymbol{\epsilon}^-_{x,k})^T\right](\boldsymbol{I} - \boldsymbol{K}_k\boldsymbol{H}_k)^T + \boldsymbol{K}_k\mathbb{E}\left[\boldsymbol{v}_k\boldsymbol{v}_k^T\right]\boldsymbol{K}_k^T$$
$$- \boldsymbol{K}_k\mathbb{E}\left[\boldsymbol{v}_k(\boldsymbol{\epsilon}^-_{x,k})^T\right](\boldsymbol{I} - \boldsymbol{K}_k)^T - (\boldsymbol{I} - \boldsymbol{K}_k)\mathbb{E}\left[\boldsymbol{\epsilon}^-_{x,k}(\boldsymbol{v}_k)^T\right]\boldsymbol{K}_k^T. \tag{3.17}$$

Since $\boldsymbol{\epsilon}^+_{x,k}$ is the error *before* assimilating measurement $\boldsymbol{v}_k$ at time k ($\boldsymbol{\epsilon}_{x,k}-$), the prior estimation $\boldsymbol{\epsilon}^+_{x,k}$ is independent of the measurement noise $\boldsymbol{v}_k$. Therefore the terms $\mathbb{E}\left[\boldsymbol{v}_k(\boldsymbol{\epsilon}^-_{x,k})^T\right]$ and $\mathbb{E}\left[\boldsymbol{\epsilon}^-_{x,k}(\boldsymbol{v}_k)^T\right]$ in equation 3.17 become

$$\mathbb{E}\left[\boldsymbol{\epsilon}^-_{x,k}(\boldsymbol{v}_k)^T\right] = \mathbb{E}\left[\boldsymbol{\epsilon}^-_{x,k}\right]\mathbb{E}\left[(\boldsymbol{v}_k)^T\right] = \boldsymbol{0}, \tag{3.18}$$

$$\mathbb{E}\left[\boldsymbol{\epsilon}^-_{x,k}(\boldsymbol{v}_k)^T\right] = \mathbb{E}\left[\boldsymbol{\epsilon}^-_{x,k}\right]\mathbb{E}\left[(\boldsymbol{v}_k)^T\right] = \boldsymbol{0}. \tag{3.19}$$

Substituting from the above equations for the terms in equation 3.17, we have

$$\boldsymbol{P}^+_k = (\boldsymbol{I} - \boldsymbol{K}_k\boldsymbol{H}_k)\mathbb{E}\left[(\boldsymbol{\epsilon}^-_{x,k})(\boldsymbol{\epsilon}^-_{x,k})^T\right](\boldsymbol{I} - \boldsymbol{K}_k\boldsymbol{H}_k)^T + \boldsymbol{K}_k\mathbb{E}\left[\boldsymbol{v}_k\boldsymbol{v}_k^T\right]\boldsymbol{K}_k^T, \tag{3.20}$$

$$= (\boldsymbol{I} - \boldsymbol{K}_k\boldsymbol{H}_k)\boldsymbol{P}^-_k(\boldsymbol{I} - \boldsymbol{K}_k\boldsymbol{H}_k)^T + \boldsymbol{K}_k\boldsymbol{R}\boldsymbol{K}_k^T. \tag{3.21}$$

Based on the above equation and equation 3.8 of the optimality criterion, we can derive the optimal gain matrix $\boldsymbol{K}_k$ by minimising J_k with respect to $\boldsymbol{K}_k$, i.e.,

$$\frac{\partial J_k}{\partial \boldsymbol{K}_k} = 2(\boldsymbol{I} - \boldsymbol{K}_k \boldsymbol{H}_k)\boldsymbol{P}_k^-(-\boldsymbol{H}_k^T) + 2\boldsymbol{K}_k \boldsymbol{R}_k, \tag{3.22}$$

where the equality

$$\frac{\partial \operatorname{tr}(\boldsymbol{K}_k \boldsymbol{R} \boldsymbol{K}_k^T)}{\partial \boldsymbol{K}_k} = \boldsymbol{K}_k(\boldsymbol{R} + \boldsymbol{R}^T) = 2\boldsymbol{K}\boldsymbol{R}. \tag{3.23}$$

has been used. Set equation 3.22 to be zero and solve for $\boldsymbol{K}_k$, we have

$$\boldsymbol{K}_k = \boldsymbol{P}_k^- \boldsymbol{H}_k^T (\boldsymbol{H}_k \boldsymbol{P}_k^- \boldsymbol{H}_k^T + \boldsymbol{R}_k)^{-1}. \tag{3.24}$$

In summary, equations (3.7), (3.21) and (3.24) form the measurement update component of Kalman filter, which, viewed from another Bayesian perspective, is based on the optimality criterion in equation 3.8 to recursively maximise the likelihood of estimated state variable (and parameters) given available observations (Evensen 2009, Chapter 9).

3.1.2 Derivation of time update component of KF

Now we generalise equation 3.6 to have a temporal transient. That is, the estimated vector $\boldsymbol{x}$ is no longer constant, but the *state variable* of a linear time-invariant (LTI) system:

$$\boldsymbol{x}_k = \boldsymbol{F}\boldsymbol{x}_{k-1}, \quad k = 1, 2, ..., K, \tag{3.25}$$

where $\boldsymbol{F}$ is the *system transition matrix*.

The above system is generalised further to have an additive stochastic noise term $\boldsymbol{w}_k$ (the *system noise*) which reflects the system error due to, e.g., the uncertainty of system initial condition or parameters, which is a common practice of the standard state-space representation of LTI stochastic system:

$$\boldsymbol{x}_k = \boldsymbol{F}\boldsymbol{x}_{k-1} + \boldsymbol{w}_{k-1}, \quad k = 1, 2, ..., K. \tag{3.26}$$

Same as the measurement noise in equation 3.5, we assume $\boldsymbol{w}_k$ is white and of Gaussian type. That is,

$$\boldsymbol{w}_k \in \mathcal{N}(\boldsymbol{0}, \boldsymbol{Q}), \tag{3.27}$$

$$\mathbb{E}\left[\boldsymbol{w}_i \boldsymbol{w}_j^T\right] = \boldsymbol{O}, \quad i \neq j. \tag{3.28}$$

With the introduction of system equation 3.26, the time update of mean $\hat{\boldsymbol{x}}_k^-$ in Kalman filter (equation 3.6) is rewritten as

$$\hat{\boldsymbol{x}}_k^- = \mathbb{E}\left[\boldsymbol{x}_k^-\right], \tag{3.29}$$

$$= \mathbb{E}\left[\boldsymbol{F}\boldsymbol{x}_{k-1}^+ + \boldsymbol{w}_{k-1}\right], \tag{3.30}$$

$$= \boldsymbol{F}\,\mathbb{E}\left[\boldsymbol{x}_{k-1}^+\right] + \mathbb{E}\left[\boldsymbol{w}_{k-1}\right], \tag{3.31}$$

$$= \boldsymbol{F}\hat{\boldsymbol{x}}_{k-1}^+. \tag{3.32}$$

Besides the update of mean $\hat{\boldsymbol{x}}_k^-$, the update of error covariance matrix $\boldsymbol{P}_k^-$ follows

$$\boldsymbol{P}_k^- = \mathbb{E}\left[\boldsymbol{x}_k^-(\boldsymbol{x}_k^-)^T\right], \tag{3.33}$$

$$= \mathbb{E}\left[(\boldsymbol{F}\boldsymbol{x}_{k-1}^+ + \boldsymbol{w}_{k-1})(\boldsymbol{F}\boldsymbol{x}_{k-1}^+ + \boldsymbol{w}_{k-1})^T\right], \tag{3.34}$$

$$= \boldsymbol{F}\mathbb{E}\left[\boldsymbol{x}_{k-1}^+(\boldsymbol{x}_{k-1}^+)^T\right]\boldsymbol{F}^T + \mathbb{E}\left[\boldsymbol{w}_{k-1}\boldsymbol{w}_{k-1}^T\right] + \boldsymbol{F}\mathbb{E}\left[\boldsymbol{x}_{k-1}^+\boldsymbol{w}_{k-1}^T\right] + \mathbb{E}\left[\boldsymbol{w}_{k-1}(\boldsymbol{x}_{k-1}^+)^T\right]\boldsymbol{F}^T, \tag{3.35}$$

Since the system state $\boldsymbol{x}_k$ at time k is independent of the system noise $\boldsymbol{Q}_k$ at the same time, the terms $\mathbb{E}\left[\boldsymbol{x}_k^+\boldsymbol{w}_k^T\right]$ and $\mathbb{E}\left[\boldsymbol{w}_k(\boldsymbol{x}_k^+)^T\right]$ in equation 3.35 are simplified as

$$\mathbb{E}\left[\boldsymbol{x}_k^+\boldsymbol{w}_k^T\right] = \mathbb{E}\left[\boldsymbol{x}_k^+\right]\mathbb{E}\left[\boldsymbol{w}_k^T\right] = \boldsymbol{O}, \tag{3.36}$$

$$\mathbb{E}\left[\boldsymbol{w}_k(\boldsymbol{x}_k^+)^T\right] = \mathbb{E}\left[\boldsymbol{w}_k\right]\mathbb{E}\left[(\boldsymbol{x}_k^+)^T\right] = \boldsymbol{O}, \tag{3.37}$$

where the assumption of equation 3.27 is used. Therefore equation 3.35 (the time update of estimation-error covariance $\boldsymbol{P}_{k+1}^-$) becomes

$$\boldsymbol{P}_k^- = \boldsymbol{F}\boldsymbol{P}_{K-1}^+\boldsymbol{F}^T + \boldsymbol{Q}. \tag{3.38}$$

Finally, equations 3.32 and 3.38 form the time update component of Kalman filter, which are based on the propagation of mean and covariance through a linear transformation. Later in unscented Kalman filter (UKF), this prorogation is achieved through carefully-selected sampling, where the transformation is nonlinear (section 3.3.1).

As a summary, table 3.1 lists all the components of Kalman filter developed in this section. For further references on the optimal estimation, Kailath et al. 2000 provides an in-depth treatment by starting from the so-called asymptotic observer and the modification in the presence of random disturbances, particularly useful for better understanding of properties of the Kalman filter, e.g., its asymptotic behaviour.

Table 3.1: Summary of discrete-time Kalman filter in section 3.1

Filter components	referenced equations
(System equations)	
$\boldsymbol{x}_k = \boldsymbol{F}\boldsymbol{x}_{k-1} + \boldsymbol{w}_{k-1}$	3.26
$\boldsymbol{w} \in \mathcal{N}(\boldsymbol{0}, \boldsymbol{Q})$	3.27
$\mathbb{E}\left[\boldsymbol{w}_i \boldsymbol{w}_i^T\right] = \boldsymbol{Q}$	3.27
$\mathbb{E}\left[\boldsymbol{w}_i \boldsymbol{w}_j^T\right] = \boldsymbol{O}, \quad i \neq j$	3.27
(Measurement equations)	
$\boldsymbol{y}_k = \boldsymbol{H}_k \boldsymbol{x}_k + \boldsymbol{v}_k$	3.1
$\boldsymbol{v} \sim \mathcal{N}(\boldsymbol{0}, \boldsymbol{R})$	3.4
$\mathbb{E}\left[\boldsymbol{v}_i \boldsymbol{v}_j\right] = \boldsymbol{O}, \quad i \neq j$	3.5
Initialize $\hat{\boldsymbol{x}}_0^+$ and $\boldsymbol{P}_0^+$	
(Time update)	
$\hat{\boldsymbol{x}}_k^- = \boldsymbol{F}\hat{\boldsymbol{x}}_{k-1}^+$	3.32
$\boldsymbol{P}_k^- = \boldsymbol{F}\boldsymbol{P}_{K-1}^+\boldsymbol{F}^T + \boldsymbol{Q}$	3.38
(Measurement update)	
$\hat{\boldsymbol{x}}_k^+ = \boldsymbol{K}_k(\boldsymbol{y}_k - \boldsymbol{H}_k\hat{\boldsymbol{x}}_k^-)$	3.7
$\boldsymbol{K}_k = \boldsymbol{P}_k^-\boldsymbol{H}_k^T(\boldsymbol{H}_k\boldsymbol{P}_k^-\boldsymbol{H}_k^T + \boldsymbol{R}_k)^{-1}$	3.24
$\boldsymbol{P}_k^+ = (\boldsymbol{I} - \boldsymbol{K}_k\boldsymbol{H}_k)\boldsymbol{P}_k^-(\boldsymbol{I} - \boldsymbol{K}_k\boldsymbol{H}_k)^T + \boldsymbol{K}_k\boldsymbol{R}\boldsymbol{K}_k^T$	3.21

3.2 Discrete-time extended Kalman filter (EKF)

The Kalman filter developed in the previous section only applies to linear systems, whereas in general the systems in many areas are seldom linear (e.g., the finite-deformation mechanical system of the heart). For this reason, the extended Kalman filter was developed

as an extension of Kalman filter to nonlinear systems (Welch and Bishop 1995). Although not used in our applications, the EKF serves as the theoretical foundation for the reduced-order filters (i.e., SEEK filter in sections 3.4, and the reduced-order UKF in section 3.5) which we will rely heavily on in chapter 4 for the application to parameter estimations in cardiac mechanical systems.

In this section, for the purpose of theoretical developments, we will consider the problem of estimating the parameter (conductivity) and state (the temperature distribution) in the heat equation, given noisy temperature measurements.

3.2.1 Joint state-parameter estimation formulation

System equation

The model problem is the one-dimensional heat equation in the spatial domain Ω with Dirichlet boundary condition, that is,

$$\dot{u}(x,t) = \theta(x) u_{xx}, \tag{3.39}$$

$$u(x,0) = 0, \quad x \in \Omega = [0,1], \tag{3.40}$$

$$u(0,t) = 0, \quad t \in [0,\, T], \tag{3.41}$$

$$u(1,t) = 1, \quad t \in [0,\, T], \tag{3.42}$$

where is $u(x,t)$ is the temperature at spatial location x and time t, and $\theta(x)$ the diffusivity parameter at x.

Discretised in space by finite element method and in time by (backward) finite difference method, the above model is written as

$$(\boldsymbol{M} + \Delta t \boldsymbol{K})\boldsymbol{u}_k = \boldsymbol{M}\boldsymbol{u}_{k-1} + \Delta t \boldsymbol{u}_\infty, \tag{3.43}$$

where Δt is the time interval, $\boldsymbol{M}$ the mass matrix, $\boldsymbol{K}$ the stiffness matrix, and $\boldsymbol{u}_k$ a vector of unknowns with steady values $\boldsymbol{u}_\infty$ (Hunter and Pullan 2001).

The above equation can be rewritten as the standard discrete system in the state-space form as

$$\boldsymbol{u}_k = \boldsymbol{F}^u_{k-1}(\boldsymbol{\theta}_{k-1})\boldsymbol{u}_{k-1} + \boldsymbol{q}_{k-1}(\boldsymbol{\theta}_{k-1}), \quad k = 1, ..., K+1, \tag{3.44}$$

with

$$\boldsymbol{F}^u_{k-1}(\boldsymbol{\theta}_{k-1}) = (\boldsymbol{M} + \Delta t\boldsymbol{K})^{-1}\boldsymbol{M}, \tag{3.45}$$

$$\boldsymbol{q}_{k-1}(\boldsymbol{\theta}_{k-1}) = \Delta t(\boldsymbol{M} + \Delta t\boldsymbol{K})^{-1}\boldsymbol{u}_\infty. \tag{3.46}$$

In the above equations, $\boldsymbol{u}_k \in \mathbb{R}^{n^u}$ is a state vector which represents temperature of discretised points at time k, $\boldsymbol{\theta} \in \mathbb{R}^{n^\theta}$ is a parameter vector which represents spatially-varying (constant over time) diffusivity in the problem domain , $\boldsymbol{q}_{k-1}$ is the system input, and $\boldsymbol{F}^u_{k-1} \in \mathbb{R}^{n^u \times n^u}$ is the system transition matrix which is dependent on the parameter vector $\boldsymbol{\theta}$.

The diffusivity parameter is constant over time, i.e.

$$\boldsymbol{\theta}_k = \boldsymbol{\theta}_{k-1}, \quad k = 1, ..., K+1. \tag{3.47}$$

Since we want to estimate the state $\boldsymbol{u}_k$ and parameter $\boldsymbol{\theta}$ together, we define the *augmented state variable* $\boldsymbol{x}_k \in \mathbb{R}^{n^x}(n^x = n^u + n^\theta)$ as

$$\boldsymbol{x}_k = \begin{pmatrix} \boldsymbol{u}_k \\ \boldsymbol{\theta} \end{pmatrix}. \tag{3.48}$$

With the above definition, equation 3.44 and 3.47 are written together as

$$\begin{pmatrix} \boldsymbol{u}_k \\ \boldsymbol{\theta} \end{pmatrix} = \begin{pmatrix} \boldsymbol{F}^u_{k-1}(\boldsymbol{\theta}_{k-1}) & \boldsymbol{O} \\ \boldsymbol{O} & \boldsymbol{I} \end{pmatrix} \begin{pmatrix} \boldsymbol{u}_{k-1} \\ \boldsymbol{\theta}_{k-1} \end{pmatrix} + \begin{pmatrix} \boldsymbol{q}_{k-1} \\ \boldsymbol{O} \end{pmatrix} + \boldsymbol{w}_{k-1}, \tag{3.49}$$

$$\boldsymbol{x}_k = f(\boldsymbol{x}_{k-1}, \boldsymbol{q}_{k-1}, \boldsymbol{w}_{k-1}), \tag{3.50}$$

where $f(.)$, the nonlinear (with respect to $\boldsymbol{\theta}$) *system transition operator*, is defined by the above equation. As with equation 3.26, the system noise $\boldsymbol{w}_{k-1} \in \mathbb{R}^{n^x+n^\theta}$ is introduced

from the uncertainty of the system knowledge (e.g. the uncertainty of the model parameters). Similar to equation 3.26 and 3.27 in previous section, we assume $\boldsymbol{w}_k$ is white and belongs to the Gaussian distribution. That is,

$$\boldsymbol{w}_k \sim \mathcal{N}(\boldsymbol{0}, \boldsymbol{Q}_k), \tag{3.51}$$

$$\mathbb{E}\left[\boldsymbol{w}_i \boldsymbol{w}_j^T\right] = \boldsymbol{O}, \quad i \neq j. \tag{3.52}$$

Remark 3.2.1. *(Nonlinearity of the system transition operator) System transition operator $f(\cdot)$ is generally nonlinear in the context of joint state-parameter estimation, that is, where the augmented state variable consists of both $\boldsymbol{u}_k$ and $\boldsymbol{\theta}_k$, because the gradient $\frac{\partial \boldsymbol{x}_k}{\partial \boldsymbol{x}_{k-1}}$ is dependent on the system parameter, i.e.,*

$$\frac{\partial \boldsymbol{x}_k}{\partial \boldsymbol{x}_{k-1}}\Big|_{\left(\boldsymbol{u}_{k-1}^+, \boldsymbol{\theta}_{k-1}^+;\, \boldsymbol{q}_{k-1}, \boldsymbol{w}_{k-1}\right)} = \begin{pmatrix} \frac{\partial \boldsymbol{u}_k}{\partial \boldsymbol{u}_{k-1}} & \frac{\partial \boldsymbol{u}_k}{\partial \boldsymbol{\theta}_{k-1}} \\ \frac{\partial \boldsymbol{\theta}_k}{\partial \boldsymbol{u}_{k-1}} & \frac{\partial \boldsymbol{\theta}_k}{\partial \boldsymbol{\theta}_{k-1}} \end{pmatrix}\Big|_{\left(\boldsymbol{u}_{k-1}^+, \boldsymbol{\theta}_{k-1}^+\right)} \tag{3.53}$$

$$= \begin{pmatrix} \boldsymbol{F}_{k-1}^u(\boldsymbol{\theta}_{k-1}^+) & \frac{\partial \boldsymbol{u}_k}{\partial \boldsymbol{\theta}_{k-1}}(\boldsymbol{u}_{k-1}^+, \boldsymbol{\theta}_{k-1}^+;\ \boldsymbol{q}_{k-1}(\boldsymbol{\theta}_{k-1}^+)) \\ \boldsymbol{O} & \boldsymbol{I} \end{pmatrix}. \tag{3.54}$$

In this case, the parameter $\boldsymbol{\theta}_{k-1}$ is part of the augmented state variable. Therefore the terms $\frac{\partial \boldsymbol{u}_k}{\partial \boldsymbol{\theta}_{k-1}}(\boldsymbol{u}_{k-1}^+, \boldsymbol{\theta}_{k-1}^+;\ \boldsymbol{q}_{k-1}(\boldsymbol{\theta}_{k-1}^+))$ and $\boldsymbol{F}_{k-1}^u(\boldsymbol{\theta}_{k-1}^+)$ (equation 3.54), the dependence of the state $\boldsymbol{u}_k$ on the previous state $\boldsymbol{u}_{k-1}$ and parameter $\boldsymbol{\theta}_{k-1}$, become nonlinear terms. In cardiac mechanics, the deformation (equivalent state variable $\boldsymbol{u}_k$) is highly nonlinear with respect to the constitutive parameters (equivalent parameter variable $\boldsymbol{\theta}_{k-1}$). In general these nonlinearities would render extended Kalman filter to have a poor performance.

Measurement equation

For the observations $\{\boldsymbol{y}_k \in \mathbb{R}^m, k = 1, ..., K\}$, the general form is that

$$\boldsymbol{y}_k = h[\boldsymbol{x}_k] + \boldsymbol{v}_k, \tag{3.55}$$

where h is the general *observation operator* [2], and $\boldsymbol{v}_k \in \mathbb{R}^m$ is the measurement noise with the same assumption as 3.5 in previous section, that is,

$$\boldsymbol{v}_k \sim \mathcal{N}(\boldsymbol{0}, \boldsymbol{R}_k), \tag{3.56}$$

$$\mathbb{E}\left[\boldsymbol{v}_i \boldsymbol{v}_j^T\right] = \boldsymbol{O}, \quad i \neq j. \tag{3.57}$$

Further assume that we can measure the temperature at all discretised points, that is,

$$\boldsymbol{y}_k = (\boldsymbol{I} \quad \boldsymbol{O}) \begin{pmatrix} \boldsymbol{u}_k \\ \boldsymbol{\theta}_k \end{pmatrix} + \boldsymbol{v}_k \tag{3.58}$$

$$= \boldsymbol{H}\, \boldsymbol{x}_k + \boldsymbol{v}_k, \tag{3.59}$$

where $\boldsymbol{H}$ is the linear observational operator defined in the above equation (also recall equation 3.1 in the section of Kalman filter), $\boldsymbol{I} \in \mathbb{R}^{m \times n^u}$ the identity matrix and $\boldsymbol{O} \in \mathbb{R}^{m \times n^\theta}$ the zero matrix.

3.2.2 Derivation of EKF from KF

At this point, to apply the Kalman filter developed in the previous section *directly* on the system 3.50 and 3.59, we need to linearise the nonlinear *system transition operator* f in order to obtain the *system transition matrix* F , as that in equation 3.54. In fact, that's the motivation of EKF.

Following equation 3.54, the system transition matrix $\boldsymbol{F}_{k-1}$ at time $k-1$ is given by

$$\boldsymbol{F}_{k-1} = \frac{\partial \boldsymbol{x}_k}{\partial \boldsymbol{x}_{k-1}}\Big|_{\left(\boldsymbol{u}_{k-1}^+, \boldsymbol{\theta}_{k-1}^+;\, \boldsymbol{q}_{k-1}, \boldsymbol{w}_{k-1}\right)} \tag{3.60}$$

$$= \begin{pmatrix} \boldsymbol{F}_{k-1}^u(\boldsymbol{\theta}_{k-1}^+) & \frac{\partial \boldsymbol{u}_k}{\partial \boldsymbol{\theta}_{k-1}}(\boldsymbol{u}_{k-1}^+, \boldsymbol{\theta}_{k-1}^+;\ \boldsymbol{q}_{k-1}(\boldsymbol{\theta}_{k-1}^+)) \\ \boldsymbol{O} & \boldsymbol{I} \end{pmatrix}. \tag{3.61}$$

After this linearisation in the above equation, we reach the standard formulation of Kalman filter, which is summarised in table 3.2. However in practical implementation,

[2] We use the lowercase letter for nonlinear operator (e.g., h for the nonlinear observational operator), and its uppercase letter for the linear operator (e.g., $\boldsymbol{H}$ for the linear observational matrix).

we can calculate this linearisation term numerically by finite difference at each time point, at the cost of additional model evaluations.

Table 3.2: Discrete-time extend Kalman filter summary

Filter components	referenced equations
(System equations)	
$\boldsymbol{x}_k = f(\boldsymbol{x}_{k-1}, \boldsymbol{w}_{k-1})$	3.50
$\boldsymbol{w}_k \sim \mathcal{N}(\boldsymbol{0}, \boldsymbol{Q}_k)$	3.51
$\mathbb{E}\left[\boldsymbol{w}_i \boldsymbol{w}_j^T\right] = \boldsymbol{O}, \quad i \neq j$	3.52
$\boldsymbol{F}_{k-1} = \begin{pmatrix} \boldsymbol{F}^u_{k-1}(\boldsymbol{\theta}^+_{k-1}) & \frac{\partial \boldsymbol{u}_k}{\partial \boldsymbol{\theta}_{k-1}}(\boldsymbol{u}^+_{k-1}, \boldsymbol{\theta}^+_{k-1};\ \boldsymbol{q}_{k-1}(\boldsymbol{\theta}^+_{k-1})) \\ \boldsymbol{O} & \boldsymbol{I} \end{pmatrix}$	3.61
(Measurement equations)	
$\boldsymbol{y}_k = \boldsymbol{H}\boldsymbol{x}_k + \boldsymbol{v}_k, \boldsymbol{H} = (\boldsymbol{I} \quad \boldsymbol{O})$	3.59
$\boldsymbol{v}_k \sim \mathcal{N}(\boldsymbol{0}, \boldsymbol{R}_k)$	3.56
$\mathbb{E}\left[\boldsymbol{v}_i \boldsymbol{v}_j^T\right] = \boldsymbol{O}, \quad i \neq j$	3.57
Initialize $\hat{\boldsymbol{x}}^+_0$ and $\boldsymbol{P}^+_0$	
(Time update)	
same as Kalman filter	table 3.1
$\boldsymbol{F}_{k-1}$ is linearized in equation 3.61	$\boldsymbol{F}_{k-1}$ corresponds to F in 3.26
(Measurement update)	
same as Kalman filter	table 3.1

3.3 Discrete-time unscented Kalman filter (UKF)

The EKF derived in previous section is theoretically straightforward as an extension to KF in section 3.1 and particularly useful when the gradient of the system transition operator ($\frac{\partial f}{\partial \boldsymbol{x}}$) is well available (e.g., in equation 3.61). However for applications in cardiac mechanics, we are interested in the constitutive parameters that control the system behaviour in a highly nonlinear manner, e.g., the exponential anisotropic constitutive law in section 1.2.3. For such systems, extended Kalman filter is not a good choice, since, as mentioned before, severe nonlinearity would render EKF to have a poor performance.

Recall that the EKF propagates the mean and covariance of the state based on linearisation. By contrast, Julier et al. (1995) proposed the unscented Kalman filter (UKF) as an extension to EKF, using the observation that it is easier to approximate a Gaussian prob-

ability distribution than to approximate an arbitrary nonlinear function via linearisation (demonstrated in section 3.3.1). UKF generalises elegantly to nonlinear systems without linearisation [3], based on the principle that a set of carefully selected sampling points (or *sigma points*) can be used to parameterise mean and covariance. It is shown by Julier and Uhlmann (1997) that the performance of UKF is superior to EKF. In this section, we will derive the UKF based on EKF and apply it to our previous joint state-parameter estimation problem for the heat equation.

3.3.1 The propagation of probability distribution function through a transformation

In all Kalman filters, the estimation of the state variable is not (just) a value $\hat{\boldsymbol{x}}$, but a probability density function (PDF) $f^p(\boldsymbol{x}) = Pr(X = \boldsymbol{x}), \boldsymbol{x} \in \mathbb{R}^{n_x}$ (typically assumed to be of Gaussian distribution $\mathcal{N}(\hat{\boldsymbol{x}}, P^x)$, see Remark 3.3.1). Maintaining the accuracy of this probability density function as the state evolves (i.e., goes through the system transition operator $f(\cdot)$) is crucial for Kalman filters to perform well. Therefore we need to have a thorough understanding of how a PDF changes when going through a (nonlinear) transformation.

Remark 3.3.1. *(Error assumption based on Gaussian distribution) By the central limit theorem, the sum of a number of independent random variables with finite means and variances approaches a normal distribution as the number of variables increases. For this reason, the normal distribution is commonly encountered in practice, and is used as a simple model for complex phenomena where each influencing variable is assumed random and independent. Therefore the observational error in an experiment is usually assumed to follow a normal distribution.*

[3] Interesting to note that in [Lefebvre et al. 2002], it is pointed out that UKF can actually be derived from the so called statistic linear regression, which *linearise* the system transition operator and observation operator through some sampling points.

Suppose, as an example of nonlinear transformation, $f^1[\cdot]$ is the Polar coordinate to Cartesian coordinate transformation:

$$f^1: \quad \boldsymbol{x} = \begin{pmatrix} x_1 \\ x_2 \end{pmatrix} \longrightarrow \begin{pmatrix} x_1 \cos(x_2) \\ x_1 \sin(x_2) \end{pmatrix}, \boldsymbol{x} \in \mathbb{R}^2, \tag{3.62}$$

and the PDF of x is :

$$\boldsymbol{x} \sim \mathcal{N}\left(\begin{pmatrix} 100 \\ 90 \end{pmatrix}, \begin{pmatrix} 2 & 0 \\ 0 & 15 \end{pmatrix} \right). \tag{3.63}$$

The gradient of $f^1[\cdot]$ is given by

$$\frac{df}{dx} = \frac{\pi}{180} \begin{pmatrix} \cos(x_2) & -x_1 \sin(x_2) \\ \sin(x_2) & x_1 \cos(x_2) \end{pmatrix}, \tag{3.64}$$

and its value at the mean point is

$$\frac{df}{dx}\Big|_{\begin{pmatrix} 100 \\ 90 \end{pmatrix}} = \frac{\pi}{180} \begin{pmatrix} 0 & -100 \\ 1 & 0 \end{pmatrix}. \tag{3.65}$$

As a comparison, table 3.3 lists the estimation of the transformed PDF, by f^1 from its initial distribution (equation 3.63), using methods of EKF (i.e., linearisation based on equation 3.65), UKF (i.e., unscented transformation with 4 sigma points. See next section) and Monte Carlo simulation with 3.5×10^6 samples (as the ground-truth).

For the mean, the linearisation method gives an estimation error of 3.5122% , while the unscented transformation has only 0.50410% error. This indicates that EKF is significantly more biased (i.e., it introduces an error of about one standard derivation) for the mean estimation than UKF. And since this bias comes from the linearisation itself, the same error with the same sign will be introduced at each time update (equation 3.32), and influence the subsequent measurement update (equation 3.7).

For the covariance, the linearisation method gives an estimation error of 4.1389% , while the unscented transformation has only 0.5334% error. Specifically, the EKF has significantly underestimated the error of x_2, which indicates that EKF will pay less attention to

the measurement of x_2 (equation 3.24 and 3.7) and the estimation of x_2 may diverge from the true value. Therefore in practice the EKF needs a stabilising noise term to increase the transformed error covariance (Julier and Uhlmann 1997). This is probably why the EKF is not as robust as UKF and difficult to tune.

Table 3.3: Comparison of statistical estimation of PDF transformed by $f^1[\cdot]$ using different methods (see text for detailed explanation).

	mean	error of mean	covariance	error of covariance
linearization (EKF)	$\begin{pmatrix} 0.0000e+0 \\ 1.0000e+2 \end{pmatrix}$	3.5121%	$\begin{pmatrix} 6.8539e+2 & 0.0000e+0 \\ 0.0000e+0 & 4.0000e+0 \end{pmatrix}$	4.1389%
unscented transformation (UKF)	$\begin{pmatrix} 0.0000e+0 \\ 9.6120e+1 \end{pmatrix}$	0.50411%	$\begin{pmatrix} 6.5464e+2 & 0.0000e+0 \\ 0.0000e+0 & 1.5478e+1 \end{pmatrix}$	0.5334%
Monte Carlo simulation	$\begin{pmatrix} 1.5115e-3 \\ 9.6607e+1 \end{pmatrix}$	truth	$\begin{pmatrix} 6.5815e+2 & 5.5665e-2 \\ 5.5665e-2 & 1.2866e+1 \end{pmatrix}$	truth

3.3.2 Unscented transformation

The essential part of UKF is the *unscented transformation*, which is a technique to calculate the statistics of a random variable that undergoes a nonlinear transformation (Julier and Uhlmann 1997). More specifically, suppose vector $\boldsymbol{x} \in \mathbb{R}^{n_x}$ is a random variable with mean $\bar{\boldsymbol{x}}$ and covariance $\boldsymbol{P}$, that is,

$$\boldsymbol{x} \sim \mathcal{N}(\bar{\boldsymbol{x}}, \boldsymbol{P}). \tag{3.66}$$

We want to find a set of *deterministic* vectors, called *sigma points*, whose ensemble mean and covariance are equal to $\bar{\boldsymbol{x}}$ and $\boldsymbol{P}$. We then apply the nonlinear transformation $\boldsymbol{y} = h(\boldsymbol{x})$ to each of these sigma points to obtain transformed vectors. The purpose is that the ensemble mean and covariance of these transformed vectors will give a good estimate of the true mean and covariance of y.

One of the commonly employed schemes is the symmetric set of $2n_x$ sigma points where n_x is the size of state variable $\boldsymbol{x}$. This scheme is also named as *canonical unscented*

transformation (Moireau and Chapelle 2011). These $2n_x$ sigma points can be determined from the square root of covariance matrix $\boldsymbol{P}$ as follows:

$$\boldsymbol{x}^{(i)} = \bar{\boldsymbol{x}} + \tilde{\boldsymbol{x}}^{(i)}, \quad i = 1..2n_x, \tag{3.67}$$

where

$$\tilde{\boldsymbol{x}}^{(i)} = (\sqrt{n\boldsymbol{P}}^T)_{(:,i)}, \quad i = 1..n_x, \tag{3.68}$$

$$\tilde{\boldsymbol{x}}^{(i)} = -(\sqrt{n\boldsymbol{P}}^T)_{(:,i)}, \quad i = n_x + 1..2n_x, \tag{3.69}$$

and

$$w_i = \frac{1}{2n_x}, \tag{3.70}$$

In the above equations, $(\sqrt{n_x\boldsymbol{P}}^T)_{(:,i)}$ [4] denotes the ith column of $\sqrt{n_x\boldsymbol{P}}^T$, and w_i is the weight for each sigma points (here we choose equal weight since the sigma points are in a symmetric position geometrically).

The canonical unscented transformation presented here is not the only one that exits. There are other possibilities with $n_x + 1$ or $2n_x + 1$ sigma points (Simon 2006, p. 452; Julier et al. 2003), which can be used when we have particular knowledge of the statics of noise, or if we are interested in computational saving.

3.3.3 From EKF to UKF

The UKF is derived from EKF essentially by replacing the propagation of mean and covariance in EKF with the unscented transformation described above.

[4] $\boldsymbol{M}$(:,i) denote the sub-matrix or sub-vector consisting of all the rows and i-th column(s) of $\boldsymbol{M}$. For example, $\boldsymbol{M}$(1:2, 3:5) is the 2 by 3 sub-matrix consisting of 1st and 2nd rows and 3rd to 5th columns of $\boldsymbol{M}$.

Time update

To propagate the estimation of the state and its error-covariance from the previous time $(k-1)^+$ [5] to current time k^-, instead of linearisation as in EKF or KF (equation 3.32 and 3.38), we sample at sigma points $\hat{\boldsymbol{x}}_{k-1}^{+(i)}$ by

$$\hat{\boldsymbol{x}}_k^{-(i)} = f(\hat{\boldsymbol{x}}_{k-1}^{+(i)}, \mathbf{0}), \tag{3.71}$$

where $f(.)$ is the system transition operator (equation 3.50).

From the *ensemble matrix* $\left[\hat{\boldsymbol{x}}_k^{-(i)}\right]$ $(i = 1..2n_x)$ [6], we can obtain the *prior* estimation of state and error-covariance by

$$\hat{\boldsymbol{x}}_k^- = \left[\hat{\boldsymbol{x}}_k^{-(i)}\right] \begin{pmatrix} w_1 \\ w_2 \\ \vdots \\ w_{2n_x} \end{pmatrix}, \tag{3.72}$$

and

$$\boldsymbol{P}_k^- = \left[\hat{\boldsymbol{x}}_k^{-(i)} - \hat{\boldsymbol{x}}_k^-\right] \begin{pmatrix} w_1 & & \\ & \ddots & \\ & & w_{2n_x} \end{pmatrix} \left[\hat{\boldsymbol{x}}_k^{-(i)} - \hat{\boldsymbol{x}}_k^-\right]^T + \boldsymbol{Q}_k, \tag{3.73}$$

where the additive term $\boldsymbol{Q}_k$ (the covariance matrix of system noise) is introduced by the system noise $\boldsymbol{w}_k$ in equation 3.51.

Measurement update

Based on the fact that the measurement operator $h(.)$ is in the same position in the measurement update as the system transition operator $f(.)$ in the time update, we derive equations similar to equations 3.71 to 3.73, for measurement update from the ensemble matrix

[5] '$+$' denotes the moment just after measurement assimilation, or *posterior*. '$-$' denotes the moment just before measurement assimilation, or *prior*.

[6] $\left[\hat{\boldsymbol{x}}_k^{-(i)}\right] \in \mathbb{M}^{n_x \times 2n_x}$ is constructed by piling up $\hat{\boldsymbol{x}}_k^{-(i)} \in \mathbb{R}^{n_x} (i = 1..2n_x)$ column-wise, that is, $\left[\hat{\boldsymbol{x}}_k^{-(i)}\right]_{(:,i)} = \hat{\boldsymbol{x}}_k^{-(i)}$. From now on, we will $[\boldsymbol{v}_i]$ in this way where $\boldsymbol{v}_i$ is a vector.

$\left[\hat{\boldsymbol{y}}_k^{(i)}\right]$:

$$\hat{\boldsymbol{y}}_k^{(i)} = h(\hat{\boldsymbol{x}}_k^{-(i)}), \tag{3.74}$$

$$\hat{\boldsymbol{y}}_k = \left[\hat{\boldsymbol{y}}_k^{(i)}\right] \begin{pmatrix} w_1 \\ w_2 \\ \vdots \\ w_{2n_x} \end{pmatrix}, \tag{3.75}$$

$$\boldsymbol{P}_k^y = \left[\hat{\boldsymbol{y}}_k^{(i)} - \hat{\boldsymbol{y}}_k\right] \begin{pmatrix} w_1 & & \\ & \ddots & \\ & & w_{2n_x} \end{pmatrix} \left[\hat{\boldsymbol{y}}_k^{(i)} - \hat{\boldsymbol{y}}_k\right]^T + \boldsymbol{R}_k, \tag{3.76}$$

where $\hat{\boldsymbol{y}}_k$ is the measurement estimation and $\boldsymbol{P}_k^y$ is the error covariance matrix of measurement estimation.

In addition, we will also compute the state-measurement cross covariance

$$\boldsymbol{P}_k^{xy} = \left[\hat{\boldsymbol{x}}_k^{(i)} - \hat{\boldsymbol{x}}_k^-\right] \begin{pmatrix} w_1 & & \\ & \ddots & \\ & & w_{2n_x} \end{pmatrix} \left[\hat{\boldsymbol{y}}_k^{(i)} - \hat{\boldsymbol{y}}_k\right]^T. \tag{3.77}$$

The reason for computing $\boldsymbol{P}_k^{xy}$ is that it is an equivalent term for $\boldsymbol{P}_k^- \boldsymbol{H}^T$ (equation 3.24) in the case of linear measurement operator $\boldsymbol{H}$, that is,

$$\boldsymbol{P}_k^{xy} \cong \boldsymbol{P}_k^- \boldsymbol{H}^T, \tag{3.78}$$

which is noticed by the fact that

$$\boldsymbol{P}_k^{xy} = \left[\hat{\boldsymbol{x}}_k^{(i)} - \hat{\boldsymbol{x}}_k^-\right] \begin{pmatrix} w_1 & & \\ & \ddots & \\ & & w_{2n_x} \end{pmatrix} \left[\hat{\boldsymbol{y}}_k^{(i)} - \hat{\boldsymbol{y}}_k\right]^T \tag{3.79}$$

$$= \left[\hat{\boldsymbol{x}}_k^{(i)} - \hat{\boldsymbol{x}}_k^-\right] \begin{pmatrix} w_1 & & \\ & \ddots & \\ & & w_{2n_x} \end{pmatrix} (\boldsymbol{H}\left[\hat{\boldsymbol{x}}_k^{(i)} - \hat{\boldsymbol{x}}_k^-\right])^T \tag{3.80}$$

$$= \boldsymbol{P}_k^- \boldsymbol{H}^T. \tag{3.81}$$

Similar derivation indicates that $\boldsymbol{P}_k^y$ is the equivalent term for $\boldsymbol{H}_k \boldsymbol{P}_k^- \boldsymbol{H}_k^T + \boldsymbol{R}_k$ in equation 3.24 of EKF

$$\boldsymbol{P}_k^y \cong \boldsymbol{H}_k \boldsymbol{P}_k^- \boldsymbol{H}_k^T + \boldsymbol{R}_k, \tag{3.82}$$

Based on the relationships of equation 3.78 and 3.82, the gain matrix $\boldsymbol{K}_k$ in equation 3.24 can be adapted to UKF by

$$\boldsymbol{K}_k = (\boldsymbol{P}_k^- \boldsymbol{H}_k^T)(\boldsymbol{H}_k \boldsymbol{P}_k^- \boldsymbol{H}_k^T + \boldsymbol{R}_k)^{-1} \tag{3.83}$$

$$= \boldsymbol{P}_k^{xy} (\boldsymbol{P}_k^y)^{-1}. \tag{3.84}$$

From the gain matrix, we have the state update equation (eq. 3.7) for UKF:

$$\hat{\boldsymbol{x}}_k^+ = \hat{\boldsymbol{x}}_k^- + \boldsymbol{K}_k(\boldsymbol{y}_k - \hat{\boldsymbol{y}}_k). \tag{3.85}$$

The covariance update equation for UKF is derived, by basic linear algebra, based on equation 3.21:

$$\boldsymbol{P}_k^+ = (\boldsymbol{I} - \boldsymbol{K}_k \boldsymbol{H}_k)\boldsymbol{P}_k^- (\boldsymbol{I} - \boldsymbol{K}_k \boldsymbol{H}_k)^T + \boldsymbol{K}_k \boldsymbol{R} \boldsymbol{K}_k^T \tag{3.86}$$

$$= \boldsymbol{P}_k^- (\boldsymbol{I} - \boldsymbol{H}_k^T \boldsymbol{K}_k^T) - \boldsymbol{K}_k \boldsymbol{H}_k \boldsymbol{P}_k^- (\boldsymbol{I} - \boldsymbol{H}_k^T \boldsymbol{K}_k^T) + \boldsymbol{K}_k \boldsymbol{R} \boldsymbol{K}_k^T \tag{3.87}$$

$$= \boldsymbol{P}_k^- - \boldsymbol{P}_k^- \boldsymbol{H}_k^T \boldsymbol{K}_k^T - \boldsymbol{K}_k \boldsymbol{H}_k \boldsymbol{P}_k^- + \boldsymbol{K}_k \boldsymbol{H}_k \boldsymbol{P}_k^- \boldsymbol{H}_k^T \boldsymbol{K}_k^T + \boldsymbol{K}_k \boldsymbol{R} \boldsymbol{K}_k^T \tag{3.88}$$

$$= \boldsymbol{P}_k^- - \boldsymbol{P}_k^- \boldsymbol{H}_k^T \boldsymbol{K}_k^T - \boldsymbol{K}_k \boldsymbol{H}_k \boldsymbol{P}_k^- + \boldsymbol{K}_k (\boldsymbol{H}_k \boldsymbol{P}_k^- \boldsymbol{H}_k^T + \boldsymbol{R}) \boldsymbol{K}_k^T \tag{3.89}$$

$$= \boldsymbol{P}_k^- - \boldsymbol{P}_k^- \boldsymbol{H}_k^T \boldsymbol{K}_k^T - \boldsymbol{K}_k \boldsymbol{H}_k \boldsymbol{P}_k^- + \boldsymbol{P}_k^- \boldsymbol{H}_k^T \boldsymbol{K}_k^T \tag{3.90}$$

$$= \boldsymbol{P}_k^- - \boldsymbol{K}_k \boldsymbol{H}_k \boldsymbol{P}_k^- \tag{3.91}$$

$$= \boldsymbol{P}_k^- - \boldsymbol{K}_k (\boldsymbol{P}_k^{xy})^T \tag{3.92}$$

$$= \boldsymbol{P}_k^- - \boldsymbol{P}_k^{xy} (\boldsymbol{P}_k^y)^{-1} (\boldsymbol{P}_k^{xy})^T \tag{3.93}$$

where in the last two steps, equations (3.82) and (3.84) are used.

As a summary, table 3.4 lists all the components of UKF filter developed in this section.

3.4 Singular Evolutive Extended Kalman filter (SEEK) as a reduced-order EKF

EKF (section 3.2) requires the operation (e.g. matrix inverse in equation 3.24) on a matrix of size $n_m \times n_m$ ($m \sim O(n_x)$ is the size of measurement vector $\boldsymbol{y}$ defined in section

Table 3.4: Discrete-time UKF summary

Filter components	referenced equations
(System equations) Same as EKF	table 3.2
(Measurement equations) $\boldsymbol{y}_k = h(\boldsymbol{x}_k, \boldsymbol{v}_k)$ $v \sim \mathcal{N}(\boldsymbol{0}, R)$ $\mathbb{E}\left[\boldsymbol{v}_i \boldsymbol{v}_i\right] = R$ $\mathbb{E}\left[\boldsymbol{v}_i \boldsymbol{v}_j\right] = \boldsymbol{O}, \quad i \neq j$	 3.55 3.4 3.5 3.5
Initialize $\hat{\boldsymbol{x}}_0^+$ and $\boldsymbol{P}_0^+$	
(Time update) $\hat{\boldsymbol{x}}_k^- = \left[\hat{\boldsymbol{x}}_k^{-(i)}\right] \begin{pmatrix} w_1 \\ w_2 \\ \vdots \\ w_{2n_x} \end{pmatrix}$ $\boldsymbol{P}_k^- = \left[\hat{\boldsymbol{x}}_k^{-(i)} - \hat{\boldsymbol{x}}_k^-\right] \begin{pmatrix} w_1 & & \\ & \ddots & \\ & & w_{2n_x} \end{pmatrix} \left[\hat{\boldsymbol{x}}_k^{-(i)} - \hat{\boldsymbol{x}}_k^-\right]^T + \boldsymbol{Q}_k$	 3.72 3.73
(Measurement update) $\hat{\boldsymbol{y}}_k = \left[\hat{\boldsymbol{y}}_k^{(i)}\right] \begin{pmatrix} w_1 \\ w_2 \\ \vdots \\ w_{2n_x} \end{pmatrix}$ $\boldsymbol{P}_k^y = \left[\hat{\boldsymbol{y}}_k^{(i)} - \hat{\boldsymbol{y}}_k\right] \begin{pmatrix} w_1 & & \\ & \ddots & \\ & & w_{2n_x} \end{pmatrix} \left[\hat{\boldsymbol{y}}_k^{(i)} - \hat{\boldsymbol{y}}_k\right]^T + \boldsymbol{R}_k$ $\boldsymbol{P}_k^{xy} = \left[\hat{\boldsymbol{x}}_k^{(i)} - \hat{\boldsymbol{x}}_k^-\right] \begin{pmatrix} w_1 & & \\ & \ddots & \\ & & w_{2n_x} \end{pmatrix} \left[\hat{\boldsymbol{y}}_k^{(i)} - \hat{\boldsymbol{y}}_k\right]^T$ $\hat{\boldsymbol{x}}_k^+ = \hat{\boldsymbol{x}}_k^- + \boldsymbol{K}_k(\boldsymbol{y}_k - \hat{\boldsymbol{y}}_k)$ $\boldsymbol{K}_k = \boldsymbol{P}_k^{xy}(\boldsymbol{P}_k^y)^{-1}$ $\boldsymbol{P}_k^+ = \boldsymbol{P}_k^- - \boldsymbol{P}_k^{xy}(\boldsymbol{P}_k^y)^{-1}(\boldsymbol{P}_k^{xy})^T$	 3.75 3.76 3.77 3.85 3.84 3.93

3.1.1), and storage of the matrix of size $n_x \times n_x$. When the size (n_x) of state variable ($\boldsymbol{x}$ in equation 3.48) becomes large – e.g., in the context of finite element (FE) models with a fine spatial discretisation – this heavy computational burden prohibits EKF's application to large systems. Moreover, apart from the unaffordable matrix operation and storage cost in EKF, UKF (in section 3.3) also requires a significant amount of sigma points to propagate the mean and covariance (i.e., $2n_x$ sigma points according to equation

3.67), which is practically impossible for the models whose single-time-step simulation is expensive.

This problem introduces the need to seek a computational affordable extension to EKF and UKF. The idea is to reduce the rank of error covariance matrix $\boldsymbol{P}$ from full-rank n_x to r ($r \ll n_x$, $r \ll m$) so that the most expensive matrix operation can be performed in a subspace $\mathbb{M}^{r\times r}$ instead of $\mathbb{M}^{m\times m}$ (see remark 3.4.1 later in this section), and the number of sigma points can be reduced from $2n_x$ to $2r$.

3.4.1 Low-rank approximation of covariance matrix

Based on the EKF derived in section 3.2, Singular Evolutive Extended Kalman filter (SEEK) (Pham 1995; Pham et al. 1998b; Brasseur and Verron 2006) was designed for dynamical systems of very large dimension in the context of data assimilation in oceanography. SEEK applies SVD (singular value decomposition) to error-covariance matrix $\boldsymbol{P} \in \mathbb{M}^{n_x\times n_x}$ ($\boldsymbol{P}$ is symmetric),

$$\mathcal{SVD}(\boldsymbol{P}) \rightarrow \boldsymbol{U}\boldsymbol{\Lambda}\boldsymbol{U}^T, \tag{3.94}$$

where $\boldsymbol{U} \in \mathbb{M}^{n_x\times n_x}$ is an orthonormal matrix ($\boldsymbol{U}\boldsymbol{U}^T = I$), and $\boldsymbol{\Lambda} \in \mathbb{M}^{n_x\times n_x}$ is a diagonal matrix. The full-rank matrix $\boldsymbol{P}$ can be approximated by $\tilde{\boldsymbol{P}}$ as

$$\tilde{\boldsymbol{P}} = \sum_{j=1}^{r} \sigma_j \boldsymbol{u}_j \otimes \boldsymbol{u}_j, \tag{3.95}$$

where

$$\sigma_j = \Lambda_{jj}, \sigma_1 \geq \sigma_2 \geq ... \geq \sigma_{n_x} \geq 0, \tag{3.96}$$

and

$$\boldsymbol{u}_j = \boldsymbol{U}(:, j). \tag{3.97}$$

Furthermore, $\tilde{\boldsymbol{P}}$ is the best approximation of $\boldsymbol{P}$ in the subspace $\mathbb{M}^{r\times r}$, with an approximation error σ_{r+1} under $\mathbb{L}^2$ norm (Trefethen 2009). That is,

$$\left\|\boldsymbol{P}-\tilde{\boldsymbol{P}}\right\|_{\mathbb{L}^2}=\sigma_{r+1}\leq\|\boldsymbol{P}-\boldsymbol{P}'\|_{\mathbb{L}^2}\,,\quad \text{for all } \boldsymbol{P}'\in\mathbb{M}^{r\times r}. \tag{3.98}$$

3.4.2 Derivation of SEEK filter from EKF

Time update

With the low-rank approximation available (equation 3.95), we derive the time update equations for the SEEK filter from EKF. Recall that the goal is to convert matrix operations from $\mathbb{M}^{n_x\times n_x}$ to $\mathbb{M}^{r\times r}$.

Equation 3.95 can be rewritten using definition [7]

$$\boldsymbol{S}=\left[\sqrt{\sigma_j}\boldsymbol{u}_j\right],j=1..r, \tag{3.99}$$

as

$$\tilde{\boldsymbol{P}}=\boldsymbol{S}\boldsymbol{S}^T. \tag{3.100}$$

Recall the time update equation 3.38 of EKF (or KF)

$$\boldsymbol{P}_k^-=\boldsymbol{F}_{k-1}\boldsymbol{P}_{k-1}^+\boldsymbol{F}_{k-1}^T+\boldsymbol{Q}_d.$$

Substituting from equation 3.100 for covariance $\boldsymbol{P}_k^-$ in the above equation gives

$$\begin{aligned}\boldsymbol{P}_k^- &= \boldsymbol{F}_{k-1}\boldsymbol{S}_{k-1}^+(\boldsymbol{S}_{k-1}^+)^T\boldsymbol{F}_{k-1}^T+\boldsymbol{Q}_d &(3.101)\\ &= \tilde{\boldsymbol{S}}_k^-(\tilde{\boldsymbol{S}}_k^-)^T+\boldsymbol{Q}_d &(3.102)\\ &= \frac{1}{\rho}(\tilde{\boldsymbol{S}}_k^-(\tilde{\boldsymbol{S}}_k^-)^T) &(3.103)\\ &= \boldsymbol{S}_k^-(\boldsymbol{S}_k^-)^T, &(3.104)\end{aligned}$$

[7] Recall notation $\left[\sqrt{\sigma_j}\boldsymbol{u}_j\right]\in\mathbb{M}^{n_x\times r}$ is constructed by piling up $\sqrt{\sigma_j}\boldsymbol{u}_j\in\mathbb{R}^{n_x}(j=1..r)$ column-wise. See footnote in section 3.3.3.

where we define

$$\tilde{\boldsymbol{S}}_k^- = \boldsymbol{F}_{k-1}\boldsymbol{S}_{k-1}^+, \tag{3.105}$$

$$\boldsymbol{S}_k^- = \frac{1}{\sqrt{\rho}}\tilde{\boldsymbol{S}}_k^-, \tag{3.106}$$

and assume the system noise

$$\boldsymbol{Q}_d = (\frac{1}{\rho} - 1)(\tilde{\boldsymbol{S}}_k^-(\tilde{\boldsymbol{S}}_k^-)^T). \tag{3.107}$$

Here $\rho \in (0, 1]$ is the so-called "forgetting factor" (Brasseur and Verron 2006) to increase the estimation error covariance. Since we want to keep the rank of error covariance $\boldsymbol{P}$ to be r during the time update, the additive system noise term Q should also be of rank r, therefore we define $\boldsymbol{Q}_d$ in equation 3.107 with the help of ρ and $\tilde{\boldsymbol{S}}_k^-$. Another alternative is to project $\boldsymbol{Q}_d$ into the $\mathbb{M}^{r\times r}$ in the way of equation 3.95 if rank of $\boldsymbol{Q}_d$ is larger than r; however this is computationally expensive since the projection needs to be performed at each time update.

Measurement update

Next we derive the measurement update equations.

First, it is necessary to introduce the famous matrix inverse lemma (e.g., see Simon 2006)

$$(\boldsymbol{A} + \boldsymbol{B}\boldsymbol{D}^{-1}\boldsymbol{C})^{-1} = \boldsymbol{A}^{-1} - \boldsymbol{A}^{-1}\boldsymbol{B}(\boldsymbol{D} + \boldsymbol{C}\boldsymbol{A}^{-1}\boldsymbol{B})^{-1}\boldsymbol{C}\boldsymbol{A}^{-1}, \tag{3.108}$$

where $\boldsymbol{A}$ and $\boldsymbol{D}$ are invertible square matrices, and matrices $\boldsymbol{B}$ and $\boldsymbol{C}$ matrices may not necessarily be square.

Recall the gain matrix (equation 3.24) for EKF (or KF)

$$\boldsymbol{K}_k = \boldsymbol{P}_k^-\boldsymbol{H}_k^T(\boldsymbol{H}_k\boldsymbol{P}_k^-\boldsymbol{H}_k^T + \boldsymbol{R}_d)^{-1}. \tag{3.109}$$

According to equation 3.100, the prior estimation-error covariance matrix $\boldsymbol{P}_k^-$ is replaced by its low-rank square root approximation, i.e.,

$$\boldsymbol{P}_k^- = \boldsymbol{S}_k^- (\boldsymbol{S}_k^-)^T. \tag{3.110}$$

Therefore equation 3.109 becomes

$$\boldsymbol{K}_k = \boldsymbol{S}_k^- (\boldsymbol{S}_k^-)^T \boldsymbol{H}_k^T (\bar{\boldsymbol{S}}_k^- (\bar{\boldsymbol{S}}_k^-)^T + \boldsymbol{R}_d)^{-1}, \tag{3.111}$$

where we define

$$\bar{\boldsymbol{S}}_k^- = \boldsymbol{H}_k \boldsymbol{S}_k^-. \tag{3.112}$$

Next we apply the matrix inverse lemma (eq. 3.108) to the equation 3.111:

$$\boldsymbol{K}_k = \boldsymbol{S}_k^- ((\bar{\boldsymbol{S}}_k^-)^T \boldsymbol{R}_d^{-1} - (\bar{\boldsymbol{S}}_k^-)^T \boldsymbol{R}_d^{-1} (\bar{\boldsymbol{S}}_k^-)(\boldsymbol{I} + (\bar{\boldsymbol{S}}_k^-)^T \boldsymbol{R}_d^{-1} (\bar{\boldsymbol{S}}_k^-))^{-1} (\bar{\boldsymbol{S}}_k^-)^T \boldsymbol{R}_d^{-1}) \tag{3.113}$$

$$= \boldsymbol{S}_k^- (I - (\bar{\boldsymbol{S}}_k^-)^T \boldsymbol{R}_d^{-1} (\bar{\boldsymbol{S}}_k^-)(\boldsymbol{I} + (\bar{\boldsymbol{S}}_k^-)^T \boldsymbol{R}_d^{-1} (\bar{\boldsymbol{S}}_k^-))^{-1}) (\bar{\boldsymbol{S}}_k^-)^T \boldsymbol{R}_d^{-1}. \tag{3.114}$$

By defining in the above equation

$$\boldsymbol{P}^r = \boldsymbol{I} + (\bar{\boldsymbol{S}}_k^-)^T \boldsymbol{R}_d^{-1} (\bar{\boldsymbol{S}}_k^-), \tag{3.115}$$

equation 3.114 can be simplified as

$$\boldsymbol{K}_k = \boldsymbol{S}_k^- (\boldsymbol{P}^r (\boldsymbol{P}^r)^{-1} - (\boldsymbol{P}^r - \boldsymbol{I})(\boldsymbol{P}^r)^{-1}) (\bar{\boldsymbol{S}}_k^-)^T \boldsymbol{R}_d^{-1} \tag{3.116}$$

$$= \boldsymbol{S}_k^- (\boldsymbol{P}^r)^{-1} (\bar{\boldsymbol{S}}_k^-)^T \boldsymbol{R}_d^{-1}. \tag{3.117}$$

Similar to the derivation in equations (3.109)–(3.117), we derive the covariance update

equation of SEEK filter from that equation (eq. 3.21) of EKF as follows:

$$\boldsymbol{P}_k^+ = (\boldsymbol{I} - \boldsymbol{K}_k\boldsymbol{H}_k)\boldsymbol{P}_k^- \tag{3.118}$$

$$= (\boldsymbol{I} - \boldsymbol{S}_k^-(\boldsymbol{P}^r)^{-1}(\bar{\boldsymbol{S}}_k^-)^T\boldsymbol{R}_d^{-1}\boldsymbol{H}_k)\boldsymbol{S}_k^-(\boldsymbol{S}_k^-)^T \tag{3.119}$$

$$= \boldsymbol{S}_k^-(\boldsymbol{I} - (\boldsymbol{P}^r)^{-1}(\bar{\boldsymbol{S}}_k^-)^T\boldsymbol{R}_d^{-1}\boldsymbol{H}_k\boldsymbol{S}_k^-)(\boldsymbol{S}_k^-)^T \tag{3.120}$$

$$= \boldsymbol{S}_k^-((\boldsymbol{P}^r)^{-1}\boldsymbol{P}^r - (\boldsymbol{P}^r)^{-1}(\boldsymbol{P}^r - \boldsymbol{I}))(\boldsymbol{S}_k^-)^T \tag{3.121}$$

$$= \boldsymbol{S}_k^-(\boldsymbol{P}^r)^{-1}(\boldsymbol{S}_k^-)^T \tag{3.122}$$

$$= \boldsymbol{S}_k^-(\boldsymbol{P}^r)^{-1/2}((\boldsymbol{P}^r)^{-1/2})^T(\boldsymbol{S}_k^-)^T \tag{3.123}$$

$$= \boldsymbol{S}_k^+(\boldsymbol{S}_k^+)^T, \tag{3.124}$$

where

$$\boldsymbol{S}_k^+ = \boldsymbol{S}_k^-(\boldsymbol{P}^r)^{-1/2}, \tag{3.125}$$

and equation 3.110, 3.115 and 3.117 are used.

Remark 3.4.1. *(The reduction of computational complexity in matrix operations) Note that the most expensive operations ($(\boldsymbol{P}^r)^{-1}$ and $(\boldsymbol{P}^r)^{-1/2}$) in measurement update equations (eq. 3.117 and 3.125) are now on matrix $\boldsymbol{P}^r \in \mathbb{M}^{r\times r}$, instead of in the space $\mathbb{M}^{m\times m}$ as that in EKF($(\boldsymbol{H}_k\boldsymbol{P}_k^-\boldsymbol{H}_k^T + \boldsymbol{R}_d)^{-1}$ in eq. 3.24) and UKF ($(\boldsymbol{P}_k^y)^{-1}$ in eq. 3.84) where m ($r \ll m$) is the size of measurement vector $\boldsymbol{y}$ defined in section 3.1.1.*

Although the measurement error covariance matrix $\boldsymbol{R}_d$ is still in $\mathbb{M}^{m\times m}$, the cost of the operation $\boldsymbol{R}_d^{-1}$ in equation 3.115 is negligible since $\boldsymbol{R}_d^{-1}$ is assumed to be diagonal (i.e., no correlation between individual measurements at different spatial location).

As a summary, table 3.5 lists all the components of SEEK filter developed in this section.

Table 3.5: Summary of discrete-time SEEK filter (reduced-order EKF)

Filter components	referenced equations
(System equations) Same as EKF	table 3.2
(Measurement equations) Same as EKF	table 3.2
Initialize $\hat{\boldsymbol{x}}_0^+$ and $\boldsymbol{S}_0^+$	3.99
(Time update) $\hat{\boldsymbol{x}}_k^- = \boldsymbol{F}_{k-1}\hat{\boldsymbol{x}}_{k-1}^+$ (Same as EKF) $\boldsymbol{S}_k^- = \frac{1}{\sqrt{\rho}}\boldsymbol{F}_{k-1}\boldsymbol{S}_{k-1}^+$	3.32 and 3.61 3.105 and 3.106
(Measurement update) $\bar{\boldsymbol{S}}_k^- = \boldsymbol{H}_k\boldsymbol{S}_k^-$ $\boldsymbol{P}^r = \boldsymbol{I} + (\bar{\boldsymbol{S}}_k^-)^T\boldsymbol{R}_d^{-1}(\bar{\boldsymbol{S}}_k^-)$ $\boldsymbol{K}_k = \boldsymbol{S}_k^-(\boldsymbol{P}^r)^{-1}(\bar{\boldsymbol{S}}_k^-)^T\boldsymbol{R}_d^{-1}$ $\hat{\boldsymbol{x}}_k^+ = \boldsymbol{K}_k(\boldsymbol{y}_k - \boldsymbol{H}_k\hat{\boldsymbol{x}}_k^-)$ (Same as EKF) $\boldsymbol{S}_k^+ = \boldsymbol{S}_k^-(\boldsymbol{P}^r)^{-1/2}$	3.112 3.115 3.117 3.7 3.125

3.5 Singular Evolutive Unscented Kalman filter (SEUK) as a reduced-order UKF (rUKF)

The SEEK filter developed in previous section reduces the unaffordable matrix operation cost in EKF. However, the time update phase is essentially based on the linearisation as EKF (equation 3.32, 3.61, 3.105 and 3.106 in table 3.5). As pointed out in section 3.3.1, the unscented transformation in UKF significantly improves the estimation accuracy of the mean and covariance, in the context of nonlinear systems.

This naturally motivates the idea of improving the accuracy of time update phase in SEEK filter by replacing its time update phase using the unscented transformation, which results in a hybrid filter of SEEK and UKF. We name it as the singular evolutive unscented Kalman filter (SEUK) given its root from *singular evolutive* extend filter (SEEK) and unscented Kalman filter (UKF), and it is one of the approaches to the more general *reduced-order UKF* (rUKF). Since this derivation was completed, we have been made aware of a recent paper in which Moireau and Chapelle (2011) presented a deviation of the reduced-order UKF developed in parallel by applying SVD directly to UKF.

3.5.1 From SEEK to SEUK

Time update

As mentioned before, it is straightforward to apply unscented transformation to replace the time update equation of SEEK (equation 3.32, 3.61, 3.105 and 3.106 in table 3.5), i.e.,

$$\hat{\boldsymbol{x}}_k^- = \left[\hat{\boldsymbol{x}}_k^{-(i)}\right] \begin{pmatrix} w_1 \\ w_2 \\ \vdots \\ w_{2r} \end{pmatrix}, \tag{3.126}$$

$$\boldsymbol{P}_k^- = \left[\hat{\boldsymbol{x}}_k^{-(i)} - \hat{\boldsymbol{x}}_k^-\right] \begin{pmatrix} w_1 & & \\ & \ddots & \\ & & w_{2r} \end{pmatrix} \left[\hat{\boldsymbol{x}}_k^{-(i)} - \hat{\boldsymbol{x}}_k^-\right]^T + \boldsymbol{Q}_k. \tag{3.127}$$

where

$$\hat{\boldsymbol{x}}_k^{-(i)} = f(\hat{\boldsymbol{x}}_{k-1}^{+(i)}, \boldsymbol{0}), \quad i = 1...2r. \tag{3.128}$$

Note that above equations are directly from UKF (eq. 3.71 to 3.73).

With the same assumption as the that for the system error covariance matrix $\boldsymbol{Q}_k$ in SEEK (equation 3.107)

$$\boldsymbol{Q}_k = (\frac{1}{\rho} - 1)(\tilde{\boldsymbol{S}}_k^-(\tilde{\boldsymbol{S}}_k^-)^T) \tag{3.129}$$

$$= (\frac{1}{\rho} - 1)\boldsymbol{P}_k^-, \tag{3.130}$$

the covariance update equation 3.127 becomes

$$\boldsymbol{P}_k^- = \frac{1}{\rho}\left[\hat{\boldsymbol{x}}_k^{-(i)} - \hat{\boldsymbol{x}}_k^-\right] \begin{pmatrix} w_1 & & \\ & \ddots & \\ & & w_{2r} \end{pmatrix} \left[\hat{\boldsymbol{x}}_k^{-(i)} - \hat{\boldsymbol{x}}_k^-\right]^T. \tag{3.131}$$

To meet the input of the measurement update equation 3.117 in SEEK, we apply SVD to error covariance matrix $\boldsymbol{P}_k^-$ to get $\boldsymbol{S}_k^-$, that is,

$$\mathcal{SVD}(\boldsymbol{P}_k^-) \rightarrow \boldsymbol{U}_k^- \boldsymbol{\Lambda}_k^- (\boldsymbol{U}_k^-)^T, \tag{3.132}$$

and we define

$$\boldsymbol{S}_k^- = \boldsymbol{U}_k^-(:, 1:r)\sqrt{\boldsymbol{\Lambda}_k^-(1:r, 1:r)}. \tag{3.133}$$

For convenience, we will write the above equations (3.132 and 3.133) as

$$\mathcal{SVD}(\boldsymbol{P}_k^-) \rightarrow \boldsymbol{S}_k^-(\boldsymbol{S}_k^-)^T. \tag{3.134}$$

Measurement update

As explained in the beginning of section 3.5, the measurement update of SEUK remains the same as SEEK.

As a summary of section 3.5, table 3.6 lists all the components of SEUK filter.

3.6 Summary

In this chapter, the derivation of Kalman filter and its extensions are presented in a unified framework, including the EKF and UKF as extensions to nonlinear systems, and the reduced-order EKF and UKF (SEEK and SEUK) as extensions to large systems.

In next chapter, the application of the Singular Evolutive Unscented Kalman filter (SEUK, developed in section 3.5)) or equivalently the reduced-order UKF (rUKF) to estimating myocardial constitutive material parameters will be formulated.

Table 3.6: Summary of discrete-time SEUK filter (reduced-order UKF)

Filter components	referenced equations
(System equations)	
$\boldsymbol{x}_k = f(\boldsymbol{x}_{k-1}, \boldsymbol{w}_{k-1})$	3.50
$\boldsymbol{w}_k \sim \mathcal{N}(\boldsymbol{0}, \boldsymbol{Q}_k)$	3.51
$\mathbb{E}\left[\boldsymbol{w}_i \boldsymbol{w}_j^T\right] = \boldsymbol{O}, \quad i \neq j$	3.52
(Measurement equations)	
$\boldsymbol{y}_k = \boldsymbol{H}\boldsymbol{x}_k + \boldsymbol{v}_k, \boldsymbol{H} = (\boldsymbol{I} \quad \boldsymbol{O})$	3.59
$\boldsymbol{v}_k \sim \mathcal{N}(\boldsymbol{0}, \boldsymbol{R}_k)$	3.56
$\mathbb{E}\left[\boldsymbol{v}_i \boldsymbol{v}_j^T\right] = \boldsymbol{O}, \quad i \neq j$	3.57
Initialize $\hat{\boldsymbol{x}}_0^+$ and $\boldsymbol{S}_0^+$	3.99
(Time update)	
$\hat{\boldsymbol{x}}_k^{-(i)} = f(\hat{\boldsymbol{x}}_{k-1}^{+(i)}, \boldsymbol{0}), i = 1...2r$	3.128
$\hat{\boldsymbol{x}}_k^- = \left[\hat{\boldsymbol{x}}_k^{-(i)}\right] \begin{pmatrix} w_1 \\ w_2 \\ \vdots \\ w_{2n_x} \end{pmatrix}$	3.126
$\boldsymbol{P}_k^- = \frac{1}{\rho}\left[\hat{\boldsymbol{x}}_k^{-(i)} - \hat{\boldsymbol{x}}_k^-\right] \begin{pmatrix} w_1 & & \\ & \ddots & \\ & & w_{2n_x} \end{pmatrix} \left[\hat{\boldsymbol{x}}_k^{-(i)} - \hat{\boldsymbol{x}}_k^-\right]^T$	3.131
$\mathcal{SVD}(\boldsymbol{P}_k^-) \rightarrow \boldsymbol{S}_k^-(\boldsymbol{S}_k^-)^T$	3.134
(Measurement update)	
$\bar{\boldsymbol{S}}_k^- = \boldsymbol{H}_k \boldsymbol{S}_k^-$	3.112
$\boldsymbol{P}^r = \boldsymbol{I} + (\bar{\boldsymbol{S}}_k^-)^T \boldsymbol{R}_d^{-1} (\bar{\boldsymbol{S}}_k^-)$	3.115
$\boldsymbol{K}_k = \boldsymbol{S}_k^- (\boldsymbol{P}^r)^{-1} (\bar{\boldsymbol{S}}_k^-)^T \boldsymbol{R}_d^{-1}$	3.117
$\hat{\boldsymbol{x}}_k^+ = \boldsymbol{K}_k(\boldsymbol{y}_k - \boldsymbol{H}_k \hat{\boldsymbol{x}}_k^-)$	3.7
$\boldsymbol{S}_k^+ = \boldsymbol{S}_k^- (\boldsymbol{P}^r)^{-1/2}$	3.125

Part III

Results and Contributions

Chapter 4

Myocardial transversely isotropic material parameters estimation from *in silico* measurements

Parameter estimation from non-invasive measurements is a crucial step in patient-specific cardiac modelling and provides potentially significant assistance in the clinical diagnosis of cardiac diseases through the quantification of myocardial heterogeneity of constitutive properties. In this chapter, we apply a novel approach based on a reduced-order unscented Kalman filter (rUKF), to estimate spatially-heterogeneous parameters in the widely-employed transversely isotropic Guccione's material law within a quasi-static left ventricular (LV) mechanical model using cubic-Hermite finite element interpolation. We demonstrate the performance of this approach on a set of *in silico* data whose ground-truth parameters are unknown. We conclude that the constitutive parameters in Guccione's law can be accurately determined from *in silico* noisy displacement measurements of material points from the myocardial surfaces. Given the effectiveness (high tolerance of noisy measurements) and computational efficiency (natural parallelism and efficiency for assimilating multiple measurements), the future application of this approach to state-of-art cardiac models coupled with *in vivo* motion and pressure measurements is promising. The work presented in this chapter has been published in Xi et al. 2011a.

4.1 Introduction

The measurement of regional myocardial function and contractility are vital for the assessment of heart diseases. From these measurements, the quantification of local myocardial stiffness provides significant values for the diagnosis assistance from the investigation of diastolic dysfunction (Wang and Nagueh 2009) to better selection of patient candidates with infarcted or hibernating tissue for further therapy (Nagel and Schuster 2010).

Accordingly, model-based parameter estimation from non-invasive clinical measurements of cardiac function has been an active research area. Various frameworks and methods have been proposed (Sermesant et al. 2006, Moireau et al. 2008, Sermesant et al. 2001). In Sermesant et al. (2006), a variational data assimilation method was employed to estimate the contractility parameters of a electromechanical model from clinical MRI. In order to achieve tractable solutions, simplified assumptions were needed for modelling the complexities of myocardial electromechanical activities and the details of material constitutive laws (e.g., an electromechanical model for better cardiac image analysis in Sermesant et al. 2001).

However, the non-invasive determination of passive constitutive parameters still remains a challenging inverse problem when we increase the model complexity by using anisotropic and nonlinear myocardial constitutive laws (e.g., Guccione et al. 1991; Hunter 1995; Costa et al. 2001; Nash and Hunter 2000)[1]. In previous studies (Omens et al. 1993; Augenstein et al. 2005; Wang et al. 2009; Sun et al. 2009), this inverse problem was typically formulated as a nonlinear optimisation problem to minimise–with respect to all unknown

[1]The mechanical and constitutive model in this chapter is defined and solved within the CMISS (Continuum Mechanics, Image processing, Signal processing and System identification) software package, written in FORTRAN and developed at the University of Auckland (www.cmiss.org). The code was compiled using the INTEL FORTRAN compilers for XEON CPUs and solved using 2 Quad core CPUs and 16 GB RAM. All geometrical visualisations of the model are generated using the freely available CMGUI graphical user interface.

parameters–a functional criterion based on the observation error, with the model equations taken as constraints. However, the highly nonlinear dependency of the simulated mechanical behaviour on material parameters and the interdependence between material parameters typically compromises the ability of an optimiser to retrieve the parameter values correctly. This situation is further exacerbated with the introduction of inevitable measurement noise.

An alternative to the traditional nonlinear optimisation formulation are filtering approaches (Simon 2006), which can naturally incorporate the knowledge of model error and measurement noise to improve the estimation result. Among filtering approaches, the unscented Kalman filter (UKF) (Julier et al. 1995) has shown to be robust for nonlinear systems, and possess natural parallelism. For this reason, UKF has been extensively applied to state estimation problems, including myocardial motion recovery from MR images (Wong and Shi 2004, Wong et al. 2007, Wong et al. 2010) and electrical activity recovery from body surface potential measurements (Wang et al. 2010a). Moireau et al. (2008) has also applied UKF to the more challenging problems of joint state-parameter estimation where myocardial parameters are identified from synthetic MR measurements. However, the UKF approach is not tractable for the current parameter estimation problem in this chapter, since it requires a significant number of computationally expensive model evaluations and manipulations of large matrices solely for the estimation of model state. For this reason, we developed the Reduced-order Unscented Kalman Filter (rUKF) as a tractable filtering algorithm (Moireau and Chapelle 2011). Nevertheless, the feasibility of identifying material parameters using rUKF in the context of detailed nonlinear mechanical models with microstructurally based transversely isotropic constitutive law has not yet been investigated in literature. Our goal of this chapter is to directly address this gap through the formulation of rUKF on this nonlinear mechanical model, and investigate feasibility of identifying Guccione's material parameters by using noisy synthetic measurements.

4.2 Material and methods

4.2.1 Personalised geometrical modelling based on cubic-Hermite Finite Elements

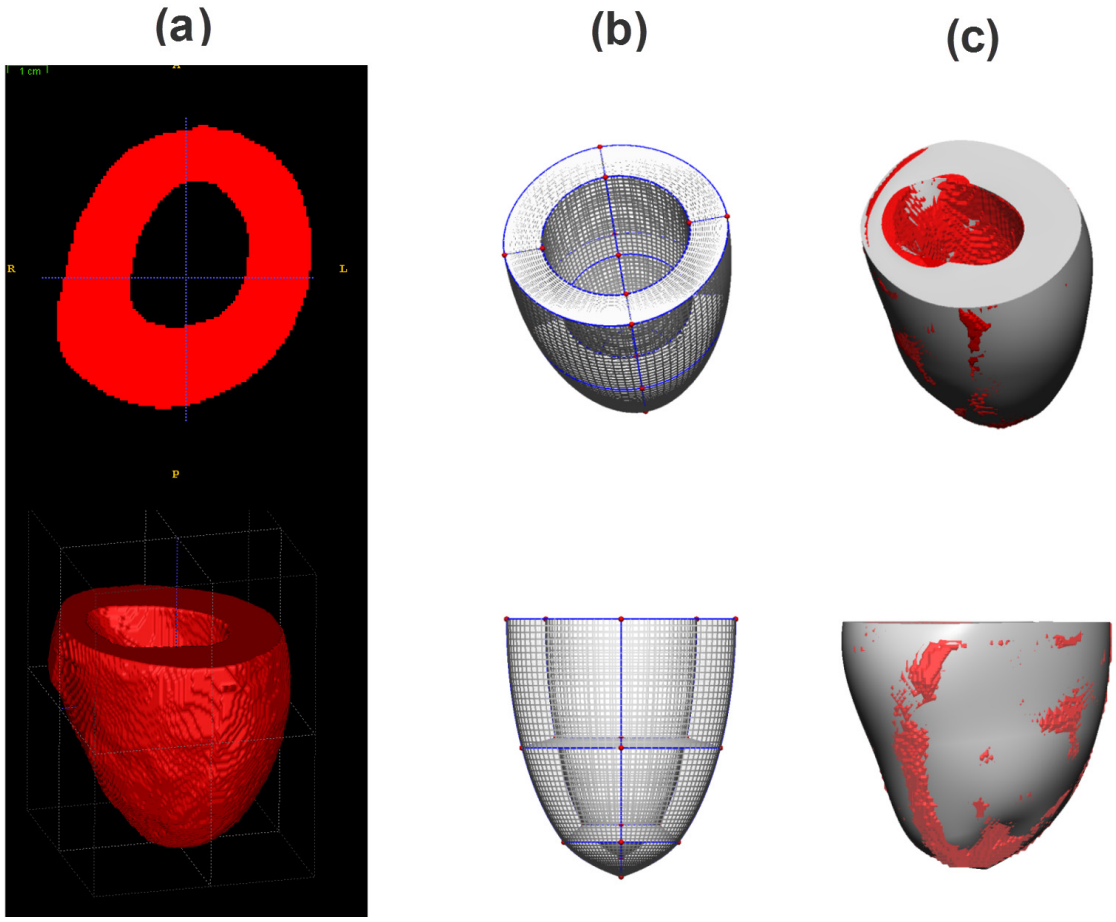

Figure 4.1: Mesh construction. (a) Voxelized representation of the LV at the beginning of diastole after its segmentation from the cine CT data set. The LV is cropped at its base, just underneath its valve planes. (b) Cubic-Hermite template of a generic left ventricle, with 12 elements and 26 nodes. (c) Cubic-Hermite mesh personalised (white) overlaid with a surface representation of the binary image (red).

Using the geometrical segmentation from cine CT measurement (shown in fig 4.1(a), provided by Dr. Olivier Ecabert, Peters et al. 2009)), an anatomically accurate mesh for the mechanical simulation of the left ventricle (LV) is built with cubic-Hermite elements. The mesh is constructed by Dr. Pablo Lamata using a novel approach detailed in

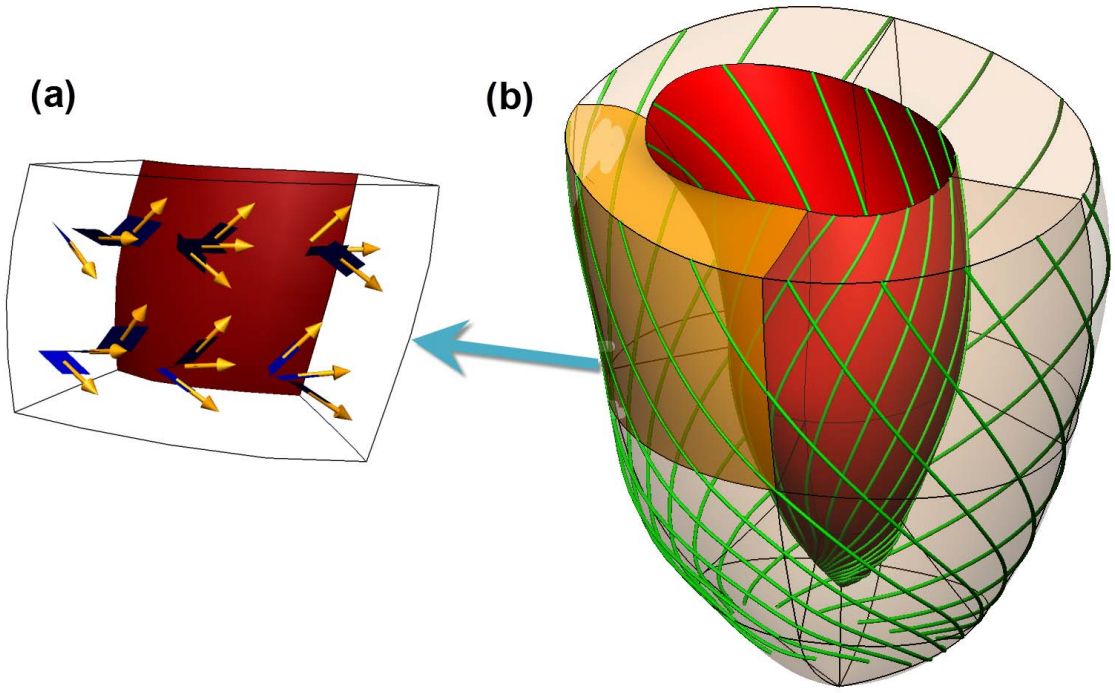

Figure 4.2: Personalised LV geometrical model with embedded micro fibre structure. The constructed mesh (b) consists of 12 cubic-Hermite elements with 26 nodes and 624 degree of freedom (before the application of boundary conditions). The streamlines on the epi- and endocardium in (b) are along fibre directions, and the fibre field with transmural and apex-to-based heterogeneity, further illustrated in (a), is generated based on Usyk et al. (2000).

Lamata et al. (2010a), which uses medical image registration and a cubic-Hermite warping technique to fit a template mesh to a given geometry. Firstly, the geometry of the LV myocardium is segmented from the image frame at the beginning of diastole using the method of Ecabert et al. (2008). The topology of the template mesh is then adapted to the binary image from the segmentation. Finally the fibre field inside LV myocardium with transmural and apex-to-base heterogeneity was automatically generated based on data by Usyk et al. (2000). This process is illustrated schematically in figures 4.1 and 4.2.

4.2.2 Mechanical modelling based on the theory of finite deformation

Passive LV mechanics is simulated using the finite element method (FEM) to solve finite elasticity stress equilibrium governing equations, which are derived from the laws of conservation of mass, linear momentum, angular momentum and the principle of virtual work (Malvern 1977; Nash and Hunter 2000).

Kinematics

Central to determining the kinematics of an object is the deformation gradient tensor ($\boldsymbol{F}$), which relates a infinitesimal material segment ($d\boldsymbol{x}$) in the deformed state to the same material segment ($d\boldsymbol{X}$) in the reference configuration

$$\boldsymbol{F} = \frac{\partial \boldsymbol{x}}{\partial \boldsymbol{X}}. \tag{4.1}$$

The concept of strain, established upon gradient tensor $\boldsymbol{F}$, is to measure how much a given displacement differs locally from a rigid body motion (Lubliner and Moran 1992). The Green-Lagrange strain tensor $\boldsymbol{E}$ is one of such strains for large deformation, determined by

$$\boldsymbol{E} = \frac{1}{2}(\boldsymbol{F}^T\boldsymbol{F} - \mathtt{1}), \tag{4.2}$$

where $\mathtt{1}$ is the identity tensor.

Stress and equation of equilibrium

Deformation and motion of a body is governed by stress equilibrium equations. To define equilibrium, consider the spatial configuration of a general deformable body defined by a volume V with boundary area ∂V, and assume that the body is under the action of a surface force $\boldsymbol{s}$ on the boundary ∂V. Making a quasi-static assumption, the inertia force

is ignored. The principle of virtual work states that in the equilibrium state, for a body that undergoes an arbitrary small displacement $\partial \boldsymbol{v}$ from the current position, the work done by the residual force during this process is zero. To express the material behaviour conveniently, the stress is represented by material forces measured per unit undeformed area, which is given by the second Piola-Kirchhoff stress tensor ($\boldsymbol{T}$). The residual force can thus be expressed in terms of the second Piola-Kirchhoff stress tensor $\boldsymbol{T}$ and surface force $\boldsymbol{s}$, and the principle of virtual work relates $\boldsymbol{s}$ to $\boldsymbol{T}$ by

$$\int_V T^{MN} \frac{1}{\det(\boldsymbol{F})} \frac{\partial x_j}{\partial X_M} \frac{\partial \delta v_j}{\partial X_N} dV = \int_{\partial V} \boldsymbol{s} \cdot \delta \boldsymbol{v} dS, \quad M, N, j = 1, 2, 3, \tag{4.3}$$

where $\boldsymbol{X}$ and $\boldsymbol{x}$ are the positions of a material point in the undeformed and deformed configurations respectively.

Constitutive relationship

The equilibrium equations in the previous subsection are written in terms of the stresses ($\boldsymbol{T}$). These stresses result from the deformation, and thus for a hyperelastic material, they can be expressed in terms of the measure of this deformation, for instance, the Green-Lagrange strain tensor $\boldsymbol{E}$.

$$T^{MN} = \frac{1}{2} \left(\frac{\partial W}{\partial E_{MN}} + \frac{\partial W}{\partial E_{NM}} \right) - p \left(\frac{\partial X_M}{\partial x_k} \frac{\partial X_N}{\partial x_k} \right), \quad M, N, k = 1, 2, 3. \tag{4.4}$$

In the above equation, the second Piola-Kirchhoff stress tensor ($\boldsymbol{T}$) is decomposed into deviatoric and hydrostatic components. The deviatoric component of the stress tensor is characterised by the strain energy function W, which is associated with the volume-preserving motion, that is,

$$\det(\boldsymbol{F}) = 1. \tag{4.5}$$

The functional W, defined in equation (6.4), incorporates parameters that directly reflect mechanical and structural properties of myocardium (see next section). In the hydrostatic component of the stress tensor, the variable p is the hydrostatic pressure due to the bulk modulus of the tissue.

Strain energy density function of the myocardium

The strain energy function W in the constitutive equation (4.4) depends on the type of material under consideration. In literature, based on the experimental results of uniaxial and biaxial tests in isolated cardiac muscle (Fung 1981, Yin et al. 1987), the myocardium was assumed to be a transversely isotropic material with preferred directions that vary transmurally (Guccione et al. 1991). More recently, LeGrice et al. (1995) has shown that the ventricular myocardium has a fibre-sheet laminar structure, which suggested orthotropic mechanical response with respect to fibre, sheet and sheet-normal directions. Based on this experimental finding, the myocardium has been modelled as orthotropic hyperelastic material, including the 12-parameter Pole-zero law by Nash and Hunter (2000) and the 7-parameter Costa law by Costa et al. (2001). For the type of hyperelastic strain-energy functions, Fung (1973) argued persuasively that exponential functions (e.g., Costa and Guccione law) are preferable because there is less ambiguity in interpretation of the coefficients. Recently a comparative study by Schmid et al. (2008) reported a higher level of parameter identifiability for the Costa law among the five tested well-known nonlinear constitutive laws using data from ex-vivo bi-axial tests. However, for our study, this detailed 7-parameter constitutive law compromises the parameter identifiability using imaged-derived deformation measurements. Thus we chose the 4-parameter transversely isotropic Guccione law (Guccione et al. 1991), from which the Costa law was extended. This law provides a good balance between feasibility of estimating its parameters and the ability to accurately account for the physiological properties that result from the myocardial laminar structure. Moreover, the Guccione law has been extensively employed in previous parameter estimation studies using in-vivo or in-silico imaging measurement data (Omens et al. 1993, Augenstein et al. 2005, Wang et al. 2009, Sun et al. 2009).

The transversely isotropic strain-energy function in Guccione law has the exponential

form

$$W = \frac{1}{2} C_1 (e^Q - 1) \tag{4.6}$$

where

$$Q = C_2 E_{\text{ff}}^2 + C_3 (E_{\text{ss}}^2 + E_{\text{nn}}^2 + 2E_{\text{sn}}^2) + C_4 (2E_{\text{fs}}^2 + 2E_{\text{fn}}^2). \tag{4.7}$$

In the above equation, the strain energy density function W is a functional of six independent components of Green-Lagrange strain tensor $\boldsymbol{E}$ defined in fibre (f), sheet (s) and sheet-normal (n) coordinates, and has four material parameters $C_i\,(i = 1, ..., 4)$. In table 4.1, we list the four parameter values, which are assumed to be the ground-truth in our model simulation to generate synthetic measurements.

parameter symbol	C_1(kPa)	C_2	C_3	C_4
ground-truth values	0.189	29.9	13.5	13.3

Table 4.1: Parameters in Guccione law (Guccione et al. 1991). These parameter values were reduced from the Costa Law parameter values fitted by Schmid et al. (2008), using 8 by 8 by 8 finite element cube model, to data from the three dimensional simple shear experiments done by Dokos et al. (2002).

4.2.3 Estimation of passive material properties via rUKF

State-space representation of quasi-static nonlinear mechanical model

Spatial and temporal discretisation

Applying finite element discretisation with the cubic-Hermite interpolation for displacement field and linear Lagrange interpolation for hydrostatic pressure, the quasi-static nonlinear mechanical model based on the equilibrium equation (4.3) is first written as a finite dimensional nonlinear system

$$F^{\text{in}(a,j)}(\boldsymbol{x}(t), \boldsymbol{\theta}) = F^{\text{ex}(a,j)}(t), \quad j = 1, 2, 3, \quad a = 1, 2, \ldots, N_{\text{node}}, \tag{4.8}$$

where the terms $F^{\text{in}(a,j)}(\boldsymbol{x}(t), \boldsymbol{\theta})$ and $F^{\text{ex}(a,j)}(t)$ are given in equations (4.9) and (4.10) below. The above equation states that the j-th component of the equivalent internal nodal

force vector $F^{\text{in}(a,j)}(t)$ at time t and node a of the finite element mesh, as a function of deformed configuration $\boldsymbol{x}(t)$ and given material parameter $\boldsymbol{\theta}$, is in equilibrium with the equivalent external nodal force vector $F^{\text{ex}(a,j)}(t)$ (Bonet and Wood 1997). N_{node} is the number of total nodes of the geometrical mesh.

The equivalent internal nodal force vector $\boldsymbol{F}^{\text{in}} \in \mathbb{R}^{3N_{\text{node}}}$ is given, at node a of the finite element mesh, by

$$F^{\text{in}(a,j)}(\boldsymbol{x}(t), \boldsymbol{\theta}) = \int_V T^{MN}(\boldsymbol{x}(t), \boldsymbol{\theta}) \frac{1}{\det(\boldsymbol{F})} \frac{\partial x_j}{\partial X_M} \frac{\partial \phi_a}{\partial X_N} dV, \quad j = 1, 2, 3, \quad a = 1, 2, \ldots, N_{\text{node}}, \tag{4.9}$$

where the scalar-valued function ϕ_a, defined over the body volume V, is the finite element basis function of node a, and T^{MN} is the nine components of the second Piola-Kirchhoff stress tensor, whose dependency on the material parameter vector $\boldsymbol{\theta}$ is given by equation (4.4)–(4.7). Similarly the equivalent external nodal force vector $\boldsymbol{F}^{\text{ex}}(t) \in \mathbb{R}^{3N_{\text{node}}}$, coming from the external surface force $\boldsymbol{s}$, is given by

$$F^{\text{ex}(a,j)}(t) = \int_{\partial V} s_j(t) \phi_a dS, \quad j = 1, 2, 3, \quad a = 1, 2, \ldots, N_{\text{node}}. \tag{4.10}$$

Given the external forces $\boldsymbol{F}^{\text{ex}}(t)$ at a set of discretised time points $\{t_k,\ k = 1, 2, \ldots, K\}$, we solve the nonlinear system (equation 4.8) for the deformed configuration $\boldsymbol{x}_k$ via applying the Newton-Raphson method, i.e.,

$$\boldsymbol{x}_k \triangleq \boldsymbol{x}(t_k) = G(\boldsymbol{F}^{\text{ex}}(t_k), \boldsymbol{\theta}), \tag{4.11}$$

where the operator G denotes the solution process.

System equations

In order to formulate the filtering problem, we will describe the spatially and temporally discretised model (outlined in the previous section) with the standard form of a discrete nonlinear state-space system (Franklin et al. 2005, chapter 6). A system in this standard

form is characterised by the augmented state vector $\boldsymbol{z}$, the system transition operator f (mapping the current state to the future state) and system input vector $\boldsymbol{u}$.

We define the external nodal force vector $\boldsymbol{F}^{\text{ex}}(t_k)$ in equation (4.11) as the system input vector $\boldsymbol{u}_{k-1}$ at time $k-1$, i.e.,

$$\boldsymbol{u}_{k-1} \triangleq \boldsymbol{F}_k^{\text{ex}} = \boldsymbol{F}^{\text{ex}}(t_k). \tag{4.12}$$

The system augmented state vector $\boldsymbol{z}_k$ is the combined deformed configuration $\boldsymbol{x}$ and parameter vector $\boldsymbol{\theta}$

$$\boldsymbol{z}_k = \begin{pmatrix} \boldsymbol{x}_k \\ \boldsymbol{\theta}_k \end{pmatrix}. \tag{4.13}$$

Furthermore, the material parameter $\boldsymbol{\theta}$ is independent of the deformation, i.e.,

$$\boldsymbol{\theta}_k = \boldsymbol{\theta}_{k-1}. \tag{4.14}$$

Note that although parameter $\boldsymbol{\theta}_k$ has no time dependence itself, it will be recursively changed by the estimator over time.

Combining equation (4.11) – (4.14), the nonlinear mechanical system can be described by the following discrete-time, nonlinear system

$$\boldsymbol{z}_k = \begin{pmatrix} G(\boldsymbol{\theta}_{k-1}, \boldsymbol{u}_{k-1}) \\ \boldsymbol{\theta}_{k-1} \end{pmatrix} \tag{4.15}$$

$$= f(\boldsymbol{z}_{k-1}, \boldsymbol{u}_{k-1}), \tag{4.16}$$

where f, the system transition operator, is defined by the above equation.

Since the mathematical model is seldom a perfect representation of reality and the parameters for the model are yet to be estimated, the system described by the model (equation 4.16) has prediction errors. This is represented by the system noise $\boldsymbol{w_k}$ as

$$\boldsymbol{z}_k = f(\boldsymbol{z}_{k-1}, \boldsymbol{u}_{k-1}) + \boldsymbol{w}_{k-1}, \tag{4.17}$$

where the *white, additive* system noise for $\boldsymbol{x}_k$ is assumed to be of Gaussian type with zero mean and covariance $\boldsymbol{Q}$ reflecting the confidence on the model prediction.

Remark 4.2.1. *We point out that with quasi-static assumption, it is sufficient to write the system equation (4.17) as*

$$\boldsymbol{z}_k = f(\boldsymbol{\theta}_{k-1}, \boldsymbol{u}_{k-1}) + \boldsymbol{w}_{k-1}, \tag{4.18}$$

since the augmented state vector $\boldsymbol{z}$ at time point k has no dependency on $\boldsymbol{x}_{k-1}$ (the deformed configuration at time point $k-1$). This justifies the usage of the reduced-order filter for estimation of the augmented state vector since the rank of error covariance matrix $\boldsymbol{P}_k$ is only of the size of parameter vector $\boldsymbol{\theta}$. In contrast, for the dynamic systems where the quasi-static assumption does not hold, there is the necessity to apply a first-stage observer (Moireau et al. 2008) to essentially reduce the uncertainty of augmented state vector to the parameter space.

Measurement equations

The measurements $\boldsymbol{y}_k \in \mathbb{R}^m$ are given by

$$\boldsymbol{y}_k = h(\boldsymbol{z}_k) + \boldsymbol{v}_k, \tag{4.19}$$

$$\boldsymbol{v}_k \sim (\mathbf{o}, \boldsymbol{R}_{\mathrm{d}}), \tag{4.20}$$

where $h(\boldsymbol{z}_k) = h^x(\boldsymbol{x}_k)$, and $h^x(\cdot)$ is a operator that maps deformed model configuration $\boldsymbol{x}_k$ to its measurements. These measurements are assumed to be corrupted by a noise term $\boldsymbol{v}_k$ with zero mean and covariance $\boldsymbol{R}_{\mathrm{d}}$. Assume that we can track the positions of some material points over time, $h^x(\cdot)$ is the linear interpolation matrix that maps all degrees of freedom (coordinates and their spatial derivatives at nodes of the cubic-Hermite mesh) in the model to the coordinates of these material points, that is,

$$\boldsymbol{y}_k = \boldsymbol{H}\, \boldsymbol{z}_k + \boldsymbol{v}_k. \tag{4.21}$$

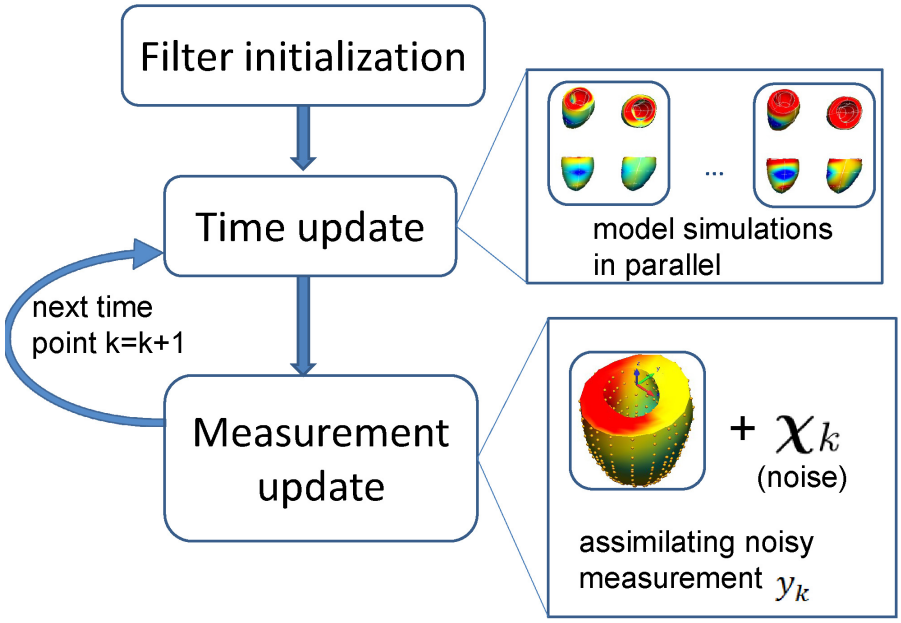

Figure 4.3: Schematic illustration of the estimation procedure via rUKF.

Parameter estimator equations

Our objective is to estimate constitutive parameters (table 4.1) in the mechanical system (eq. 4.17 and 4.19) formulated in previous section. This is achieved by applying filtering to the problem of estimating the augmented state vector $\boldsymbol{z}_k$ (equation 4.13).

Compared with widely-employed UKF, rUKF essentially reduces the rank of the error covariance matrix of the augmented state vector $\boldsymbol{z}_k$ from full rank n_z to r, where

$$r \ll n_z, \quad \boldsymbol{z}_k \in \mathbb{R}^{n_z} \text{ (i.e., } n_z \text{ is the size of augmented state vector } \boldsymbol{z}_k), \tag{4.22}$$

and

$$r \ll m, \quad \boldsymbol{y}_k \in \mathbb{R}^{m} \text{ (i.e., } m \text{ is the size of measurement vector } \boldsymbol{y}_k). \tag{4.23}$$

With this simplification, the covariance matrix storage is reduced from $n_z \times n_z$ to $n_z \times r$ and the matrix inversion operation can be performed in a subspace $\mathbb{M}^{r\times r}$ instead of $\mathbb{M}^{m\times m}$. Furthermore, the number of model evaluations required by the filter at each time point is also significant decreased, roughly from $O(n_z)$ to $O(r)$. As mentioned in remark

(4.2.1), in the quasi-static systems the uncertainties primarily lie in the parameter space, and thus r can be chosen as the dimension of parameter space, that is

$$r = n_\theta, \quad \boldsymbol{\theta}_k \in \mathbb{R}^{n_\theta} \text{ (i.e., } n_\theta \text{ is the size of parameter vector } \boldsymbol{\theta}_k). \tag{4.24}$$

The filtering process consists of three steps (figure 4.3) – (1) initialisation of the augmented state vector $\hat{\boldsymbol{z}}_0^+$ and its error matrix $\boldsymbol{P}_0^+$, (2) time updates involving one-step model evaluations, and (3) measurement updates where the noisy data are assimilated based on the relative confidence of the model prediction and measurements accuracy. In the following notations, we use superscripts $-$ and $+$ to differentiate the prior and posterior estimations (variables before and after assimilating measurements), and $\hat{}$ for indicating estimated variables (the mean of the true variable value).

Filter initialisation

For filter initialisation, the initial error-covariance $\boldsymbol{P}_0^+ \in \mathbb{M}^{n_z \times n_z}$, which is typically prescribed as a diagonal matrix with r non-zero elements representing the uncertainties of the system parameters, is decomposed using singular value decomposition (SVD) method

$$\boldsymbol{P}_0^+ = \boldsymbol{L}_0^+ \boldsymbol{\Lambda}_0^+ {\boldsymbol{L}_0^+}^T, \tag{4.25}$$

where $\boldsymbol{L}_0^+ \in \mathbb{M}^{n_z \times n_z}$ and $\boldsymbol{\Lambda}_0^+ \in \mathbb{M}^{n_z \times n_z}$ are orthonormal and diagonal matrices respectively.

We keep the first r eigenvectors $\boldsymbol{L}_0^+(:, 1:r)$ (here this notation denotes the sub-matrix consisting of all the rows and 1 to r columns of $\boldsymbol{L}_0^+$) of $\boldsymbol{P}_0^+$, and define its reduced-rank square-root approximation $\boldsymbol{S}_0^+ \in \mathbb{M}^{n_z \times r}$ as

$$\boldsymbol{S}_0^+ = \boldsymbol{L}_0(:, 1:r)\sqrt{\boldsymbol{\Lambda}_0^+(1:r, 1:r)}. \tag{4.26}$$

The r column vectors of $\boldsymbol{S}$ span the space in which the filter is allowed to make corrections to the augmented state vector $\boldsymbol{z}$.

Time update

In time update phase, $2r$ model simulations $f(\hat{\boldsymbol{z}}_{k-1}^{+(i)}, \boldsymbol{u}_{k-1})$ (recall equation 4.17) are performed at a set of sampling points $\hat{\boldsymbol{z}}_{k-1}^{+(i)}$, in parallel:

$$\hat{\boldsymbol{z}}_{k}^{-(i)} = f(\hat{\boldsymbol{z}}_{k-1}^{+(i)}, \boldsymbol{u}_{k-1}). \tag{4.27}$$

These sampling points are referred to as *sigma points* if they are constructed by the so-called *unscented transformation* (Julier and Uhlmann 1997). Sigma points are deliberately constructed so that they have the same known statics, e.g., first and second and possibly higher moments, as the given estimate.

While a minimal set of $r + 1$ sigma points are adequate to preserve the first and second moments (mean and covariance), we have adopted a *symmetric* set of $2r$-sigma points to improve estimation accuracy, based on the assumption that error processes associated with calibrated measuring devices exhibit the symmetries about a set of principle measurement axes, and such symmetries provide information about the third central moment of the unknown distribution of estimated variables (Julier and Uhlmann 2002). We generate the $2r$ sigma points $\hat{\boldsymbol{z}}_{k-1}^{+(i)}$ from the reduced-rank square-root approximation matrix $\boldsymbol{S}$ by

$$\hat{\boldsymbol{z}}_{k-1}^{+(i)} = \hat{\boldsymbol{z}}_{k-1}^{+} + \tilde{\boldsymbol{z}}_{k-1}^{+(i)}, \quad i = 1, ..., 2r, \tag{4.28}$$

where

$$\tilde{\boldsymbol{z}}_{k-1}^{+(i)} = \boldsymbol{S}_{k-1}^{-}(:, i), \quad i = 1, ..., r, \tag{4.29}$$

and

$$\tilde{\boldsymbol{z}}_{k-1}^{+(i)} = -\boldsymbol{S}_{k-1}^{-}(:, i - r), \quad i = r + 1, ..., 2r. \tag{4.30}$$

The statistics (mean $\hat{\boldsymbol{z}}_k^-$ and error covariance $\boldsymbol{P}_k^-$) of the augmented state variable $\boldsymbol{z}_k^-$ are estimated from the transformed sampling set by

$$\hat{\boldsymbol{z}}_k^- = \frac{1}{2r}\sum_{i=1}^{2r}\hat{\boldsymbol{z}}_k^{-(i)}, \tag{4.31}$$

$$\boldsymbol{P}_k^- = \frac{1}{\sqrt{2r}}\sum_{i=1}^{2r}(\hat{\boldsymbol{z}}_k^{-(i)} - \hat{\boldsymbol{z}}_k^-)(\hat{\boldsymbol{z}}_k^{-(i)} - \hat{\boldsymbol{z}}_k^-)^T + Q, \tag{4.32}$$

where Q is the covariance matrix of the system noise (equation 4.17). As mentioned earlier, the magnitude of Q, typically initialised as a diagonal matrix, reflects our confidence on the accuracy of the model predication.

To keep the rank of $\boldsymbol{P}_k^-$ to be r, we again decompose $\boldsymbol{P}_k^-$ as eq. (4.25) and (4.26) to reobtain the reduced-rank square-root approximation $\boldsymbol{S}_k^-$ of $\boldsymbol{P}_k^-$:

$$\mathcal{SVD}(\boldsymbol{P}_k^-) \rightarrow \boldsymbol{S}_k^-(\boldsymbol{S}_k^-)^T. \tag{4.33}$$

Remark 4.2.2. *Equation 4.32 incorporates the additive system-noise covariance matrix Q of any structure. However, from the view of implementation, SVD operation (equation 4.33) on the covariance matrix P_k^- resulted from equation 4.32 is computationally expensive for large systems.*

We point out that the SVD operation on the first additive term of equation 4.32 can be implemented with efficiency independent of the system size, as detailed by Moireau and Chapelle 2011. Moreover, some particular choices of model noise statistics allow to preserve the structure of P_k^-, such as

$$Q = \frac{1}{\sqrt{2r}}(\frac{1}{\sqrt{\rho}} - 1)\sum_{i=1}^{2r}(\hat{\boldsymbol{z}}_k^{-(i)} - \hat{\boldsymbol{z}}_k^-)(\hat{\boldsymbol{z}}_k^{-(i)} - \hat{\boldsymbol{z}}_k^-)^T, \tag{4.34}$$

where ρ (typically $\rho \in [0.9, 1]$) is a "forgetting factor" used by Brasseur and Verron (2006) for SEEK filter, which characterises the scale of system-error covariance. Thus equation 4.32 becomes

$$\boldsymbol{P}_k^- = \frac{1}{\sqrt{2\rho r}}\sum_{i=1}^{2r}(\hat{\boldsymbol{z}}_k^{-(i)} - \hat{\boldsymbol{z}}_k^-)(\hat{\boldsymbol{z}}_k^{-(i)} - \hat{\boldsymbol{z}}_k^-)^T, \tag{4.35}$$

from which $\boldsymbol{P}_k^-$ can be reduced by SVD efficiently as mentioned before.

As it is usually impossible to specify the model error perfectly, the simple reparameterization in equation 4.34 provides a technique with tradeoff between the computational efficiency of the SVD operation and the accurate representation of error covariance matrix $\boldsymbol{P}_k^-$, and yet in practice the reparameterization gives satisfactory results in terms of filter performance.

Measurement update

Recalling equation (4.21), the observation operator can be adequately written as the observational matrix $\boldsymbol{H}$ for our problem. In the measurement update phase, the observation $\boldsymbol{y}_k$ is assimilated into the prior estimation $\hat{\boldsymbol{z}}_k^-$ to give the posterior estimation based on the *innovation or Kalman gain matrix* $\boldsymbol{K}_k$ by

$$\hat{\boldsymbol{z}}_k^+ = \hat{\boldsymbol{z}}_k^- + \boldsymbol{K}_k(\boldsymbol{y}_k - \boldsymbol{H}\hat{\boldsymbol{z}}_k^-), \tag{4.36}$$

In the above equation, the Kalman gain matrix $\boldsymbol{K}_k$ in rUKF can be obtained by applying the matrix inverse lemma (see e.g., Simon 2006) to that for the UKF

$$\boldsymbol{K}_k = \boldsymbol{S}_k^-(\boldsymbol{I} + (\boldsymbol{H}\boldsymbol{S}_k^-)^T\boldsymbol{R}_{\mathrm{d}}^{-1}\boldsymbol{H}\boldsymbol{S}_k^-)^{-1}(\boldsymbol{H}\boldsymbol{S}_k^-)^T\boldsymbol{R}_{\mathrm{d}}^{-1}, \tag{4.37}$$

where $\boldsymbol{R}_{\mathrm{d}}$ is the measurement error covariance matrix (recall equation 4.20). The square-root approximation of error covariance $\boldsymbol{S}_k$ is updated as

$$\boldsymbol{S}_k^+ = \boldsymbol{S}_k^-(\boldsymbol{I} + (\boldsymbol{H}\boldsymbol{S}_k^-)^T\boldsymbol{R}_{\mathrm{d}}^{-1}\boldsymbol{H}\boldsymbol{S}_k^-)^{-1/2}. \tag{4.38}$$

Note that the matrix inverse and square-root operations in the above equations are performed on $\boldsymbol{I} + (\boldsymbol{H}\boldsymbol{S}_k^-)^T\boldsymbol{R}_{\mathrm{d}}^{-1}\boldsymbol{H}\boldsymbol{S}_k^-$ (as mentioned before at the beginning of this section), which reduces the computational cost significantly for large systems.

The previous chapter provides further details and derivations of the equations in rUKF. rUKF decreases the computational costs dramatically based on the assumption that the

rank of error covariance (second order moment) can be reduced. However, filter optimality might be lost because of this simplification. Thus the effectiveness of this filter applied to the nonlinear mechanical model is assessed numerically in next section.

4.3 Results

The performance of estimating Guccione constitutive parameters via rUKF is analysed using noisy synthetic measurements with known ground-truth.

4.3.1 Synthetic measurement setup

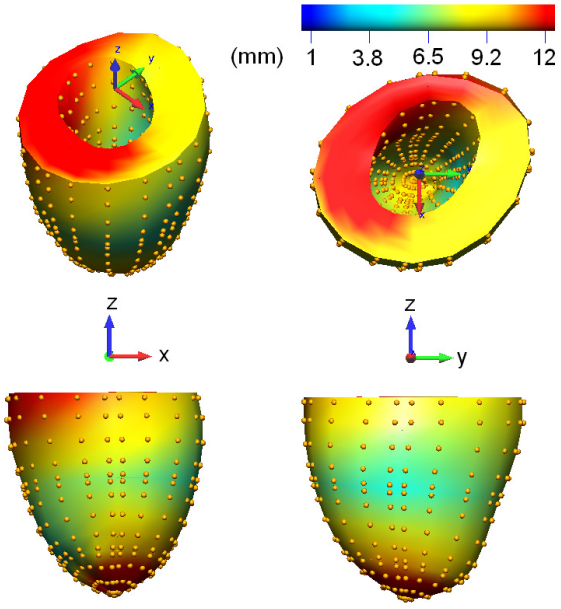

Figure 4.4: The noise-free synthetic measurement ($\bar{\boldsymbol{y}}$): end-diastolic displacement field with 600 observational data points on epi- and endocardium. It is numerically generated by the model with ground-truth parameter values, following equations (4.19)-(4.21).

The model is loaded with ventricular pressure set at 3.7 kPa on endocardium to simulate the myocardial dilation. The noise-free synthetic measurement $\bar{\boldsymbol{y}}$, generated from the model with ground-truth parameters, are the end-diastolic displacements of the 600 material points located at the epi- and endocardium (figure 4). Noisy measurements $\{\boldsymbol{y}^{\mathbf{1}}$,

$\boldsymbol{y^2}$, $\boldsymbol{y^3}$ ... $\}$ are determined from the sum of the noise-free measurement $\bar{\boldsymbol{y}}$ and a series of white Gaussian noise vectors $\{\boldsymbol{\chi^1}, \boldsymbol{\chi^2}, \boldsymbol{\chi^3}$ ... $\}$.

The next two sections present the filtering results of homogeneous and spatially varying parameters, where the size of parameter vector n_θ is 4 and 12 respectively. Note that the synthetic measurements are not always available for all time points of forward model simulation. Thus in these experiments, only the time update of the filter (i.e., the update which only requires the model simulation results for one additional time step) is performed at the time point when no measurement is available.

4.3.2 Estimation of homogeneous material parameters

The 4 homogeneous parameters in Guccione's constitutive law are estimated from synthetic measurements (table 4.2 and figures 4.5a-c).

Table 4.2 lists the results from 5 experiments with two level of measurement noise (standard deviation of 1.8 and 3.5 mm). The initial parameter guesses are chosen randomly with 40% error from the ground-truth parameter values (table 4.1). The estimation error is defined as $\frac{\left|\left|\boldsymbol{\theta}^{\text{estimated}} - \boldsymbol{\theta}^{\text{truth}}\right|\right|}{||\boldsymbol{\theta}^{\text{estimated}}||}$.

Estimation experiments	1	2	3	4	5
1.8 mm noise level	1.19%	1.05%	1.03%	0.55%	1.24%
3.5 mm noise level	2.22%	4.19%	1.42%	0.71%	0.71%

Table 4.2: Five experiments showing the estimation error of homogeneous parameters for 1.8 and 3.5 mm noise levels. The parameters are initialised randomly with 40% error from the ground-truth parameter values. The results for first experiments are further shown in figures 4.5b-c.

Figures 4.5b-c shows a typical estimation for both noise levels of table 4.2, and figure 4.5a is the estimation result from noise-free measurement. The 4 parameters are well estimated in spite of the observational noise. The estimation errors are 2.77×10^{-4} %, 1.19%, and 2.22% respectively.

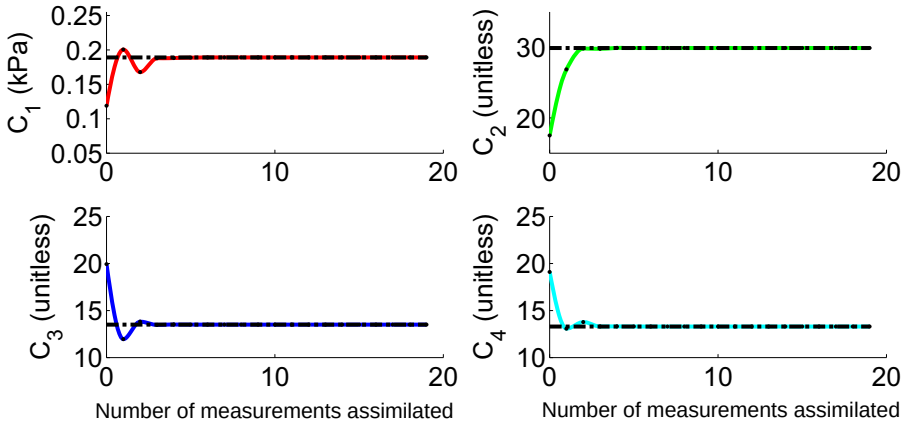

(a)

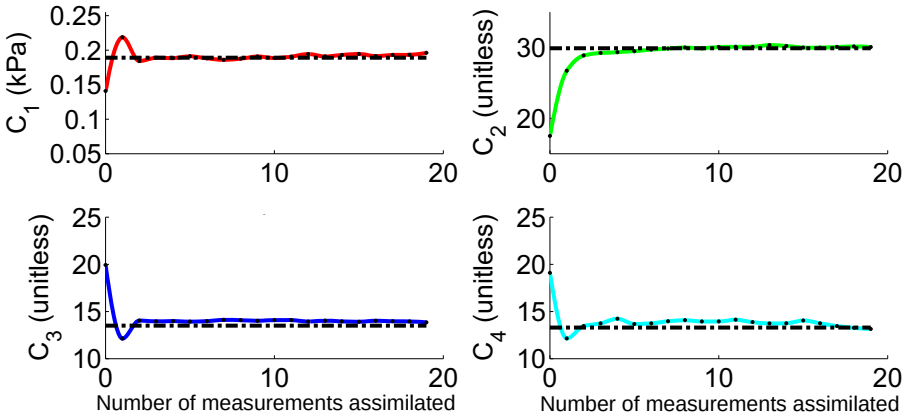

(b)

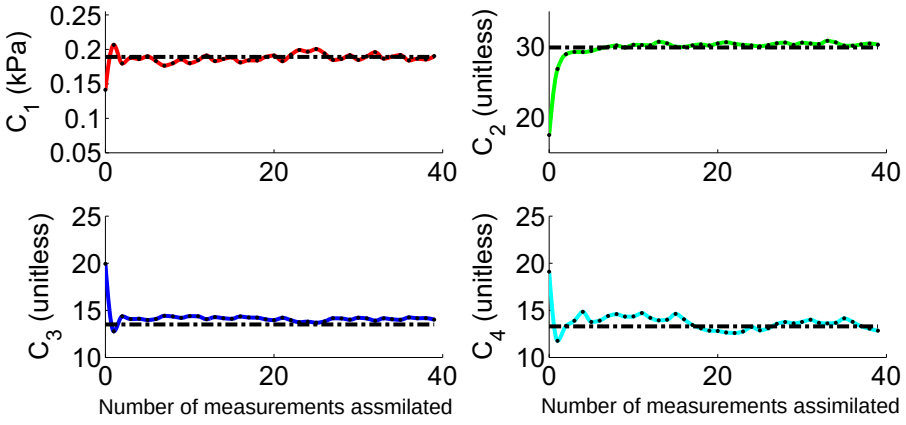

(c)

Figure 4.5: Estimation of four homogeneous parameters in Guccione's constitutive law from (noisy) synthetic data. The *in silico* measurements are corrupted by the Gaussian noise with standard derivation of 0, 1.8 and 3.5 mm in (a)-(c) respectively. The parameter estimation error are 2.77×10^{-4} %, 1.19%, and 2.22%.

4.3.3 Estimation of regional stiffness parameters

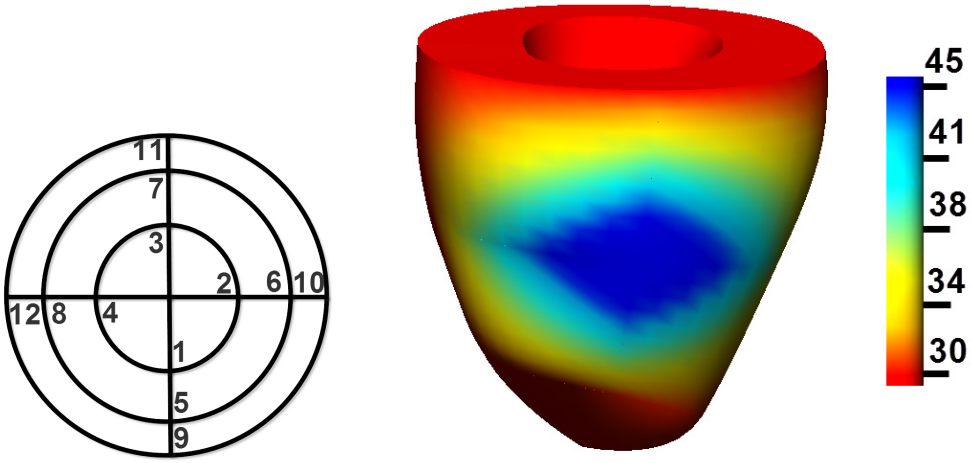

(a) (b)

Figure 4.6: Regional C_2 parameter field (b) presented by values at 12 interpolation points (a). This is the ground-truth parameters for regional stiffness estimation. (a): Long-axis view (from base to apex) of interpolation points distribution. (b): Ground-truth material field. Blue area ($C_2 = 45$) corresponds to the region with increased stiffness while red area ($C_2 = 29.9$) is normal.

After validating the estimation of homogeneous parameters, we apply the rUKF to a synthetic case of inhomogeneous myocardial stiffness. This inhomogeneity is represented by spatially varying C_2 parameter (the stiffness in myocardium fibre direction, Costa et al. 2001). The C_2 parameter field is linearly interpolated, with 12 values for all the interpolation points (figure 4.6). We set C_2 at point 5 to be 45 (high stiffness) while keeping the others to be 29.9 at the remaining 11 interpolation points.

Figures 4.7a-c list three estimation results using measurements with 0, 0.75 and 1.5 mm noise. The estimation error are 0.30%, 0.70% and 1.54% respectively.

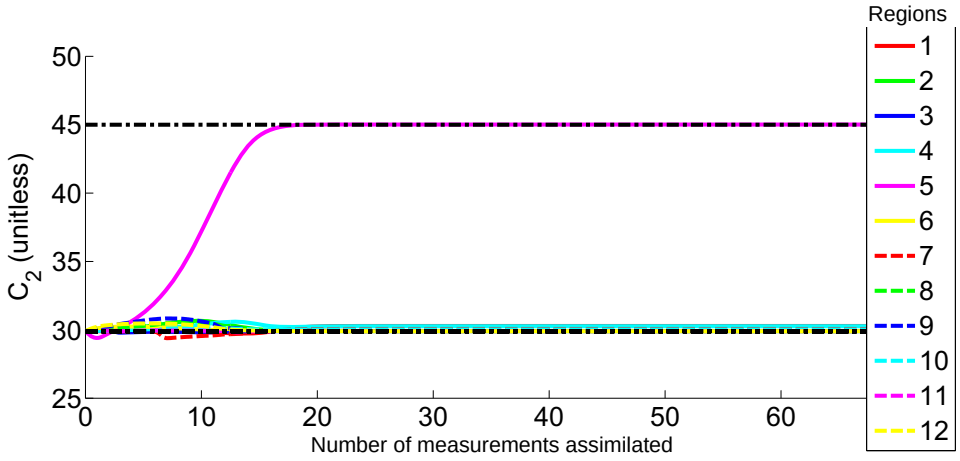

(a)

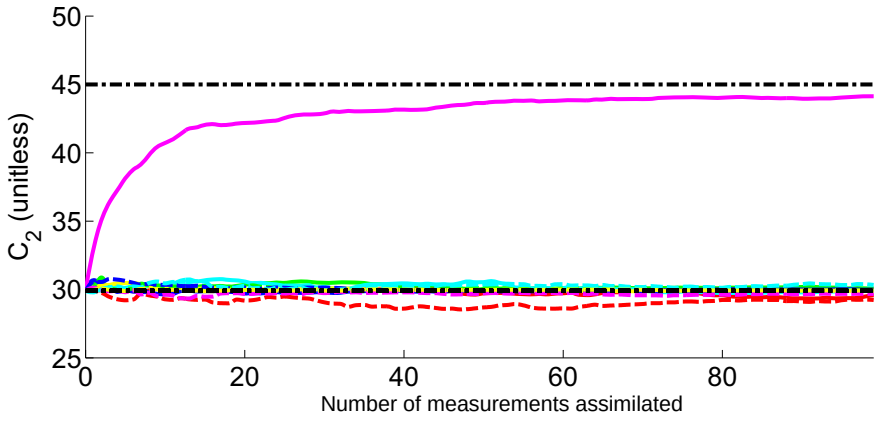

(b)

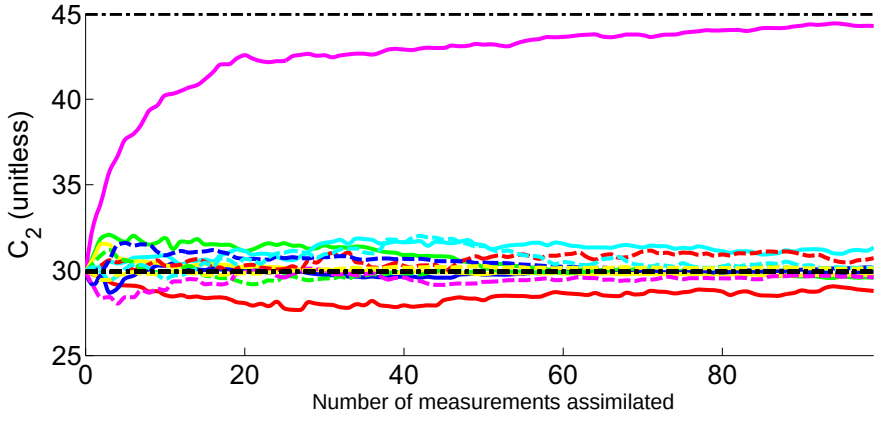

(c)

Figure 4.7: Estimation of regional C_2 parameter in Guccione's law. The *in silico* measurements are corrupted by Gaussian noises with standard derivations of 0.75 and 1.5 mm in (a)-(c) respectively. The parameter estimation errors are 0.30%, 0.70%, 1.54%. The myocardium material is approximated by linearly interpolated field with 12 nodal values, and the nodes distribution and ground-truth material field are illustrated in figure 4.6.

	C_1(kPa)	C_2	C_3	C_4
C_1	1.000	0.612	-0.601	-0.486
C_2		1.000	0.087	0.093
C_3			1.000	-0.608
C_4				1.000

Table 4.3: The correlation matrix of four parameters of the Guccione law at the ground-truth parameter point. This correlation matrix is similar to the one reported in Augenstein et al. 2006, indicating a strong coupling between C_1 and C_2-C_4 (see section 4.4.1 for more discussions on constitutive laws). For technical details calculating correlation matrix, please see Hill and Osterby 2003.

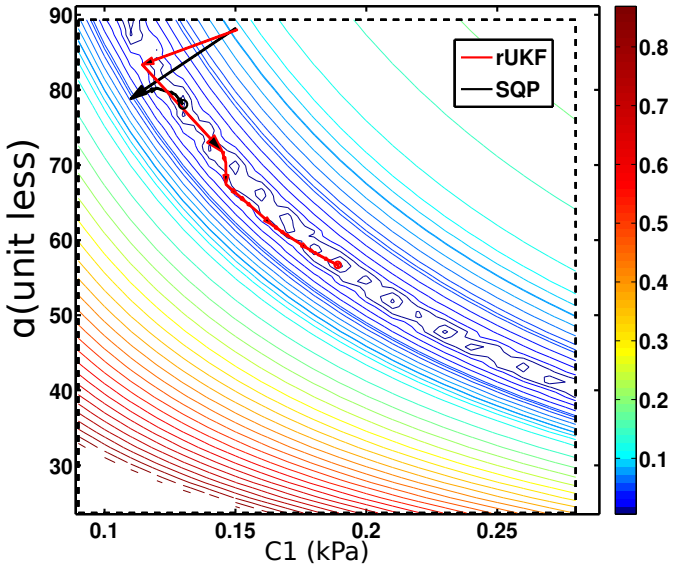

Figure 4.8: The landscape of the objective function based on the sum of the squared differences of all material points' position. The colour represents the normalised error. The arrowed lines show typical optimisation paths of SQP and rUKF. The landscape is plotted again parameter C_1 and α (α=C_2+C_3+C_4). This objective function is explicitly minimised by SQP using gradient-descent method. rUKF estimate the parameters by implicitly minimising this objective function as well. In this experiment, rUKF estimated the global minimal set of parameter successfully, while SQP was trapped in the local minimum close to the initialization point. See discussion section 4.2 for further details.

4.4 Discussions

The results in the previous section demonstrate that our rUKF approach can accurately retrieve the homogeneous and regionally varying nonlinear Guccione constitutive parameters. The low level of estimation errors is highly encouraging.

4.4.1 Comments on constitutive laws

The transversely isotropic Guccione law chosen in this study has been widely used for cardiac modelling (Fung 1993, Weiss et al. 1996), and thus is of interest for parameter estimation studies. It is important to note that the four parameters of the Guccione law are not independent - in that an increase of C1 can be compensated by a decrease of C2, C3, C4 at any particular inflation state. This leads to uncertainty in the parameter estimation reflected by higher off-diagonal values in the correlation matrix (Augenstein et al. 2006). In our study, we observed a similar correlation matrix at the ground-truth parameter point (table 3). We visualised this coupling relationship in figure 4.8, where the objective function of SQP approach differs only in an order of 0.04 mm in the coupling valley (the area with blue curves in figure 4.8).

In our preliminary investigations, we considered the 7-parameter exponential-form Costa law. However these results indicated that the in-silico imaging measurements were not able to constrain the filtering approach to obtain a global convergent estimation. Thus, we reduced the complexity of embedded within our material assumption by assuming the myocardium was transversely isotropic rather than orthotropic. For the strain energy functions in the transversely isotropic class, we showed the rUKF can uniquely identify the parameters of the Guccione law. As explained in section 2.2.4, the Guccione law, with a lower level of complexity, is still a good representative of the extensive myocardial modelling studies published. Nevertheless, although the identifiability of parameters is problem dependent, we believe the rUKF approach is likely to have similar performance for alternative transversely isotropic strain energies (e.g., polynomial form strain energy function by Humphrey et al. (1990), and the optimised strain energy function based on uncoupled strain attributes by Criscione et al. (2003)).

4.4.2 rUKF and SQP approaches

It can be theoretically demonstrated that the filtering approach is equivalent to a classic nonlinear optimisation approach in that the goal of both is to minimise the same objective function based on the sum of squared differences (Simon 2006). However rUKF-based filtering method is robust at handling the nonlinearities within the system, because of its UKF-like sampling scheme. It is well established that the sampling-scheme of UKF, known as unscented transformation, captures the nonlinear transformation process more accurately than the gradient-like linearisation (Julier and Uhlmann 1997, Moireau et al. 2008). Practically we also observed that gradient-based SQP method [2] seems to be more frequently trapped in the local minima while rUKF was consistently able to retrieves the globally minimal set of parameter values (see figure 8 for a typical example). However, the performance of the unscented transformation in rUKF essentially depends on the accuracy of the statistical assumptions of the filter estimation and the measurement noise distribution. This advantage of rUKF may be undermined if the noise is not distributed as expected. In terms of computational efficiency, rUKF is more straightforward to parallelise the independent model simulations (at sigma points) than SQP. This feature fits seamlessly to implementations optimised for high performance shared or distributed memory clusters.

4.4.3 Synthetic imaging protocol

The primary aim of the simulations presented in section 4.3 is to assess the performance of rUKF approach in the context of large measurement noise (0, 1.8 and 3.5 mm). The noise-free measurement is taken at the end of diastole, when the magnitudes of noise are maximal (1.8 and 3.5 mm for homogeneous case and 0.75 and 1.5 mm for hetero-

[2] In our experiments, we use the SQP implementation in the standard optimisation toolkit of MATLAB 2010b.

geneous case). With this single noise-free measurement (figure 4.5a and figure 4.7a), it is shown that the homogeneous material parameters can be typically estimated within 5 updates and that regional parameters estimation requires approximately 15 updates. In the presence of additive measurement noise of white (uncorrelated in time) and Gaussian type, the results (figures 4.5b-c and figures 4.7b-c) indicate that the parameters can be still correctly estimated when more measurements are taken into account.

For the clinical data–e.g. tagged Magnetic Resonance Images (tagged MRI)–there are typically 3-5 image frames acquired in the diastole. The synthetic measurement in our experiments is analogous to the displacements extracted from end-diastolic frames. The end-diastolic measurement has the biggest signal to noise ratio compared to intermediate frames, because the myocardium has the maximal displacements at end-diastole and thus most distinguishable from the early-diastolic state. Furthermore, quasi-static approximation of the mechanical models is likely to be best at the end-diastole, and may introduce undesirable error in its prediction of the intermediate deformed states (Nash and Hunter 2000). Therefore for these two reasons, the conclusion on the identifiability of Guccione parameters using end-diastolic measurements is valuable for the future application to tagged MR data. In addition, for the imaging modalities where the extraction of actual point-wise displacements may be out of reach (e.g., cine MRI), Moireau et al. 2009 provides an in-depth analysis of how to incorporate such type of measurements.

4.4.4 Limitations

While our results are encouraging, it is important to note the limitations in our study presented in this chapter. Although the geometric model we used is sufficient for the purpose of this study, there is a clear need to improve the model in two aspects for further applications. The fibre field is reconstructed based on an empirical model, and could be improved by incorporating *in vivo* measurements (e.g. DT-MRI). The parameters are

defined in the local coordinates aligned with fibre directions, and thus the error in fibre orientation will render the estimations unreliable. In addition, there is a clear need for a bi-ventricular model to take into account the inflation pressure in the right ventricle, and it would also be necessary to refine the mesh for convergent solution of the physiology simulation if applied to coupled electromechanical models (Niederer and Smith 2008). These improvements will result in a mesh with much more degrees of freedom, and thus an increase of the state vector size. However, as explained, rUKF is well-equipped to deal with such a change with little overhead due to its reduced-order nature.

In addition, unlike SQP, rUKF cannot be categorised as a choice for constrained optimisation. That is, there is no guarantee that the parameter updated by rUKF will be in a valid range (e.g., the stiffness should not be negative). In our study, the Newton solution process fails to converge because of the non-positive parameters determined via rUKF. This typically happens when the initialization point lies in or near the corner of the valid parameter subspace. One solution to this problem might be to decrease the gain matrix heuristically (either directly, or indirectly through increasing the measurement noise covariance) such that the correction made to the parameter vector is decreased. However, this has the potential to cause the filter to diverge from the ground-truth of state variable. Another solution is to constrain the parametric space, which necessitates the extension of the so-called constrained Kalman filter to rUKF so as to achieve a constrained rUKF. Finally, we could also re-parameterise the problem by introducing $\theta = e^{\alpha}$. In this case, the additional non-linearity changes the understanding of the covariance that should then be considered with respect to α instead of θ, hence the covariance initialization must be accordingly modified to achieve comparable performance.

4.5 Summary

This chapter formulated a novel and effective non-invasive material parameter estimation approach for estimating material parameters in nonlinear cardiac mechanics. The reduced-order unscented Kalman filter is well adapted to solve the inverse problem of estimating the material parameters in widely-employed Guccione's constitutive law. These material parameters can be accurately estimated from the noisy measurements of material displacements of data points from the epi- and endo-cardium. With the ongoing advances in medical imaging which has the potential to meet the demands of measurement requirement of this approach, the application to *in vivo* measurements of motion and pressure is very promising.

Appendices

This appendix provides more information on the details of rUKF initialisation and error covariance matrix estimation.

4.A rUKF initialisation

Corresponding figure	4.5(a)	4.5(b)	4.5(c)	4.7(a)	4.7(b)	4.6(c)
measurement error (mm)	0	1.8	3.5	0	0.75	1.5
parameter initialisation error (%)[3]	40%	40%	40%	14%	14%	14%
final parameter estimation error (%)[4]	$2.77 \times 10^{-4}\%$	1.19%	2.22%	0.30%	0.70%	1.54%
measurement error covariance matrix[5]	$0.10^2\boldsymbol{I}$	$0.10^2\boldsymbol{I}$	$0.20^2\boldsymbol{I}$	$0.10^2\boldsymbol{I}$	$0.10^2\boldsymbol{I}$	$0.20^2\boldsymbol{I}$
initial error covariance matrix for parameters [6]	$1.0^2\boldsymbol{I}$	$1.0^2\boldsymbol{I}$	$1.0^2\boldsymbol{I}$	$1.0^2\boldsymbol{I}$	$1.0^2\boldsymbol{I}$	$1.0^2\boldsymbol{I}$
system error covariance matrix [7]	**o**	**o**	**o**	**o**	**o**	**o**

Table 4.4: rUKF initialisation details.

[3]The initialisation error is defined as $\frac{\left|\left|\boldsymbol{\theta}^{\text{initialisation}}-\boldsymbol{\theta}^{\text{truth}}\right|\right|}{\left|\left|\boldsymbol{\theta}^{\text{initialisation}}\right|\right|}$.

[4]The estimation error is defined as $\frac{\left|\left|\boldsymbol{\theta}^{\text{estimated}}-\boldsymbol{\theta}^{\text{truth}}\right|\right|}{\left|\left|\boldsymbol{\theta}^{\text{estimated}}\right|\right|}$.

[5]The measurement values are normalised by a maximum value of $15mm$ (realistic LV maximal diastolic displacement). $0.10^2\boldsymbol{I}$ means that measurements can have 10% (i.e., 1.5 mm) error.

[6]The parameter values are first non-dimentionalised via normalising using initial values. The parameter estimation error covariance matrix is initialised as identity matrix, which indicates that the initial parameter values can have up to 100% error. Larger error covariance matrix will force the filter to pay more attention to the assimilated measurements.

[7]We set the system error covariance matrix (modelling error) to be null matrix, following the rationale that the measurement (observed reality) was synthetically produced by the same model and thus our model should not have any systematic modelling error. This practice brings the benefits that the error covariance of parameter estimation converges to zero after enough measurements are assimilated (full confidence on the estimated parameters). Please note that the system error covariance matrix can be set to be non-zero as well, in which case the variance of the parameter estimation error will not converge to zero and thus the parameter estimation will not converge to a steady value (typically oscillate around the ground-truth parameters).

4.B rUKF error covariance matrix

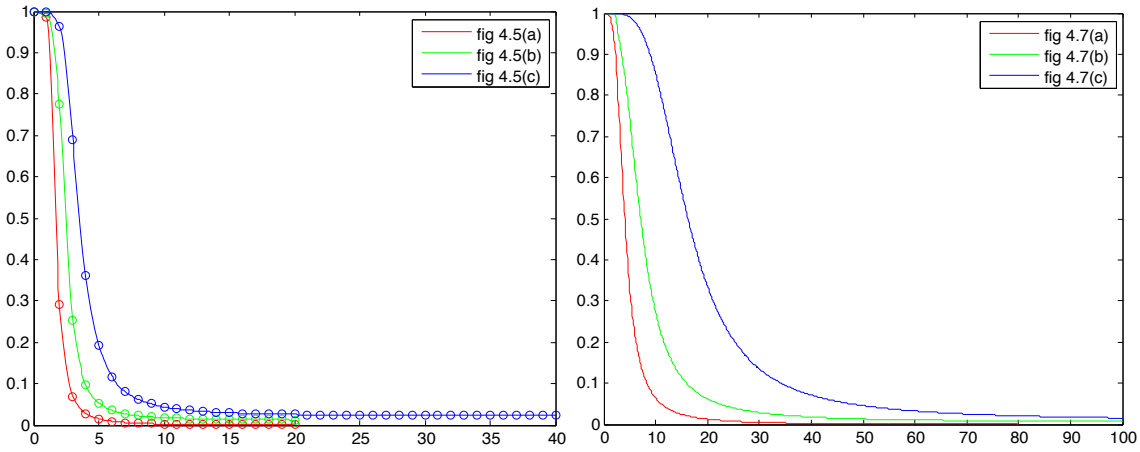

Figure 4.9: Variance/uncertainty of the parameter estimation in figure 4.5(a-c) and 4.7(a-c). The y axis plots the square root of averaged diagonal values in the error covariance matrix, which reflects the averaged variance/uncertainty of the estimated parameters. It decreases from 1.0 (100% error/uncertainty) to be close to zero after enough measurements are assimilated. This final uncertainty reflects the final parameter estimation uncertainty/error, which agrees well with the errors that are directly calculated using the ground-truth parameters (as shown by "final parameter estimation error" column in table 4.4).

Chapter 5

Constitutive parameter estimation from clinical data

Following the estimation of constitutive parameters from synthetic data, we have investigated the development of methods which can be applied to clinical data. This introduces additional difficulties as well as opportunities. Specifically, in this chapter, we present an automatic workflow to extract myocardial constitutive parameters from clinical data. Our framework assimilates cine and 3D tagged Magnetic Resonance Images (MRI) together with left ventricular (LV) cavity pressure recordings to characterise the mechanics of the LV. Dynamic C^1-continuous meshes are automatically fitted using both the cine MRI and 4D displacement fields extracted from the tagged MRI. The passive filling of the LV is simulated, with patient-specific geometry, kinematic boundary and loading conditions. The mechanical parameters are identified by matching the simulated diastolic deformation to observed end-diastolic displacements. We applied our framework to two heart failure patient cases and one normal case. The results indicate that while the diastolic motion (the myocardium displacements between the beginning of diastole and the end of diastole) does not constrain the mechanical parameters uniquely, it does provide a potentially robust indicator of myocardial stiffness. The work presented in this chapter has been published in Xi et al. 2011b.

5.1 Introduction

Myocardial stiffness substantially influences cardiac function, as evidenced by the changes in material properties often being associated with disease processes such as myocardial infarction and diastolic heart failure (Abraham et al. 2006, Wang and Nagueh 2009). The quantification of this myocardial stiffness can be provided by patient-specific mechanical parameters, which are also crucial for the in-silico research on underlying mechanisms of heart failure using personalised models (Niederer et al. 2010). Thus there has been a significant interest in being able to perform *in vivo* parameter estimation through the coupling of biophysically based cardiac models with clinical measurements of the cardiac function (Sermesant et al. 2006, Wang et al. 2010a,Wang et al. 2010b). Previously, Wang et al. (2009) have described a work flow involving interactive actions to estimate mechanical parameters from detailed high-resolution MRI data acquired from a canine heart. However, there is currently still a lack of an automatic pipeline to assimilate clinically available data to identify human myocardial mechanical parameters.

In this chapter, we present such an automatic framework, reporting parameter values obtained for one healthy and two heart failure cases. With these results we analyse the properties of strain energy function whose parameters are estimated in this work and conclude with a proposal for an index of myocardial stiffness.

5.2 Material and methods

The mechanical parameters are identified by comparing a simulated diastolic inflation to observed heart deformation. Passive filling of the human left ventricle (LV) is simulated with patient-specific finite element geometry and boundary conditions extracted from MRI and with the loading condition determined from LV cavity pressure recordings. The geometry and displacement boundary conditions are obtained with an automatic dynamic

meshing process that captures both the LV anatomy and tracked deformations from MRI data. Figure 5.1 schematically illustrates this complete process, where the numbered labels correspond to the subsequent sections in this chapter.

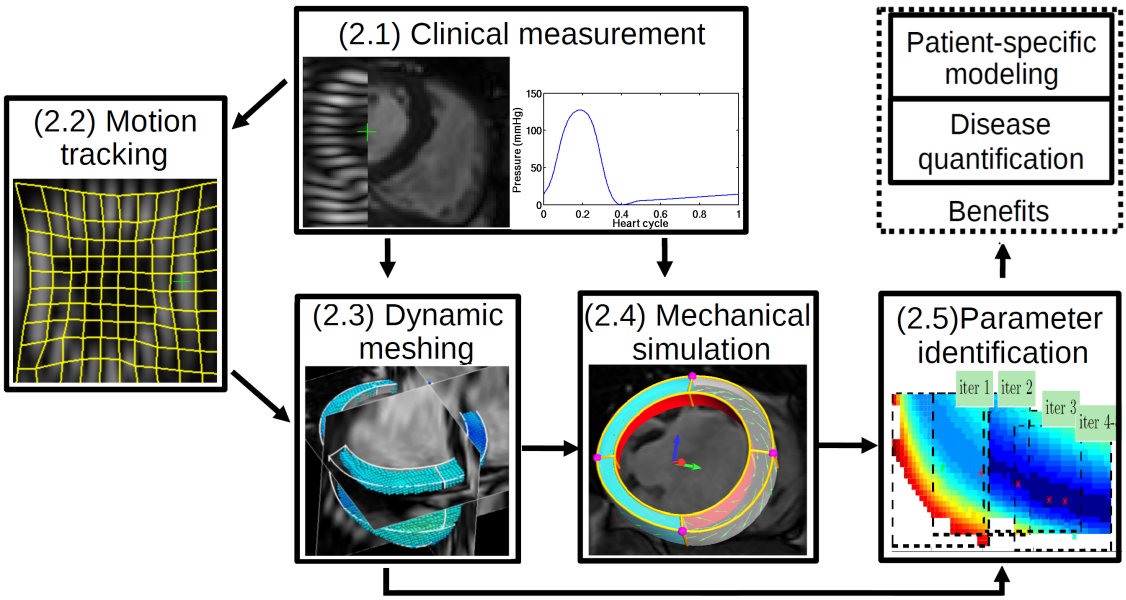

Figure 5.1: Workflow of proposed data assimilation framework for patient-specific parameter estimation. The text labels correspond to the section number in this chapter.

5.2.1 Clinical measurements

The data used in this study were acquired from two patients selected for Cardiac Resynchronisation Therapy (CRT) in St Thomas' Hospital, London and one healthy subject for control. This study conforms to the principles outlined in the Declaration of Helsinki and was carried out as part of a local ethics committee-approved protocol with informed consent obtained from the patient. Cardiac deformation is characterised by spatially aligned cine MRI (29 frames per heart cycle, short-axis view, voxel size $1.3 \times 1.3 \times 10$ mm) and 3D tagged MRI (23 frames per heart cycle, voxel size $0.96 \times 0.96 \times 0.96$ mm, tagging line width ~ 5 voxels). The LV cavity pressure transient is obtained from the cardiac catheterisation procedure (separately from the MR scan), when the rate of change of LV pressure is measured.

Patient case 1 is a 74-year-old female with NYHA Class II heart failure despite optimal medical treatment. There was significant LV systolic dysfunction with an LV ejection fraction of 16% and QRS duration of 168 ms. The LV is significantly dilated with an end systolic volume (ESV) of 335 ml. Figure 5.2 summarises this data set. Patient case 2, a 78-year-old male, has the same disease classification as case 1, with ejection fraction of 17% and an ESV of 186 ml. The control case used in this chapter is a healthy 36-year-old male. The diastolic cavity pressure for the healthy case is taken by digitising the data of a typical pressure profile (Klabunde 2005, Chapter 4, page 62). End diastolic pressure is 1.47 kPa for the control case, while case 1 and 2 are 1.93 and 1.69 kPa respectively.

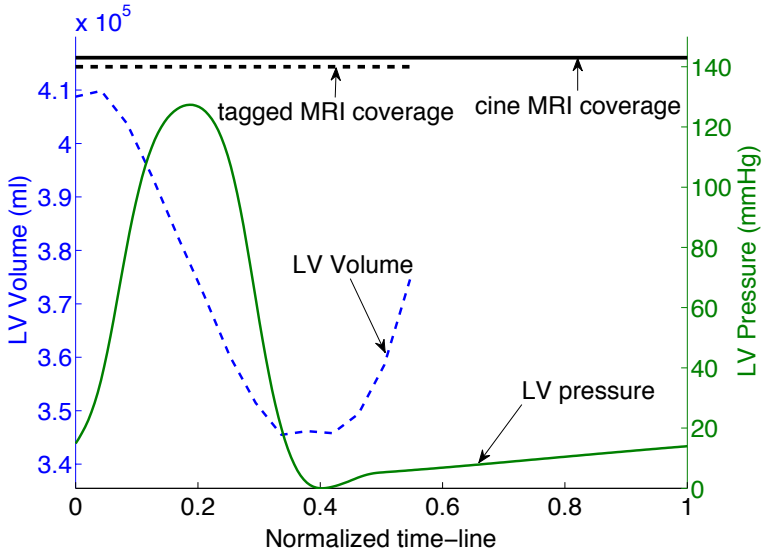

Figure 5.2: The coverage of cine and tagged MRI, pressure transient, and derived volume transient for patient case 1. The x-axis is the normalised heart cycle (R-R interval). The top horizontal line shows the coverage of the 29 frames of cine MRI and the 23 frames of tagged MRI. The beginning of diastole is at the frame 18 of the tagged MRI sequence, and thus 5 frames at early diastole are available while the frame of end-diastole is assumed to be synchronous to the R wave. The volume transient is calculated as the LV cavity volume of the fitted FM meshes (described in section 5.2.3). The pressure transient is the averaged value recorded over multiple heart cycles.

5.2.2 Myocardial motion tracking

Central information for the guidance of mechanical parameter estimation are the 3-dimensional displacements of N tracked myocardial points, or a time series of the Lagrangian displacement vectors from frame j to frame i $\{_j\boldsymbol{Z}_i \in \mathbb{R}^{3N} \quad | \quad i = 1, 2...T\}$ where T is the number of MRI frames. The automatic extraction of these displacements from the combined short-axis cine and 3D tagged MRI is performed with the Image Registration Toolkit[1], which uses a non-rigid registration method based on free-form deformations developed by Rueckert et al. (1999) and extended to the cardiac MRI motion tracking by Chandrashekara et al. (2004). Temporal alignment is achieved by interpolating cine MRI at the time points of tagged MRI. The spatial alignment of cine and tagged MRI is done by rigid registration between cine MRI and detagged tagged MRI, and the tagging line is removed in Fourier space. The aligned short-axis cine and tagged MRI provides information of the ventricular radial movement while the long-axis tagged MRI is for the apex-to-base movement. This complete process of motion tracking using combined information from cine and tagged MRI is detailed by Shi et al. (2012), which shows the relative registration error compared to manually tracked landmarks is less than 15% of the cardiac displacement throughout the cardiac cycle.

5.2.3 Dynamic mesh personalisation

Geometric model construction

As shown in figure 5.3, based on clinical segmentation of the end-diastolic (ED) frame of cine MRI, the LV mechanical mesh at ED is built with cubic-Hermite (CH) elements using methods developed by Lamata et al. (2011). This CH mesh, with nodal positions and derivatives as degrees of freedom (DOF), provides a C^1-continuous representation of the

[1]IRTK, http://www.doc.ic.ac.uk/ dr/software/

geometry. The fibre field, representing the preferred orientation of tissue microstructure within the LV, is embedded in the geometric model with transmural heterogeneity ($\pm 60^o$ as shown in figure 5.3), based on the data of Usyk et al. (2000). The fibre field values are stored as angles of fibre at each node and interpolated within the material space of the finite element mesh using tri-linear basis functions.

Geometric model propagation

Given the constructed geometrical model at end-diastole and the 4D myocardial displacement field from section 5.2.2, a simple technique is employed to propagate this geometrical model to the time points of the displacement field. Specifically, given an initial mesh fitted to the anatomical data at a time point $\boldsymbol{U}_j$ (in our specific case this is at ED) and a time-series of N ($\sim$6000, regular grid points inside the LV myocardium) material points' displacement ${}_j\boldsymbol{Z}_i \in \mathbb{R}^{3N}$ (with the size of $\sim$ 18000) from time point j to i, we find, for each of the time points i (i=1,2...,T), the nodal positions and derivatives $\boldsymbol{U}_i$ (or DOF vector, with the size of $\sim$1872) that define a M-node cubic-Hermite mesh. This mesh is found by minimising the error in the mesh approximation to the observed positions of data points, which is a standard linear least-squared minimisation problem.

This mesh approximation error e_i is defined as the L_2 norm of the residual vector–the difference between the observed positions of material points

$$\boldsymbol{z}_i = \boldsymbol{H}_{\boldsymbol{\xi}}\boldsymbol{U}_j + {}_j\boldsymbol{Z}_i \tag{5.1}$$

and the embedded positions in the fitted mesh

$$\boldsymbol{y}_i = \boldsymbol{H}_{\boldsymbol{\xi}}\boldsymbol{U}_i, \tag{5.2}$$

i.e.,

$$e_i = \|\boldsymbol{z}_i - \boldsymbol{y}_i\|_{\mathbb{L}^2} = \|\boldsymbol{H}_{\boldsymbol{\xi}}\boldsymbol{U}_j + {}_j\boldsymbol{Z}_i - \boldsymbol{H}_{\boldsymbol{\xi}}\boldsymbol{U}_i\|_{\mathbb{L}^2}\,, \tag{5.3}$$

where $\boldsymbol{H_\xi} \in \mathbb{M}^{3N\times 8M}$ is the shape matrix related to the CH basis functions (Smith et al. 2004), and $\boldsymbol{H_\xi U}_i$ is spatial coordinates of the local ξ-coordinates embedded in the mesh $\boldsymbol{U}_i$. Solving the standard linear weighted least-square minimisation problem described in equation 5.3, we obtain the DOF vectors of new meshes $\{\boldsymbol{U}_i\}$ given by

$$\boldsymbol{U}_i = (\boldsymbol{H_\xi}^T \boldsymbol{H_\xi})^{-1} \boldsymbol{H_\xi}^T (\boldsymbol{H_\xi U}_j + {}_j\boldsymbol{Z}_i). \tag{5.4}$$

5.2.4 Mechanical simulation

Using the geometric meshes developed in section 5.2.3, we simulate the passive diastolic filling phase of the cardiac cycle, by inflating the early-diastolic LV model to an end-diastolic LV cavity pressure (table 5.1, column 2). Deformation is simulated using the standard finite deformation theory, where the finite element method (FEM) is utilised to solve a stress equilibrium governing equation, which is derived from the laws of conservation of mass and momentum, and the principle of virtual work (Nordsletten et al. 2010).

Boundary Conditions

The model developed in this chapter only represents the LV, and does not include representations of the right ventricle (RV), great vessels, pericardium and organs around the heart. Thus the effects of these structures on the LV mechanics are not explicitly modelled. To account for these physical constraints on the heart, we prescribe the kinematic movement of the LV model at its base plane and apex node (figure 5.3) to match the displacements extracted from the tagged MRI.

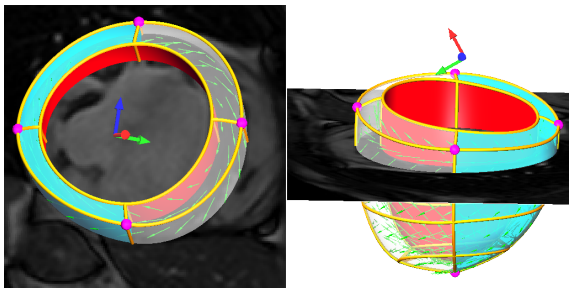

Figure 5.3: Geometric model with fibre vectors embedded. Kinematic boundary conditions (displacement and its derivatives) are prescribed on the purple nodal points (four at the base plane and one in the apex). The movements of the free wall region (transparent green area) are compared with the measurements in the parameter fitting process.

Passive constitutive parameters of the myocardium

The myocardium is modeled as a transversely isotropic hyperelastic material. The constitutive equations are defined by a well-known strain-energy function (Guccione et al. 1991), given by

$$W = C_1(e^Q - 1), \text{ and } Q = C_2E_{\text{ff}}^2 + C_3(E_{\text{ss}}^2 + E_{\text{nn}}^2 + 2E_{\text{sn}}^2) + C_4(2E_{\text{fs}}^2 + 2E_{\text{fn}}^2), \quad (5.5)$$

where C_1, C_2, C_3 and C_4 are the constitutive parameters, E_{ff}, E_{ss} and E_{nn} are the Green-Lagrange strains in in fibre (f), sheet (s) and sheet normal (n) directions, and E_{sn}, E_{fn} and E_{fs} are the Green-Lagrange shear strains in the fs, fn and fs planes. The f, s and n directions correspond to the fibre axes aligned with the microstructure of the myocardium, shown in figure 5.3.

5.2.5 Identification of myocardial passive constitutive parameters

The mechanical simulation is performed by inflating the early-diastolic LV model to an end-diastolic LV cavity pressure (table 5.1, column 2), with kinematic boundary constraints (section 6.2.1). The simulated result is then compared with the corresponding mesh fitted in section 5.2.3, and the constitutive parameters are tuned to minimise an objective function based on the shape differences, defined by integrating the distance between equivalent material points in the two meshes over the myocardial free wall volume

(see figure 5.3 for visualisation of free wall volume). In order to reduce the influence of the RV and its unknown cavity pressure, the difference to minimise is only defined in those elements belonging to the LV free wall region.

To solve this optimisation problem, we first re parameterise the constitutive parameters

$$C_1 = C_1,\ C_2 = \alpha r_2,\ C_3 = \alpha r_3,\ C_4 = \alpha r_4,\ r_2 + r_3 + r_4 = 1, \tag{5.6}$$

where α and r_2-r_4 are the scale factors and anisotropies of C_2-C_4 respectively. The reason for this is that we identified that the difficulty with the Guccione formulation in the context of parameter estimation is that multiple parameter sets are able to reproduce similar end-diastolic deformation states. The reparameterization is able to clarify the parameter coupling issue. We design a two-step optimisation procedure in which C_1 and α are first optimised, followed by optimising r_2 and r_3. This two-step process is iterated until the estimated parameters are converged. In each step, the optimisation is solved using 2-D exhaustive searching, chosen in order to explore the landscape of objective function and to avoid convergence within local minima.

5.3 Results

The proposed automatic data assimilation framework was applied to two CRT patient data sets and one healthy control case. For each case, the processing time is approximately 40 minutes for the motion tracking, 1 minute for the dynamic meshing, and 30 minutes for the mechanical property estimation[2].

[2]We used a highly optimised cubic-Hermite elements based mechanical simulation code (Land et al. 2011), running on a standard desktop computer (4 2.5GHz cores and 4GB RAM). For non-optimised implementations, the mechanical property estimation can take up to 12 hours.

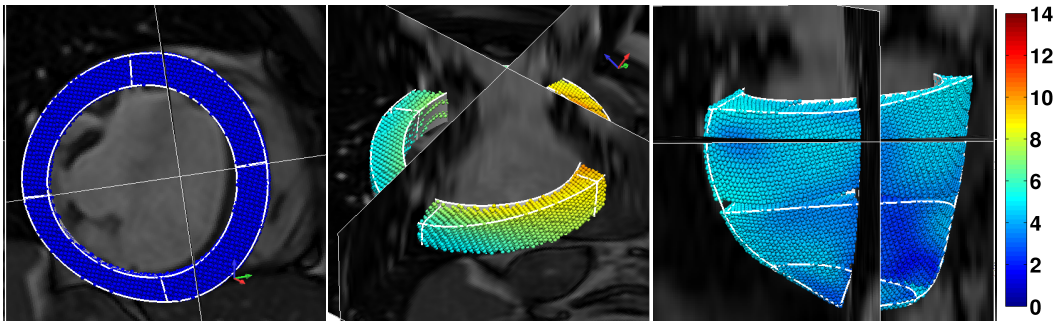

Figure 5.4: Results of dynamic meshing stage in figure 5.1 (healthy case, visualised with the cine MRI from different views, corresponding to frame 1, 9 and 17). The whole-heart-cycle dynamic meshes are automatically reconstructed from the displacements of data points (embedded in the mesh) extracted from the tagged MRI. The colour represents the magnitude of displacement referencing to the end-diastole in mm.

5.3.1 Dynamic meshing

Figure 5.4 shows the C^1-continuous CH geometrical meshes for patient case 16, which are automatically constructed over a heart cycle following the methods outlined in section 2.3. The residual of this fit (i.e., components of the fitting residual vector $\boldsymbol{Z}_k - \boldsymbol{H}(\boldsymbol{\Xi})\boldsymbol{U}_k$), see equation 5.3) has a zero mean, standard deviation of 0.28-0.53 mm, and in general no obvious spatial correlations. As a result of this process, the displacements of discrete data points, which are extracted from the MRI data, are now smoothed and regularised into the local material coordinates (model space).

5.3.2 Mechanical property estimation

Following the methods described in section 5.2.5, table 5.1 shows the mechanical parameter estimation results (parameters C_1 to C_4 and its fitting residual), with comparison to the values reported in literature. Figure 5.5(a) further plots the landscape of fitting residual with respect to $log(C_1)$-$log(\alpha)$ for case 16, gathered in the last iteration of the two-step optimisation procedure. We fitted the iso-curves (coupling relationships between C_1

Table 5.1: Estimated constitutive parameters for one healthy case and two patient cases, and comparison to three studies in literature. Initial parameter values are $C_1 = 0.4, C_2 = 9.2, C_3 = 2.0, C_4 = 3.7$, taken from Niederer et al. 2010.

-	EDP(kPa)	ESV(ml)	EF	C_1	C_2	C_3	C_4	R[1]
healthy case	1.81 [2]	67	51%	0.15	41.71	9.07	51.52	2.76
case 16	1.93	345	16%	3.40	9.22	2.05	17.92	1.73
case 28	1.69	186	17%	1.40	34.21	5.86	66.39	2.36
Wang et al. 2009, dog	0.5	-	-	0.831	14.3	4.49	0.762	1.81
Augenstein et al. 2005, dog	-	-	-	1.5[3]	11.1	1.76	10.0	-
Omens et al. 1993, rat	-	-	-	1.2	26.7	2.0	14.7	-

EDP, end-diastolic LV cavity pressure; ESV: end-systolic LV cavity volume; EF, ejection fraction.
[1] Residual (mm) – the root-mean-squared-error (RMSE) between simulated and fitted mesh at end-diastole over free wall. [2] Average EDP of cases 16 and 18. [3] $C_1 = 3.0$ in this study is defined with a multiplier of $\frac{1}{2}$.

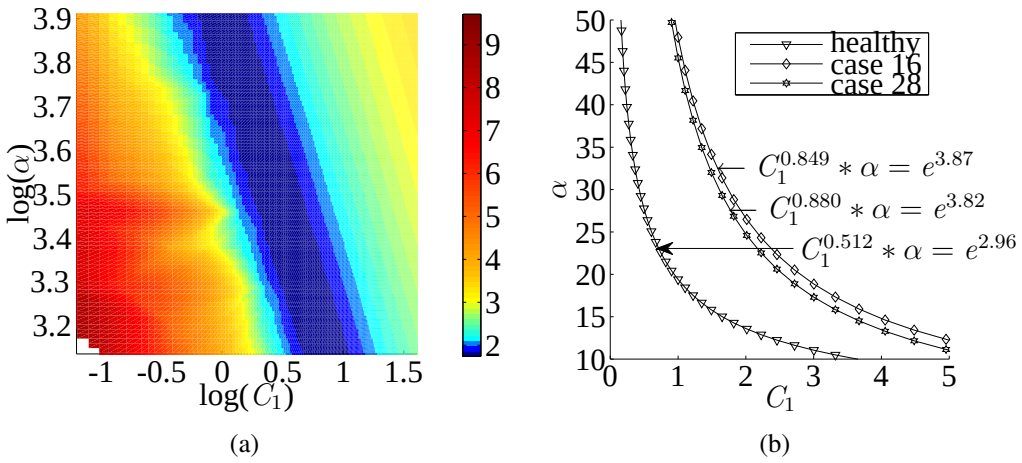

(a) (b)

Figure 5.5: (a) The landscape of fitting residual with respect to C_1-α for case 16, showing coupling of C-α (dark blue valley). The colour represents the fitting residual in mm. (b) The three fitted iso-curves ($C_1^a\alpha = b$), showing the coupling relationships between C-α for cases listed in table 5.1. These curves can be easy-to-estimate indicators of myocardial stiffness for differentiating normal and heart failure patient cases (see text for more discussion).

and α) with the form of $C_1^a\alpha = b$ (a, b are constants) to the minimum valley in figure 5.5(b). This coupling relationship can also be derived from the stress-strain relationship for Guccione's law. The exponential coefficient a is proportional to the magnitude of deformation, and the value of b could provide an easy-to-estimate metric to quantify myocardial stiffness (discussed in next section).

5.4 Discussion and Summary

In this chapter, we have described, to our knowledge, the first automatic pipeline to assimilate clinical measurements into the mechanical modelling framework in order to estimate myocardial constitutive parameters. This fast pipeline enables us to explore the value and associated issues of patient-specific in-vivo parameter estimation.

The proposed framework converts the displacements extracted from the tagged MRI registration into model space, in which the analysis of strain and stress can be performed in local material coordinates using standard finite element (FE) theory. The representation of this deformation in model space also provides patient-specific kinematic boundary conditions and makes the comparison to FE model simulations straightforward.

The results in table 5.1 indicate a wide range of mechanical parameter values estimated from in-vivo observations. The reason for this is likely to be the coupling between C_1 and α, which produces the valley in the landscape of objective function shown in figure 5.5(a). Previous studies (Wang et al. 2009, Omens et al. 1993) optimised C_1-C_4 sequentially. In these cases, the two-way coupling between C_1 and C_2-C_4 is unnoticed. However, those final parameter values may well be dependent on the initial values. Nevertheless, despite this C_1-α coupling, the comparison between healthy ($a = 0.512$, $b = 19.3$) and diseased cases ($a = 0.880$, $b = 53.6$ and $a = 0.849$, $b = 48.0$) in figure 5.5(b) indicates that $C_1^a \alpha = b$ could be a potentially reliable and easy-to-estimate indicator of the myocardial stiffness.

There are a number of limitations in the study presented in this chapter. In particular, we did not consider the residual active tension in the early-diastolic geometry, which would render the estimated stiffness lower than reality. Furthermore, the fibre distribution of our LV model does not incorporate directly the patient-specific measurements, and this may influence the estimation of material anisotropies.

From these results, we conclude that one end-diastolic measurement does not constrain the mechanical parameters uniquely, but it does already provide an easy-to-estimate indicator of myocardial stiffness. In order to obtain the complete set of unique parameter values, more constraints need to be added to the optimisation criteria. Additional measurements points during diastolic filling can potentially provide the necessary constraints. However, accurate time registration between imaging data sets and pressure recordings is required for this. In the future, we plan to acquire additional clinical data sets with optimised protocols (e.g., synchronised pressure, ECG and MR recordings, ideally with the diffusion-tensor imaging for the patient-specific fibre distribution), in order to further investigate the identifiability of parameters and to correlate our parameter estimation results with clinical diagnosis.

Appendices

5.A Constitutive parameter coupling

5.A.1 Derivations of the C_1-α coupling

The Guccione parameters are identified by matching the simulated deformed meshes to the fitted mesh's from the MRI frames. However, from the current clinical data, the Guccione parameters can not be reliably identified using only the ED frame in the sense that an increase of C_1 can be compensated for by a decrease of C_2-C_4 or α.

To explicitly reveal this problem, our goal is to find the coupling direction $\boldsymbol{d}$ in C_1-α space (if any) along which two sets of different parameters would render the same (or very similar) mechanical simulation. In the following analysis, the hydrostatic tensor term can be safely eliminated. From the numerical solution perspective, given the same external loading conditions (external forces) and temporary trial solution of a strain tensor (displacement DOF), the whole stress tensor (deviatoric plus hydrostatic) should be always the same as long as the deviatoric stress tensors are the same. This is because the solver for the hydrostatic term is only concerned with the strain and residual stress, not the material parameters.

For notations, $\boldsymbol{T}$ is the deviatoric second Piola-Kirchhoff stress tensors. $\boldsymbol{E}$ is the Green-Lagrangian strain tensor.

$$\boldsymbol{T} = \frac{\partial W}{\partial \boldsymbol{E}} = 2C_1 e^Q \begin{pmatrix} C_2 & C_4 & C_4 \\ C_4 & C_3 & C_3 \\ C_4 & C_3 & C_3 \end{pmatrix} \cdot \boldsymbol{E}. \tag{5.7}$$

The material elastic tensor $\boldsymbol{K}$ for Guccione's constitutive law is defined as:

$$\boldsymbol{K} = 2C_1 e^Q \begin{pmatrix} C_2 & C_4 & C_4 \\ C_4 & C_3 & C_3 \\ C_4 & C_3 & C_3 \end{pmatrix} = 2C_1 \alpha e^Q \begin{pmatrix} r_2 & r_4 & r_4 \\ r_4 & r_3 & r_3 \\ r_4 & r_3 & r_3 \end{pmatrix} \tag{5.8}$$

The coupling direction $\boldsymbol{d}$ in C_1-α space (if it exists) is defined where the directional gradient of $\boldsymbol{K}$ along d is a zero-tensor. Intuitively the material response (stress-strain

relationship) is the same along this (local) direction.

$$\begin{pmatrix} \frac{\partial \boldsymbol{K}_i}{\partial C_1} \\ \frac{\partial \boldsymbol{K}_i}{\partial \alpha} \end{pmatrix} \cdot \boldsymbol{d} = 0, \ i = 1, ..., 9. \tag{5.9}$$

These nine conditions from the above equations are combined to be one constraint independent of r_2-r_4:

$$\begin{pmatrix} \alpha e^Q \\ C_1 e^Q + C_1 \alpha \frac{\partial e^Q}{\partial \alpha} \end{pmatrix} \cdot \boldsymbol{d} = e^Q \begin{pmatrix} \alpha \\ C_1(1 + \alpha \frac{\partial Q}{\partial \alpha}) \end{pmatrix} \cdot \boldsymbol{d} = 0. \tag{5.10}$$

The existence of the coupling direction

The coupling direction $\boldsymbol{d}$ exists if and only if equation 5.10 has a solution. The term $\frac{\partial Q}{\partial \alpha}$ in equation 5.10 can be further expanded by using equations 6.4 and 6.9, i.e.

$$\frac{\partial Q}{\partial \alpha} = \frac{\partial \left(\sum_{i,j} \alpha r_{ij} E_{ij}^2 \right)}{\partial \alpha} \tag{5.11}$$

$$= \frac{Q}{\alpha} + \sum_{i,j=1} \alpha (2 r_{ij} E_{ij} \frac{\partial E_{ij}}{\partial \alpha}), \quad i, j = 1, 2, 3, \tag{5.12}$$

where r_{ij} denotes the corresponding elements of rightmost matrix in equation 5.8, and E_{ij} are the Green-Lagrange strains in fibre (f:=1), sheet (s:=2) and sheet normal (n:=3) directions. The second term $\frac{\partial E_{ij}}{\partial \alpha}$ is varying at different (C_1,α) points, and thus dependent on the coupling direction $\boldsymbol{d}$ which we are solving for. Therefore equation 5.10 is nonlinear.

The solution of a nonlinear equation does not necessarily exist. Thus the "zero-coupling direction" (the direction along which the deformation is exactly the same) may not exist. However, as evidenced by figure 5.6 and reported by Xi et al. (2011a), there does exist a "principle-coupling direction"–the direction along which the change is very close to zero and significantly smaller than other directions.

The approximated exponential coupling curve

If we ignore the second nonlinear term in $\frac{\partial Q}{\partial \alpha}$, that is,

$$\frac{\partial Q}{\partial \alpha} \approx \frac{Q}{\alpha}, \tag{5.13}$$

equation 5.10 can be simplified as

$$e^{Q} \begin{pmatrix} \alpha \\ C_1(1+Q) \end{pmatrix} \cdot \boldsymbol{d} = 0. \tag{5.14}$$

Therefore the coupling curve in (C_1, α) space roughly has the tangent direction $\boldsymbol{d} = (\frac{C_1}{\alpha} \quad -\frac{1}{1+Q})^T$, which indicates the curve is

$$C_1^{\frac{1}{1+Q}} \alpha = b, \tag{5.15}$$

where b is a constant.

Note that we ignored the second nonlinear term in equation 5.12 and use the assumption that the slope of the curve $\frac{1}{1+Q}$ is constant when we derive the approximated yet simple curve expression (equation 5.15). While these are mathematical approximations, in practice it already provides a good agreement with the coupling curves fitted numerically (see figure 5.6).

5.A.2 The landscape of minimisation objective function

The landscape of objective function using only the ED measurement (i.e., the equation 6.15 when $i = n$) with respect C_1-α and $r_3 - r_4$ are shown in figure 5.6 and figure 5.7 respectively. These landscape empirically demonstrated that, from the parameter estimation point of view, C_1 and α are coupled while r_3 and r_4 are relatively uncoupled.

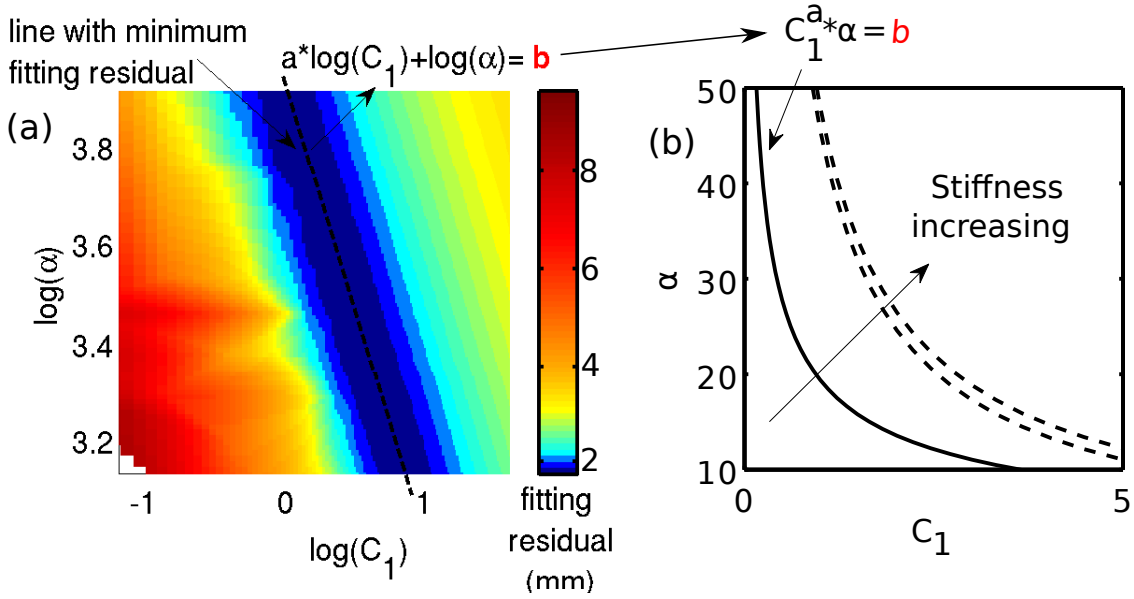

Figure 5.6: Parameter optimization and C_1-α curve fitting. (a) The landscape of objective function (equation 6.15, using only end diastolic tagged MRI frame) with respect to C_1-α for case 1. This landscape is obtained from our two-step optimization process. The colour represents the magnitude of the objective function in mm. The dark blue valley indicates a straight line with equal optimal parameter fits. (b) A linear line in the log-scale space with the form of a*log(C_1)+log(α)=b is fitted to optimal fitting valley in (a). This line in the log-space corresponds to the curve of $C_1^a\alpha = b$ in (b).

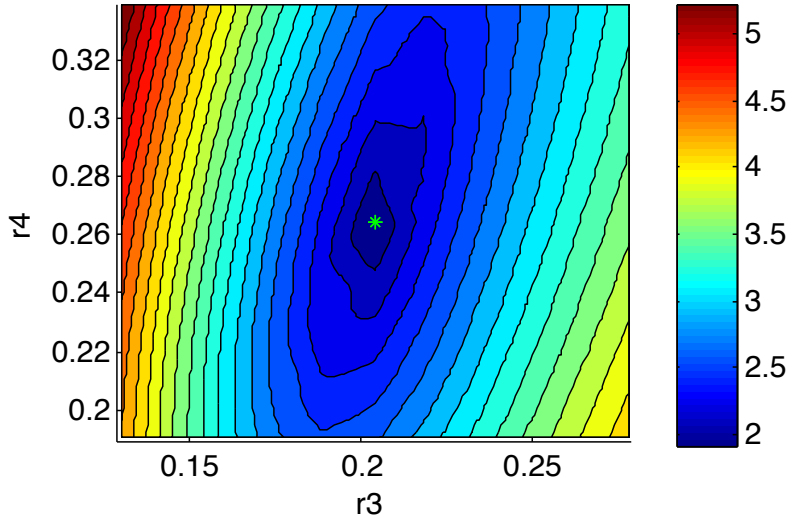

Figure 5.7: Objective function plot with respect to r_3 and r_4 for patient case 1. The colour represents the magnitude of objective function in mm. The correlation between r_3 and r_4 is 0.53. Unlike the strong C_1-α coupling, the optimization problem in r_3-r_4 space is better posed.

Chapter 6

Diastolic residual active tension estimation from clinical data

An unresolved issue in patients with diastolic dysfunction is that the estimation of myocardial stiffness cannot be decoupled from diastolic residual active tension (AT) because of the impaired ventricular relaxation during diastole. To address this problem, this chapter presents a method for estimating diastolic mechanical parameters of the left ventricle (LV) from cine and tagged MRI measurements and LV cavity pressure recordings, separating the passive myocardial constitutive properties and diastolic residual AT. Dynamic C_1-continuous meshes are automatically built from the anatomy and deformation captured from dynamic MRI sequences. Diastolic deformation is simulated using a mechanical model that combines passive and active material properties. The problem of non-uniqueness of constitutive parameter estimation using the well known Guccione law is characterised by reformulation of this law. Using this reformulated form, and by constraining the constitutive parameters to be constant across time points during diastole, we separate the effects of passive constitutive properties and the residual AT during diastolic relaxation. Finally, the method is applied to two clinical cases and one control, demonstrating that increased residual AT during diastole provides a potential novel index for delineating healthy and pathological cases. The work presented in this chapter has been published in Xi et al. 2012a.

6.1 Introduction

The quantification of diastolic dysfunction is vital for the diagnosis and assessment of heart disease, enabling improved selection and treatment of individuals with pathological myocardial mechanics for further therapy (Nagel and Schuster 2010). Patient-specific cardiac models, parameterised from clinical measurements on an individual basis, provide a powerful approach for this purpose (Smith et al. 2011). Accordingly, model-based parameter estimation from clinical measurements of cardiac function has been an active research area.

Parameters in organ-level cardiac mechanical models can be broadly classified as passive and active. Typically within computational models, passive constitutive parameters have been used to characterise the diastolic function, and with the addition of active contraction models simulate systole (Nash and Hunter 2000, Nordsletten et al. 2011). Various frameworks and methods have been proposed to estimate these parameters (Sermesant et al. 2006, Sermesant et al. 2011, Marchesseau et al. 2013a, Marchesseau et al. 2013b, Marchesseau et al. 2012, Chabiniok et al. 2011, Delingette et al. 2012, Moireau and Chapelle 2011, Wang et al. 2009, Wang et al. 2010b). In Sermesant et al. (2006), a variational data assimilation method was developed to estimate the contractility parameters of an electromechanical model from clinical cine MRI. Focusing on passive parameters, Wang et al. (2009) have described a workflow to estimate the Guccione constitutive parameters using high-resolution MRI data acquired from a canine heart. An approach which these authors further extended in Wang et al. 2010b to estimate the active tension (AT) during the isovolumetric contraction, systole and isovolumetric relaxation using the constitutive parameters pre-estimated during diastole.

However, an unsolved problem in patients with diastolic dysfunction is that the estimation of myocardial stiffness cannot be decoupled from impaired ventricular relaxation (one

of the lusitropic abnormalities commonly present in heart failure, Katz 2010). For this reason, the development of methods which can robustly estimate both the stiffness and residual AT during diastole would have significant potential for application within clinical cardiology.

The focus of this chapter is to address this issue directly through the inclusion and estimation of an AT term during diastole. Specifically, built upon the parameter estimation framework for passive constitutive properties in our previous work (Xi et al. 2011b), we propose an approach to further estimate the residual AT during diastole to directly characterise the delayed relaxation often present in heart failure patients. We first undertake the necessary step for our estimation problem of reformulating the constitutive law to reveal and address the issue of the non-uniqueness of material parameters. Using this reformulated form, we then introduce an AT term in our mechanical model and estimate the residual AT in early diastole. Finally we apply this methodology to clinical cases with pressure, cine and tagged MRI measurements, with the results showing that estimated myocardial stiffness and residual AT appear to be promising candidates to delineate healthy and pathological patient cases.

6.2 Material and methods

The parameter estimation framework, schematically illustrated in figure 5.1 in previous chapter, for estimating the passive constitutive properties in our previous work (Xi et al. 2011b) is extended. As outlined in the previous chapter and briefly reminded here, the mechanical parameters are identified by comparing simulated diastolic inflation to a set of observed deformations extracted from dynamic 3D tagged MRI. Specifically, passive filling of the human left ventricle (LV) is simulated with a patient-specific finite element geometry and displacement boundary conditions and with the loading condition determined from LV cavity pressure recordings. The geometry and displacement boundary

conditions are obtained with an automatic dynamic meshing process, which captures the LV anatomy using one frame of cine MRI, and extract the deformation fields using combined cine and tagged MRI data.

The methods of clinical measurements acquisition, myocardial motion tracking and dynamic mesh personalisation remain unchanged from the previous chapter, and thus the description of those components is omitted here. In the following sections, we focus on the extension of our methods in two aspects. Firstly, the mechanical model is extended with an addition of AT component. The motivation for considering AT apart from the passive materials is explained. Secondly, we present a comprehensive method for estimating not only the passive materials, but also the reference (or stress-free) state, which enables us to gain a better quantitative understanding of patient-specific diastolic heart functions.

6.2.1 LV Mechanical model

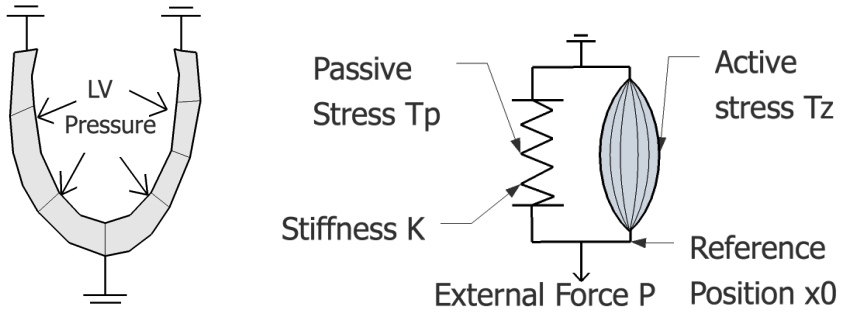

(a) LV model (b) Schematic 1D spring model

Figure 6.1: Schematic illustration of LV mechanical model. As illustrated by the schematic 1D spring model in subplot (b), the deformation of the spring (analogous to the deformation of LV myocardium in subplot (a)) is driven by two factors–the external force (analogous to the LV cavity pressure) and the active stress (analogous to the active tension developed by the contraction of the myocardial fibre).

The passive diastolic filling phase of the cardiac cycle is simulated by inflating the unloaded LV model up to cavity pressures corresponding to each frame of tagged MRI, as

schematically illustrated by figure 6.1a. Deformation is then simulated using the standard finite deformation theory. The finite element method (FEM) is utilised to solve the stress equilibrium governing equation, with the measured LV cavity pressure being applied as the loading condition on the endocardium (Nash and Hunter 2000, Nordsletten et al. 2011). The stress equilibrium governing equation is derived from the laws of conservation of mass and momentum, and the principle of virtual work. As demonstrated in appendix 6.B.1, our preliminary results necessitate an active tension term to be included in our mechanical model, to account for the residual tension generated by the contraction of myofibres. This active component is illustrated schematically by figure 6.1(b), in which the 1D spring is not only stretched by the external force P, but also contracted by the active component parallel to the spring. The deformation of the spring, for this simple 1D case, is analogous to the deformation of the LV myocardium.

Our LV mechanical model, denoted by an operator $\mathbb{M}$, determines the deformed position $\boldsymbol{x}_i$ of material points whose initial positions at unloaded state are $\boldsymbol{x}_0$. In addition to the unloaded state, the model operator also takes as its inputs $\boldsymbol{C} \in \mathbb{R}^4$ (constitutive parameters characterising the stiffness of myocardium), P_i (LV cavity pressure at time point i), $T_z(i)$ (residual AT), $\boldsymbol{y}_i^B$ (displacement boundary conditions based on the observed displacements $\boldsymbol{y}_i$). That is,

$$\boldsymbol{x}_i = \mathbb{M}(\boldsymbol{x}_0, \boldsymbol{C}, P_i, T_z(i), \boldsymbol{y}_i^B). \tag{6.1}$$

Each of these inputs are further explained in the following subsections. The backward mechanical model (or deflation model), denoted by the inverse operator $\mathbb{M}^{-1}$, takes the deformed position $\boldsymbol{x}_i$ as its input and retrieves the unloaded initial position $\boldsymbol{x}_0$ (Rajagopal et al. 2008).

$$\boldsymbol{x}_0 = \mathbb{M}^{-1}(\boldsymbol{x}_i, \boldsymbol{C}, P_i, T_z(i), \boldsymbol{y}_i^B). \tag{6.2}$$

Constitutive parameters of the myocardium

Consistent with existing literature and based on the experimental results of uniaxial and biaxial tests in isolated cardiac muscle (Fung 1981,Yin et al. 1987), the myocardium in this chapter is modeled as a transversely isotropic material with preferred directions that vary transmurally. We chose the widely employed 4-parameter Guccione law (Guccione et al. 1991) to balance the feasibility of estimating parameters with the ability to accurately account for the nonlinear mechanical properties that result from the myocardial laminar structure. The Guccione strain-energy function W is defined as

$$W = \underline{C_1}(e^Q - 1), \tag{6.3}$$

$$Q = \underline{C_2}E_{\text{ff}}^2 + \underline{C_3}(E_{\text{ss}}^2 + E_{\text{nn}}^2 + 2E_{\text{sn}}^2) + \underline{C_4}(2E_{\text{fs}}^2 + 2E_{\text{fn}}^2), \tag{6.4}$$

where C_1, C_2, C_3 and C_4 are the constitutive parameters to be estimated, E_{ff}, E_{ss} and E_{nn} are the Green-Lagrange strains in fibre (f), sheet (s) and sheet normal (n) directions, and E_{sn}, E_{fn} and E_{fs} are the Green-Lagrange shear strains in the fs, fn and fs planes. The f, s and n directions correspond to the fibre axes aligned with the microstructure of the myocardium.

Reformulation of the Guccione law

As outlined in the introduction, in our previous study (Xi et al. 2011b), we identified that the difficulty with the Guccione formulation in the context of parameter estimation is that multiple parameter sets are able to reproduce similar end-diastolic deformation states. To clarify this issue further, we can reformulate the constitutive parameters by introducing α and r_2-r_4 as

$$\underline{C_1} = C_1, \tag{6.5}$$

$$\underline{\alpha} = C_2 + C_3 + C_4, \tag{6.6}$$

$$r_2 = \frac{C_2}{\alpha} = 1 - r_3 - r_4, \tag{6.7}$$

$$\underline{r_3} = \frac{C_3}{\alpha}, \tag{6.8}$$

$$\underline{r_4} = \frac{C_4}{\alpha}, \tag{6.9}$$

where α and r_2-r_4 (non-negative) are the scale factor and anisotropies of C_2-C_4, respectively. The underlined parameters (C_1, α, r_3 and r_4) on the left side of the above equations are those to be actually estimated in the following section. As we outline below, this reformulation uncouples C_1-C_4 into C_1-α (homogeneous stiffness scale) and r_3-r_4 (anisotropy stiffness ratios), which clearly reveals the parameter correlation of the original Guccione's law in the C_1-α space. The motivation for using this formulated version of the law is that C_1-α assists in the interpretation of parameter estimation results in terms of myocardial homogeneous stiffness, and r_2 indicates the relative stiffness along the myofibre compared to other material directions. This coupling relationship was explained in detail in our previous work (Xi et al. 2011b) and summarised in appendix 5.A.1 of the previous chapter, including the plots of optimization objective function with respect to C_1-α and r_3-r_4.

Active tension model

In literature, the diastolic cardiac mechanics is usually modeled as pure passive inflation (e.g., Wang et al. 2009). That is, the myocardial stress is assumed to be the passive stress, caused by deformation of the elastic (incompressible) myocardial material.

$$\boldsymbol{T} = \frac{\partial W}{\partial \boldsymbol{E}} + p\boldsymbol{C}^{-1}, \tag{6.10}$$

where $\boldsymbol{T}$ is the second Piola-Kirchhoff stress tensors, W is the strain energy function, and $\boldsymbol{E}$ is the Green-Lagrangian strain tensor in the local material directions. $p\boldsymbol{C}^{-1}$ is the hydrostatic stress tensor because of the incompressible nature of the tissue, while $\frac{\partial W}{\partial \boldsymbol{E}}$ is the deviatoric stress tensor due to the distortion of the tissue.

However, in this chapter, we found that the pure passive mechanical model could not fully explain the deformation presented in the early diastole (as demonstrated in appendix 6.B.1). To account for this discrepancy, we introduce a compensatory AT term along the fibre direction to the model.

$$\boldsymbol{T} = \underbrace{\frac{\partial W}{\partial \boldsymbol{E}}}_{\text{deviatoric stress tensor}} + \underbrace{p\boldsymbol{C}^{-1}}_{\text{hydrostatic stress tensor}} + \underbrace{\begin{pmatrix} T_a & 0 & 0 \\ 0 & 0 & 0 \\ 0 & 0 & 0 \end{pmatrix}}_{\text{active stress tensor}}, \tag{6.11}$$

where the length-dependent AT T_a, as explained in the HMT model (Hunter et al. 1998, Nash 1998, Wang et al. 2010b), is defined by

$$T_a = T_{\text{z}}(1 + \beta(\sqrt{2E_{\text{ff}} + 1} - 1)),\ T_{\text{z}} = T_{\text{ref}} \cdot z. \tag{6.12}$$

In the above equation, T_a is the length-dependent AT along fibre direction, T_{ref} is the maximum homogeneous reference tension, $T_{\text{ref}} \cdot z$ is the tension developed at activation level z ($0 \leq z \leq 1$), constant β is the coefficient for the linear length dependence of AT, E_{ff} is the Lagrangian-Green strain along fibre direction, and $\sqrt{2E_{\text{ff}} + 1} - 1$ is the extension ratio.

The activation level z during diastole, which can be obtained from electrical activation models such as monodomain or bidomain models (Smith et al. 2004), is assumed to be spatially homogeneous over the LV. The combined $T_{\text{ref}} \cdot z$ term (renamed as T_z, and referred as the "AT term" or "AT parameter" from now on) is estimated at each time point

of diastolic MR images, using a pre-estimated constant passive material parameter set (explained in detail below). At the end-diastole, the heart is assumed to be completely relaxed (i.e., no residual AT) and thus T_z is zero.

6.2.2 Model parameter estimation

As outlined above, model parameters are estimated by matching the simulated LV deformation with that observed in each of the diastolic MRI frame i during diastole ($i \in [1, n]$ is the diastolic frame number, and n is the total number of diastolic MRI frames). The first diastolic frame ($i = 1$, i.e., the beginning-of-diastole frame) is defined as the minimum pressure frame, while the last diastolic frame ($i = n$, i.e., the end-diastole frame) is defined as the frame synchronous to the R wave. The LV reference state (unloaded state, or stress-free state), defined as the state at which both the cavity pressure and myocardial AT are zero, is unknown. The state measured by the first diastolic frame is unlikely to be the reference state because while the pressure for this frame is assumed to be zero, the AT, particularly in the diseased cases, is likely to exist, and thus the the LV measured by the first diastolic frame is expected to be smaller than its reference state in terms of cavity volume.

Thus the model parameters to be estimated includes constitutive parameters $\tilde{\boldsymbol{C}}$, ATs $\{\tilde{T}_z(i)\}$ ($i = 1, ..., n$ is the diastolic MRI frame number)), as well as the reference state $\tilde{\boldsymbol{x}}_0$. These parameters are estimated by minimising objective functions $\{J_i\}$ (defined below in equation 6.15) based on the averaged geometrical difference between i-th simulated mesh and the mesh fitted from the i-th MRI frame. There are thus only n independent objective functions, from which $n + 2$ variables are to be determined. Therefore this inverse problem is under-determined. This concept is schematically illustrated in figure 6.2 using the previously introduced 1D system, where 6 model parameters are to be determined from only 4 measurements/equations at all time points.

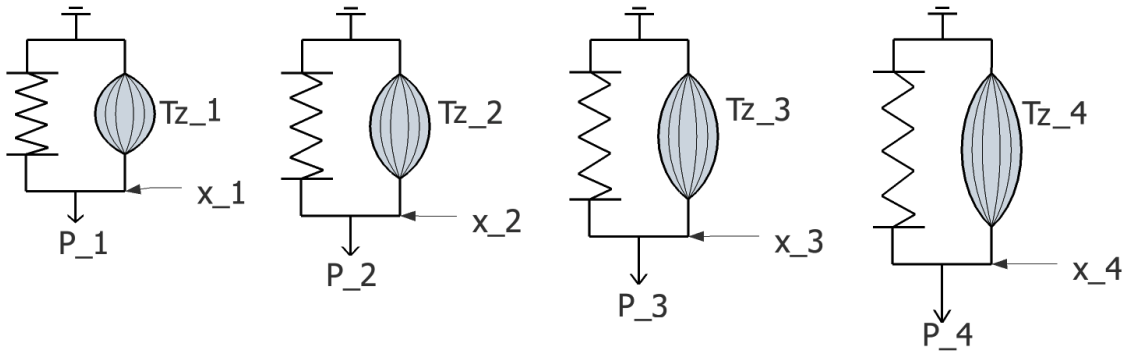

Figure 6.2: Schematic illustration of the inverse problem using the 1D model: 6 model parameters to be determined are active forces $T_z(1)$, $T_z(2)$, $T_z(3)$, $T_z(4)$ and two other variables illustrated in figure 6.1(b) – K (stiffness) and x_0 (reference position), However, only 4 measurements (x_1, x_2, x_3, x_4) at 4 time points are available.

Further assumptions

To fully determine the system, two assumptions are added. Firstly, the AT is set to zero at the end-diastole, assuming the myocardium is fully relaxed.

$$T_z(n) = 0. \tag{6.13}$$

Secondly, the unloaded state $\boldsymbol{x}_0$ can be initially approximated (note this approximation will be later refined – see below) by the LV shape measured in one of the diastolic MRI frames (i.e., the reference MRI frame), where LV inflating pressure and contracting residual tension are assumed to be roughly balanced. $k \in [1, n-1]$ is defined as the reference frame number.

$$\boldsymbol{x}_0 \sim \boldsymbol{y}_k. \tag{6.14}$$

Algorithmic description of parameter estimation procedure

Applying this approach, algorithm 1 details the procedures for estimating constitutive parameters, reference state, and active tensions during diastole. This algorithm consists of

five main steps as explained in the comments. Firstly, the assumption defined in equation 6.14 is applied to each diastolic MRI frame k before the ED frame, and the reference state $\boldsymbol{x}_0^k$ is set to be the state measured by MRI frame k (line 3 of algorithm 1). This reference state is then used in the second step to estimated the constitutive parameters $\boldsymbol{C}^k$ (line 4), which are chosen as the optimal parameters with which the reference state can be best deformed to the ED state. These estimated constitutive parameters are in turn used in the third step to refine the reference state $\boldsymbol{x}_0^k$, by deflating from the ED state (line 5). AT at each time point of MRI frames before the ED are estimated, using the pre-estimated reference state $\boldsymbol{x}_0^k$ and constitutive parameters $\boldsymbol{C}^k$ (line 7). Finally a criterion based on the physiological constraints of estimated AT, which is explained below, is devised to retrospectively choose the most sensible reference frame number (line 8) and the most plausible estimation of constitutive parameters, reference state, and active tensions (line 9).

The objective functions $\{J_i\}$ for estimating constitutive parameters and active tensions (used in lines 4 and 7 of algorithm 1) are introduced below in section 9. The details of methods for minimising these objective functions $\{J_i\}$ are explained in section 9. Finally the criterion in line 8 for choosing the most sensible reference frame number is described in section 9.

Algorithm 1: Estimating constitutive parameters $\tilde{\boldsymbol{C}}$, reference state $\tilde{\boldsymbol{x}_0}$, and diastolic residual active tensions $\{\tilde{T}_z(i)\}$, given the MRI observations $\{\boldsymbol{y}_i\}$ during diastole and corresponding LV pressures $\{P_i\}$. $\tilde{\boldsymbol{x}_0}$ are the 3D coordinates of Gauss points at the reference state. $\boldsymbol{y}_i$ are the coordinates of the same Gauss points given by the fitted meshes at time point i during diastole.

Data: $\{\boldsymbol{y}_i\}, \{P_i\}$
Result: $\tilde{\boldsymbol{C}}, \tilde{\boldsymbol{x}_0}, \{\tilde{T}_z(i)\}$

1 **begin**
  // Try each frame k before the ED as the reference frame
2 **for** k=1 *to* $n-1$ **do**
    // Step 1: First set reference state $\boldsymbol{x}_0^k$ to be the state measured by MRI frame k
3    $\boldsymbol{x}_0^k = \boldsymbol{y}_k$
    // Step 2: Estimate constitutive parameters $\boldsymbol{C}^k$ from ED measurement $\boldsymbol{y}_n$
4    $\boldsymbol{C}^k = \underset{\boldsymbol{C}}{\text{argmin}}\ J_n(\boldsymbol{x}_n, \boldsymbol{y}_n)$, where $\boldsymbol{x}_n = \mathbb{M}(\boldsymbol{x}_0^k, \boldsymbol{C}, P_n, T_z(n)=0, \boldsymbol{y}_n^B)$
    // Step 3: Refine the estimation of reference state $\boldsymbol{x}_0^k$ by deflation
5    $\boldsymbol{x}_0^k = \mathbb{M}^{-1}(\boldsymbol{y}_n, \boldsymbol{C}^k, P_n, T_z(n)=0, \boldsymbol{y}_n^B)$
    // For each diastolic frame i before the ED
6   **for** i=1 *to* $n-1$ **do**
      // Step 4: Estimate AT $T_z^k(i)$ from $\boldsymbol{y}_i$ using result from line 4 & 5
7      $T_z^k(i) = \underset{T_z}{\text{argmin}}\ J_i(\boldsymbol{x}_i, \boldsymbol{y}_i)$, where $\boldsymbol{x}_i = \mathbb{M}(\boldsymbol{x}_0^k, \boldsymbol{C}^k, P_i, T_z, \boldsymbol{y}_n^B)$
  // Step 5: Choose retrospectively which MRI frame should be initially assumed to be the reference frame using AT-based criterion (eq. 6.16)
8 $k = \text{AT-Criterion}(\{T_z^k(i)\})$
9 $[\tilde{\boldsymbol{C}}, \tilde{\boldsymbol{x}_0}, \{\tilde{T}_z(i)\}] = [\boldsymbol{C}^k, \boldsymbol{x}_0^k, \{T_z^k(i)\}]$

Objective functions for estimating $\boldsymbol{C}$ and $\boldsymbol{T_z}$

The objective functions $\{J_i\}$ for estimating constitutive parameters and active tensions (used in lines 4 and 7 of algorithm 1) are defined as the averaged distance between equivalent Gauss point $g \in [1, G]$ of the simulated ($\boldsymbol{x}_{ig}$) and fitted ($\boldsymbol{y}_{ig}$) meshes at time point of $i-$th MRI frame, i.e.

$$J_i(\boldsymbol{x}_{i\cdot}, \boldsymbol{y}_{i\cdot}) = \sqrt{\frac{1}{G}\sum_g \|\boldsymbol{x}_{ig} - \boldsymbol{y}_{ig}\|^2_{\mathbb{L}^2}}, \tag{6.15}$$

where $i \in [1, n]$ is the diastolic MRI frame number, g enumerates the index of Gauss points embedded inside each mesh volume (typically 4th order, G=768 per element), and $\boldsymbol{x}_{ig}$ and $\boldsymbol{y}_{ig}$ denote the spatial coordinates of a Gauss point g at time point of ith MRI frame in the simulated and fitted mesh respectively. Gauss points are the sample points used in the standard Gauss-Legendre quadrature scheme for computing numerical integration (Hunter and Pullan 2001).

Minimisation method for estimating $\boldsymbol{C}$ and $\boldsymbol{T_z}$

Having defined the objective function, the estimation of parameters described in algorithm 1 is reduced to two minimisation problems. We solve these minimisation problems using the method of parameter sweeps, in which simulations are performed with varying parameter sets and the optimal parameter set is chosen. This kind of method is embarrassingly parallel, and it enables us to explore the landscape of the objective function, which in turn, helps to characterise the problems of parameter identifiability.

The method of minimisation for constitutive parameters $\boldsymbol{C}$ (line 4 of algorithm 1) is a two-step procedure. Using the reformulated Guccione law defined in equations (6.5)-(6.9), C_1 and α are first optimised by choosing the global minimum point across a grid that regularly samples 2D parameter space, followed by optimization of r_3 and r_4 using

the same parameter sweeps method. This two-step process is iterated until the estimated parameters are converged. As we reported previously (Xi et al. 2011b), this optimization approach reveals the landscape of the objective function with respect to C_1-α, in which the two parameters are strongly coupled. Because of the coupling between C_1 and α, C_1 needs to be fixed during the parameter estimation process to allow the remaining parameters to be uniquely determined. C_1 was fixed at 1, based on average value of previous estimates of the Guccione law in literature (see table 6.1). How this assumption $C_1 = 1$ affects the results of this study is provided in the results section.

The method of minimisation for AT T_z (line 7 of algorithm 1) is implemented as parameter sweeps in 1D parameter space, which regularly sample the AT parameter in a typical range of [-10, 30] kPa. To reduce the parameter samples, we first start with a coarsely even distributed parameter samples (typically with an interval of 1 kPa), from which we choose the optimal parameter and refine it locally using a smaller interval (typically 0.033 kPa).

AT criterion for selecting reference frame

In line 8 algorithm 1, a criterion based on physiological constraints is devised to select the most plausible frame as the reference frame. If frame k is the reference frame, then the estimated AT is expected to be monotonically decreasing during diastole and be positive (meaning that the AT is a contracting force). That is,

$$T_z^k(i) > T_z^k(j), \text{ for any } i > j; \text{ and } T_z^k(n-1) > 0. \tag{6.16}$$

Starting from $k = 1$, the first frame satisfying this criterion is chosen. We have tested and demonstrated the validity of this criterion using synthetic data where the ground-truth is known (details are provided in appendix 6.B.2).

6.3 Results

Our methodology is applied to three clinical cases. For each case, the processing time is approximately 40 minutes for the motion tracking, 1 minute for the dynamic meshing, and 3 hours for the parameter estimation. We used a highly optimised cubic-Hermite elements based mechanical simulation code (Land et al. 2011), running on a standard desktop computer (4 2.5GHz cores and 4GB RAM). The results of the dynamic meshing stage are the same as those presented in the previous chapter, and thus omitted here.

6.3.1 Estimated constitutive parameters

Table 6.1 lists the estimated constitutive parameters ($\tilde{\boldsymbol{C}}$) for the three clinical cases. The results indicate consistently that the myocardium of two diseased patients is about three-fold stiffer than the healthy case.

Table 6.1: Estimated constitutive parameters ($\tilde{\boldsymbol{C}}$) for one healthy case and two patient cases, and comparison to studies in literature.

-	ESV(ml)	EF	C_1	C_2	C_3	C_4	Residual[1]
healthy case	67	51%	1.0	19.13	10.67	12.76	1.78
case 1	345	16%	1.0	53.44	22.01	29.34	1.58
case 2	186	17%	1.0	50.50	16.83	27.19	1.39
Augenstein et al. (2005), dog	-	-	1.5[2]	11.1	1.76	10.0	-
Wang et al. (2009), dog	-	-	0.831	14.3	4.49	0.762	1.81
Omens et al. (1993), dog	-	-	1.2	26.7	2.0	14.7	-
Okamoto et al. (2000), dog	-	-	0.51	67.07	24.16	21.60	-
Omens et al. (1993), rat	-	-	1.1	9.2	2.0	3.7	-
Walker et al. (2005), sheep	84.7	21.6%	0.233	49.25	19.25	17.44	-

EDP, end-diastolic LV cavity pressure; ESV: end-systolic LV cavity volume; EF, ejection fraction.

[1] The root-mean-squared-error (RMSE) in mm between simulated and fitted mesh at end-diastole over free wall. [2] $C_1 = 3.0$ in this study is defined with a multiplier of $\frac{1}{2}$.

6.3.2 Estimated diastolic AT

In figure 6.3, the colour-coded points show the estimated residual AT $\{\tilde{T}_z(i)\}$ at all time points of diastole for the three cases. The relaxation (i.e., the tension decay) profiles, which in figure 6.3 are the exponentially fitted lines to the data points, of the patient cases show AT to be significantly different when compared to the healthy case. The values of k (i.e., reference frame number) are 2,4,4 for healthy and two diseased cases.

To test the sensitivity of the residual AT profile against the assumption of C_1, we also estimated the tension profiles for each case using $C_1 = 0.5$ and $C_1 = 2.0$, based on the variability of C_1 in the literature. The right panel of figure 6.3 shows these results. In each of the three cases, the variability introduced by varying C_1 is much smaller than the difference across patient cases. In addition, the estimated AT increases with the increase of C_1, which is a result of the decreased nonlinearity in the Guccione constitutive law due to the compensatory decrease of α.

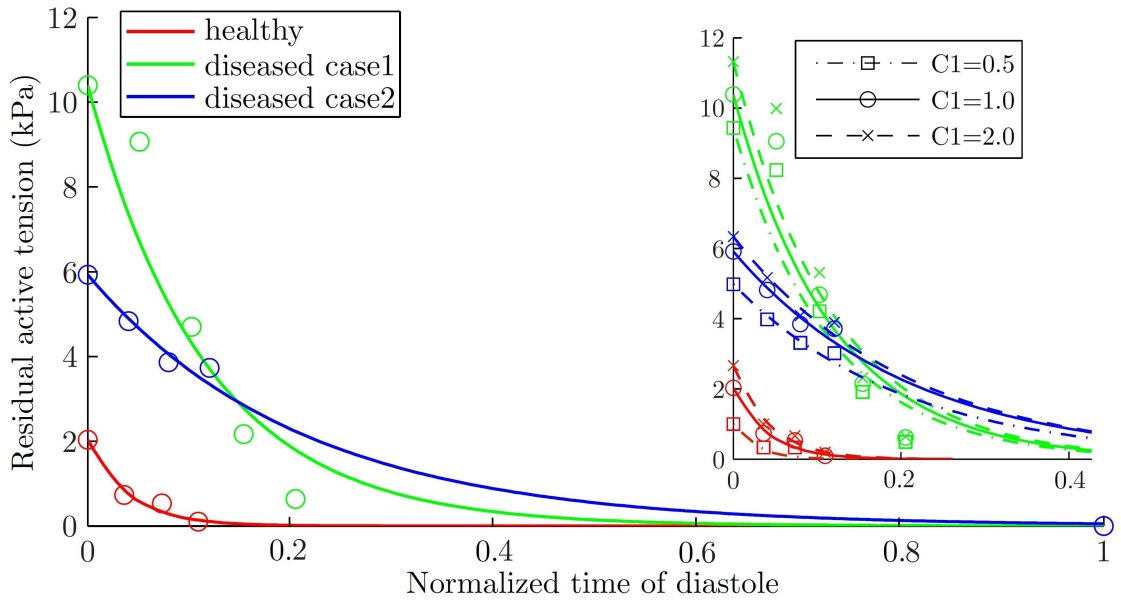

Figure 6.3: The estimated residual diastolic active tensions (T_z term defined in equation 6.12) with its sensitivity against C_1 assumption shown in the right panel. The data points show the optimised values of residual tension for each frame. The lines are the exponential fits to the data points. The time-line is the normalised time in a heart cycle, starting with end-diastole. Because limitations in clinical data acquisition protocol, tagged MRI only covers roughly one third of the early diastole. The residual AT of the two patient cases are significantly higher than the healthy one, indicating delayed tension decay. The differences among the estimated AT using $C_1 = 0.5, 1.0$, and 2.0 are very small, and this variability introduced by varying C_1 is much smaller than the difference across patient cases.

6.3.3 Model simulation with estimated parameters

Figure 6.4 shows the final model simulation results for the three clinical cases, using the estimated constitutive parameters, reference state and active parameters. As reported previously in table 6.1, the residual at the ED (100%) is 1.78, 1.58 and 1.39 mm for the healthy case, disease 1 and 2 respectively.

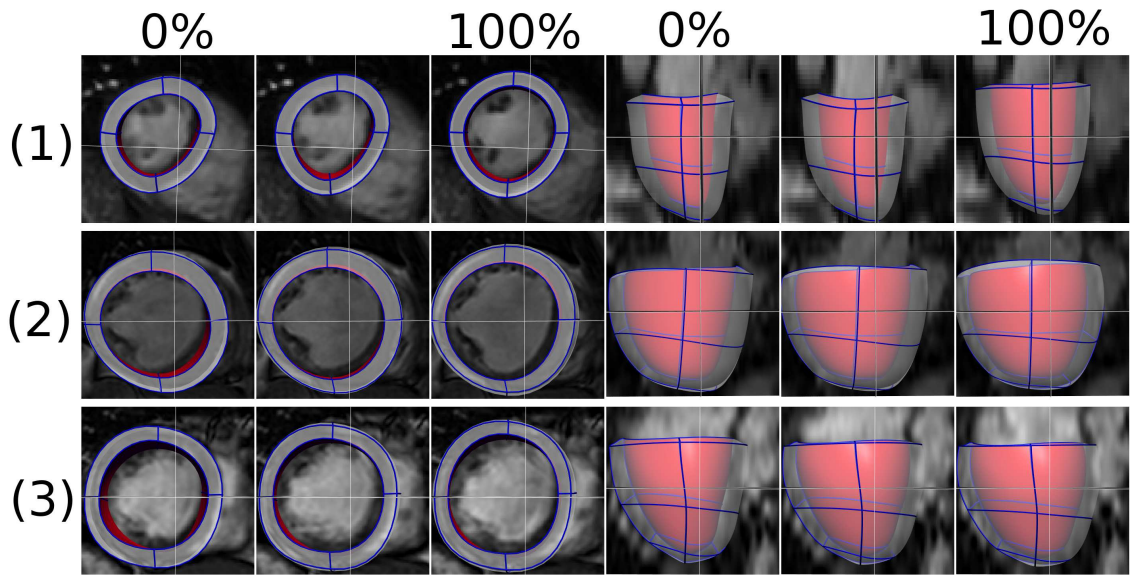

Figure 6.4: The final simulated meshes for the diastole process of the three cases (1 is healthy, and 2,3 are diseased 1 and 2), using estimated constitutive parameters, reference (unloaded) state, and AT parameters. These simulated meshes are visualised with the corresponding cine MRI frames. The meshes are shown in short axis view (left three columns) and long axis view (right three columns), each view consisting of the simulation results at 0%, 15%/24%/16% and 100% of the diastole phase.

6.4 Discussion

In this study, we present a method for estimating diastolic active and passive myocardium parameters–namely the myocardial constitutive properties and diastolic residual AT–from combined cine and tagged MR images and cavity pressure measurements. Applying this method to three clinical cases, the diastolic AT estimation results show a significant difference between healthy and two diseased cases, which may provide an interesting starting point for further clinical research. Below we discuss the issues related to the estimation of myocardial constitutive parameters, and the sensitivity of key steps in our methods on AT estimation results.

6.4.1 Issues related to the estimation of constitutive parameters

Parameter identifiability and C_1 assumption

Clinically, tagged MRI data covering the whole of diastole is difficult to record, while the end-diastolic frame (typically the first frame when synchronised with the R-wave of ECG) is always available. Thus, it is desirable to characterise myocardial stiffness using displacements (relative to the reference state) extracted from the end-diastolic frame of tagged MRI. However, the issues associated with the identification of the Guccione parameters using displacements extracted from only one MRI frame have been already reported by several previous studies (Omens et al. 1993, Augenstein et al. 2005, Augenstein et al. 2006, Xi et al. 2011b). For this reason, Omens et al. (1993) only estimated C_1 and the ratio of C_2:C_3. Augenstein et al. (2006) has reported identifiability problems in the form of a correlation matrix, which interestingly showed a low level of linear correlation between C_1 and α. Our previous study (Xi et al. 2011b) further explicitly reveals the nonlinear (or log-linear) correlation between C_1 and α ($C_1^a\alpha$=b, where a and b are constant).

In order to obtain the complete set of unique parameter values, multiple tagged MRI frames during diastole can be used. Each frame can provide information from which a distinct curve of the form $C_1^a\alpha = b$ can be estimated. For example, the synthetic results provided in the appendix (figure 6.8(a)) show that all C_1-α curves estimated from different MRI frames intersect at the ground-truth parameter point. Augenstein et al. (2005) has also showed that five MRI frames were sufficient to characterise the material parameters to within 5% error. However, results with patient data showed that there is not a unique intersection point in the parameter space, and the presence of residual AT is likely the main reason. This is illustrated by figure 6.8(f) where the rapid decrease of residual AT between early diastolic frames leads to estimation of softer myocardial stiffness in fibre direction. Thus, the high level of residual AT compromises the feasibility

of estimating full set of Guccione parameter using early-diastole frames, particularly in the clinical cases where diastolic pathologies are indicated.

For this reason, it is assumed that C_1 is one, based on the average value reported in literature (see table 6.1). For the range of the variability in C_1 as reported in literature, our analysis was consistent in its ability to identify a significant difference between tension profiles of the healthy and diseased cases as shown in figure 6.3.

Choice of constitutive laws

There are a number of existing constitutive models for passive cardiac mechanics (e.g., see Holzapfel and Ogden 2009 for a comprehensive survey). In particular, to solve the parameter identifiability problem, a number of researchers have proposed new constitutive laws, such as the 5-parameter polynomial form strain energy function by Humphrey et al. (1990), and the optimised strain energy function based on uncoupled strain attributes by Criscione et al. (2001). In our study, in order to facilitate the comparison of estimated parameter values with those reported in literature, we employed and reformulated the Fung-type Guccione's law, which is consistent with the widely-used approach in the cardiac modelling community for both forward simulation of cardiac mechanics and inverse model parameter estimation (Omens et al. 1993, Augenstein et al. 2006, Wang et al. 2009, Sun et al. 2009, Niederer and Smith 2009, Xi et al. 2011a). Nevertheless, the general principles of our proposed method for estimating diastolic AT apply to other constitutive laws as well.

6.4.2 Sensitivity of individual components in our methods on AT

The algorithm 1 outlined in section 6.2.2 is the core of our AT estimation method. In this method, we proposed to estimate not only the passive constitutive parameters (step

2 in algorithm 1), but also the reference state by deflating from the ED state (step 3 in algorithm 1). Both of these two steps depend on assumption defined in eq. 6.14 – the state measured by k-th diastolic MRI frame is close to the reference state (i.e., the step 1 in algorithm 1). The validity of our proposed approach clearly relies on both assumption 6.14 and individual step of algorithm 1, which in turn motivates the analysis of the contribution to the accuracy of the final AT result.

In figure 6.5, we investigate, using six scenarios, the analysis of the relative importance of

1) step 1 – the choice of reference frame number k and

2) step 3 – the deflation step of estimating reference state.

Figure 6.5(a) and 6.5(b) shows the errors for in-silico case and patient case 1 respectively in each of six scenarios. Scenario 1 is the simplest form of algorithm 1, in which $k = 1$ and the deflation step is omitted. This scenario is effectively equivalent to directly using the state measured by the first diastolic MRI frame as the unloaded reference state, a situation that is only true if the residual AT and LV cavity pressure are both zero. In scenario 2, the deflation step is included on top of scenario 1. Similarly, the frame number k determined by the criterion of equation 6.16 is used in scenario 3 (without deflation) and 4 (with deflation). Note that scenario 4, which uses the whole algorithm 1, produces the gold standard result for comparison for the patient case where ground-truth AT is unknown. Scenario 5 and 6 (both with deflation) use one frame before and after the correct reference frame used in scenario 3 and 4.

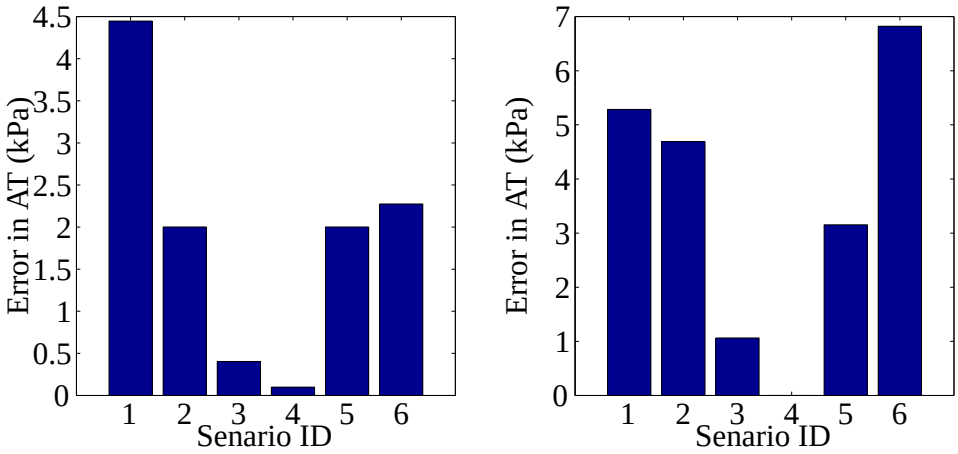

(a) In-silico case.

(b) Patient case 1.

Scenario ID	Explanation
1	using the first diastolic MRI frame and without deflation
2	using the first diastolic MRI frame and with deflation
3	using the correct frame without deflation
4	using the correct frame with deflation (our methods)
5	choosing one frame before the reference frame with deflation
6	choosing one frame after the reference frame with deflation

(c) Summary of each scenario (see the text in section 6.4.2 for more details).

Figure 6.5: The error of AT introduced under six scenarios for an in-silico case and the patient case 1, to assess the importance of choice of reference frame and deflation step in our methods (see the text in section 6.4.2 for details). The error of AT (in kPa) is defined as the root of mean squared error (RMSE) between AT estimated in each scenario and the known ground-truth (in-silico case)/AT estimated in scenario 4 (patient case 1). In the in-silico case, the measurement used are the simulated meshes, which are produced by our model using a linearly increasing LV pressure (0.33, 0.67, 1.00, 1.33, 1.67 and 2.00 kPa) and exponentially decaying AT (8.00, 2.35, 0.68, 0.21, 0.05, and 0 kPa).

These results indicate that the inclusion of deflation step improves the accuracy of AT estimation. Nevertheless, the deflation is relatively less important when choosing the correct reference frame since the state at correct reference frame is already very close to the reference state.

In addition, the choice of k is the most important step, because this affects both the estimation of constitutive parameters and reference state. In particular, if $k = 1$ and the deflation step is omitted (scenario 1), the influence of AT is not considered (Wang et al. 2009, Xi et al. 2011b), possibly leading to biased estimation of constitutive parameters.

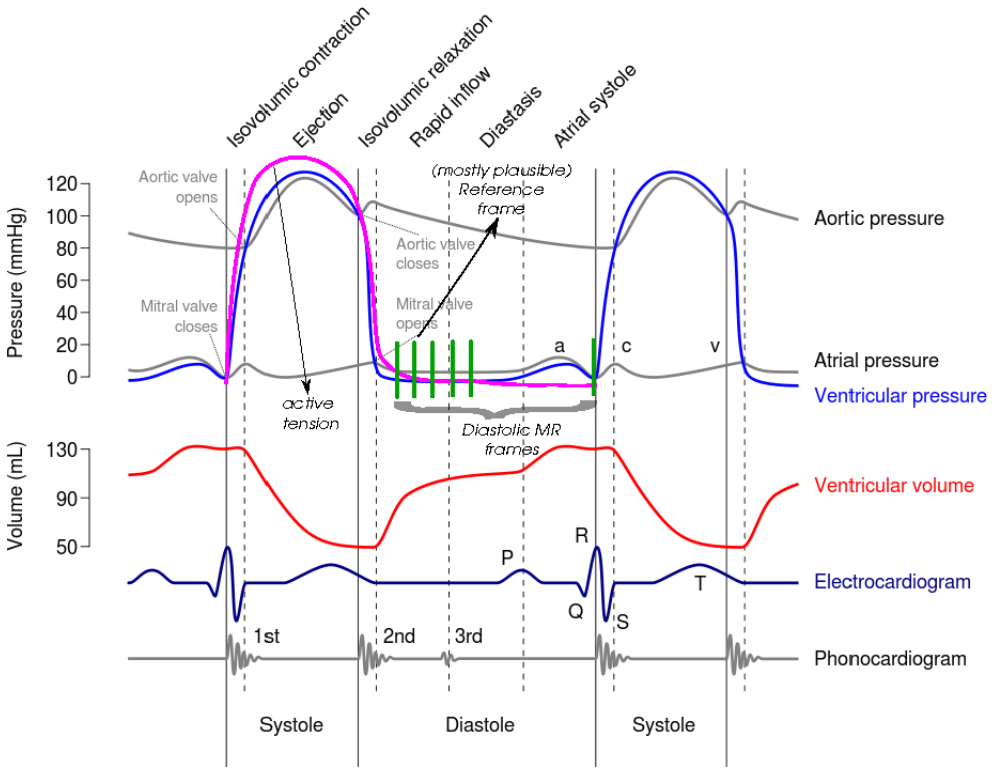

Figure 6.6: Schematic illustration of the timing of the diastolic MR frame and the estimated reference frame (for illustrative purpose) using a standard Wiggers diagram of the LV pressure and volume, together with self-drawn typical active tension profile for a healthy subject.

Estimation of the reference state

For a schematic illustration of the timing of the reference frame, a standard Wiggers diagram (Landis 1976) in figure 6.6 is included to show the pressure and volume transient of LV in the diastole phase, together with the timing of MR measurement, in the context of a whole cardiac cycle events. The reference state, for our modelling purpose, is defined as the LV state at which the LV does not experience any passive inflating or active contracting force (please refer to figure 6.6 for illustration). The reference frame is defined as the MR frame which approximately measures the reference state when the contracting residual AT and inflating pressure are best balanced. The first diastolic MR frame is by our definition the minimum-pressure frame, which is shortly after the LV valve opens.

For a healthy subject, the LV is in the rapid filling phase at the time of the first diastolic frame (when the LV pressure drops to minimum), and residual AT should have already significantly decayed during the previous isovolumetric relaxation phase (if not zero). Thus for a healthy subject, it is reasonable to assume that the first diastolic MR frame is the reference frame, which is also the assumption in a very similar work performed by Wang et al. (2009) from the Auckland Group. However, for patient whose LV relaxation is impaired, the rate of decay of LV AT is relatively low, and there could be still a considerable amount of residual AT (relative to the magnitude of the passive pressure at this stage) in the first diastolic frame. Therefore the reference frame can be better approximated by one of the subsequent frames when the AT are further reduced and LV pressure is further increased, which is essentially one of the extensions proposed by this thesis based upon the work of Wang et al. 2009.

For patients with impaired relaxation, if the first frame is assumed to the reference frame, the LV volume at the reference state is actually underestimated due to the existence of contracting AT. In turn, this would cause the estimated myocardium stiffness to appear to be softer if this incorrect reference frame is used. Similarly if the reference is assumed to be the frame after the correct one, the myocardium stiffness will be overestimated.

6.4.3 Comments on the parameter estimation using only diastolic measurements

Being able to directly estimate the diastolic residual active tension is clinically vital for identifying the mechanism of diastolic heart dysfunction. The motion in the diastolic phase is least affected by the large magnitude of active tension during the contraction. Thus it is the closest approximation we can obtain from the available measurement to a pure passive mechanical movement. The parameter estimation problem should be better posed before attempting to estimate both active and passive parameters using the whole

heart cycle measurement, because the diastolic parameters could then be, to certain degree, decoupled from other unknown active contraction model parameters. For this reason, there has been a number of very similar studies on diastolic parameter estimation which have the same focus on diastolic only measurements as our study (Wang et al. 2009, Augenstein et al. 2006). Using the obtained diastolic parameters, in particular the stiffness parameters, the active parameters are then be further estimated by incorporating the systolic measurements (Wang et al. 2010b)

6.4.4 Limitations and future work

Limitations

While our results appear promising, it is important to note that there are a number of limitations in our approach. The rule-based fibre distribution of our LV model does not incorporate directly the patient-specific measurements, and this may influence the estimation of material anisotropies and the accuracy of AT estimated. To address this issue, we are currently in the process of building a human fibre model by acquiring and post-processing in-vivo diffusion-tensor images. In addition, because we have not included the mechanical effects of organs around left ventricle, kinematic displacements are imposed as boundary conditions at both the LV apex and the base in order to constrain the predicted movement. However, this is likely to affect the finite elasticity solution and motion prediction in the free wall, possibly leading to a biased material property estimate. Ideally models of pericardium, right ventricle, and atrium would be included. However, such additions would clearly be at the cost of increasing complexity in both model simulations and inverse parameter estimation.

Limitations in the measurements include the pressure data recordings which have a level of uncertainty due to the calibration error, in part because only the $\frac{dP}{dt}$ trace was available without a reference to the absolute value of P. To account for this gap in the data, we

assumed that the minimum pressure (at the beginning of diastole) is zero, based on the data reported by Wang et al. 2009. Another limitation regarding pressure data is that the clinical protocol limits the pressure measurements to being recorded separately from the MR imaging. While the patients were in the same physical position in both MRI scan and catherisation procedure (rest on their back), it is possible there might be small changes in haemodynamics states in the pressure and imaging recordings due to the insertion of the pressure catheter lead and the surgical anesthetisation.

Future work

We choose a robust but computational expensive approach to sample the parameter space. As explained above, this enabled us to fully explore and understand the coupling relationships between parameter values. In the future, it would be possible to adopt more sophisticated but computationally effective approaches to directly estimate the coupling coefficients a and b, such as SQP (Augenstein et al. 2005) or filtering approaches (Xi et al. 2011a).

Finally, this study brings about a significant requirement on the completeness and accuracy of various clinical data. Limitations of the patient data used in this study restrict the analysis to early filling, in which passive diastolic recoil is combined with the relaxation of AT. Since the tagged MRI measurements do not cover the period of pure passive filling, passive material properties are confounded with active relaxation. In the future, we plan to acquire additional clinical data sets with optimised protocols (e.g., whole-heart-cycle tagged MRI coverage, diffusion-tensor imaging for the patient-specific fibre distribution), in order to further investigate and correlate our new indices with clinical diagnosis.

6.5 Summary

Our methods of integrating the clinical MRI and LV cavity pressure data across multiple measurement points in the diastole enabled us to provide, to our knowledge, the first attempt to estimate the diastolic residual active tension profile in human subjects, which has significant potential to provide an important metric characterising diastolic heart failure. The results from our preliminary application of this method indicates that early diastolic residual AT in the two diseased cases are significantly higher than the normal cases, which may well indicate that myocardial relaxation (i.e., lusitropy) is impaired in those two patient cases.

Appendices

6.A Constitutive parameter coupling

6.A.1 The theoretical implication of incorporating multiple measurements

As demonstrated in appendix 5.A.1 of the previous chapter, C_1 and α are coupled which sufficiently render the optimization problem effectively ill posed. However, the coupling relationships at different deformation state are different, because $\frac{1}{1+Q}$ is dependent on the strains. Thus we can improve our estimation by comparing the simulated deformations with *multiple* displacement measurements instead of only the end-diastolic one.

The theoretical implication of incorporating multiple measurements is intuitive. The Guccione constitutive law is a Fung-type or exponential-type strain energy function. Its linear (C_1) and exponential (α) coefficients are coupled at one measurement point, but differently coupled across multiple measurements. Figure 6.7 shows changes of the Guccione strain energy with respect to $C_1 - \alpha$, where the increase of measurement points improves the identifiability of the parameters.

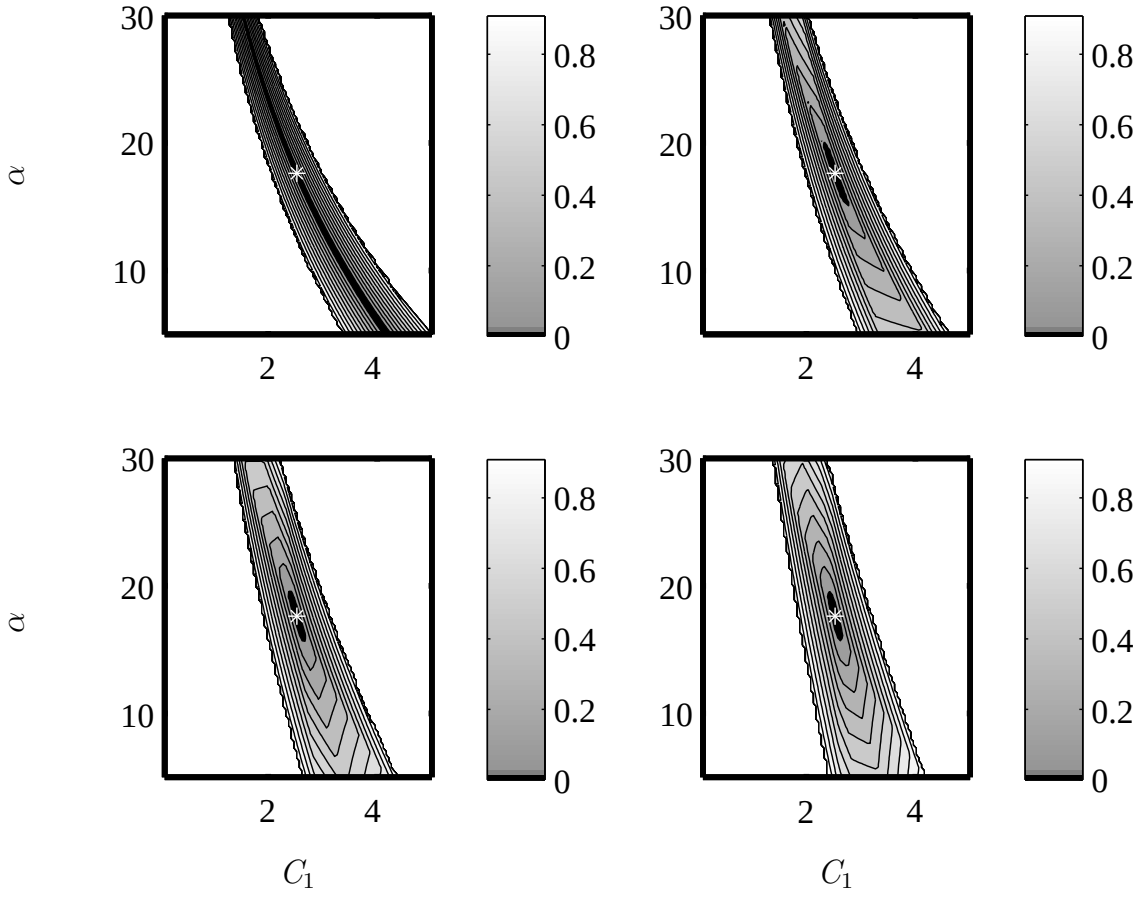

Figure 6.7: Changes of the Guccione strain energy with respect to $C_1 - \alpha$, averaged over 1, 2, 3 and 4 "measurement point(s)". The optimization problem becomes less ill defined with the increase of measurement constraints. This reveals the possibility of obtaining a unique global minimum solution of parameter estimation when incorporating multiple measurements.

6.B Estimation of diastolic active tension

6.B.1 Motivation of accounting for diastolic AT in the model

Although the idea of incorporating multiple measurements (appendix 6.A.1) is appealing, the reality of its application is not. Figure 6.8 shows the constitutive parameter estimation results without accounting for AT in the model, which, in turn, motivates the necessity of adding an AT component into the model to explain the deformation fields. These results are the estimation of four reformulated Guccione parameters – C_1, α, $r3$ and $r4$ ($r_2 =$

$1 - r_3 - r_4$), using observations of meshes fitted to different MRI frames or synthetically simulated meshes. Since C_1-α is coupled and cannot be uniquely identified from one displacement measurement, figure 6.8(a,b,d,f) show C_1-α (coupling) curves, instead of only one unique (C_1, α) point. These exponential C_1-α lines are fitted separately, in log space, to a set of equally optimal parameters points (refer figure 5.6 and Xi et al. 2011b for more details of the C_1-α curve and its fitting).

The in-silico results (figure 6.8(a,b,c)) are the estimation results from synthetically simulated meshes. In figure 6.8(a), varying LV endocardium pressure (0-2 kPa) are applied as loading conditions with zero AT within simulation, and C_1-α relationship is estimated separately from each of these measurements. In figure 6.8(b,c), the synthetic meshes are simulated with the same pressure (2 kPa) and varying AT (0-8 kPa), a C_1-α relationship is estimated separately from each of these measurements (figure 6.8b), together with corresponding r_3-r_4 estimation results (figure 6.8c).

The results for the healthy and diseased cases (figure 6.8(d,e,f,g)) are obtained from the meshes fitted to different MRI frames. In this estimation process, the reference mesh is set to be the beginning-of-diastole frame (defined in section 6.2.2 as the 1st diastolic frame whose LV pressure is assumed to be zero). This is because when AT is not considered in the model, the LV is unloaded if and only if LV cavity pressure is zero.

The result for the in-silico case indicates that the inclusion of AT in the measurement would shift the C_1-α curve in parallel, as well as changing the r_2 (the stiffness ratio in fibre direction) consistently. This behaviour is hardly noticeable in the healthy case, but is clearly demonstrated in the disease cases, which motivates the needs of considering AT for estimating parameters in the disease cases.

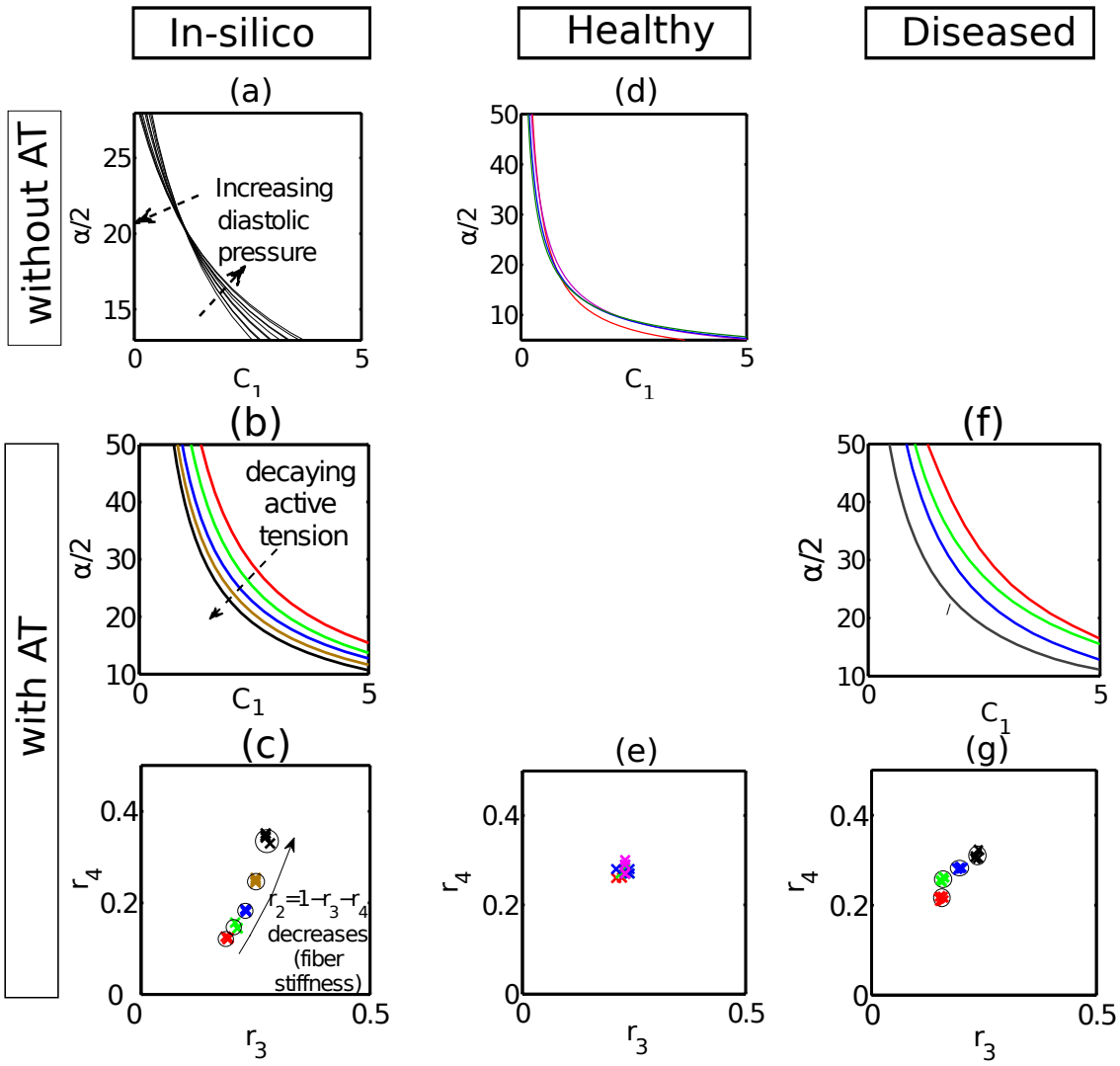

Figure 6.8: Constitutive parameter estimation without accounting for AT in mechanical model, showing that the $C1 - \alpha$ curves (subplots a, d, b and f) and $r_2 = 1 - r_3 - r_4$ (subplots c and g) estimated from different MRI frames are not constant. All the models assume zero AT as part of the parameter estimation process. The "with AT" plots refers to AT added to the in-silico simulation (figure b) or assumed in the patient data (figure f), and please refer to section 6.B.1 for details.

6.B.2 Illustration of the criterion of selecting reference frame

Since each early diastolic MRI frame is initially assumed to be the reference frame in algorithm 1, we use the physiological constraints on AT to devise a criterion (defined in equation 6.16) to retrospectively choose which MRI frame should be the most correct reference frame. This criterion implies that AT is monotonically decreasing during diastole

and non-negative (since a positive AT denotes a contracting force).

To demonstrate this idea, the same in-silico case as previously described in figure 6.5 is used. In this in-silico case, the measurement used are the six simulated LV meshes, which are produced by the mechanical model using a linearly increasing LV pressure (0.33, 0.67, 1.00, 1.33, 1.67 and 2.00 kPa) and exponentially decaying AT (8.00, 2.35, 0.68, 0.21, 0.05, and 0 kPa). The volume of these simulated meshes (the ground-truth PV curve) is shown in figure 6.5(c). The AT estimation method (algorithm 1) is applied and the estimated AT is shown in figure 6.5(a,b), in which the AT 1-4 corresponds to the AT estimated using 1st, 2nd, 3rd and 4th frame as the reference frame (i.e., when k=1,2,3,4 in algorithm 1).

According to the AT criterion defined in equation 6.16, frame 2 is selected as the reference frame and AT 2 of figure 6.5(b) is selected as the AT estimation result, which in turn, produces a very small error between estimated and ground-truth AT. Note that AT 3 and AT 4 also satisfy the criterion. However, as stated previously in the text explaining the AT criterion, only the first frame satisfying the criterion should be selected. The reason for this is demonstrated by figure 6.5(a) where the simulated PV curves using the mostly plausible reference frame (i.e., PV 2) should the one tangent to the ground-truth PV curve at the ED point. Subsequent PV curves (PV 3 and 4 using frame 3 and 4 as reference frame) would overestimate the stiffness in constitutive parameters (i.e., the slope of PV curve) while the PV curve before (PV 1) would underestimate the stiffness.

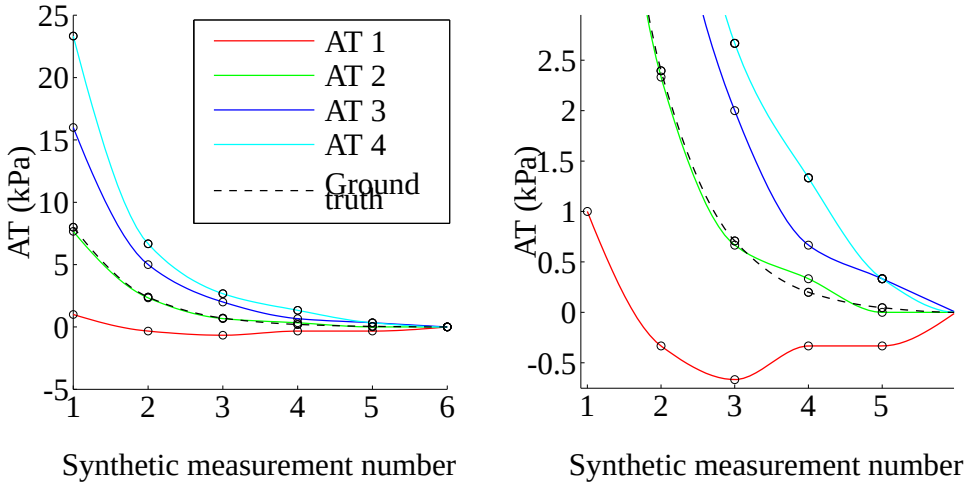

(a) In-silico AT estimation

(b) Enlargement of (a)

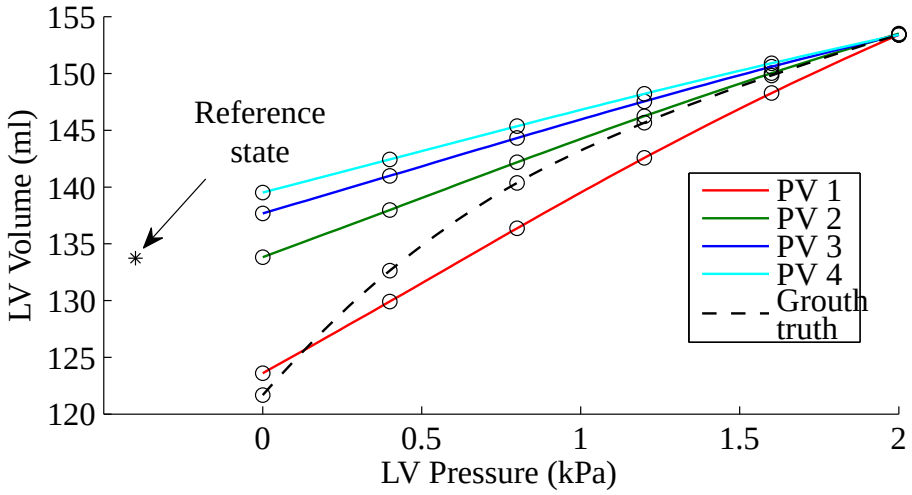

(c) PV curves (PV 1-4) of the in-silico purely LV inflation simulations without AT.

Figure 6.9: In-silico AT estimation using different frames as the reference frame (a,b) and the corresponding simulated PV curves using estimated parameters without accounting for AT (c). In subplots (a) and (b), AT 1-4 are the in-silico AT estimation results using the 1st, 2nd, 3rd and 4th measurement as the reference frame. In subplot (c), the corresponding PV 1-4 are produced by the pure passive inflation with estimated constitutive parameters and reference state. The difference between each of PV 1-4 curves and the ground-truth PV curve in subplot (c) corresponds to the sign of AT 1-4 in subplot (a). That is, AT are estimated to effectively match the ground-truth PV curve of the in-silico measurements. The positive AT decreases the volume of LV while the negative AT increases the volume of LV (e.g., see AT 1 and PV 1). Note that the volume curves in subplot (c) are only for schematically illustrating the meaning of the sign of AT, and the actual minimised objective function for estimating the parameters is based on the 3D displacement of the LV (equation 6.15), which is similar but not identical to the objective function based on LV volume.

Chapter 7

Understanding the need of LV pressure for the estimation of LV diastolic functions

The diastolic function (i.e. blood filling) of the left ventricle (LV) is affected by its capacity for relaxation, or the decay in residual active tension (AT), whose inhibition limits the relaxation of the LV chamber, which in turn affects its compliance (or its reciprocal, stiffness). The clinical determination of these two factors (the stiffness and diastolic residual AT) is thus essential for assessing LV diastolic function. To quantify these two factors, in the previous chapter, a novel model-based parameter estimation approach was proposed and successfully applied to multiple cases using clinically acquired motion and ventricular pressure data. However, the need to invasively acquire LV pressure measurement limits the wide application of this approach. We address this issue in the current work by analysing the feasibility of using two kinds of non-invasively available pressure measurements for the purpose of inverse parameter estimation. Firstly, we investigate the reliability of estimating stiffness and diastolic residual AT using data sets of 18 clinical cases (10 healthy and 8 diseased) with MR imaging data but no specific LV pressure data, by prescribing pressure boundary conditions based on a generic pressure-volume (PV) relationship reported in literature. To overcome the significantly reduced quality of these

estimation results without any pressure data, we then further investigate scenarios of parameter estimation with additional information about LV pressure, specifically using only the relative pressure measures that are now becoming available experimentally. To quantitatively analyse the influence of the pressure offset values needed to transform these relative measures into absolute values, we design three sets of physiologically realistic synthetic data sets with three levels of diastolic residual active tension (i.e. impaired relaxation capability) and quantify the percentage error in the parameter estimation against the possible pressure offsets within the physiological limits. The results indicate that the knowledge of LV pressure transient (at least the relative pressure) is required for the estimation of cardiac diastolic properties. Without this knowledge of pressure, the information implied by the estimated parameters is no more than that can be directly extracted from imaging measurements. However, we also show that the relative LV pressure provides valuable information for estimating diastolic parameters, with errors quantified in this chapter as 11% for the magnitude of stiffness α and 22% for AT with averaged 0.17 kPa error in pressure measurement using the state-of-the-art non-invasive pressure estimation method. Finally we illustrate that given a fixed accuracy of relative pressure measurement, increased resolution of diastolic MR measurements should be able to improve the accuracy of estimated parameters. The work presented in this chapter has been submitted for publication in Xi et al. 2012b.

7.1 Introduction

An increasingly important research area within the field of cardiac modelling is the development and study of methods of model-based parameter estimation from clinical measurements of cardiac function (Sermesant et al. 2006, Wang et al. 2009, Wang et al. 2010b, Moireau and Chapelle 2011, Chabiniok et al. 2011, Xi et al. 2012a). This set of techniques provides a potentially powerful approach for the quantification of cardiac

function, with the potential for improved selection of individuals with pathological myocardial mechanics for further therapy (Nagel and Schuster 2010). In organ-level cardiac mechanical models, both passive constitutive material parameters and active contractility parameters are required for the simulation of diastolic and systolic functions respectively (Niederer and Smith 2009, Nordsletten et al. 2011). As such, these active and passive parameters are important physiological variables related to the function of the heart.

In particular, the diastolic function (i.e. LV blood filling) is affected by two main characteristics of the myocardium (Zile et al. 2004, Maeder and Kaye 2009): (1) its capacity to relax, produced by the release of the actin-myosin cross-bridges, and (2) its compliance (or its reciprocal, stiffness), often quantified within models via constitutive material parameters that dictate the capacity of the LV chamber to passively dilate. These two physiological properties, corresponding to the diastolic residual active tension (AT) and passive constitutive parameters in the mechanical model, are difficult to be assessed *in vivo*, and the traditional criterion to diagnose diastolic dysfunction is subject to many limitations and controversies.

In the previous chapter (Xi et al. 2012a), we demonstrated that estimating these diastolic mechanical parameters and decoupling the estimates from the effects of active recoil and passive inflation were possible. Using this model-based approach we showed a clear difference in the diastolic mechanical parameters (i.e. the stiffness and diastolic residual active tension) between healthy and diseased subjects. In particular, the high level of diastolic residual active tension (AT) in early diastole, estimated from the diseased cases, indicated an impaired ventricular relaxation capability (Zile et al. 2004, Xi et al. 2012a).

This parameter methodology used a novel computational framework incorporating both clinical imaging and LV pressure measurements. However, the requirement of needing both motion and pressure measurements in a single subject to utilise this method limits the application of this approach. Specifically, accurate values of LV pressure are only

available in the clinic with an invasive cardiac catheterisation procedure, where a catheter is typically introduced through a femoral artery and advanced to the LV (Sasayama et al. 1984, Urheim et al. 2002, Zile et al. 2004). Furthermore, while the cardiac catheterisation remains the clinical standard, these measurements can be affected by calibration errors (Solomon and Stevenson 2009), and the potential complications and health risks associated with this invasive technique underscore the need for reliable noninvasive methods to measure LV pressures (Chatterjee 2009, Solomon and Stevenson 2009).

As a potential alternative to invasively acquired data, there are three main non-invasive methodologies for estimating the LV diastolic pressure. The first approach uses 4D velocity fields available via specialised US, CT or MR imaging protocols, and then computes the pressure gradients by solving the pressure Poisson equation (Krittian et al. 2012, Song et al. 1994, Yotti et al. 2011). This method can potentially provide a high spatial-temporal resolution pressure maps, but it is limited to the domain captured by the image, and perhaps more significantly, pressure values can only be computed relative to one point in that domain (and not relative to a known pressure data). This technique has been successfully applied to compute LV filling pressure gradients (Ebbers et al. 2001, Yotti et al. 2011), and thus has the potential to be also used for the estimation of diastolic parameters. The second methodology uses a microbubble-based ultrasound contrast agent (UCA), and is based on the fact that the change in the non-invasive measurement of the acoustic properties of this agent using ultrasound depends on the blood pressure (Forsberg et al. 2005, Dave et al. 2012). This use of the UCA has been approved in the United States for clinical LV opacification studies (Dave et al. 2012), and has the potential to non-invasively monitor LV pressures in real-time, with reported pressure offset errors ranging from 0.025 to 0.33 kPa when calibrated with aortic pressure using transferred cuff-based measurements (Dave et al. 2012, Geoffrey et al. 2003). With both these developing methods, LV pressure can effectively be estimated in relative terms, with an uncertain amount of offset in its absolute value. A further approach to the central blood pressure estimation is to

non-invasively measure radial artery pressures, from which a transfer function is applied, as introduced by (Karamanoglu et al. 1993). While this approach has been widely used in the last few years for the systolic pressure estimation (Hope et al. 2008), as currently implemented it does not provide accurate information about the central pressure during diastole. As such this method, for the purpose of our study, should be regarded as complementary to the aforementioned two methodologies which are able to estimate the LV relative pressure during diastole phase.

These developments in LV pressure measurement technology present both challenges in the relative nature of the resulting data and opportunities for using this information of relative pressure to estimate mechanical properties. In this context this chapter addresses two important questions for the clinical translation of the estimation of passive stiffness and active tension parameters: are absolute pressure measurements required for parameter estimation? If so, what is the impact of the presence of errors in the pressure offset value required to transform the relative pressure measures into absolute values?

Specifically, the investigation of the importance of the LV pressure boundary condition on estimation of diastolic proprieties is developed as follows. Firstly, we investigate the reliability of estimating stiffness and active tension (AT) using data sets of 18 clinical cases (10 healthy and 8 diseased) with MR imaging data but no LV pressure data, by prescribing pressure boundary conditions based on a P-V relationship reported in established literature. Using this approach, we show that this generic pressure data adds little to our ability to discriminate the parameter difference between healthy and diseased cases, compared to the information extracted only from the imaging measurements. Secondly, due to the low quality of the estimation results without any pressure data (shown below), we investigate scenarios of parameter estimation with additional information about LV pressure – specifically using the relative pressure with offset. To quantitatively analyse the influence of the pressure offsets we design three sets of physiologically realistic synthetic

measurements with three levels of diastolic residual active tension (i.e. impaired relaxation capability) as benchmarks, and quantify the percentage error in both residual AT and passive constitutive parameter estimation against the possible pressure offsets within the physiological limits.

7.2 Materials and Methods

7.2.1 Parameter estimation without knowing the LV pressure

As discussed above, LV pressure data has previously been an important element to parameter estimation. However, in many clinical scenarios an estimate of the LV pressure is completely unknown. In this situation, in order to apply our model-based parameter estimation methodology to clinical cases, we would thus need a method to infer it from the available measurements (i.e. the MRI data), as it is required in the model as an essential boundary condition. In literature, the LV pressure-volume (P-V) data has been reported extensively (Kawaguchi et al. 2001, Steendijk et al. 2006, ten Brinke et al. 2010), and the LV P-V relationship has been well studied (Zile and Brutsaert 2002, Zile et al. 2004, Klotz et al. 2007). Thus, for the purpose of parameter estimation without pressure information we consider the implications of inferring the LV pressure using relationships defined from this data.

LV pressure surrogates using normalised LV volume

The diastolic LV P-V relationship has previously been described by an exponential equation (Zile and Brutsaert 2002 and Zile et al. 2004), P=$Ae^{\beta V}$, where P is the left ventricular diastolic pressure, V is the left ventricular diastolic volume, and A and β are empirically determined constants used to quantify passive stiffness. This empirical P-V relationship has been widely used, and the stiffness constant β is currently the gold-standard for

the characterisation of the stiffness of the heart in the clinical practice (Aurigemma and Gaasch 2004, Burkhoff et al. 2005,Westermann et al. 2008). To understand the impact of pressure on the parameter estimation, we use the P-V relationship ($P = 2.3e^{0.01\,V}$) measured in the control cases in Zile et al. 2004 for our following experiments. The reason for this choice is that using this single pressure profile prescribed in the same way (i.e. without biasing the estimation result by the prescribed pressure), our goal is to analyse, as a criteria of assessing the plausibility of estimated parameters, how the estimation of AT and stiffness differs between healthy and diseased subjects.

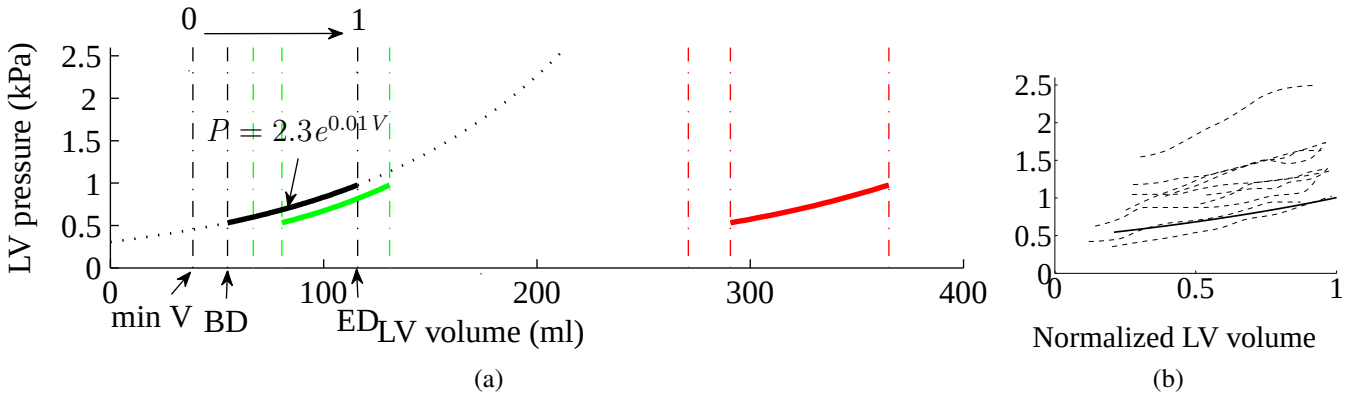

Figure 7.1: Illustration of the pressure surrogate using "Zile2004" normalized diastolic P-V relationship (Zile et al. 2004). (a): the dash line is the direct application of "Zile2004" (black solid line) to LV with large volume; the green and red lines are the application to two new cases using normalized volume (detailed in section 7.2.1). (b): validation of the normalized P-V relationship (solid line) against the diastolic PV data (dash lines, the same volume normalisation is performed) reported in literature for AHA class II and III patients (with large LV volumes).

However, it is important to note that the P-V relationship cannot be used directly, because when applied to diseased hearts with a large LV volume this relationship will produce an unrealistic pressure (figure 7.1a). To address this limitation we use the normalized volume as suggested by Klotz et al. 2007. As shown in figure 7.1a, this normalisation is done using the diastolic LV minimum and maximum volume (denoted by the black leftmost and rightmost vertical dashed lines). To infer the LV pressure for new cases (the green and red curves in figure 7.1a), the same normalisation is done on each of the new cases to get the normalized volume. Pressure is then determined by indexing

the normalized P-V relationship. In figure 7.1b, we verify this normalisation-based PV relationship by comparing it to the diastolic PV data reported in literature for AHA class II and III patients (Lorusso et al. 1997, Kawaguchi et al. 2001, Steendijk et al. 2006, ten Brinke et al. 2010). The same normalization is performed on these diastolic PV data in figure 7.1b, where the "Zile2004" relationship (bold black line) is consistent with the normalized PV data in literature (dash lines).

Application of LV pressure surrogate to 18 clinical cases

Using the method of prescribing the LV pressure outlined above, we apply the parameter estimation methodology proposed in our previous work (Xi et al. 2012a) to a total of 18 clinical cases with only imaging measurements. As introduced earlier, we analyse the parameter difference between healthy and diseased cases, and compared these results to the information extracted only from the imaging measurements.

The imaging data are short axis cine MRI and low resolution 2D tagged MRI, acquired in St Thomas' Hospital London using an MR imaging machine produced by Philips Medical Systems. The data sets used in the study conform to the principles outlined in the Declaration of Helsinki and the study was carried out as part of a local ethics committee-approved protocol with informed consent obtained from the subjects. In these 18 cases, 10 cases are healthy volunteers and 8 are heart failure patients. A summary of each case is provided in table 7.3. The LV volume transients (normalized) are plotted in figure 7.2 which, interestingly, shows a clear difference in the timing of the minimum volume points, suggesting a delayed diastolic relaxation for the diseased cases.

The parameter estimation methodologies, including the methods for processing the MR measurements, mechanical model simulation and algorithm for estimating the AT and material properties, are described in detail in Xi et al. 2012a. In brief, the cine MRI sequence is first processed using a motion tracking algorithm (Shi et al. 2012) to extract the

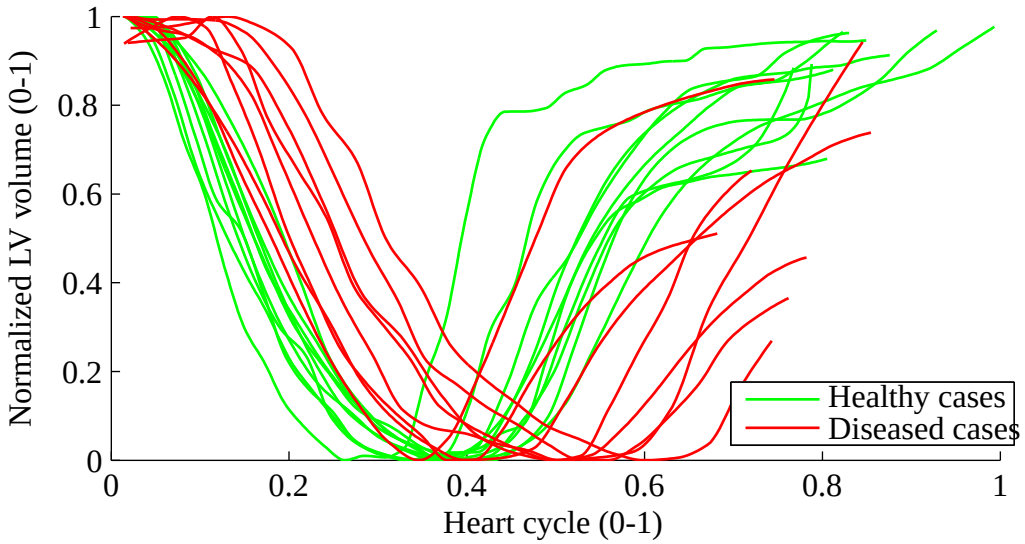

Figure 7.2: Normalized volume transients over a heart cycle for the 18 clinical cases.

	Sex	Age	Heart Rate	Weight	EF	AHA	minV	maxV
H1	M	34	74	72	49%	0	67	131
H2	M	32	77	82	44%	0	62	110
H3	M	27	50	89	49%	0	98	193
H4	M	29	61	65	41%	0	97	165
H5	M	22	67	65	45%	0	65	118
H6	M	22	69	73	40%	0	85	143
H7	M	30	54	74	36%	0	102	160
H8	M	31	71	65	38%	0	96	153
H9	F	24	50	54	54%	0	77	156
H10	M	20	74	85	43%	0	116	204
D1	M	79	43	70	26%	3	271	365
D2	M	66	83	85	18%	3	262	318
D3	F	65	57	65	19%	2	264	328
D4	M	62	51	110	23%	3	218	282
D5	M	80	62	90	30%	3	169	243
D6	M	58	54	90	33%	2	236	353
D7	M	58	77	104	26%	2	166	225
D8	F	76	59	54	30%	3	142	204

Figure 7.3: Table of patient information of the 18 clinical cases. H stands for healthy, and D stands for diseased. The minimum and maximum LV volume is in milli-liter (ml). The ejection fraction calculated here seems to be consistently underestimated, possibly due to the lower base plan cropping in the LV blood pool segmentation and underestimated myocardial movements by the motion tracking algorithm.

myocardial displacements, based on which a sequence of cubic-Hermite meshes are then constructed and aligned to the motion observed in each frame of MRI sequence (Lamata

et al. 2011). These meshes are compared to the simulation results generated using our finite deformation based mechanical model, with the previously defined pressure surrogate (illustrated in figure 7.1d) as its boundary condition. The mechanical parameters are then estimated using our novel parameter algorithm (detailed in Xi et al. 2012a).

It is important to note that only cine MRI sequences were in these cases reliable for the estimation of myocardial movement. Because the cine MRI data did not provide accurate 3D displacements within the myocardium, the parameter optimization criterion is based on the residual of LV volume instead of the residual of 3D displacements. The parameter estimation results are reported and compared, to assess the ability of using estimated parameters to distinguish between healthy and diseased cases below.

7.2.2 Parameter estimation using the relative LV pressure

Our second goal in this study is to assess the accuracy of parameter estimation using relative pressure measurements (i.e. the relative LV pressure transient with an estimated absolute offset). In order to achieve this, synthetic cases with ground-truth values provide clean benchmarks to quantitatively analyse the error introduced with the presence of pressure offsets.

Synthetic measurements are simulated using our LV mechanical model. The reference geometrical model, with patient-specific geometry published in Xi et al. 2012a, is shown in figure 7.4a. A set of typical Guccione constitutive parameters (1,30,20,20) is prescribed and three types of decaying residual active tension were simulated respectively, representing different levels of diseased conditions with impaired LV relaxation capabilities during early diastole (figure 7.4b). The pressure range (figure 7.4c), from the beginning of diastole pressure (BDP) to the end of diastole pressure (EDP), is prescribed as 1.1 kPa to 1.9 kPa, based on the average values of AHA class II and III patients reported in literature (Lorusso et al. 1997, Kawaguchi et al. 2001, Steendijk et al. 2006,

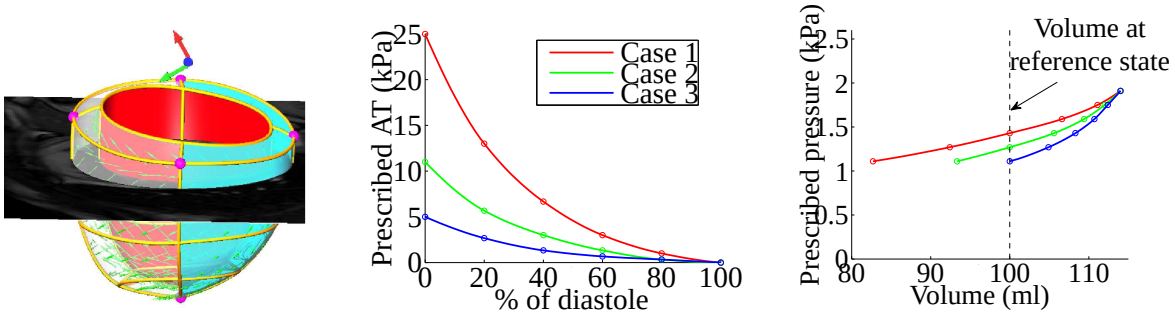

(a) (b) (c)

Figure 7.4: Illustration of the generation of three synthetic measurements used for parameter estimation experiments. Figure (a) shows the stress-free reference geometry (visualised with one slice of short-axis cine MRI), a patient-specific geometrical model constructed from MR images (Xi et al. 2012a). Figure (b) shows three types of decaying residual active tension profiles, which are prescribed in the synthetic simulations to present three levels of disease conditions (i.e. impaired relaxation during early diastole). Figure (c) shows the volume of the six simulated synthetic measurements for each case, together with the corresponding prescribed LV pressure. Note that since the reference geometry and constitutive parameters are assumed to be the same for the three synthetic cases and the residual tension is zero at end-diastole, the simulated end-diastolic volume is thus the same.

ten Brinke et al. 2010). Six evenly distributed measurements were simulated, which is the typical number of MRI frames covering the diastole phase. Note that the under the prescribed levels of AT, the volume at 3rd, 2nd and 1st measurements points for cases 1, 2 and 3 respectively is close to the volume of the stress-free reference geometry (i.e. the reference volume denoted by the dash line in figure 7.4c). The method outlined below is based on the assumption that at these measurement points the active contractile stress and passive inflating pressure are roughly balanced.

Parameter estimation, using the same method as applied to the cases in section 7.2.1, is performed using each of the three sets of synthetic measurements. We assume that for the purpose of parameter estimation, the pressure is only known relatively (i.e. up to an offset). We performed the parameter estimation with eight evenly distributed values of pressure offset (-1.10 kPa, -0.73 kPa, -0.36 kPa, 0 kPa, 0.39 kPa, 0.76 kPa, 1.13 kPa, 1.50 kPa), which shift the BDP from a minimum of 0 kPa to a maximum of 2.6 kPa, corresponding to the physiological range of BDP reported in literature (Lorusso et al.

1997, Kawaguchi et al. 2001, Steendijk et al. 2006, ten Brinke et al. 2010).

7.3 Results

We present the results of parameter estimation using both the prescribed pressure and the relative pressure respectively in the following two subsections.

7.3.1 The effect of prescribed pressures and the feasibility of parameter estimation without any pressure data

Figure 7.5 plots the α values (stiffness, defined in Xi et al. 2012a) of the estimated Guccione parameters for the 18 clinical cases using the prescribed pressure. Overall, there is a significant difference between healthy and diseased cases in terms of the stiffness implied by α, which agrees with the prior knowledge of disease classification. However, we are aware that the difference in the α values between the healthy and diseased cases might be already implied by the difference in the ejection fraction (EF) calculated from the volume (discussed below in section 7.4.1).

Figure 7.6 plots the estimated diastolic AT transients for the 18 clinical cases using the prescribed pressure. The AT transients are quite similar among the healthy and diseased cases, which is inconsistent with disease classification. The difference in the timing of AT can be explained by the volume transient in figure 7.2, which shows the different timing at the beginning of diastole. Notably, although the deformation of the 18 clinical cases are significantly different (in terms of the LV volume and ejection fraction), surprisingly the estimated AT transients (especially in terms of the maximal AT) are similar, indicating that AT is likely to be highly correlated with the prescribed pressure. This difference in the estimated AT transients between healthy and diseased cases is significantly smaller then that reported in Xi et al. 2012a, using the measured LV pressure.

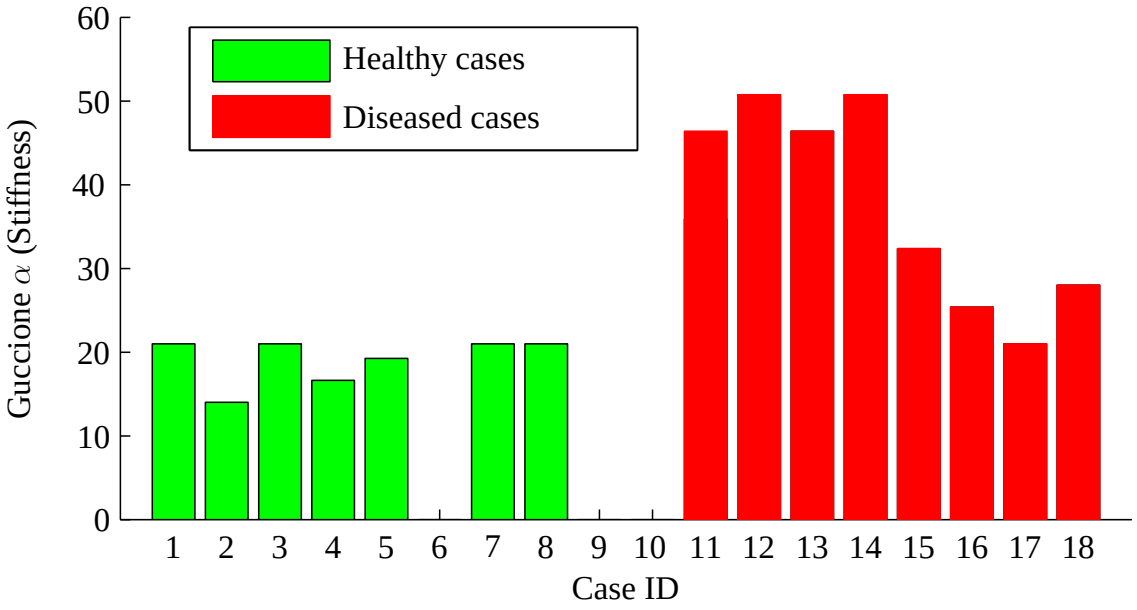

Figure 7.5: The estimated α (stiffness) of the Guccione material parameters for the 18 clinical cases: cases 1-10 are healthy and cases 11-18 are diseased. Due to the convergence issue, 3 of the 10 healthy cases cannot be simulated.

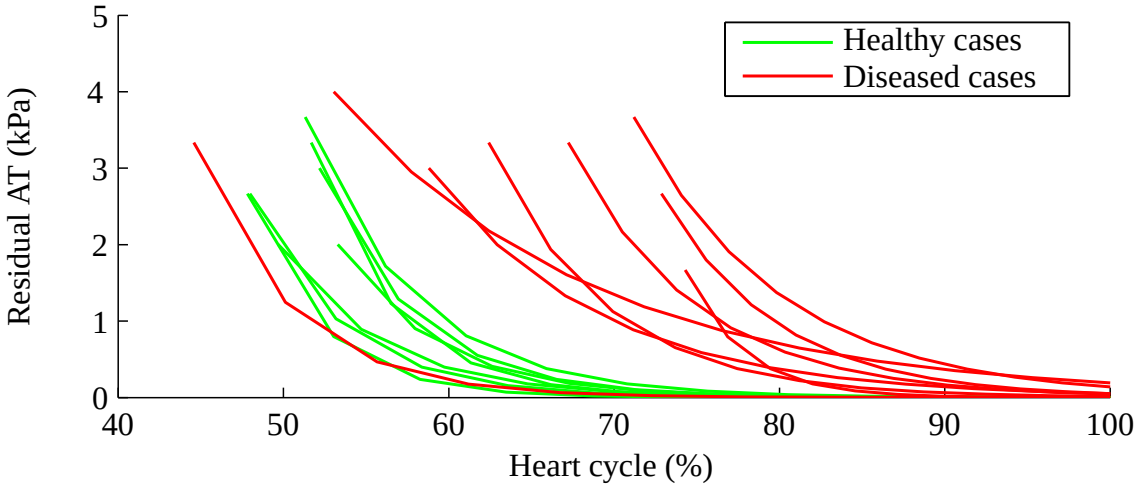

Figure 7.6: Estimated diastolic AT transient for the 18 clinical cases with only imaging measurements. These AT transients are grouped by disease class: healthy (green) and diseased (red). As described in previous chapter (Xi et al. 2012a), the AT transients shown here are fitted exponential curves.

7.3.2 The effects of pressure offset and the accuracy of parameter estimation using relative pressure

Figures 7.7 shows, using the three sets of synthetic benchmark cases, the percentage change of estimated parameters–α of Guccione parameters (figure 7.7a), maximal diastolic AT (figure 7.7b) – with respect to the percentage offset of relative pressure with respect to the beginning-of-diastole pressure (1.10 kPa) from -100% to +136% (or -1.10, -0.73, -0.36, 0, 0.39, 0.76, 1.13 and 1.50 kPa in their absolute values, -100% corresponding to an offset of -1.10 kPa and +136% to an offset of +1.50 kPa). The traditional empirically derived clinical stiffness index β is calculated for all these experiments, and shown in figure 7.7c, with comparison to the stiffness parameter α calculated using our model-based methods.

Overall, the changes in α and AT are not monotonically increasing/decreasing until the pressure offset reaches a positive limit (i.e. shifted up to a limit). This limit is first reached in case 3 (from 0%), where the AT is the smallest among the three cases. This is because the 1st measurement is already close to the reference state and a positive pressure offset would cause the estimated reference state go beyond the 1st measurement (explained in details in the discussion section).

When the pressure offset is negative (i.e. pressure shifted downwards), α changes by a maximum amount of 35% (in contrast, β changes by -51% to +1120%), and AT by a maximum of 60%. The maximal error ranges of α and AT also hold for the positive pressure offset, but not after the monotonically increasing limit, after which the estimated parameter will increase without an upper bound.

In the $\pm$30% window of pressure offset, which corresponds to the reported maximal measurement error 0.33 kPa using the current state-of-art non-invasive pressure estimation method (Dave et al. 2012), the maximal changes are 27% for α and 45% for AT

respectively. In the $\pm 16\%$ window of pressure offset, which corresponds to the reported mean error (0.17 kPa) in the pressure estimation, the maximal changes become 11% for α and 22% for AT respectively. It is important to note that based on the published results in Xi et al. 2012a, the healthy and diseased cases have differences of approximately 42% in α, and 69% in AT. As such, under the mean error assumption, these results show promise for delineating the healthy and diseased cases using the relative pressure obtained from the current non-invasive pressure estimation method.

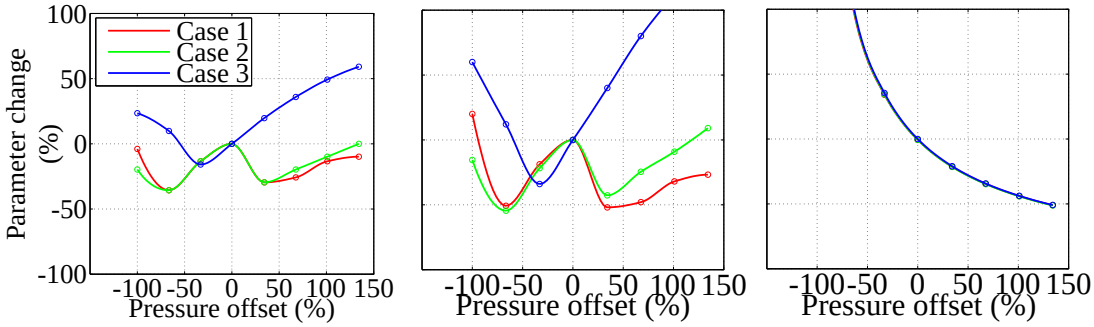

(a) α (b) AT (c) β

Figure 7.7: The percentage change of estimated parameters (α(a) and AT (b)) with respect to the percentage offset of the LV pressure, comparing to the percentage change of clinical stiffness index β in (c). The percentages are calculated using the ground-truth parameters prescribed in the three synthetic cases. These results are explained in details in section 7.3.2.

7.4 Discussion

We have performed the first study, to our best knowledge, to analyse the feasibility of using prescribed and relative pressure measurement, for the purpose of inverse parameter estimation. In the following, we discuss the reliability and implications of the parameter estimation results using both these two types of LV pressure.

7.4.1 The feasibility of using the prescribed pressure for parameter estimation

Despite the significant advantage such a technique would offer in the clinic, our results show that estimation of diastolic AT and constitutive parameters without LV pressure is an ill-posed problem. Specifically we have shown there is a clear need for both stimuli (pressure) and response (deformation) to estimate parameters of the LV mechanical system. The prescription of pressure based on a P-V relationship significantly affects the computation of AT – high similarity among the 18 clinical cases despite of clear differences in the cardiac deformation and diseased conditions. In addition, the estimated stiffness seems to be highly correlated to the ejection fraction (discussed in the next subsection).

The correlation between constitutive parameters α and ejection fraction

Despite the clear bias introduced by a pressure surrogate, the stiffness estimated differentiated healthy and diseased cases in a cohort of 21 clinical cases. The relationship between ejections fraction (EF) and the α-stiffness estimated in the previous experiments is shown in figure 7.8. When the α-stiffness or the material properties are estimated using the same pressure surrogate prescribed according to Zile et al. 2004, they are essentially negatively correlated to the EF. Therefore, the information implied by the stiffness estimated using the prescribed pressure is no more than that can be directly measured, in terms of ejection fraction, using only the data observable from the image.

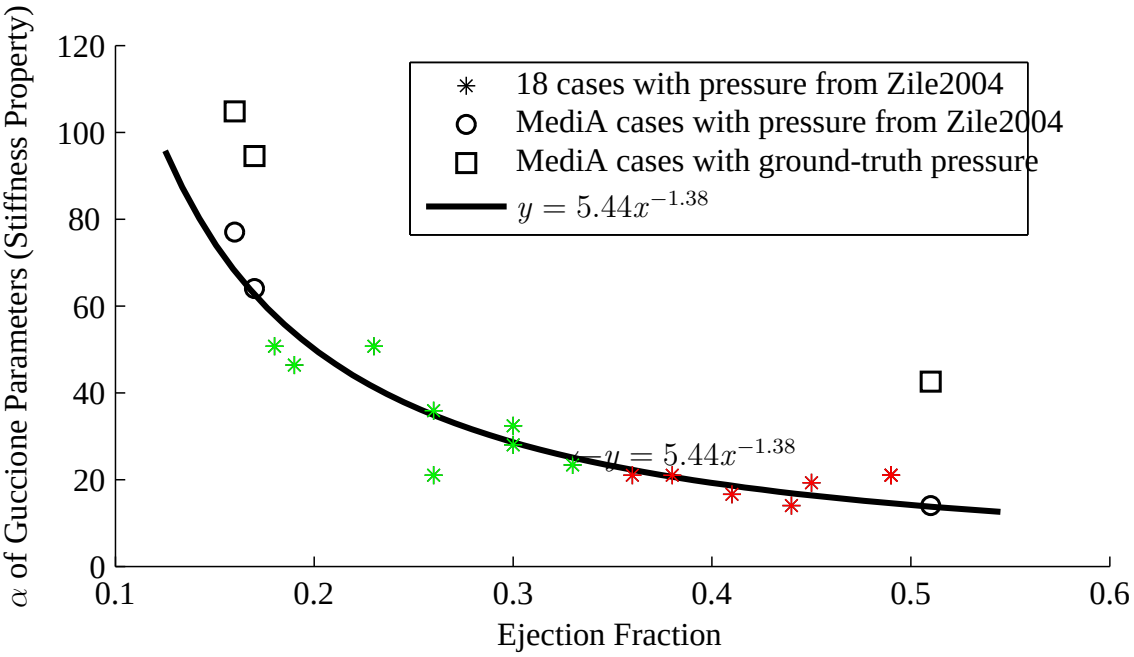

Figure 7.8: Regression line between stiffness and EF in the clinical cases (18 cine-only cases and 3 MediA cases (Xi et al. 2012a)), when estimated using the "Zile2004" pressure. The ground-truth α (estimated using the measured pressure) of the three MediA cases are plotted in box marks. The green star marks correspond to the healthy cases among the 18 cine-only cases, while the red stars marks correspond to the diseased ones.

Comments on the way of prescribing the LV pressure

We acknowledge that pressures of LV with different volumes have a large variability, and it is less likely that there is a universally applicable way of determining the pressure solely based on LV volume. The way we prescribed the LV pressure is just a preliminary trial to investigate the influence of pressure on parameter estimation. More complex methods of determining the LV pressure could be investigated (e.g. taking account of the influence of the LV absolute volume), which lies beyond the main purpose of our study in this chapter.

7.4.2 The in-silico benchmarks for parameter estimation experiments using relative pressure

The three sets of synthetic measurement provide benchmarks to quantify the error that could be possibly introduced by the uncertainty in transforming relative pressure into the absolute values. These three synthetic cases have different levels of diastolic residual active tension covering a wide range of diseased condition (i.e. impaired ventricular relaxation capability) in terms of the magnitude of possible residual tensions (Xi et al. 2012a). We adopted our assumptions for generating those synthetic benchmarks based on the averaged PV data reported in literature (Lorusso et al. 1997, Kawaguchi et al. 2001, Steendijk et al. 2006, ten Brinke et al. 2010) and tested a large range of possible pressure offsets according to physiologically realistic variability of diastolic PV data. However, we acknowledge that the experiments done on the in-silico cases have an inherent limitation: the measurements (both the pressure and motion measurement) are free of noise compared to the real measurements obtained in the clinic. Most often these errors are not white noise and knowing the distribution is challenging. Nevertheless, we believe these in-silico experiments do provide a clean and reliable estimate of the possible errors in estimated parameters using relative pressure measurements.

7.4.3 The error mechanism of using relative pressure for the parameter estimation

To better understand the mechanism of how pressure shifts influence the parameter estimation, a 1D spring model provides helpful insights into the influence of pressure offsets and ways to reduce the parameter estimation error.

As shown in figure 7.9(a-b), the deformation of the spring (analogous to the deformation of LV) is driven by two factors–stretched by the external force P (analogous to the LV cavity pressure) and contracted by the active stress Tz (analogous to the active tension

developed by the contraction of the myocardial fibre). Passive stress Tp is developed when the spring is stretched/compressed from the reference position x_0 to position x_i (i=1,2,3,4,5), for a classical Hookean spring this is a linear relationship with the displacement $x_i - x_0$ and the spring constant K (stiffness). Assuming that the external force P and active stress Tz are balanced at the 3rd measurement, then x_3 should be equal to x_0.

At five measurement points the external force P_i and deformed position x_i are measured as shown in the left panel of figure 7.9c. Using these measurements, the parameters to be estimated include the stiffness K, the reference position x_0 and the active stress T_z at each time point.

Using our estimation methods, if the ground-truth measured pressure (without an offset) is used for the parameter estimation, the correct stiffness K and correct reference position x_0 are estimated, by drawing a tangent line (red line in the left panel of figure 7.9c) for the P-X curve at the final measurement point, reaching the horizontal line of $P = 0$ (essentially analogous to deflating from the end diastolic state to zero pressure for the LV model), assuming Tz_5=0. The amount of active tension is proportional to the length of the 5 horizontal dashed lines at the 5 measurement points, because that is the amount of force needed to compress the spring from the red line to the corresponding positions of the P-x curve. The blue line in the left panel of figure 7.9c represents the scenario where x_2 is assumed to the reference position. With this assumption, the AT estimated at measurement point 4 (denoted by the dash vertical line) is negative, as the blue line falls to the left of the P-x curve (i.e. negative AT is needed to stretch the spring to match the P-x curve). Therefore the assumption of x_2 being the reference position will be rejected based on the proposed retrospective AT criteria (Xi et al. 2012a) – the estimated AT at these five measurement points should be decreasing and all non-negative. Since the assumption of x_2 being the reference position has been rejected, the correct estimation of reference position x_3 (the red line in the left panel of figure 7.9c) is obtained based on our proposed estimation methods (detailed in Xi et al. 2012a) – the first assumption

of reference position that satisfies the decreasing and nonnegative criteria is the correct reference position. This results in the correct estimation of stiffness and AT as well.

The right panel of figure 7.9c shows the scenario of using shifted pressure for parameter estimation. The correct estimation of stiffness K should be the red line, the same as the red line in the left panel of figure 7.9c. However, due to the limited resolution of measurements, the reference state indicated by the red line (between the 2nd and 3rd measurements) is not measured. The 2nd measurement will be selected as the reference state, as the AT estimated by the green line is the first one that satisfies the decreasing and non-negative AT criteria (as introduced above). Compared to the red line (ground-truth) the green line (taking 2nd measurement as the reference state) underestimates the stiffness K as well the AT. This situation happens also in our previous experiments and explains the reasons why the stiffness and AT is often underestimated, as shown above in figure 7.7 in the results section.

If we have more measurements available between x_2 and x_3 to cover also the reference state, we will still not be able to improve the parameter estimation results. The reason is because the 2nd measurement (the green line), as the first one satisfies the AT criteria, will still be selected as the reference state. This incorrect selection of reference state happens because of a lack of measurement towards the end of deformation. If more measurements are available at the rightmost horizontal dash line, the error of selecting the wrong reference state will be corrected since the AT of the green line at that measurement point will be shown as negative, and thus reject the assumption that 2nd measurement is the reference state. In this situation the correct reference frame (the red line) will be chosen, resulting in the correct estimation of both constitutive parameters and AT.

Therefore, in summary, in order to improve the robustness of parameter estimation against the pressure offsets, more measurements during the whole deformation process are needed.

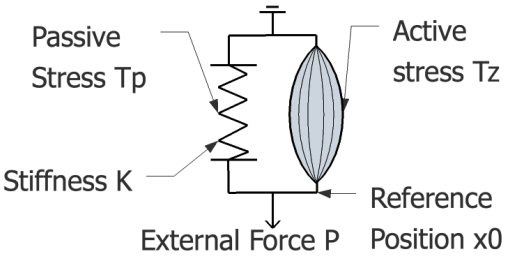

(a) Schematic 1D spring model.

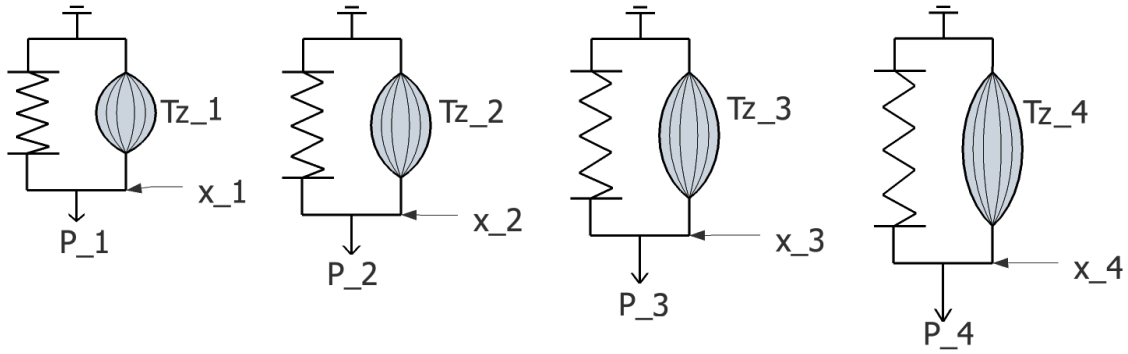

(b) Illustration of the available measurements for the 1D spring model.

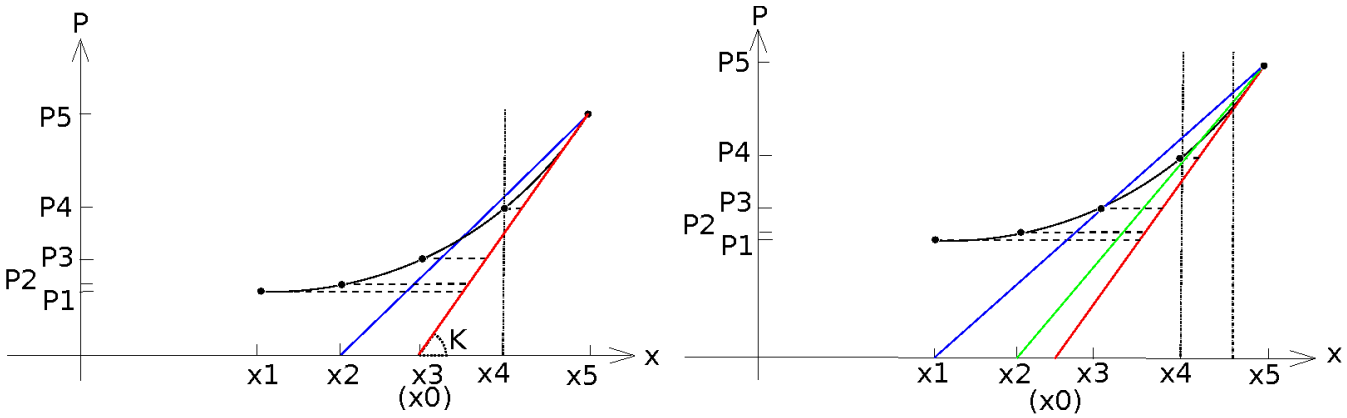

(c) Illustration of the parameter estimation process for the 1D spring model.

Figure 7.9: (a) Schematic 1D spring model, demonstrates the key concepts in the LV mechanical model. The displacement of the spring x, relative to the reference position x_0, is driven by both the external force P and the active stress T_z. The passive stress T_p is developed as the spring is deformed, relating to the spring stiffness constant K. This is detailed in section 7.4.3. (b) Illustration of the available measurements for the 1D spring model–the deformed position x_i (analogous to the MR measurement of the LV deformation), and the external loading force P_i (analogous to the measurement of the LV cavity pressure). (c) Illustration of the parameter estimation process for the 1D spring model, using ground-truth pressure (left) and the shifted pressure (right). This process is explained in details in section 7.4.3.

7.5 Summary

This chapter presents the first study, to our best knowledge, to analyse the feasibility of using prescribed and relative pressure measurement for the purpose of inverse diastolic cardiac parameter estimation (using our previously published methodology, Xi et al. 2012a). It is concluded that the knowledge of LV pressure transient is required for the estimation of cardiac diastolic properties. Without this knowledge, the information implied by the estimation parameters is no more useful than that extracted from the imaging measurements (i.e., the stiffness is correlated with the ejection fraction calculated from the volume transients). The relative LV pressure can be used for estimating parameters, with errors quantified in this study as 11% for α and 22% for AT with averaged 0.17 kPa error in pressure measurement using the state-of-art non-invasive pressure estimation method. We believe that the accuracy of pressure offset is important for the estimation of parameters, and given a fixed accuracy of pressure measurement, increased resolution of diastolic MR measurements could improve the accuracy of estimated parameters.

Part IV

Summary, Future Directions and Conclusion

Chapter 8

Summary and future directions

8.1 Summary

This thesis on the patient-specific model-based parameter estimation has presented contributions that are both methodological and clinical applicable. In particular, it has developed methods of integrating dynamic MRI and LV cavity pressure data within a physiologically realistic mechanical model, providing methods for, to our best knowledge, the first estimation of both myocardial stiffness and diastolic residual active tension (AT) profile in human subjects. Preliminary results show that early diastolic residual AT in the two diseased cases is significantly higher than the normal case, which confirms that myocardial relaxation is impaired in those two heart failure patients. In addition, this work also reports how the estimated constitutive parameters provide a potential robust indicator of the myocardial stiffness.

One of contributions of this model-based method of quantifying the degree of active tension during diastole lies in the potential application of our approach to diastolic heart failure (DHF) and dysfunction in patients in the clinic. As explained in detail by Fuster et al. (2001) and briefly summarised here, diastolic heart failure and diastolic dysfunction refers to the decline in performance of ventricles (usually the left ventricle) during dias-

tole. The clinical determination of the mechanisms which cause the diastolic heart failure remains challenging. A number of studies have sought to characterise LV diastolic function, and current guidelines rely on bulk and indirect measures – such as pressure volume loop measures or Doppler ultrasound (Paulus et al. 2007). Current diagnostic metrics are surrogates of the actual complex physiological processes occurring in the heart itself. For example, one of the difficulties of using pure analysis of image and pressure measurements lies in the fact that ejection fraction and LV pressure could appear normal for DHF patients. In addition, systolic and diastolic heart failure commonly coexist in patients present with many ischemic and nonischemic etiologies of heart failure. These problems bring difficulties to the determination of and therapy-planning for DHF using traditional non-model based methods (i.e., pure analysis of clinical measurements) (Zile and Brutsaert 2002).

The difficulty is, to a significant degree, because any condition or process that leads to stiffening of the left ventricle can lead to diastolic failure (i.e., ventricle can't be filled properly), including impaired relaxation or increased wall thickness and/or stiffness (Fuster et al. 2001). These two causes of impaired ventricular filling are explicitly modeled and quantified in our approach – the reduction in the passive muscular elasticity and increase in diastolic active tension. The quantification of these two factors provides the potential for the identification of the true root cause of the stiff left ventricle in a clinical context, and thus guides the therapy to target the underlying root of DHF.

However, there are a number of steps to be completed before bringing proposed methods into clinical practice (discussed in more details in the following sections). Firstly, this thesis has provided the proof of concept and demonstrated feasibility of the approach through the positive validation of the reported results in three clinical cases. However clearly the clinical significance of the proposed approach has to be further analysed (e.g., in a large patient universe). Additionally, the confirmation and validation of the physiological mechanism of increased residual active tension, using electrophysiology exper-

iments and modelling, represents an interesting and important aspect in its own right. Secondly, the invasiveness of pressure measurement would limit potentially wide clinical application. As analysed in chapter 7, there is a clear need for both stimuli (pressure) and response (deformation) to estimate parameters of the left ventricular (LV) mechanical system. In current clinical practice LV pressure is measured with invasive cardiac catheterisation procedures, which are subject to associated risks and complications. This limitation, of requiring LV pressure measurements, prevents the potentially wide application of the proposed methodological approach. Nevertheless, there are already promising non-invasive pressure estimation methods (Forsberg et al. 2005, Dave et al. 2012), still not fully integrated into clinical practice, that have the possibility of providing the required LV pressure estimates. The combination of these non-invasive pressure measures with our proposed parameter estimation approach have the ability to widen potential clinical application, however, the accuracy and sensitivity of the integrated approach needs to be assessed in its own right.

8.2 Future directions

A number of directions of further research are outlined here in order to achieve the ultimate and exciting goal of the envisioned clinical application.

8.2.1 Clinical application and experimental validation

Current clinical practice makes use of the required invasive pressure transients in selected cases, and the analysis of more diseased cases is thus a necessary step to assess the diagnostic value of the diastolic relaxation and stiffness estimated with proposed methodology. This thesis has provided the proof of concept and feasibility through the positive validation results in three clinical cases, but clearly the clinical significance of the di-

astolic indexes has to be further analysed. Further validation using a large number of clinical data sets is needed to link the estimated abnormal diastolic AT and stiffness parameters to the pathology of LV dysfunctions in patients. To understand the fundamental mechanism underlying this link would be a promising research area.

The main challenge in this direction of clinical validation is the data acquisition and data quality. Both pressure and deformation data need to be complete and temporally aligned. The acquisition of MRI in disease conditions is specially challenging due to breathing and heart rhythm irregularities. It is therefore important to assess the uncertainty in the parameters estimated, the sensitivity of results to noise and bias in data. In addition, this thesis has analysed the effect of an offset in the pressure transient, but further work is needed to assess the impact of other sources of uncertainties in the clinical measurements.

The observed increase in the residual active tension in our patient cases can be well explained using the existing well-established cellular electrophysiological experiments and models (ten Tusscher et al. 2004, ten Tusscher and Panfilov 2006, Grandi et al. 2010). When the cell is depolarised, calcium ions are released into the intracellular space, which causes the myocyte to contract via the sliding-filament mechanism. During the repolarisation, if the cell's ability of pumping calcium and/or potassium ions back to extracellular compartment is decreased due to a reduction of key membrane proteins, the developed active tension remain high in the early diastole, limiting the LV to relax. The confirmation of this mechanism (i.e., blockage of a specific calcium or potassium channel) could be very interesting and significant for future research directions using electrophysiological experiments.

8.2.2 The usage of non-invasive LV pressure estimation methods

The results described in chapter 7 demonstrate that the LV pressure data, characterising the amount of force per unit area applied to the endocardium, is required to correctly es-

timate the material properties and residual active tension of the myocardium. However, current clinical methods of pressure acquisition employ invasive catheters, and their associated risks limit the wide application of the proposed methodology for the assessment of diastolic parameters. Results in chapter 7 also demonstrate the possibility of using relative pressure obtained via non-invasive methods (Krittian et al. 2012) to estimate the myocardial material properties, and further work is needed to confirm this hypothesis.

Specifically, pressure differences can be computed from the velocity data captured by phase-contrast MRI (Krittian et al. 2012). The possibility of using this information for the estimation of parameters requires the existence of an anatomical point of constant or known pressure, which is used to convert the relative measures into absolute values of pressure in the left ventricle. This imaging modality is also limited in temporal resolution (current technology enables the acquisition of 15 to 20 frames per heart beat), and the signal to noise ratio during diastole can be quite low. An alternative is the use of Doppler ultrasound for the acquisition of blood velocity (Yotti et al. 2011), a modality that offers much higher temporal resolution at the expense of a more limited field of view.

Alternatively, absolute values of blood pressure can be estimated through micro-bubble based ultrasound contrast agent (Dave et al. 2012). This method has been approved in the United States for clinical LV opacification studies, and has the potential to non-invasively monitor LV pressures in real-time, with reported pressure offset errors ranging from 0.025 to 0.33 kPa (Geoffrey et al. 2003). Due to its relatively high accuracy, performing non-invasive parameter estimation using pressure estimated from this method is promising.

8.2.3 Model assumptions

Patient-specific fibre structure

Cardiac fibre architecture has an important role in the cardiac function, affecting the electro-physiological and mechanical behaviour of the myocardium. In this study, due to the limitation of the data, rule-based fibre distribution is used (Usyk et al. (2000)), which does not incorporate directly the patient-specific measurements. Although previous studies (Niederer et al. 2009, Vendelin et al. 2002, Bovendeerd et al. 1992) have suggested that fibre orientation has a limited effect on organ scale metrics of cardiac function, the absence of patient-specific fibre orientation may influence the estimation of material anisotropies and the accuracy of AT estimated. To address this issue, in our group we are currently in the process of developing robust and time efficient methods which enable the creation of a human fibre model from in-vivo diffusion-tensor MR images (Toussaint et al. 2010, Lamata et al. 2010b). Using this data it will then be straightforward to incorporate a patient-specific fibre distribution model into our current framework.

Myocardial volume change

Most of the mechanical models in literature assume the material of myocardium to be incompressible. However, based on the displacements of three clinical data sets we have observed in our study that there could be up to a 10% of volume change. This level of volume change, which has been also reported in literature (Yin et al. 1996), is likely due to myocardium perfusion with distensible blood vessels. This finding implies that more works need to be done on accounting for the impressibility of myocardium, possibly by incorporating myocardial perfusion models (Lee et al. 2009, Marchesseau et al. 2010).

Boundary conditions

For the purpose of this study, the model in this thesis only represents the LV and does not include any representation of the right ventricular atrium, valve plane and pericardium. As a result, movement of the LV is less constrained. In this study, the model simulations aim at replicating patient-specific imaging measurements, and thus boundary conditions can be defined by recording the movement of the base and apex using the patient-specific data. However, to use the developed model in its predictive way would require generic boundary conditions which can approximate the effects of the absent structures around the LV. Niederer et al. (2009) investigated the impacts of different methods of defining generic boundary conditions by constraining the LV basal movement, suggesting that simulated end-diastolic volume is relative sensitive to boundary conditions. Beside these generic boundary conditions, another alternative could be to develop the so-called "pericardia constraint" using a pericardium model which was reported to lead to the physically realistic diastolic wall motion (Nash 1998).

Regional variation of material properties

For the present purpose of estimating homogeneous indices of myocardial stiffness and relaxation functions, the model in this thesis incorporated homogeneous material properties throughout the myocardium. In reality, micro-structural observations suggest that this can be an oversimplification of ventricular wall properties as the extend of branching between myocardial sheets changes across the ventricular wall, suggesting that myocardial stiffness could be transmurally varying (LeGrice et al. 1995, Nash 1998). This regional variation of material properties could be incorporated into the LV mechanical model. This would allow the regional parameter estimation, which could be potentially valuable for identifying regional myocardial infarction using data of patients with ischemic heart disease (Chabiniok et al. 2011).

8.2.4 Methods of parameter estimation

Currently in our clinical parameter estimation framework, we choose a robust but computationally expensive approach for sampling the parameter space. This enabled us to fully explore and understand the coupling relationships between parameter values. In the future, it would be possible to adopt more sophisticated but computationally effective approaches to directly estimate the coupling coefficients a and b, such as the sequential quadratic programming or SQP (Augenstein et al. 2005) or filtering approaches (Xi et al. 2011a).

The filtering approach using various Kalman filters is commonly employed as an effective framework for assimilating large amounts of noisy measurements into a dynamic model (Moireau et al. 2008). However, in the literature, it is not uncommon that mechanical models of the heart are presented and simulated in quasi-static form. This brings the questions as to what order should measurements be assimilated. This could be a valuable point for comparison and better understanding of the Kalman filter performance when applied to quasi-static systems.

Apart from those two main streams of optimization approach using SQP and filtering approaches, genetic algorithms (GA), which generate optimization solutions using techniques inspired by natural evolution such as inheritance, mutation, selection, and crossover (Bäck and Schwefel 1993), are promising choice. GA is highly parallel, problem independent, gradient-free, and reassures a high chance of reaching a global optimum by using random cross over and mutation operators, and starting with multiple random search points. Thus it has been widely used in large real-life optimization problems such as the financial trading model parameter estimation (Pictet et al. 1995) and engineering design optimization (Gen and Cheng 1999). For our problem, it could provide a good balance between the robustness of brute-force sampling method and the computation efficiency of the filtering and SQP approaches. However, the parameter estimation al-

gorithm proposed in chapter 6 (Xi et al. 2012a) cannot be translated directly into other optimization algorithms such as GA without modification. In particular, the problem lies in the unknown stress-free state, which cannot be easily treated as a single additional unknown parameter. One solution is to define an additional parameter as the index of the MR frame to which the stress-free state is close to (Xi et al. 2012a). In this way, GA algorithm could be effectively used and thus its robustness and efficiency can be leveraged to give an optimal estimation of model parameters within a clinical applicable time frame.

8.3 Conclusion

Imagine a scenario where a patient with symptoms of cardiac disease is referred to have a set of MR scans and other regular measurements of their heart, and the referring clinician gets a report including the 3D physiologically realistic virtual heart of that specific patient, informing in mechanistic detail how their heart beats and functions both at the macro (phenomenal) and the micro (physiological) levels. Moreover, the clinical report provides key indices of this virtual heart (e.g. the stiffness of his myocardium and the residual tension during the cardiac relaxation). This rich new set of information derived from the virtual physiologically realistic heart enables the clinician to quickly and accurately assess the disease condition and give appropriate treatment.

Achieving this goal is the ultimate aim of developing and personalising patient-specific computational cardiac models that, in turn, enable the estimation of immeasurable parameters and reveal derived metrics which effectively describe the functions of the heart. While this remains a difficult task, there are already a number of promising steps in this direction that can be found in the literature (e.g. Sermesant et al. 2006, Sermesant et al. 2011, Chabiniok et al. 2011, Delingette et al. 2012, Moireau and Chapelle 2011, Wong et al. 2010, Wang et al. 2009, Wang et al. 2010b). The work presented in this thesis has

been to further push forward the frontier of the current state-of-the-art research towards achieving this exciting goal (Xi et al. 2011a, Xi et al. 2011b, Xi et al. 2012a, Xi et al. 2012b).

References

Abraham, T., Lardo, A., and Kass, D. (2006). Myocardial Dyssynchrony and Resynchronization. Heart Failure Clinics, 2(2):179–192.

Allender, S., Scarborough, P., Peto, V., Rayner, M., Leal, J., Luengo-Fernández, R., and Gray, A. (2008). European cardiovascular disease statistics, 2008 Edition. British Heart Foundation and University of Oxford.

Atanackovic, T. and Guran, A. (2000). Theory of elasticity for scientists and engineers. Birkhauser.

Augenstein, K., Cowan, B., LeGrice, I., and Young, A. (2006). Estimation of cardiac hyperelastic material properties from MRI tissue tagging and diffusion tensor imaging. Medical Image Computing and Computer-Assisted Intervention–MICCAI 2006, pages 628–635.

Augenstein, K. F., Cowan, B. R., LeGrice, I. J., Nielsen, P. M. F., and Young, A. A. (2005). Method and apparatus for soft tissue material parameter estimation using tissue tagged magnetic resonance imaging. Journal of Biomechanical Engineering, 127(1):148–157.

Aurigemma, G. and Gaasch, W. (2004). Diastolic heart failure. New England Journal of Medicine, 351(11):1097–1105.

Bäck, T. and Schwefel, H. (1993). An overview of evolutionary algorithms for parameter optimization. Evolutionary computation, 1(1):1–23.

Bassingthwaighte, J., Hunter, P., and Noble, D. (2009). The cardiac physiome: perspectives for the future. Experimental physiology, 94(5):597–605.

Bonet, J. and Wood, R. (1997). Nonlinear continuum mechanics for finite element analysis. Cambridge University Press.

Bovendeerd, P., Arts, T., Huyghe, J., Van Campen, D., and Reneman, R. (1992). Dependence of local left ventricular wall mechanics on myocardial fiber orientation: a model study. Journal of biomechanics, 25(10):1129–1140.

Bradley, C., Pullan, A., and Hunter, P. (1997). Geometric modeling of the human torso using cubic Hermite elements. Annals of biomedical engineering, 25(1):96–111.

Brain, P. (1986). Galen on bloodletting: a study of the origins, development, and validity of his opinions, with a translation of the three works. Cambridge Univ Pr.

Brasseur, P. and Verron, J. (2006). The SEEK filter method for data assimilation in oceanography: a synthesis. Ocean Dynamics, 56(5):650–661.

Burkhoff, D., Mirsky, I., and Suga, H. (2005). Assessment of systolic and diastolic ventricular properties via pressure-volume analysis: a guide for clinical, translational, and basic researchers. American Journal of Physiology-Heart and Circulatory Physiology, 289(2):H501–H512.

Chabiniok, R., Moireau, P., Lesault, P.-F., Rahmouni, A., Deux, J.-F., and Chapelle, D. (2011). Estimation of tissue contractility from cardiac cine-mri using a biomechanical heart model. Biomechanics and Modeling in Mechanobiology, pages 1–22. 10.1007/s10237-011-0337-8.

Chandrashekara, R., Mohiaddin, R., and Rueckert, D. (2004). Analysis of 3-D myocardial motion in tagged MR images using nonrigid image registration. Medical Imaging, IEEE Transactions on, 23(10):1245–1250.

Chatterjee, K. (2009). The swan-ganz catheters: Past, present, and future a viewpoint. Circulation, 119(1):147–152.

Chen, M., Liu, S., Tieszen, L., and Hollinger, D. (2008). An improved state-parameter analysis of ecosystem models using data assimilation. Ecological Modelling, 219(3-4):317–326.

Chen, W., Han, D., and Han, D. (2007). Plasticity for structural engineers. J Ross Pub.

Costa, K., Holmes, J., and McCulloch, D. (2001). Modelling cardiac mechanical properties in three dimensions. Philosophical Transactions A, 359(1783):1233.

Criscione, J., Sacks, M., and Hunter, W. (2003). Experimentally tractable, pseudo-elastic constitutive law for biomembranes: I. Theory. Journal of biomechanical engineering, 125:94.

Criscione, J. C., Douglas, A. S., and Hunter, W. C. (2001). Physically based strain invariant set for materials exhibiting transversely isotropic behavior. Journal of the Mechanics and Physics of Solids, 49(4):871 – 897.

Dave, J., Halldorsdottir, V., Eisenbrey, J., Raichlen, J., Liu, J., McDonald, M., Dickie, K., Wang, S., Leung, C., and Forsberg, F. (2012). Noninvasive lv pressure estimation using subharmonic emissions from microbubbles. JACC Cardiovascular Imaging, 5(1):87.

Delingette, H., Billet, F., Wong, K. C. L., Sermesant, M., Rhode, K. S., Ginks, M., Rinaldi, C. A., Razavi, R., and Ayache, N. (2012). Personalization of cardiac motion and contractility from images using variational data assimilation. IEEE Trans. Biomed. Engineering, 59(1):20–24.

Dokos, S., Smaill, B., Young, A., and LeGrice, I. (2002). Shear properties of passive ventricular myocardium. American Journal of Physiology- Heart and Circulatory Physiology, 283(6):H2650.

Ebbers, T., Wigström, L., Bolger, A., Engvall, J., and Karlsson, M. (2001). Estimation of relative cardiovascular pressures using time-resolved three-dimensional phase contrast mri. Magnetic resonance in medicine, 45(5):872–879.

Ecabert, O., Perters, J., Schramm, H., Lorenz, C., Berg, J., Walker, M., Vembar, M., Olszewski, M., Subramanyan, K., Lavi, G., and Weese, J. (2008). Automatic model-

based segmentation of the heart in CT images. IEEE Transcations on Medical Imaging, 27(9):1189–1201.

Evensen, G. (2009). Data assimilation: The ensemble Kalman filter. Springer Verlag.

Forsberg, F., Liu, J., Shi, W., Furuse, J., Shimizu, M., and Goldberg, B. (2005). In vivo pressure estimation using subharmonic contrast microbubble signals: proof of concept. Ultrasonics, Ferroelectrics and Frequency Control, IEEE Transactions on, 52(4):581–583.

Franklin, G. F., Powell, J. D., and Emami-Naeini, A. (2005). Feedback Control of Dynamic Systems. Prentice Hall, 5th edition edition.

Fung, Y. (1981). Biomechanics: mechanical properties of living tissues. Springer.

Fung, Y. (1993). Biomechanics: mechanical properties of living tissues, 2nd edition. Springer.

Fuster, V., Alexander, R., and O'Rouke, R. (2001). Hurst's the Heart. McGraw-Hill Professional Publishing, 10th edition edition.

Gen, M. and Cheng, R. (1999). Genetic algorithms and engineering optimization, volume 7. Wiley-interscience.

Geoffrey, C., Rajkumar, C., Kooner, J., Cooke, J., and Bulpitt, C. (2003). Estimation of central aortic pressure by sphygmocor® requires intra-arterial peripheral pressures. Clinical Science, 105:219–225.

Golub, G., Greenbaum, A., Stuart, A., and Süli, E. (2005). Finite elements and fast iterative solvers. Oxford University Press.

Grandi, E., Pasqualini, F. S., and Bers, D. M. (2010). A novel computational model of the human ventricular action potential and ca transient. Journal of Molecular and Cellular Cardiology, 48(1):112 – 121. Special Issue: Ion Channels.

Guccione, J. and McCulloch, A. (1993). Mechanics of active contraction in cardiac muscle: part Iconstitutive relations for fiber stress that describe deactivation. Journal of biomechanical engineering, 115:72–81.

Guccione, J., McCulloch, A., and Waldman, L. (1991). Passive material properties of intact ventricular myocardium determined from a cylindrical model. Journal of Biomechanical Engineering, 113:42–55.

Guccione, J., Waldman, L., and McCulloch, A. (1993). Mechanics of active contraction in cardiac muscle: Part IICylindrical models of the systolic left ventricle. Journal of biomechanical engineering, 115:82–90.

Harvey, W., Bowie, A., and Willis, R. (1889). On the Motion of the Heart and Blood in Animals. Bell.

Hill, M. C. and Osterby, O. (2003). Determining extreme parameter correlation in ground water models. Ground Water, 41(4):420–30.

Holzapfel, G. and Ogden, R. (2009). Constitutive modelling of passive myocardium: a structurally based framework for material characterization. Philosophical Transactions of the Royal Society A: Mathematical, Physical and Engineering Sciences, 367(1902):3445–3475.

Hope, S., Meredith, I., and Cameron, J. (2008). Arterial transfer functions and the reconstruction of central aortic waveforms: myths, controversies and misconceptions. Journal of hypertension, 26(1):4.

Humphrey, J., Strumpf, R., and Yin, F. (1990). Determination of a constitutive relation for passive myocardium: I. A new functional form. Journal of Biomechanical Engineering, 112:333.

Hunter, P. (1995). Myocardial constitutive laws for continuum mechanics models of the heart. Advances in experimental medicine and biology, 382:303.

Hunter, P., Crampin, E., and Nielsen, P. (2008). Bioinformatics, multiscale modeling and the iups physiome project. Briefings in bioinformatics, 9(4):333–343.

Hunter, P., McCulloch, A., and Ter Keurs, H. (1998). Modelling the mechanical properties of cardiac muscle. Progress in biophysics and molecular biology, 69(2-3):289–331.

Hunter, P. and Pullan, A. (2001). FEM BEM notes. Departament of Engineering Science. The University of Auckland, New Zealand.

Huxley, A. and Niedergerke, R. (1954). Interference microscopy of living muscle fibres. Nature, 173(1):13.

Huxley, H., Hanson, J., et al. (1954). Changes in the cross-striations of muscle during contraction and stretch and their structural interpretation. Nature, 173(4412):973.

Julier, S., Ind, I., and Jefferson City, M. (2003). The spherical simplex unscented transformation. In American Control Conference, 2003. Proceedings of the 2003, volume 3.

Julier, S. and Uhlmann, J. (1997). A new extension of the Kalman filter to nonlinear systems. In Int. Symp. Aerospace/Defense Sensing, Simul. and Controls, volume 3, page 26. Citeseer.

Julier, S. and Uhlmann, J. (2002). Reduced sigma point filters for the propagation of means and covariances through nonlinear transformations. In Proceedings of the American Control Conference, volume 2, pages 887–892. Citeseer.

Julier, S., Uhlmann, J., and Durrant-Whyte, H. (1995). A new approach for filtering nonlinear systems. In Proceedings of the American Control Conference, volume 3, pages 1628–1632. American Automatic Control Council, Evanston, IL.

Kailath, T., Sayed, A., and Hassibi, B. (2000). Linear estimation. Prentice Hall NJ:.

Kalman, R. (1960). A new approach to linear filtering and prediction problems. Journal of basic Engineering, 82(1):35–45.

Karamanoglu, M., O'ROURKE, M., Avolio, A., and Kelly, R. (1993). An analysis of the relationship between central aortic and peripheral upper limb pressure waves in man. European heart journal, 14(2):160–167.

Katz, A. (2010). Physiology of the Heart. Lippincott Williams & Wilkins.

Kawaguchi, A., Sugimachi, M., Sunagawa, K., Ishibashi-Ueda, H., Karamanoukian, H., and Batista, R. (2001). Perioperative hemodynamics in patients undergoing partial left ventriculectomy. Journal of cardiac surgery, 16(1):48–55.

Klabunde, R. (2005). Cardiovascular physiology concepts. Lippincott Williams & Wilkins.

Klotz, S., Dickstein, M., and Burkhoff, D. (2007). A computational method of prediction of the end-diastolic pressure–volume relationship by single beat. Nature Protocols, 2(9):2152–2158.

Krittian, S. B., Lamata, P., Michler, C., Nordsletten, D. A., Bock, J., Bradley, C. P., Pitcher, A., Kilner, P. J., Markl, M., and Smith, N. P. (2012). A finite-element approach to the direct computation of relative cardiovascular pressure from time-resolved mr velocity data. Medical Image Analysis, 16(5):1029 – 1037.

Lamata, P., Niederer, S., Barber, D., Norsletten, D., Lee, J., Hose, R., and Smith, N. (2010a). Personalization of cubic hermite meshes for efficient biomechanical simulations. Medical Image Computing and Computer-Assisted Intervention–MICCAI 2010, pages 380–387.

Lamata, P., Niederer, S., Nordsletten, D., Barber, D. C., Roy, I., Hose, D. R., and Smith, N. (2011). An accurate, fast and robust method to generate patient-specific cubic hermite meshes. Medical Image Analysis, 15(6):801 – 813.

Lamata, P., Niederer, S., Plank, G., and Smith, N. (2010b). Generic Conduction Parameters for Predicting Activation Waves in Customised Cardiac Electrophysiology Models. Statistical Atlases and Computational Models of the Heart, pages 252–260.

Land, S., Niederer, S., and Smith, N. (2011). Efficient computational methods for strongly coupled cardiac electromechanics. Biomedical Engineering, IEEE Transactions on, PP(99):1.

Landis, E. M. (1976). Carl John Wiggers: May 28, 1883-April 29, 1963. National Academy of Sciences.

Le Tallec, P. (1994). Numerical methods for nonlinear three-dimensional elasticity. Handbook of numerical analysis, 3:465–622.

Lee, J., Niederer, S., Nordsletten, D., Le Grice, I., Smail, B., Kay, D., and Smith, N. (2009). Coupling contraction, excitation, ventricular and coronary blood flow across scale and physics in the heart. Philosophical Transactions of the Royal Society A: Mathematical, Physical and Engineering Sciences, 367(1896):2311–2331.

Lefebvre, T., Bruyninckx, H., and De Schuller, J. (2002). Comment on " A new method for the nonlinear transformation of means and covariances in filters and estimators" [and authors' reply] . IEEE Transactions on Automatic Control, 47(8):1406–1409.

LeGrice, I., Smaill, B., Chai, L., Edgar, S., Gavin, J., and Hunter, P. (1995). Laminar structure of the heart: ventricular myocyte arrangement and connective tissue architecture in the dog. American Journal of Physiology- Heart and Circulatory Physiology, 269(2):H571.

Lorusso, R., Milan, E., Volterrani, M., Giubbini, R., van der Veen, F., Schreuder, J., Picchioni, A., and Alfieri, O. (1997). Cardiomyoplasty as an isolated procedure to treat refractory heart failure. European journal of cardio-thoracic surgery, 11(2):363–372.

Lubliner, J. and Moran, B. (1992). Plasticity theory. Journal of Applied Mechanics, 59:245.

Luenberger, D. G. (1971). an introduction to observers. IEEE Transactions on automatic control, 16(6).

Maeder, M. T. and Kaye, D. M. (2009). Heart failure with normal left ventricular ejection fraction. Journal of the American College of Cardiology, 53(11):905–918.

Malvern, L. E. (1977). Introduction to the Mechanics of a Continuous Medium. Prentice Hall.

Marchesseau, S., Delingette, H., Sermesant, M., and Ayache, N. (2012). Fast parameter calibration of a cardiac electromechanical model from medical images based on the unscented transform. Biomechanics and modeling in mechanobiology, pages 1–17.

Marchesseau, S., Delingette, H., Sermesant, M., Cabrera-Lozoya, R., Tobon-Gomez, C., Moireau, P., Figueras i Ventura, R., Lekadir, K., Hernandez, A., Garreau, M., et al. (2013a). Personalization of a cardiac electromechanical model using reduced order unscented kalman filtering from regional volumes. Medical image analysis.

Marchesseau, S., Delingette, H., Sermesant, M., Sorine, M., Rhode, K., Duckett, S., Rinaldi, C. A., Razavi, R., and Ayache, N. (2013b). Preliminary specificity study of the bestel-clement-sorine electromechanical model of the heart using parameter calibration from medical images. Journal of the mechanical behavior of biomedical materials, 20:259–271.

Marchesseau, S., Heimann, T., Chatelin, S., Willinger, R., and Delingette, H. (2010). Fast porous visco-hyperelastic soft tissue model for surgery simulation: application to liver surgery. Progress in biophysics and molecular biology, 103(2):185–196.

McKinley, M. and O'loughlin, V. (2006). Human anatomy. McGraw-Hill Higher Education.

Moireau, P. and Chapelle, D. (2011). Reduced-order Unscented Kalman Filtering with application to parameter identification in large-dimensional systems. ESAIM: Control, Optimisation and Calculus of Variations (COCV), 17:380–405. doi:10.1051/cocv/2010006.

Moireau, P., Chapelle, D., and Le Tallec, P. (2008). Joint state and parameter estimation for distributed mechanical systems. Computer Methods in Applied Mechanics and Engineering, 197:659–677.

Moireau, P., Chapelle, D., and Le Tallec, P. (2009). Filtering for distributed mechanical systems using position measurements: Perspectives in medical imaging. Inverse Problems, 25(3):035010 (25pp). doi:10.1088/0266-5611/25/3/035010.

Nagel, E. and Schuster, A. (2010). Shortening Without Contraction: New Insights Into Hibernating Myocardium. JACC Cardiovascular Imaging, 3(7):731.

Nash, M. (1998). Mechanics and material properties of the heart using an anatomically accurate mathematical model. PhD Thesis-University of Auckland.

Nash, M. and Hunter, P. (2000). Computational mechanics of the heart. Journal of elasticity, 61(1):113–141.

Niederer, S., Plank, G., Chinchapatnam, P., Ginks, M., Lamata, P., Rhode, K., Rinaldi, C., Razavi, R., and Smith, N. (2010). Length-dependent tension in the failing heart and the efficacy of cardiac resynchronization therapy. Cardiovascular Research.

Niederer, S., Rhode, K., Razavi, R., and Smith, N. (2009). The importance of model parameters and boundary conditions in whole organ models of cardiac contraction. Functional Imaging and Modeling of the Heart, pages 348–356.

Niederer, S. and Smith, N. (2008). An improved numerical method for strong coupling of excitation and contraction models in the heart. Progress in biophysics and molecular biology, 96(1-3):90–111.

Niederer, S. and Smith, N. (2009). The Role of the Frank–Starling Law in the Transduction of Cellular Work to Whole Organ Pump Function: A Computational Modeling Analysis. PLoS Computational Biology, 5(4).

Nordsletten, D., Kay, D., and Smith, N. (2010). A non-conforming monolithic finite element method for problems of coupled mechanics. Journal of Computational Physics.

Nordsletten, D., Niederer, S., Nash, M., Hunter, P., and Smith, N. (2011). Coupling multi-physics models to cardiac mechanics. Progress in Biophysics and Molecular Biology, 104(1-3):77–88.

Oden, J. (1972). Finite elements of nonlinear continua. McGraw-Hill,New York.

Okamoto, R., Moulton, M., Peterson, S., Li, D., Pasque, M., and Guccione, J. (2000). Epicardial suction: a new approach to mechanical testing of the passive ventricular wall. Journal of biomechanical engineering, 122:479.

Omens, J., MacKenna, D., and McCulloch, A. (1993). Measurement of strain and analysis of stress in resting rat left ventricular myocardium. Journal of biomechanics, 26(6):665–676.

Pathmanathan, P., Gavaghan, D., and Whiteley, J. (2009). A comparison of numerical methods used for finite element modelling of soft tissue deformation. The Journal of Strain Analysis for Engineering Design, 44(5):391–406.

Patrick J. Lynch, C. C. J. (2010). Heart posterior left ventricular wall infarction.

Paulus, W. J., Tschöpe, C., Sanderson, J. E., Rusconi, C., Flachskampf, F. A., Rademakers, F. E., Marino, P., Smiseth, O. A., De Keulenaer, G., Leite-Moreira, A. F., et al. (2007). How to diagnose diastolic heart failure: a consensus statement on the diagnosis of heart failure with normal left ventricular ejection fraction by the heart failure and echocardiography associations of the european society of cardiology. European heart journal, 28(20):2539–2550.

Peters, J., Ecabert, O., Schmitt, H., Grass, M., and Weese, J. (2009). Local cardiac wall motion estimation from retrospectively gated ct images. In FIMH '09: Proceedings of the 5th International Conference on Functional Imaging and Modeling of the Heart, pages 191–200, Berlin, Heidelberg. Springer-Verlag.

Pham, D. (2001). Stochastic methods for sequential data assimilation in strongly nonlinear systems. Monthly weather review, 129(5).

Pham, D., Verron, J., and Gourdeau, L. (1998a). Filtres de kalman singuliers volutifs pourl'assimilation de donnes en ocanographie. Comptes Rendus - Academie des Sciences Paris, 326:255–260.

Pham, D. T. (1995). Assimilation of oceanic altimeter data using a quasi-geostropghic model and the extended kalman filter. Rapport technique du project IDOPT INRIA-CNRS, RT141.

Pham, D. T. (1996). A singular evolutive interpolated kalman filter for data assimilation in occeanography. Rapport technique, INRIA.

Pham, D. T. and Hoteit, I. (2002). Some variants of the singular evolutive extended kalman (seek) filter. IMA Talks on Data Assimilation in the Oceanic and Atmospheric Sciences, University of Minnesota.

Pham, D. T., Verronb, J., and Roubauda, M. C. (1998b). A singular evolutive extended Kalman filter for data assimilation in oceanography. Journal of Marine systems, 16(3-4):323–340.

Pictet, O., Dacorogna, M., Chopard, B., Oussaidene, M., Schirru, R., Tomassini, M., et al. (1995). Using genetic algorithms for robust optimization in financial applications. Neural Network World, 5(4):573–587.

Popham, A. (1945). The drawings of Leonardo da Vinci, with an introd. Reynal & Hitchcock.

Power, S. (1897). William Harvey. T. Fisher Unwin.

Rajagopal, V., Nash, M., Highnam, R., and Nielsen, P. (2008). The breast biomechanics reference state for multi-modal image analysis. Digital Mammography, pages 385–392.

Rueckert, D., Sonoda, L., Hayes, C., Hill, D., Leach, M., and Hawkes, D. (1999). Nonrigid registration using free-form deformations: application to breast MR images. IEEE Transactions on medical imaging, 18(8):712–721.

Sasayama, S., Nonogi, H., Sakurai, T., Kawai, C., Fujita, M., Eiho, S., and Kuwahara, M. (1984). Assessment of cardiac function by left heart catheterization: an analysis of left ventricular pressure-volume (length) loops. Journal of cardiography. Supplement, -(1):25–34.

Schmid, H., Nash, M. P., Young, A. A., and Hunter, P. J. (2006). Myocardial material parameter estimation-a comparative study for simple shear. Journal of Biomechanical Engineering, 128:742.

Schmid, H., O'Callaghan, P., Nash, M. P., Lin, W., LeGrice, I. J., Smaill, B. H., Young, A. A., and Hunter, P. J. (2008). Myocardial material parameter estimation-a nonhomogeneous finite element study from simple shear tests. Biomechanics and Modeling in Mechanobiology, 7(3):161–173.

Schmid, H., Wang, W., Hunter, P., and Nash, M. (2009). A finite element study of invariant-based orthotropic constitutive equations in the context of myocardial material parameter estimation. Computer Methods in Biomechanics and Biomedical Engineering, 12(6):691–699.

Sermesant, M., Chabiniok, R., Chinchapatnam, P., Mansi, T., Billet, F., Moireau, P., Peyrat, J., Wong, K., Relan, J., Rhode, K., Ginks, M., Lambiase, P., Delingette, H.,

Sorine, M., Rinaldi, C., Chapelle, D., Razavi, R., and Ayache, N. (2011). Patient-specific electromechanical models of the heart for the prediction of pacing acute effects in crt: A preliminary clinical validation. Medical Image Analysis, In Press (doi:10.1016/j.media.2011.07.003).

Sermesant, M., Coudière, Y., Delingette, H., Ayache, N., and Désidéri, J. (2001). An electro-mechanical model of the heart for cardiac image analysis. In Medical Image Computing and Computer-Assisted Intervention–MICCAI 2001, pages 224–231. Springer. always replaced this with Sermesant2006Electromechanical.

Sermesant, M., Moireau, P., Camara, O., Sainte-Marie, J., Andriantsimiavona, R., Cimrman, R., Hill, D., Chapelle, D., and Razavi, R. (2006). Cardiac function estimation from MRI using a heart model and data assimilation: advances and difficulties. Medical Image Analysis, pages 642–656.

Shi, W., Zhuang, X., Wang, H., Luong, D., Tobon-Gomez, C., Edwards, P., Rhode, K., Razavi, R., Ourselin, S., and Rueckert, D. (2012). A comprehensive cardiac motion estimation framework using both untagged and 3d tagged mr images based on non-rigid registration. Medical Imaging, IEEE Transactions on, PP(99):1.

Shishido, T., Sugimachi, M., Kawaguchi, O., Miyano, H., Kawada, T., Matsuura, W., Ikeda, Y., Sato, T., Alexander Jr, J., and Sunagawa, K. (1998). A new method to measure regional myocardial time-varying elastance using minute vibration. American Journal of Physiology- Heart and Circulatory Physiology, 274(4):H1404.

Simon, D. (2006). Optimal State Estimation: Kalman, H-infinity, and Nonlinear Approaches. John Wiley and Sons.

Smith, N., de Vecchi, A., McCormick, M., Nordsletten, D., Camara, O., Frangi, A., Delingette, H., Sermesant, M., Relan, J., Ayache, N., et al. (2011). euheart: personalized and integrated cardiac care using patient-specific cardiovascular modelling. Interface Focus, 1(3):349.

Smith, N., Nickerson, D., Crampin, E., and Hunter, P. (2004). Multiscale computational modelling of the heart. Acta Numerica, pages 371–431.

Solomon, S. and Stevenson, L. (2009). Recalibrating the barometer. Circulation, 119(1):13–15.

Song, S., Leahy, R., Boyd, D., Brundage, B., and Napel, S. (1994). Determining cardiac velocity fields and intraventricular pressure distribution from a sequence of ultrafast ct cardiac images. Medical Imaging, IEEE Transactions on, 13(2):386–397.

Steendijk, P., Tulner, S., Bax, J., Oemrawsingh, P., Bleeker, G., van Erven, L., Putter, H., Verwey, H., van der Wall, E., and Schalij, M. (2006). Hemodynamic effects of long-term cardiac resynchronization therapy analysis by pressure-volume loops. Circulation, 113(10):1295–1304.

Sun, K., Stander, N., Jhun, C., Zhang, Z., Suzuki, T., Wang, G., Saeed, M., Wallace, A., Tseng, E., Baker, A., et al. (2009). A Computationally Efficient Formal Optimization of Regional Myocardial Contractility in a Sheep With Left Ventricular Aneurysm. Journal of biomechanical engineering, 131:111001.

ten Brinke, E., Klautz, R., Tulner, S., Verwey, H., Bax, J., Schalij, M., van der Wall, E., Versteegh, M., Dion, R., and Steendijk, P. (2010). Long-term effects of surgical ventricular restoration with additional restrictive mitral annuloplasty and/or coronary artery bypass grafting on left ventricular function: Six-month follow-up by pressure–volume loops. The Journal of Thoracic and Cardiovascular Surgery, 140(6):1338–1344.

ten Tusscher, K., Noble, D., Noble, P., and Panfilov, A. (2004). A model for human ventricular tissue. American Journal of Physiology- Heart and Circulatory Physiology, 286(4):H1573.

ten Tusscher, K. and Panfilov, A. (2006). Alternans and spiral breakup in a human ventricular tissue model. American Journal of Physiology- Heart and Circulatory Physiology, 291(3):H1088.

Toussaint, N., Sermesant, M., Stoeck, C., Kozerke, S., and Batchelor, P. (2010). In vivo human 3d cardiac fibre architecture: reconstruction using curvilinear interpolation of diffusion tensor images. Medical Image Computing and Computer-Assisted Intervention–MICCAI 2010, pages 418–425.

Trefethen, L. N. (2009). Lecture Notes of numerical linear algebra, University of Oxford. http://www.comlab.ox.ac.uk/nick.trefethen/tcc.html.

Urheim, S., Bjornerheim, R., Endresen, K., Vatne, K., Rabben, S., Sorhus, V., and Smiseth, O. (2002). Quantification of left ventricular diastolic pressure-volume relations during routine cardiac catheterization by two-dimensional digital echo quantification and left ventricular micromanometer. JOURNAL-AMERICAN SOCIETY OF ECHOCARDIOGRAPHY, 15(3):225–232.

Usyk, T., Mazhari, R., and McCulloch, A. (2000). Effect of laminar orthotropic myofiber architecture on regional stress and strain in the canine left ventricle. Journal of Elasticity, 61(1):143–164.

van Brussel, T. (2010). Anatomy of the Human Heart.

Vendelin, M., Bovendeerd, P., Engelbrecht, J., and Arts, T. (2002). Optimizing ventricular fibers: uniform strain or stress, but not atp consumption, leads to high efficiency. American Journal of Physiology-Heart and Circulatory Physiology, 283(3):H1072–H1081.

Walker, J., Ratcliffe, M., Zhang, P., Wallace, A., Fata, B., Hsu, E., Saloner, D., and Guccione, J. (2005). MRI-based finite-element analysis of left ventricular aneurysm. American Journal of Physiology-Heart and Circulatory Physiology, 289(2):H692.

Wang, J. and Nagueh, S. (2009). Current perspectives on cardiac function in patients with diastolic heart failure. Circulation, 119(8):1146.

Wang, L., Wong, K., Zhang, H., Liu, H., and Shi, P. (2010a). A Statistical Physiological-Model-Constrained Framework for Computational Imaging of Subject-Specific Volumetric Cardiac Electrophysiology Using Optical Imaging and MRI Data. Statistical Atlases and Computational Models of the Heart, pages 261–269.

Wang, V., Lam, H., Ennis, D., Cowan, B., Young, A., and Nash, M. (2009). Modelling passive diastolic mechanics with quantitative MRI of cardiac structure and function. Medical Image Analysis, 13(5):773–784.

Wang, V., Lam, H., Ennis, D., Cowan, B., Young, A., and Nash, M. (2010b). Cardiac Active Contraction Parameters Estimated from Magnetic Resonance Imaging. Statistical Atlases and Computational Models of the Heart, pages 194–203.

Weiss, J., Maker, B., and Govindjee, S. (1996). Finite element implementation of incompressible, transversely isotropic hyperelasticity. Computer methods in applied mechanics and engineering, 135(1-2):107–128.

Welch, G. and Bishop, G. (1995). An introduction to the Kalman filter. University of North Carolina at Chapel Hill, Chapel Hill, NC.

Westermann, D., Kasner, M., Steendijk, P., Spillmann, F., Riad, A., Weitmann, K., Hoffmann, W., Poller, W., Pauschinger, M., Schultheiss, H., et al. (2008). Role of left ventricular stiffness in heart failure with normal ejection fraction. Circulation, 117(16):2051–2060.

Wong, C. and Shi, P. (2004). Finite deformation guided nonlinear filtering for multi-frame cardiac motion analysis. Medical Image Computing and Computer-Assisted Intervention–MICCAI 2004, pages 895–902.

Wong, K., Wang, L., Zhang, H., and Shi, P. (2010). Physiological Fusion of Functional and Structural Data for Cardiac Deformation Recovery. Medical Image Computing and Computer-Assisted Intervention–MICCAI 2010, pages 159–166.

Wong, K., Zhang, H., Liu, H., and Shi, P. (2007). Physiome-Model-Based State-Space Framework for Cardiac Deformation Recovery1. Academic radiology, 14(11):1341–1349.

Xi, J., Lamata, P., Lee, J., Moireau, P., Chapelle, D., and Smith, N. (2011a). Myocardial transversely isotropic material parameter estimation from in-silico measurements based on a reduced-order unscented kalman filter. Journal of the Mechanical Behavior of Biomedical Materials, 4(7):1090–1102.

Xi, J., Lamata, P., Niederer, S., Land, S., Shi, W., Zhuang, X., Ourselin, S., Duckett, S., Shetty, A., Rinald, C., Rueckert, D., Razavi, R., and Smith, N. (2012a). The estimation of patient-specific cardiac diastolic functions from clinical measurements. Medical Image Analysis (In publication). http://www.cs.ox.ac.uk/people/jiahe.xi/.

Xi, J., Lamata, P., Shi, W., Niederer, S., Rueckert, D., Duckett, S. G., Shetty, A. K., Rinald, C. A., Razavi, R., and Smith, N. (2011b). An automatic data assimilation framework for patient-specific myocardial mechanical parameter estimation. Functional Imaging and Modeling of the Heart, LNCS, 6666:392–400.

Xi, J., Lamata, P., and Smith, N. (2012b). Understanding the need of LV pressure for the estimation of LV diastolic function. Biomechanics and Modeling in Mechanobiology (Submitted). http://www.cs.ox.ac.uk/people/jiahe.xi/.

Yin, F., Chan, C., and Judd, R. (1996). Compressibility of perfused passive myocardium. American Journal of Physiology-Heart and Circulatory Physiology, 271(5):H1864–H1870.

Yin, F., Strumpf, R., Chew, P., and Zeger, S. (1987). Quantification of the mechanical properties of noncontracting canine myocardium under simultaneous biaxial loading. Journal of biomechanics, 20(6):577–589.

Yotti, R., Bermejo, J., Benito, Y., Antoranz, J. C., Desco, M. M., Rodrguez-Prez, D., Cortina, C., Mombiela, T., Barrio, A., Elzaga, J., and Fernndez-Avils, F. (2011). Non-invasive estimation of the rate of relaxation by the analysis of intraventricular pressure gradients. Circulation: Cardiovascular imaging, 4(2):94–104.

Zile, M., Baicu, C., and Gaasch, W. (2004). Diastolic heart failureabnormalities in active relaxation and passive stiffness of the left ventricle. New England Journal of Medicine, 350(19):1953–1959.

Zile, M. and Brutsaert, D. (2002). New concepts in diastolic dysfunction and diastolic heart failure: part i. Circulation, 105(11):1387–1393.